Hydrodynamics and Heat Transfer in Gas-Driven Liquid Film Flows

Hydrodynamik und Wärmeübertragung in gasgetriebenen Flüssigkeitsfilmströmungen

Zur Erlangung des akademischen Grades Doktor-Ingenieur (Dr.-Ing.)
genehmigte Dissertation von M.Sc. (TU) Dipl.-Ing. (FH) Mete Budakli aus Ebersbach
January 2015 – Darmstadt – D 17

TECHNISCHE
UNIVERSITÄT
DARMSTADT

Fachbereich
Maschinenbau

Institut für Technische
Thermodynamik

Hydrodynamics and Heat Transfer in Gas-Driven Liquid Film Flows

Hydrodynamik und Wärmeübertragung in gasgetriebenen Flüssigkeitsfilmströmungen

Vom Fachbereich Maschinenbau
an der Technischen Universität Darmstadt
zur
Erlangung des akademischen Grades eines Doktor-Ingenieurs (Dr.-Ing.)
genehmigte

DISSERTATION

vorgelegt von

M.Sc. (TU) Dipl.-Ing. (FH) Mete Budakli

aus Ebersbach

Berichterstatter:	Prof. Dr.-Ing. P. Stephan
1. Mitberichterstatterin	PD Dr.-Ing. habil. T. Gambaryan-Roisman
2. Mitberichterstatter	Prof. Dr.-Ing. habil. C. Tropea
Tag der Einreichung	25. Februar 2014
Tag der mündlichen Prüfung	13. Mai 2014

Darmstadt 2015
D17

Half of the Science is asking questions.

Eidesstaatliche Erklärung zur Dissertation

Hiermit versichere ich, die vorliegende Dissertation ohne Hilfe Dritter nur mit den angegebenen Quellen und Hilfsmitteln angefertigt zu haben. Alle Stellen, die aus Quellen entnommen wurden, sind als solche kenntlich gemacht. Diese Arbeit hat in gleicher oder ähnlicher Form noch keiner Prüfungsbehörde vorgelegen.

Mannheim, 25. Februar 2014 Mete Budakli

Acknowledgements

This PhD thesis was prepared during my employment as a research assistant at the Institute of Technical Thermodynamics of the Technische Universität Darmstadt. The study was funded by the German Research Foundation DFG (Deutsche Forschungsgemeinschaft) in the framework of the Collaborative Research Group SFB 568 "Flow and Combustion in Future Gas Turbine Combustion Chambers".

I would like to express my deepest gratitude to Prof. Dr.-Ing. Peter Stephan. He trusted me to work on this challenging and exciting research topic. Without his supervision and generous research freedom, this thesis would not have been possible. As much as this thesis is a reflection of my effort, it is also a reflection of Prof. Stephan's supervision.

I also gratefully acknowledge, with many thanks, the insightful comments and helpful suggestions of my second supervisor PD Dr.-Ing. habil. Tatiana Gambaryan-Roisman. Our long and intense scientific discussions were always extremely fruitful.

I also thank Prof. Dr.-Ing. habil. Cameron Tropea, head of the Institute of Fluid Mechanics and Aerodynamics Technische Universität Darmstadt, for agreeing to examine my thesis.

Cordial thanks go to all my colleagues from the institute for creating an excellent research environment. My deepest thanks go to Dr.-Ing. Nitin Karwa, who proofread my thesis and spent many hours with me scientifically discussing my research. Many thanks to Mr. Martin Still for the proof reading and suggestions for the overall structure of the thesis. I would like to acknowledge the collaboration of my project partner Mr. Jagannath Rao Marati, who worked numerically on the same task.

I have to mention the invaluable assistance of our technician Mr. Robert Schrod throughout my work in the laboratory. Also, I want to express my thanks to Mr. Andreas Güttler from the Institute of Fluid Mechanics and Aerodynamics Technische Universität Darmstadt for supporting me in velocity measurements with the hot-wire anemometer. I have to thank our secretaries Mrs. Gaby Gunkel, Mrs. Heike Kagerbauer, and our former secretary Mrs. Ingrid Benz for prompt organizational support. In addition, I would like to thank our system administrators Mr. Denis Schinko and Mr. Moritz Mattern. Thanks also to the institute workshop head Mr. Roland Berntheisel and his team for manufacturing accurate parts which were necessary for the success of my experimental facility.

I also thank my students Mr. Ensar Kaya, Mr. Sayed Iman Nejati, Mr. Christian Dorn, Mr. Jan Hickmann, Mr. Paul Taubert, Mrs. Samira Gruber, Mr. Sebastian Ebner, Mr. Sebastian Groß, Mr. Sebastian Göhler, and Mr. Tim Knoll for their decision and enthusiasm to perform their tasks in the framework of my doctoral research project. Furthermore, I want to thank Mr. Jakob Fischer and Mr. Christoph Schwarz from the

Institute of Production Management, Technology and Machine Tools for their support in manufacturing micro-structured parts.

Sincere thanks go to my mother and my father for their great support. Finally, I want to thank with strong personal indebtedness my eternal love, my wife Merve and my son Fatih Akif for being beside me during my PhD marathon. Many thanks for your understanding, patience, and help. I love you all.

Mannheim, 25. February 2014 Mete Budakli

Abstract

In many technical applications such as cooling systems used in chemical industry and fuel injection systems of modern gas turbines, thin liquid films driven by gravity or turbulent gas stream can be found. Since the thermo-hydrodynamic process in such liquid-gas flow configuration is rather complex, the transport mechanisms are not well understood. However, numerical simulations or theoretical models rely on these mechanisms. Experimental investigations are necessary in order to delineate this complex thermo-hydrodynamic phenomenon and to provide validation data to the theoreticians.

The main objective of this work is to study the hydrodynamics and convective heat transfer in gravity and gas-driven thin liquid films on uniformly heated walls. To achieve this, an experimental set-up has been designed and measurements were performed in a flow channel. The liquid film was annularly applied on a vertically mounted heated tube. In the arranged two-phase flow domain, both fluids were thermally and hydrodynamically developing. The Reynolds numbers of liquid and gas flows were varied between $80 - 800$ and $10^4 - 10^5$, respectively. The wall heat flux was kept constant at $15\,\mathrm{W cm^{-2}}$. The gas velocity profile in the flow channel was measured with hot-wire anemometry to determine the shear stresses on the dry wall surface.

The effect of surface topography of the wall was investigated. The hydrodynamics and heat transfer of gas-driven liquid films was studied on micro-structures heated tubes. The dynamics of the liquid film flow was recorded by high-speed shadowgraphy technique. Using the high-speed images, the wave amplitudes and wave frequencies were determined. A high-speed infrared camera was used to qualitatively visualize the film rupture on micro-structured surfaces. The wall temperature distribution in streamwise direction was measured using thermocouples embedded inside the heated wall. Correlations for Nusselt number at unstructured surfaces have been proposed.

This study reveals that the action of shear stress at a thin liquid layer flowing along an unstructured wall has a remarkable influence on the stability of the liquid-gas interface. Disturbances at the liquid film surface appear as the shear stress reaches a critical value. Measurements at various axial locations show that the fluctuations grow in the flow direction. The rate of growth is determined by the gas and liquid mass flow rates. With the increase in liquid Reynolds number, the liquid free-surface deformation is suppressed and the temporal film thickness fluctuations in the flow direction either decrease slightly or remain constant.

A significant enhancement in heat transfer happens when the shear stress at the liquid-gas interface increases. However, there exists a threshold level of shear stress, only beyond which this is true. This exists as identified by comparing the experimentally determined heat transfer coefficients with the solutions

of the classical Graetz-Nusselt model. Furthermore, the Nusselt numbers are compared with the Nusselt numbers of laminar, hydrodynamically and thermally developed falling films, falling films which develop thermally and those which are in the transition regime from laminar to turbulent flow, and with a turbulence model used from the literature. The comparison shows, that above gas Reynolds numbers larger than $7 \cdot 10^4$, the heat transfer coefficient is following the trend predicted by the turbulence model.

Micro-structures have significant influence on the waviness of gas-driven liquid films. With increasing shear stress and liquid mass flow rate, the film waviness increases. Especially micro-structures embossed with obstacles normal to the flow direction lead to large wave amplitudes and high wave frequencies at low shear stress compared to the unstructured surface and the surfaces, incorporating structures oriented parallel to the flow direction. At low liquid mass flow rates and high shear stress, the area of local film rupture increases. Furthermore, micro-structures significantly enhance the heat transfer compared to the unstructured surface. Especially micro-structures combined by longitudinal and horizontal geometries are very effective in heat transfer enhancement at low shear stress and comparably low liquid mass flow rates.

Zusammenfassung

In zahlreichen technischen Anwendungen, wie Kühlsysteme in der chemischen Industrie oder Kraftstoffeinspritzsystemen von modernen Gasturbinen, spielen gasgetriebene, dünne Flüssigkeitsfilme eine wichtige Rolle für den Wärmeübergang. Aufgrund der hohen Komplexität der thermo-hydrodynamischen Vorgänge, die in solchen Flüssig/Gas-Strömungen ablaufen, sind die Transportmechanismen nicht vollständig verstanden. Numerische Simulationen und theoretische Modellierungen sind auf deren Kenntnis jedoch angewiesen. Daher sind experimentelle Untersuchungen notwendig, die dieses komplexe thermo-hydrodynamische Phänomen beschreiben und den Theoretikern Validierungsdaten liefern.

Das Ziel der vorliegenden Doktorarbeit ist ein besseres Verständnis und Beschreibung der Hydrodynamik und des konvektiven Wärmeübergangs in gravitations- und gasgetriebenen dünnen Flüssigkeitsfilmen, die entlang an einer beheizten Wand strömen. Dafür wurde ein Versuchskanal aufgebaut und Experimente durchgeführt. Der Flüssigkeitsfilm wurde ringförmig an einem vertikal montierten beheizten Rohr aufgetragen. Das entsprechende Zwei-Phasenströmungsfeld wurde so konfiguriert, dass sich beide Fluide sowohl thermisch als auch hydrodynamisch entwickeln konnten. Die Reynolds-Zahlen der Flüssigkeits- und Gasströmung wurden im Bereich von 80 bis 800 bzw. 10^4 bis 10^5 variiert. Die Wandwärmestromdichte wurde bei $15\,\mathrm{W cm^{-2}}$ konstant gehalten. Um die Scherspannung an der beheizten Wand zu bestimmen, wurden die Geschwindigkeitsprofile der Gasströmung im Versuchskanal mit der Hitzdrahtanemometrie gemessen. Außerdem wurde der Einfluss der Oberflächentopographie der beheizten Wand ermittelt. Hierfür wurden die Hydrodynamik und der Wärmeübergang von gasgetriebenen Flüssigkeitsfilmen auf mikrostrukturierten, beheizten Rohroberflächen studiert.

Zur Untersuchung der Filmdynamik, wurden schattenfotographische Hochgeschwindigkeitsaufzeichnungen durchgeführt und daraus die Wellenamplituden und Wellenfrequenzen der Filmströmung bestimmt. Der Filmaufriss an mikrostrukturierten Oberflächen wurde mit einer Hochgeschwindigkeits-Infrarotkamera qualitativ visualisiert. Die Wandtemperaturverteilung in Strömungsrichtung wurde mit Thermoelementen gemessen. Korrelationen zur Berechnung von Nußelt-Zahlen für die unstrukturierten Oberflächen wurden vorgeschlagen.

Diese Studie zeigt, dass die Stabilität der Flüssigkeits/Gas-Grenzfläche von gasgetriebenen Flüssigkeitsfilmen an unstrukturierten Oberflächen erheblich von der Scherspannung beeinflusst wird. Störungen bzw. Instabilitäten an der Filmoberfläche treten ein, sobald die Scherspannung einen kritischen Wert erreicht. Messungen zeigen, dass die Instabilitäten in Strömungsrichtung wachsen. Dabei wird die Entwicklung der Instabilitäten durch die Gas- und Flüssigkeitsmassenströme bestimmt. Mit der Zunahme der Flüssigkeits-Reynolds-Zahl werden die Deformationen an der freien Oberfläche der Flüssigkeit un-

terdrückt, die Fluktuationen der Filmdicke in Strömungsrichtung hingegen nur geringfügig bis gar nicht reduziert.

Eine wesentliche Verbesserung der Wärmeübertragung tritt ein, wenn die Scherspannung an der Flüssigkeits/Gas-Grenzfläche ansteigt, vorausgesetzt eine bestimmte kritische Scherspannung ist überschritten. Letzteres wurde insbesondere für die Filmströmung an einer unstrukturierten Oberfläche untersucht. Die Existenz dieses Schwellenwertes wurde durch den Vergleich der experimentell ermittelten Nußelt-Zahlen mit dem klassischen Graetz-Nußelt-Modell identifiziert. Darüber hinaus wurden die Nußelt-Zahlen aus dem Experiment mit denen von Fallfilmen unterschiedlicher thermohydrodynamischer Strömungszustände aus der Literatur verglichen. Für Scherspannungen unterhalb des Schwellenwertes sind die experimentellen Nußelt-Zahlen vergleichbar mit den Nußelt-Zahlen von laminaren, hydrodynamisch und thermisch entwickelten Fallfilmen bzw. von Fallfilmen, die im thermischen Anlauf sind oder sich im Übergangsbereich von laminar zu turbulent befinden. Ein weiterer Vergleich mit einem in der Literatur vorliegenden Turbulenzmodell zeigt, dass die Nußelt-Zahlen für Gas-Reynolds-Zahlen größer $7 \cdot 10^4$ der Prognose des Turbulenzmodells folgen und somit höher sind als die mit geringerer Gas-Reynolds-Zahl.

Mikrostrukturen haben einen signifikanten Einfluss auf die Welligkeit von gasgetriebenen Flüssigkeitsfilmen. Mit wachsender Scherspannung und Flüssigkeitsmassenstrom, nimmt auch die Filmwelligkeit zu. Besonders Mikrostrukturen, die rechtwinklige Hindernisse zur Strömungsrichtung darstellen, führen zu großen Wellenamplituden und hohen Wellenfrequenzen bei geringer Scherspannung. Im Vergleich dazu sind die Wellenamplituden und Wellenfrequenzen von gasgetriebenen Filmströmungen an unstrukturierten Oberflächen und Oberflächen, mit parallel zur Strömungsrichtung angeordneten Strukturen geringer. Außerdem kommt es häufiger zu lokalen Filmaufrissen bei geringerem Flüssigkeitsmassenstrom und höherer Scherspannung. Durch den Einsatz von Mikrostrukturen kann eine wesentliche Verbesserung der Wärmeübertragung verglichen mit der unstrukturierten Oberfläche erreicht werden. Besonders Oberflächen, die mit zur Strömungsrichtung längs- und horizontalangeordneten Geometriekombinationen versehen sind, führen zu einer Erhöhung der Wärmeübertragung bei verhältnismäßig geringer Scherspannung und geringem Flüssigkeitsmassenstrom.

Contents

List of Figures

List of Tables

Nomenclature

Roman Symbols

Symbol	Meaning	SI unit
a	Length	[µm]
A	Area	$[\mathrm{m}^2]$
A	Coefficient	[–]
b	Width	[m]
B	Length	[m]
c	Length	[m]
c	Concentration	$[\mathrm{mol/m}^3]$
c_p	Specific heat capacity	[J/(kgK)]
C	Pressure correction coefficient	[–]
d	Diameter	[m]
e	Length	[µm]
E	Energy	[E]
f	Frequency	[kHz]
f	Width	[m]
F	Force	[N]
g	Length	[m]
g	Gravitational acceleration	$[\mathrm{m/s}^2]$
h	Thickness, height	[m]
H	Height	[m]
I	Electrical Current	[A]
I	Intensity	[W/sr]
I	Momentum	[(kgm)/s]
k	Absorption coefficient of water	[1/cm]
l	Length	[m]
M	Mass	[kg]
n	(Sequential) number	[–]
p	Pressure	$[\mathrm{N/m}^2]$
P	Position	[–]
$\dot{q}$	Heat flux density	$[\mathrm{W/cm}^2]$
r	Radial coordinate	[µm, m]

Roman Symbols

Symbol	Meaning	SI unit
R_a	Arithmetic mean of surface roughness	[µm]
R_z	Maximum of surface roughness	[µm]
s	Wall thickness	[m]
t	Time	[s], [ms]
t	Width	[m]
T, t	Temperature	[K], [°C]
u	Velocity	[m/s]
U	Perimeter	[m]
V	Voltage	[V]
W	Point	[–]
$W(z)$	Tube deflection	[m]
x	Cartesian coordinate (length)	[m]
X	Relative humidity	[−]
y	Cartesian coordinate (height)	[m]
z	Axial coordinate, Cartesian coordinate (width)	[m]
z	Length	[m]

Greek Symbols

Symbol	Meaning	SI unit
α	Convective heat transfer coefficient	$[\mathrm{W/(m^2K)}]$
β	Angle	[°]
γ	Angle	[°]
δ	Thickness of boundary layer	[µm]
δ	Angle	[°]
Δ	Difference	[–]
ϵ	Angle	[°]
η	Surface increase factor	[–]
ϑ	Dimensionless temperature	[–]
κ	Spatial resolution	[µm]
λ	Wave length	[µm]
λ	Thermal conductivity	$[\mathrm{W/(mK)}]$
Λ	Eigenvalue	[–]
μ	Dynamic viscosity	$[\mathrm{kg/(ms)}]$
ν	Kinematic viscosity	$[\mathrm{m^2/s}]$
ξ	Friction coefficient	[–]
ρ	Density	$[\mathrm{kg/m^3}]$
σ	Standard deviation	[µm]
$\varsigma(\tilde{z})$	Auxiliary function to solve the Graetz-Nusselt problem	[–]
τ	Shear stress	$[\mathrm{N/m^2}]$
φ	Angular coordinate	[µm]
φ	Ratio of outer diameter to inner diameter	[–]
$\varGamma$	Specific flow rate	$[\mathrm{kg/(ms)}]$
$\varPhi$	Weight slope function	[–]
ψ	Eigenfunction	
$\varTheta$	Diagonal coordinate	[µm]

Dimensionless Groups

Symbol	Meaning
Bi	Biot number of liquid $= (\alpha \cdot h)/\lambda$
Ka	Kapitza number $= \left[\left(g\mu^4\right) / \left(\rho\sigma^3\right)\right]$
K_F	Film number $= Ka^{-1}$
Nu	Nusselt number
Pe	Péclet number $= RePr$
Pr	Prandtl number of the gas $= (\mu c_p)/\lambda$
Re	Reynolds number

Subscripts

Symbol	Meaning
abs	Absolute
c	Correlation
crit	Critical
cal	Calibration
CH	Flow Channel
dev	Development
dyn	Dynamic
e	End
ET	Evaporator Tube
FD	Film Distributor
G	Gas
GRN	Graetz-Nusselt
GS	Glass scale
hyd	Hydraulic
HC	Heating cartridge
HWA	Hot wire anemometer
H2O	Water
i	Sequential number
in	Inlet, inner
IR	Infrared
j	Sequential number
k	Sequential number
lam	Laminar
L	Liquid
m	Mean value
max	Maximum
min	Minimum
NI	National Instruments
sat	Saturation
stat	Static
o	Sequential number
out	Outlet, outer
O	Symbol for unstructured tube
pix	Pixel
poly	Polynomial
s	Start
S	Sequential number
struc	Structure
SG	Shadowgraphy
SV	Sleeve

Subscripts

Symbol	Meaning
T	Thermal
TC	Thermocouple
TS	Micrometer travel stage
V	Vapor
w	Wave
W	Wall
Δ	Symbol for pyramid structured tube
∇	Symbol for longitudinal V-groove structured tube
2D	2D model

Superscripts

Symbol	Meaning
¯	Mean value
$*$	Customized, dimensionless
˙	Time derivation
˜	Dimensionless

Abbreviations

Symbol	Meaning
AC	Alternating current
AI	Analog input
AISI	American iron and steel institute
AO	Analog output
A/D	Analog to digital converter
b/w	Black and white
CaF_2	Calcium fluoride
CAD	Computer aided design
CCD	Charge coupled device
CFD	Computational fluid dynamics
CHR	Confocal chromatic sensor
CTA	Constant temperature anemometer
DAQ	Data acquisition
DKD	Deutscher Kalibrierdienst (German calibration service)
DOF	Depth of field
FG	Frame grabber
FOV	Field of view
GRN	Graetz-Nusselt
HSC	High speed camera (black and white)
HWA	Hot wire anemometer
IR	Infrared
IRC	Infrared camera
LDMO	Long distance microscope objective
LED	Light-emitting diode
LPP	Lean premixed pre-vaporization
LS	Light source
MT	Manufacturing tolerance
MV	Measured value
NI	National Instruments
RGB	Red, green, blue color model

1

Introduction

1.1 Motivation

Thin liquid films play an important role in engineering, biophysics and physics [110]. Evaporating thin liquid film flows can be encountered in many technical applications including cooling systems for the thermal control of microelectronics, in the chemical industry and in power generation [14, 71]. A distinction has to be made between an evaporating liquid film which is solely driven by gravitation (falling film) or a vaporizing liquid layer sheared through a turbulent gas stream (gas-driven film). For the production of concentrated liquids, the separation of chemical components or even for gas scrubbing, evaporating falling films are used in thermal processes [25, 58, 70]. Generally, these films evaporate at saturation conditions existing at the liquid film surface. However, they can also vaporize in unsaturated conditions. The heat transfer depends on the liquid temperature and the vapor's partial pressure in the gas stream. To obtain optimal heat and mass transfer rates, the temperature of the heated wall has to be kept at moderate conditions. Besides this aspect, attention also has to be paid to preventing the liquid from rupturing. High heat transfer rates can be achieved using thin liquid layers. This can be additionally supported by the effect of a wavy liquid-gas interface.

Apart from large-scale applications, another very interesting utilization of liquid film evaporation can be found in the nozzle walls of rocket engines [12]. These walls are subjected to very high heat fluxes, and a thin liquid film flow enables safe operation by keeping the wall temperature low. Another application of thin film flows can be found in fuel preparation systems used in internal combustion engines or modern gas turbines [38, 121]. Compared to pure gravity-driven films, thin liquid films in such devices propagate along a wall assisted by a co-currently streaming turbulent gas. In Fig. 1.1, the two-phase flow configuration of this industrial application is shown, incorporating the unsteady complex coupling of mechanisms transporting mass, momentum and energy. Initially, the liquid fuel is primarily atomized through a pressure nozzle (A). At the same time, hot turbulent gas streams clockwise and anticlockwise through several inlets radially oriented into the atomizer system (B). Liquid droplets with low inertia do not impact the liquid film, since they are captured by the gas flow and stream towards the inlet of the combustion chamber [8]. In contrast, droplets with high inertia strike the heated wall and form a thin film (see Fig. 1.1a). The liquid film is heated from the wall side (C). Concurrently, the co-current gas stream accelerates the thin film and heats it up also (D). Thus, the liquid film recognizes disturbing impacts leading to the destabilization and distortion of the film. The deformation is due to the strong interfacial shear force acting at the liquid-gas interface. Multi-frequent, non-periodic, three-dimensional waves form with steep fronts propagating along the wall and result in a complex state of flow. This phenomenon is significantly determined by thermo-hydrodynamic mechanisms and topographical influences (see Fig. 1.1b) [110]. Both the fluids are normally turbulent and propagate within the thermally and hydrodynamically developing regime. Frequently, droplets are shed from the liquid film as shown in Fig. 1.1c and transported towards the exit. Along the way, they partly evaporate and mix with the gas phase [118]. It has been observed previously that the hydrodynamics of the wavy film strongly influence the atomization/break-up of the liquid film and fuel-air mixing process, which thus governs the overall process for fuel preparation [15, 38].

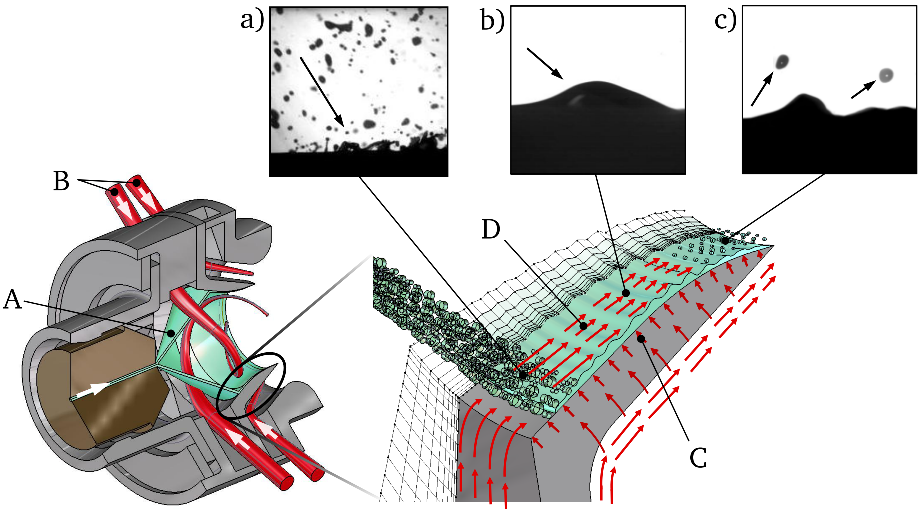

Figure 1.1. Left: CAD model of an LPP airblast atomizer; Right: Detailed view of near-wall phenomena: a) Fuel droplet impact and film formation through droplet accumulation, b) Evaporation of liquid film and wave generation by hot turbulent gas streams, c) Droplet entrainment through strong shear forces at the liquid-gas interface.

Besides fuel preparation processes, devices used to cool of electronics employ gas-driven liquid films to transfer heat from hot substrates [14]. For the range of typical operating parameters in such systems, liquid film flows under the action of a gas stream are less vulnerable to break-up compared to falling films [73]. Through the action of a gas stream, the heat transfer rates can be increased significantly compared to systems in which the cooling is achieved by only an air or liquid flow. Additionally, topographical variations at the surface of the wall lead to a higher thermo-hydrodynamic complexity of the transport mechanisms within the near-wall liquid bulk flow. As a result, the hydrodynamics and heat and mass transfer can be strongly influenced by applying appropriate micro-structuring at the hot wall [46, 63, 75, 146]. Previously, the hydrodynamics, heat and mass transfer in falling and gas-driven films have been intensively studied in many experimental, numerical and theoretical works. However, the understanding of the complex transport mechanisms leading to the enhancement of the heat transfer in both laminar and turbulent wavy two-phase flows is insufficient. To predict the overall performance and optimal operating conditions of systems mentioned above, highlighting the interdependence of relevant physical parameters, is a challenging task.

1.2 Outline of the thesis

The thesis is structured as follows:

Chapter 1:

This chapter presents some exemplary industrial applications involving the thin film cooling/evaporation process. The major conditions during thin fuel film evaporation are briefly described using the two phase flow configuration in an airblast atomizer system.

Chapter 2:

This chapter describes the historical progress of theoretical modeling and the research activities carried out on thin liquid film flows over the last century. Significant findings about the hydrodynamic behavior and the heat transfer in gravity-driven and gas-driven films are summarized. Along with this, different phenomena affecting the transport of mass and heat reported in the literature are discussed. Especially the importance of interfacial shear at the liquid film surface is emphasized, followed by the benefits of surface micro-structuring. Finally, open scientific questions and the major objectives of this work are presented.

Chapter 3:

In this chapter, the experimental setup, the method for the design of the micro-structures, and the experimental parameters used in this study are presented.

Chapter 4:

This chapter contains the description of the data acquisition system and the measurement techniques used to determine the hydrodynamic parameters and heat transfer coefficients.

Chapter 5:

In this chapter, the data analysis process, the procedure for the development of correlations for the prediction of heat transfer coefficients, and the theoretical methods used to determine the governing heat transfer mechanism are described. The calibration procedures for the thermal imaging technique and gas velocity measurement are presented.

Chapter 6:

This chapter includes the error analysis and the uncertainty estimation concerning the relevant hydrodynamic and calculated heat transfer parameters.

Chapter 7:

In this chapter, the results concerning hydrodynamics and heat transfer in gravity and gas-driven films are discussed. The effect of shear stress at the liquid-gas interface on the thermo-hydrodynamic phenomena is elucidated and the heat transfer results are compared with theoretical estimates. This is followed by a discussion about the influence of different surface topographies on the overall process.

Chapter 8:

In the last chapter, the relevant findings from this work are summarized. Finally, an outlook for future research on this subject is presented.

2

State of the Art

This chapter presents a review of the state of art on gravity and gas-driven film flows. The major recent findings regarding thermo-hydrodynamics of such flows have been summarized. Micro-structures on the wall have been known to enhance the heat transfer in thin film flows. The penultimate section summarizes the thermal performance of various micro-structures. In the final section, drawn inferences are summarized and the objectives of this thesis are outlined.

2.1 Falling liquid film flow

Various theoretical, numerical, and experimental studies which have been carried out within the last century have revealed that the determination of the governing thermo-hydrodynamic transport mechanisms of thin film flows is rather challenging. To date, the overall heat transfer process has not been fully understood.

One of the first well-established descriptions of the hydrodynamics and heat transfer in falling liquid films was presented in 1916 by Nußelt [108]. He considered the formation of a liquid layer through the steady-state condensation of a saturated vapor on a vertically aligned sub-cooled wall. The liquid layer flow was treated as a laminar. The hydrodynamics and heat transfer in the liquid film was modeled through the integration of the equations of the motion of a viscous liquid and the energy equation. Through this almost a century old but epoch-making theory, it is possible to predict quite accurately the local and overall heat transfer coefficients as well as the film thicknesses for gravity-driven wave-free film flows. However, theoretical and experimental studies reveal that laminar liquid films flowing down a vertical wall can become, depending on the flow conditions, unstable even at low Reynolds numbers [7, 65, 78, 79]. They can transfer from a laminar to wavy-laminar and to a wavy-turbulent flow [1].

A large body of scientific literature has been dedicated to understanding these complex film flows, especially those deviating from Nußelt's theory. In particular, several investigations were performed in the past in terms of thin film flow stability and long-scale evolution [17, 110]. Using statistical investigations for the analysis of the film stability, it is reported that the variation of film thickness has a random character incorporating large lumps of liquid carrying the major amount of liquid mass without constant velocity and stable shape [1, 100, 133, 143]. Compared to smooth homogeneous films, this inhomogeneity plays a significant role in enhancing heat transfer [1, 84, 124]. The rate of convective heat transfer depends strongly on the thickness and the state of the film flow [27, 84]. The liquid temperature near the wall is also determined by the waviness of the liquid film flow [93]. Challenging analytic calculations are required to predict the influence of waviness and sweeping of liquid [101]. It has been found that a heat transfer enhancement of up to $80\,\%$ can be achieved due to waves in a laminar thin film flow [99]. The transport process in heated liquid films can be also affected by instabilities induced through the coupling of surface and thermo-capillary waves deforming the liquid-gas interface [69, 119].

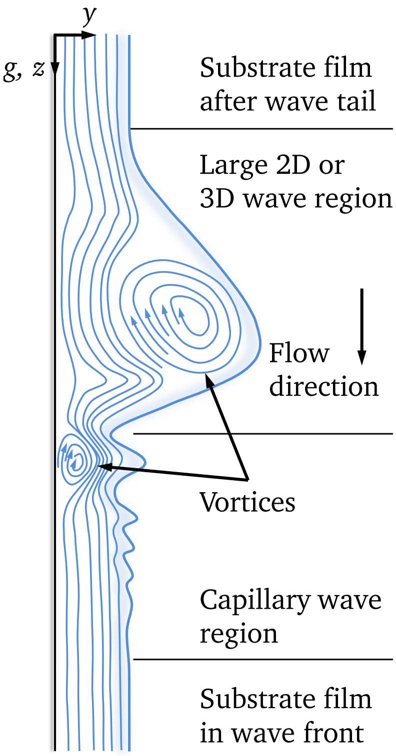

Figure 2.1. Wavy film flow with capillary waves and inter-wave thin substrate film.

Besides the large waves, short waves, called the capillary waves and with small amplitudes, slowly move and cover the thin substrate film appearing between large waves (see Fig. 2.1). It is stated that the heat and mass transfer into the film is considerably affected by this thin substrate film, while the form and magnitude of large waves also play an essential role [25]. The latter carry the major amount of liquid and also lead to heat transfer enhancement [68]. Especially for the substrate film, it is known that the majority of the heat is conducted through this thin layer of liquid. The smooth substrate film is continuously deformed by a strong thinning process caused by the motion of large waves [1, 68]. The transfer process into the gas stream is governed by the small waves traveling on the substrate film [26]. The small-amplitude waves are slowly moving and are overtaken by larger waves, hence they are suppressed immediately over a short distance in flow direction. During the overtaking process, waves with greater amplitudes are formed [133, 143]. This mechanism keeps on going until the liquid film is sheltered solely by very large waves with great distances to each other. A rise in liquid mass flow rate leads to an increase in wave velocity, which does not vary considerably with the flow direction, and enhances the heat transfer [43, 77]. Moreover, the heat transfer rate can be increased by affecting the hydrodynamics of the film flow, adding surfactants which change the fluid-physical property [77]. Due to the fact that the liquid film wetting behavior is improved, a larger area coverage results. This causes better thermal transport from the wall to the liquid film [77].

In most of the cases, a single large wave is formed through the conglomeration of many waves which grows and accelerates. However, at the surface of the large waves, smaller waves can appear which survive only over a short distance [133]. Generally, the waves are propagating periodically initiated through disturbances [7]. 2D periodic perturbations appear. They form after a particular distance due to natural instability of the smooth laminar flow [7]. Their amplitude rises fast with increasing distance and they become stationary waves [7, 132]. However, running larger liquid mass flow rates can lead to the suppression of waves [35, 122, 132]. Moreover, the film waviness can be strongly stabilized or even damped by using surface active impurities introducing higher surface tension. The liquid film flow stability improves when using high concentrations of surfactant, which leads to a decrease in wave length [104]. Nevertheless, experiments revealed the appearance of larger wavelengths in contaminated liquid films.

The relevant parameter concerning the onset of waviness in gravity-driven films is the film number $K_\mathrm{F} = \left(\rho_\mathrm{L}{\sigma_\mathrm{L}}^3\right) / \left(g{\mu_\mathrm{L}}^4\right)$ or the Kapitza number which are widely used in the literature [78, 79, 135]:

$$Ka = \frac{1}{K_\mathrm{F}} = \frac{{We_\mathrm{L}}^3}{Fr_\mathrm{L}{Re_\mathrm{L}}^4} = \frac{g{\mu_\mathrm{L}}^4}{\rho_\mathrm{L}{\sigma_\mathrm{L}}^3}. \tag{2.1}$$

Another dimensionless parameter that is used to determine the point at which the film flow transfers into an unstable behavior is the Reynolds number [13]. Usually the Reynolds number of thin liquid film flows is defined in the literature as:

$$Re_\mathrm{L} = \frac{\Gamma_\mathrm{L}}{\mu_\mathrm{L}} = \frac{\dot{M}_\mathrm{L}}{U_\mathrm{L}\mu_\mathrm{L}}. \tag{2.2}$$

It is important to mention that in some scientific papers, Re_L is defined as:

$$Re_\mathrm{L} = \frac{\bar{u}_\mathrm{L}d_\mathrm{hyd}}{\nu_\mathrm{L}} = \frac{4\Gamma_\mathrm{L}}{\mu_\mathrm{L}} = \frac{4\dot{M}_\mathrm{L}}{U_\mathrm{L}\mu_\mathrm{L}}. \tag{2.3}$$

The difference between both equations is due to the assumption that in the second definition, the hydraulic diameter d_hyd is equal to $4h_\mathrm{L}$. In this thesis the Reynolds number is determined by the definition according to Eq. 2.2.

The sensitivity for destabilization of the film flow can be increased by heating the liquid film [13]. Fluctuations of the temperature cause strong surface tension variations. The effect of destabilization further grows when film evaporation occurs. Subsequently, a wetting front appears and develops into fingers propagating over dry patches [110]. This effect sets on when the heat flux is kept constant and the liquid load is lowered. At the wetting front where the solid, liquid, and gas phases merge together large temperature variations can exist [127].

Five major film flow regimes can be distinguished (exemplarily presented for a vertically falling liquid film in Fig. 2.2). They can be categorized in detail into [66, 149]:

- laminar flow with a wave-free liquid-gas interface, $Re_{\mathrm{L}} \leq 0.47 K_{\mathrm{F}}{}^{(1/10)}$
- first transition regime, $0.47 K_{\mathrm{F}}{}^{(1/10)} \leq Re_{\mathrm{L}} \leq 2.2 K_{\mathrm{F}}{}^{(1/10)}$
- wavy flow incorporating stable wavy motions containing turbulence, $2.2 K_{\mathrm{F}}{}^{(1/10)} \leq Re_{\mathrm{L}} \leq 75$
- second transition region, $75 \leq Re_{\mathrm{L}} \leq 400$
- fully developed flow with a turbulent boundary layer at the wall $400 \leq Re_{\mathrm{L}}$

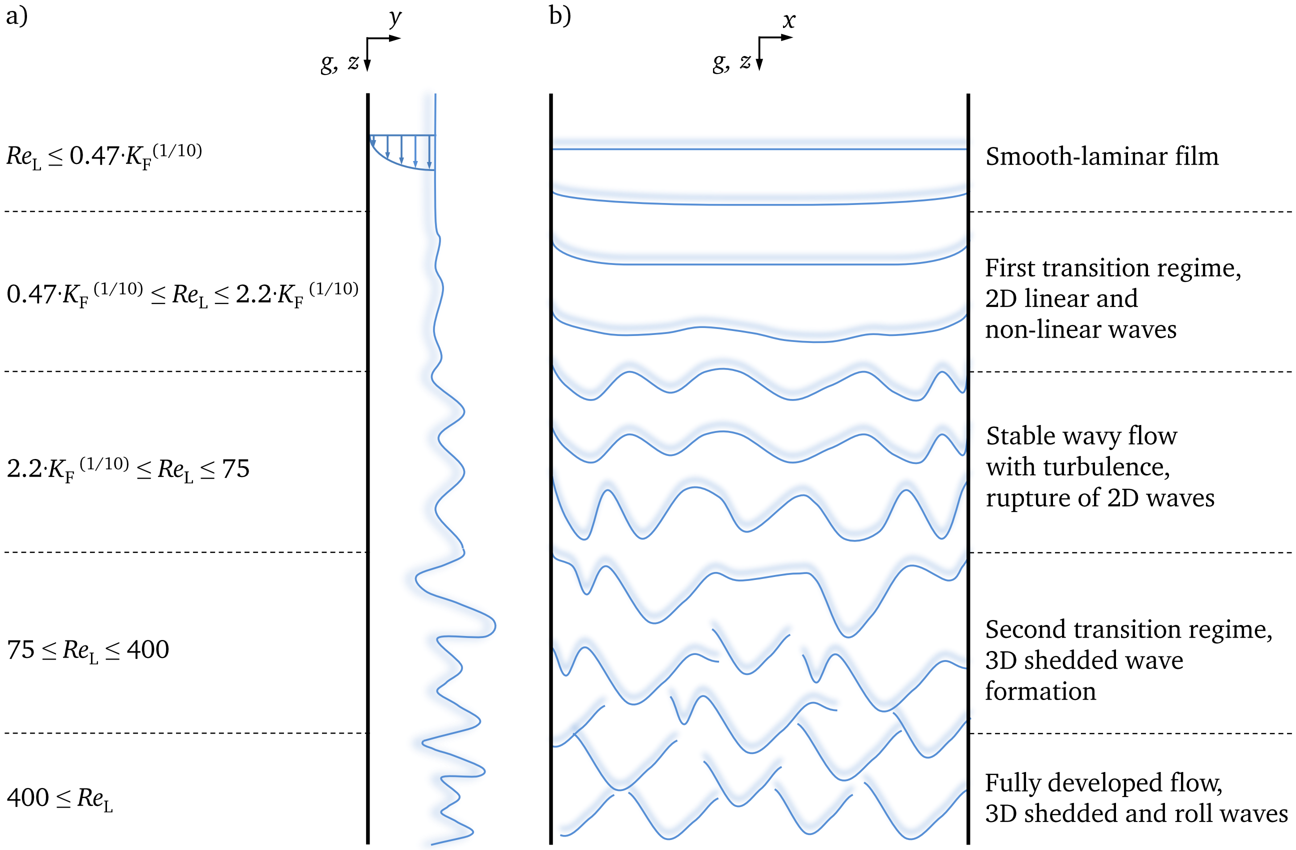

Figure 2.2. Qualitative demonstration of the state flow in gravity-driven films flowing on a vertically aligned wall: a) Side view , b) Front view [113].

The first regime can be described with the Nusselt theory. When the waves reveal a sharp increase of their slope (increase of their amplitude, increase of the standard deviation) and increase in the velocity, it can be implied that the flow reached the first transition [10]. Hereby, viscous and body forces can intensify the waviness of the liquid-gas interface. Waves with large sizes propagate over a laminar film and promote convection and hence increase heat transfer [9]. Since this type of waviness is governed by surface tension forces, it can be expressed by K_F. The dynamic pattern of the liquid-gas interface for the third type of film flows is similar for the whole range of Re_L exhibiting turbulence generation by the wavy motion. The second transition is represented by a lower rate of increase in amplitude [10]. Film flows which fit in the fourth category incorporate the existence of shear-governed turbulence while the last category shows a shear-dominated turbulent film flow. Such flows display a turbulent boundary layer on the wall. In terms of heat transfer, a minimum Nusselt number sets on at critical Reynolds number $Re_\mathrm{L,crit}$ for the transition from laminar to turbulent flow [9, 153] (see Fig 2.3). The corresponding critical Reynolds number in this case is reported in the range of $350 - 450$ [55, 99]. Chun and Seban [27] proposed correlations for the onset of transition based on $Pr_\mathrm{L} = (\mu_\mathrm{L} c_{p,\mathrm{L}})/\lambda_\mathrm{L}$ or Ka:

$$Re_\mathrm{L,crit} = \frac{5900}{{Pr_\mathrm{L}}^{1.06}}, \tag{2.4}$$

or

$$Re_\mathrm{L,crit} = \frac{0.215}{Ka^{1/3}}. \tag{2.5}$$

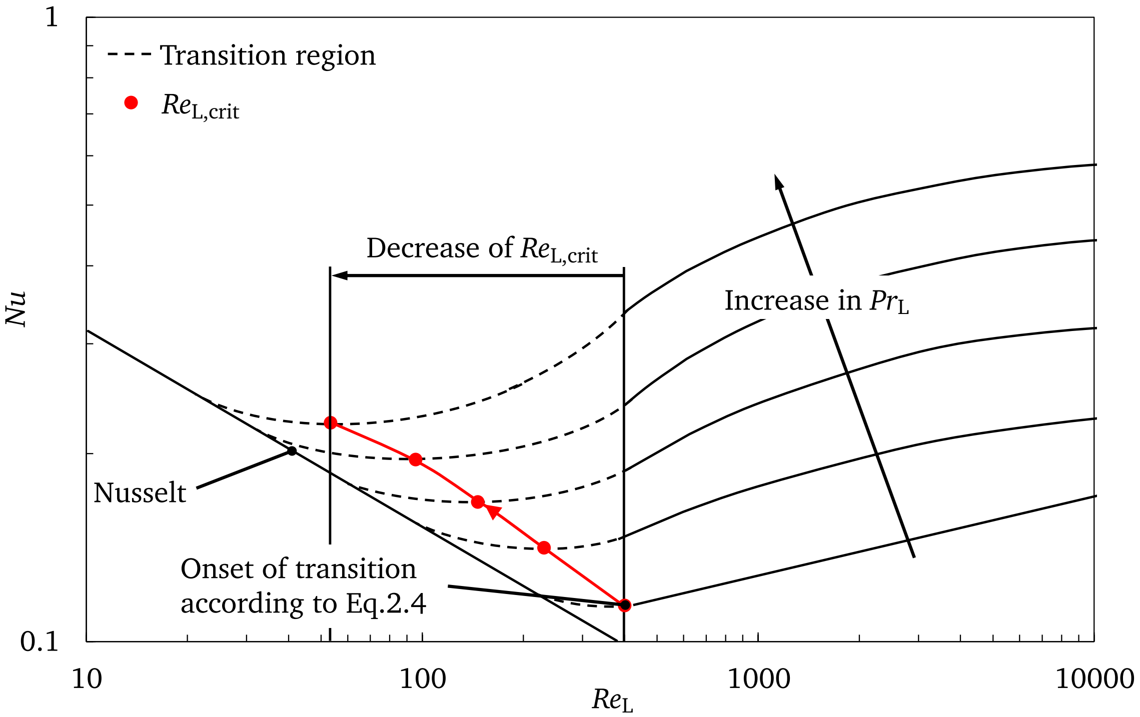

Figure 2.3. Qualitative development of the Nusselt number for varying Re_L and Pr_L for gravity-driven films streaming along a vertically aligned wall.

The above-mentioned correlations are widely used in the design of falling film evaporators. Another definition for $Re_{\mathrm{L,crit}}$ depending on Ka is presented in [84]. Possibly the decay of heat transfer coefficient is due to the thickening of the inter-wave liquid layer occurring at elevated Re_{L} in laminar regime [92, 101]. However, an increase of the Reynolds number beyond the critical value causes a rapid increase in wave velocity, which leads to the onset of a turbulent mixing mechanism [9, 10].

Also the wave frequency and the number of wave collisions can increase [1, 43]. Here, strong distortion and amplification are induced which significantly influences the wave celerity [35, 133, 136]. Strong acceleration in flow direction leads to zones of recirculating flows [143]. Smaller waves frequently merge together and separate, but their form is not significantly altered [1]. Owing to the intense mixing process promoted by waves, the temperature gradients within the liquid bulk deteriorate [92]. This mechanism becomes more and more dominant as the Re_{L} increases and thus leads to a stronger heat transfer enhancement [101]. However, it has been found that roll waves and capillary waves do not promote any noticeable turbulence within the substrate film [31]. Furthermore, the transition from laminar to turbulent flow is significantly depending on Pr_{L}, as shown in Fig. 2.3 [66, 147, 151]. Large Prandtl numbers lead to lower critical Reynolds numbers of the liquid and result in higher heat transfer coefficients [9, 27, 101, 144]. Additionally, the liquid hydrodynamics can be significantly influenced by wall heat flux. Higher heat flux can raise liquid temperature and result in a reduced surface tension and also lower kinematic viscosity [94]. Since in the definition of the liquid Reynolds number the viscosity is a parameter, a lower viscosity results in an increase in Re_{L}. Consequently, a liquid film which flows within the thermo-hydrodynamic developing regime can transit earlier into the fully turbulent regime and therefore cause an early inception of heat transfer enhancement. As a result, the thermo-hydraulic developing length can be shorter [89].

The flow characteristic of the liquid film surface within the turbulent regime is not easy to describe [61]. The first description for turbulent liquid films was proposed on the basis of the Prandtl mixing analogy for a fluid flowing through a tube and applied to the turbulently liquid film [55, 56]. Generally, turbulent films falling due to gravity were observed to be rather stable and showed only minor changes in their wave celerity in flow direction, denoting that the flow is probably not fully developed [80].

For better understanding of these complex thermo-hydrodynamic transport mechanisms in wavy thin liquid film flows, the following characteristic features of wavy film flows are qualitatively introduced (see Fig. 2.1):

- the substrate film,
- the capillary waves,
- the 2D waves,
- and 3D waves.

On the following pages, the physical mechanisms concerning hydrodynamics and heat transfer in the above elements presented in the literature are discussed.

Substrate film

As mentioned before, a thin substrate film exists between the large waves. This film is also called the thin inter-wave liquid layer (see Fig. 2.1). The smooth substrate film is almost disturbance-free and acts as a buffer layer between the wave and the wall [1, 136]. Its surface exhibits weak surface tension forces [94]. Only a small amount of liquid mass is creeping within its flow domain. Compared to the velocity of capillary waves and large waves propagating over it, the velocity of this thin layer is very small and mostly assumed to be having parabolic velocity profile [144]. Since its thermal resistance is small, it is stated that the major amount of heat is transferred through this portion [3, 68, 112]. The intensification of heat transfer is also attributed to the permanent deformation of the substrate film through the motion of waves [1, 99]. The resistance for heat conduction in the film fluctuates with the thickening and thinning of the film promoted by the motion of waves [124]. To lower the thermal resistance to heat transfer at the wall-liquid interface, liquids with small Pr_L can be used [123]. By decreasing Re_L the substrate film thickness reduces additionally. Hence, the temperature gradients in the substrate film increase and induce a further rise in heat transfer [94].

Capillary waves

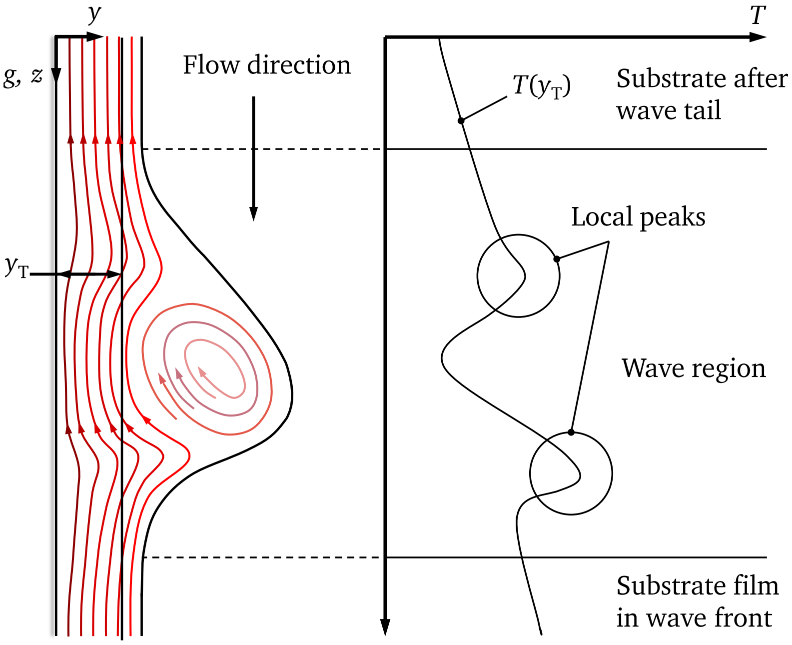

Figure 2.4. Distortion of temperature contour lines within the liquid film during the passage of a large wave [92].

Disturbing forces can generate small amplitude waves that influence the near-wall flow field [99]. When the front of a large wave is characterized by strong stream-wise decrease of the film thickness and ripples appear with amplitudes decaying exponentially downstream of the wave front, the appearing ripples are called capillary waves [32, 111]. They embody the transitional region between the substrate film and the large waves. Their typical amplitudes are small and travel slower than large waves, but have a higher velocity than the substrate film. They can have a bow shape and precede the solitary waves [47]. Since an adverse pressure distribution is initiated by the formation of capillary waves, a strong destabilization is caused. This leads to vortex formation in the region of the wall-liquid interface in the capillary wave zone which induces an internal back-flow [32, 136]. The surface deformations lead also to weak pressure peaks at the liquid-gas interface and cause action of surface tension inducing oscillating wall shear stress [32, 47]. However, within the capillary wave zone the strength of the variation of wall shear stress might depend on the size of the large waves and the substrate film thickness [136]. Fluid particles move along annular streamlines existing in separation vortices, which lead to circulation. The generation of vortices is governed by the capillary wave profiles representing the transition from the substrate film to the large wave front. There, strong velocity gradients can exist. The local separation leads to the generation of eddies with different sizes in the region of the wall-liquid interface [32]. The path lines are deformed in the crosswise direction due to passing capillary waves and have either a circle shape or look like a hook depending on the distance to the wall. Owing to this convective motion which works also in crosswise direction, heat transfer within the capillary wave zone enhances [32]. Moreover, the highest rate of heat transport is supposed in the region between the capillary waves and the peak of solitary or roll waves [124]. This has been illustrated by the temperature contour lines in capillary waves (see Fig. 2.4). The density of the temperature contour lines in the capillary wave zone is higher than those in the crest of large waves where a meager temperature contour line distribution exists [99]. Since large waves with steep fronts push capillary waves and the substrate film, a mixing of hot and cold liquid occurs which enhances the heat transfer rate. However, the contour lines for the temperature profiles in capillary waves and in the substrate film remain almost parallel to the wall, even when the Pr_{L} is elevated. Solely the contour lines in large waves are strongly deformed, which indicates that waves exhibiting large amplitudes have a strong influence on heat transfer [99]. The following equation was proposed by Kapitza to predict the formation of capillary waves on the surface of a laminar liquid film [84, 95]:

$$Re_{\mathrm{L,crit}} = 2.43\,(Ka)^{-1/11}\,. \tag{2.6}$$

2D waves

During the propagation of subsequently moving waves, the viscous boundary layer recurrently develops and is periodically destructed and re-established by an overlapping mechanism as shown in Fig. 2.5a [20]. At the wave back the boundary layer is recovered. Synchronously, it can be assumed that the thermal boundary layer is skinned as demonstrated in Fig. 2.5b and hot liquid is quickly transported toward the region where it mixes with cool liquid [94]. The interaction between the waves and the substrate film induces the mixing and promotes a highly distorted temperature profile (see Fig. 2.4) [92]. Local temperature peaks within the bulk liquid and hence a variation of local heat transfer coefficient exists along the wave [124]. Wave-induced convective mass exchange works perpendicularly to the wall-liquid interface and enhances the heat transfer in the inner zone of the film [124]. In the trough region of the

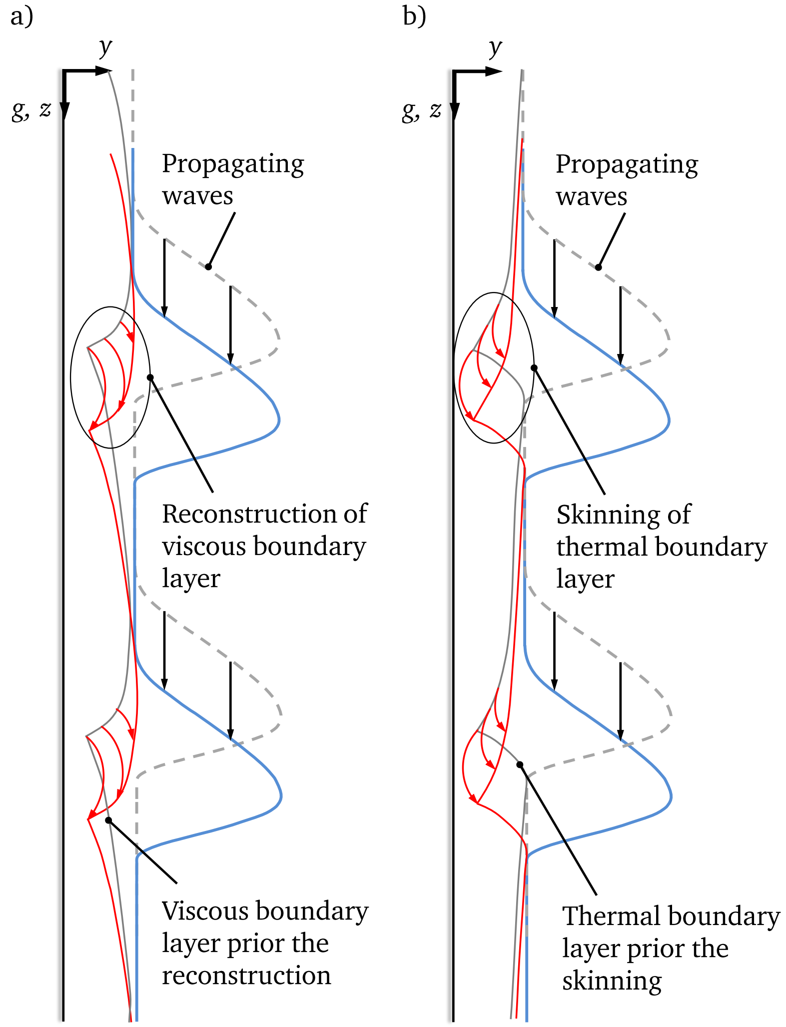

Figure 2.5. Boundary layer development by subsequently propagating waves, a) Reconstruction of viscous boundary layer, b) Skinning of thermal boundary layer.

wave and further downstream within the capillary wave zone embossed with strong deformations, sharp changes of velocity and pressure can exist [47]. Some particles stream towards the crest of the large wave where the surface tension forces are rather high. Then they circulate further to the wave tail. There its velocity reduces as part of the momentum of the flow is displaced toward the wall-liquid interface region [1, 47, 143]. This fluid motion is called as the recirculation zone. The size of this recirculation zone which is generating turbulence is defined by the wave amplitude and the wave length [47, 143].

Below the wave maximum, about 25 % of the liquid mass has constant velocity and remains as a motionless cluster moving over the substrate film [143]. Liquid is pushed from the liquid-gas interface toward the capillary wave zone and substrate film through velocity gradients in flow direction [143]. The velocity of a liquid element is typically constant in the vicinity of the wall-liquid interface and is intense in the region of the liquid film surface [143]. The increase in speed at the liquid-gas interface comes into effect in the region of the wave tail [143]. This complex motion causes an exchange of hot liquid elements with cold ones, leading to an increase of heat transfer. However, the contribution of waves to heat transfer enhancement through the recirculation mechanisms is being reported as weak [68]. Within the bulk of liquid near the liquid-gas interface, a suppression zone induced by viscous forces exists which works as resistance against turbulence [149]. Therefore, the major amount of heat would be transported by conduction through the thin substrate film, which dominates the efficiency of the overall process [68]. The arbitrary motion of cool vortices towards the wall owing to the interaction between adjacent waves might contribute to the enhancement of the mixing intensity [94]. The Prandtl number determines the state of dominance of each mechanism [99].

3D waves

At very large Re_{L} multiple-amplitude waves which lead to the generation of 3D waves (see Fig. 2.2) with a rather complex flow behavior can form [112]. The fronts of 2D waves are strongly distorted by the interaction and coalescence mechanism [111]. They cannot survive instabilities and rapidly form into 3D shaped perturbations with a naturally non-stationary behavior [7]. Re_{L} has a direct influence on the separation distance and amplitude of solitary waves [136]. Humps like teardrops (onset of solitary waves) and multiple small capillary ripples exist during the transition phase at the surface of these 2D and 3D waves [111]. Finally the flow results in 3D solitary waves. Steep leading edges, a horseshoe shape, and small-scale capillary ripples propagating ahead are other key features of a stationary 3D solitary wave [5]. The length of capillary ripples wave moving ahead of the main hump of a solitary wave varies inversely with the hump height [136]. Within the steep region of a main hump of a solitary wave, a flow reversal occurs due to negative pressure [136]. An intense mixing of liquid is provoked with large recirculation vortices formed by solitary waves with large amplitudes [68]. These vortices slowly propagate below the crest owing to the fact that the flow cross sectional area beneath the amplitude is larger compared to the substrate film [68]. By increasing the Prandtl number, the mixing process can lead to strong variation of the temperature distribution within the liquid bulk [99]. During the mixing of liquid, a variation of wall shear stress occurs, which might depend on the size of solitary waves and the substrate film thickness [136].

2.2 Gas-driven liquid film flow

As mentioned in Sec. 1.1, gas-driven thin liquid films represent a very efficient cooling method for micro-electronics or semiconductor devices [73, 154]. In advanced gas turbine combustion chambers, gas-driven liquid films are utilized in fuel preparation systems to atomize, pre-vaporize and premix fuel with compressed air [121]. Fundamental scientific research has been undertaken in the past to gain a broad knowledge of the complex two-phase flow mechanisms in gas-driven liquid films. Theoretical-numerical modeling was carried out and validated with measured data obtained through sophisticated experiments [72]. Flow maps were developed as shown in Fig. 2.6 using the occurrence and diminishment of waves to classify the state of the flow and to predict the onset of instabilities [39, 104].

Stability

Similar to gravity-driven film flows, instabilities at the liquid-gas interface can occur [86]. It is found that the region of film flow stability decreases significantly when a gas stream is in action [6]. To determine the state of neutral stability, the Kelvin-Helmholtz calculations, involving the integral momentum and rigorous long waves expansion models, were used [86]. However, in most of the gas-driven film flows, the Kelvin-Helmholtz model and the integral momentum equation did not provide proper predictions concerning the onset of instabilities. Nevertheless, the growth of a wave to large amplitude could be partly forecasted with a linear instability approach [96]. This approach implied that waves must be linearly unstable to grow to significant amplitude. However, the linear theory did not ensure the possibility to describe subharmonic and low mode generation or even saturation of the linearly growing amplitudes.

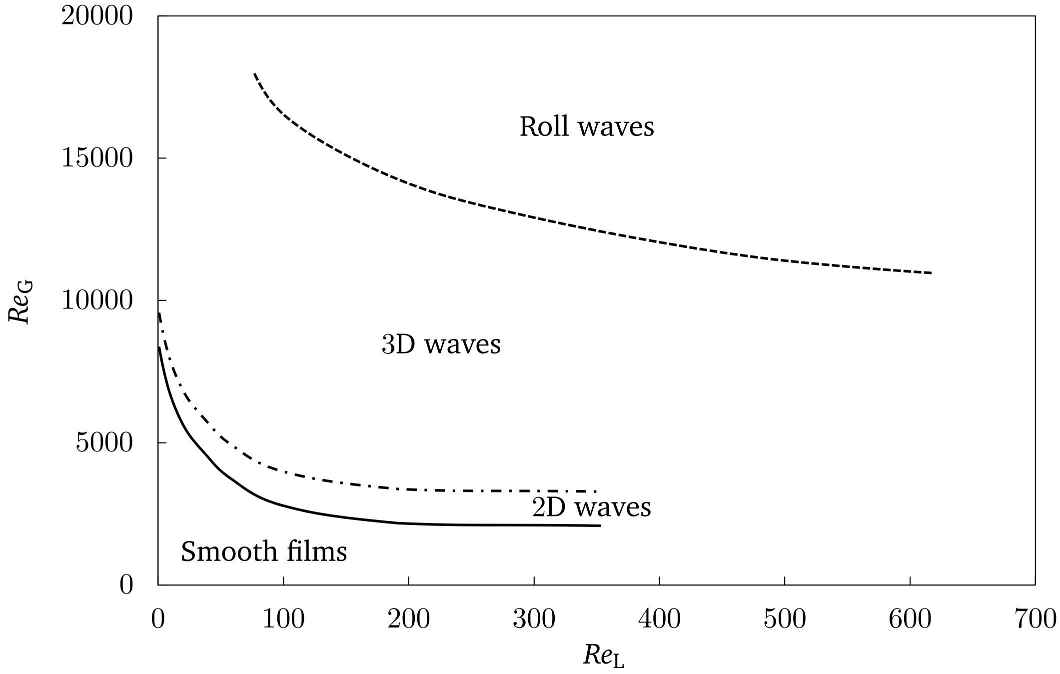

Figure 2.6. Flow regimes for varying Re_G and Re_L [104].

Investigations revealed a rather stable behavior of the liquid-gas interface at small values of Reynolds number, as no strong interaction between both the fluids existed [33]. However, at moderately high gas velocities, the film thickness starts to reduce and eventually a 3D flow behavior develops [87, 102]. First transition from a smooth liquid-gas interface into a disturbed film surface reveals as non-uniform disturbance waves, perturbing the flow such that small-size ripples called solitary waves appear [4]. Here, disturbance waves and ripples are called primary and secondary waves, respectively. Previous researchers have attributed this mechanism to the liquid viscosity combined with the shear-force at the liquid film surface [40]. The small ripples that rapidly develop to 2D waves represent the primary destabilization phenomenon which occurs when the gas velocity is increased [59]. The primary instability which leads to the change of the film surface structure requires a low Reynolds number and high shear stress at the liquid-gas interface [59]. The discharge of waves leads to pressure fluctuations in the gas stream and a resulting variation of the shear forces at the liquid-gas interface [29, 60]. The liquid phase receives energy from the gas phase by the induced shear stress and pressure fluctuations [29]. The development and increase of waves happens when the rate of viscous dissipation in the liquid is smaller than the intensity at which the energy is transferred to the waves by the above-mentioned mechanism. The development of solitary waves probably represents the second transition. Solitary waves at the gas-driven film surface seem to appear as dominant waves [114]. Their appearance can be achieved at moderately high but rather steady gas flow rates and at different liquid mass flow rates [70]. They have a much higher velocity than periodic waves and diminish at higher liquid flow rates [70]. A further rise in gas mass flow rate at constant liquid mass flow rate leads to a formation of wide-crested, steady, and periodic 2D and 3D waves [70]. Their velocity profiles are similar and exhibit larger amplitudes than those in the case of the absence of the gas stream provided the liquid mass flow rate is fixed [41]. The third transition is promoted by higher gas velocities constituted by the formation of large amplitude roll waves [59, 98]. The onset for the roll waves was investigated by linear stability analysis. It was suggested that slowly growing disturbances whose wavelength is larger than the film thickness cause the rupture of solitary waves and induce roll waves [21].

Combined with roll waves, several pebbled waves and 3D pattern with small scale wavelength travel over 2D small-amplitude waves (capillary waves) and propagate over the substrate film, leading to increased flow complexity [39, 98]. This strong and dense inter-wavy motion is similar to the flow behavior found in gravity-driven films. This indicates that the internal flow mechanisms are similar but are more intense. Transport mechanisms such as the thinning of the substrate film or the internal mixing mechanism in the wave trough are significantly enhanced due to the shear forces at the liquid-gas interface. However, in the work of Wittig et al. [148], a rather laminar than turbulent state of the film flow was surveyed, although very high gas velocities were applied in their experiments. On the other hand, based on findings on gas-driven film flows, Miyara et al. [99] argues that waves appearing at the liquid-gas interface can affect the flow field in the near-wall region. As the waviness increases by the shear forces acting at the liquid-gas interface, a liquid back-flow in the region of the wave trough and a stronger thinning process occurs. Hence, the flow characteristics can play a significant role in the overall heat transfer process [148].

Heat transfer

The heat and mass transport in thin gas-driven liquids and the developing length are governing features which may be of great significance in thin liquid film flows [49]. Methods to predict the overall and local heat transfer coefficients in turbulent gas and liquid flows have been developed. Predominantly, the heat is transferred by convection from the heated wall to the liquid and from the liquid film to the gas flow by convection and evaporation. The wavy motion at the liquid surface changes the flow conditions in the core of the liquid bulk and influences the liquid temperature distribution [30]. At increased Re_{L}, convective heat transfer becomes more dominant, provided the liquid film saturation temperature is not reached [49]. The local Nu_{L} decrease along the flow direction, since the liquid is heated up and the boundary layer develops [30]. Another significant effect is that the heat transfer coefficient between the liquid and gas increases with gas mass flow rate [30]. The gas flow rate affects the development of the thermal boundary layer towards the liquid-gas interface [49]. The critical Reynolds number for transition from laminar to turbulent flow decreases when the shear stresses at the liquid-gas interface induced by

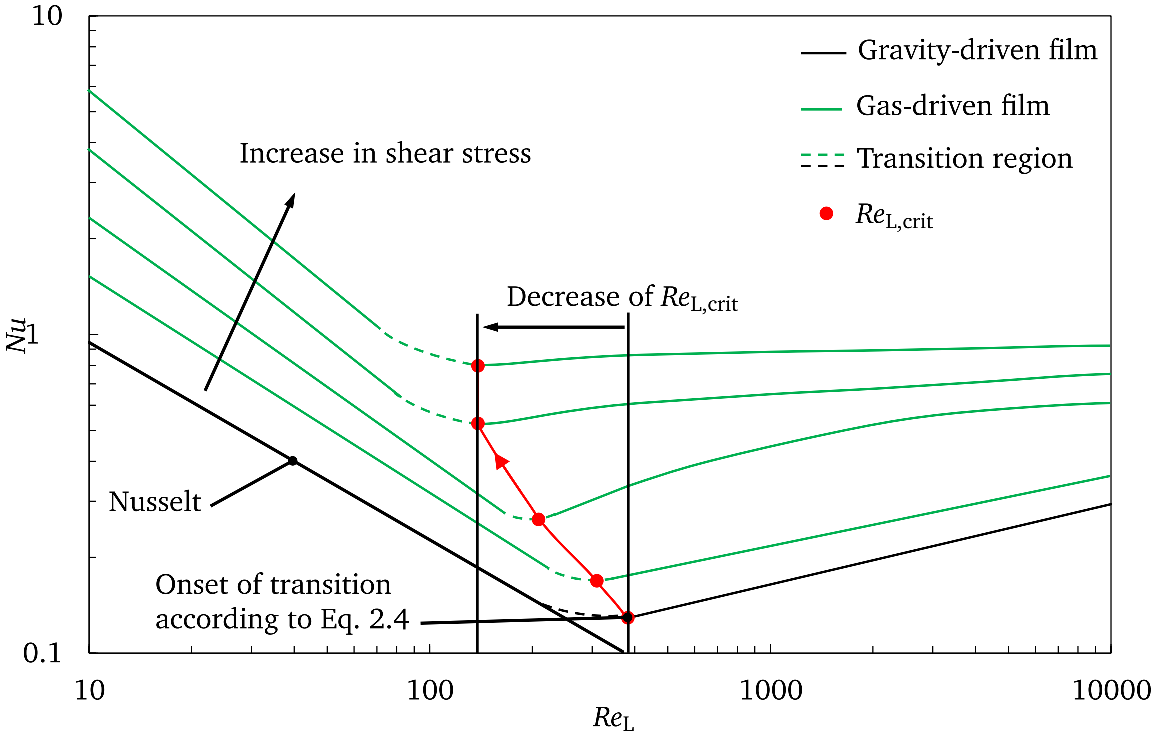

Figure 2.7. Qualitative development of Nusselt number for varying Re_L and Pr_L for gas-driven films streaming along a vertically aligned wall.

a gas stream increase [149]. In the turbulent regime the heat transfer is enhanced with increasing of Re_L. Qualitatively, this effect is shown in Fig. 2.7 and can be ascribed to more than one effect. On the one hand, increase in gas velocity leads to a significant reduction of the film thickness, which leads to a widening of the spectrum of time in which the substrate film is uncovered with waves [87, 120]. Overall, the reduction of the thermal developing length due to the stronger thinning mechanism can be obtained [25, 49]. On the other hand, the intensified momentum transfer induced by the acceleration and the turbulence in the gas boundary layer changes the turbulence pattern in the liquid flow, enhances the mixing, and hence contributes to the increase of heat transfer by convection [36, 149]. Consequently, the shear force at the liquid-gas interface, the liquid mass flow rate, and the viscosity, which is determined by the liquid temperature and the composition, are key parameters determining this phenomenon [50].

Film break-up

Gravity-driven films on heated surfaces are more sensitive for break-up compared to gas-driven films [73]. Although steady dry patches can also form in gas-driven liquid films, applying sufficiently high shear forces at the liquid film surface can prevent hot spots [73, 115]. Through the action of the interfacial shear, the liquid is pressed onto the wall, and a rather homogeneous liquid film distribution is provided. The heat flux at which the onset of break-up of gas-driven films occurs can be several times higher than that for gravity-driven films at the same liquid Reynolds number [72]. Besides, the break-up condition itself varies between the flow states and requires a local critical minimum film thickness [154].

Droplet entrainment

At sufficiently high gas velocities, droplets can be entrained from the liquid surface. This effect intensifies as the shear force at the film surface rises. Due to entrainment, the mass flow of the liquid on the wall reduces [37]. Challenging approaches were performed to model the entrainment of liquid particles using a wave undercutting mechanism [67]. However, it was revealed that the reconstruction of droplet entrainment is a much more complex mechanism and is induced by more than one mechanism [67].

2.3 Surface micro-structuring for heat transfer enhancement

The idea for structured surfaces has been borrowed from Nikrudse's experiment [106]. Corrugated surfaces have strong influence on the thermo-hydrodynamic transport mechanisms in thin liquid film flows [19, 62, 109, 139]. Compared to unstructured surfaces, strong deformations of the film surface can occur [63]. Starting with these initial investigations, several mechanisms promoting the intensification of heat and mass transfer in films flowing along structured surfaces with different geometries were identified. Besides structures oriented perpendicular (horizontal) and parallel (longitudinal) to the flow direction, structures incorporating complex shapes such as dimples, ribs, and pyramids were also adopted in the investigations [23, 140].

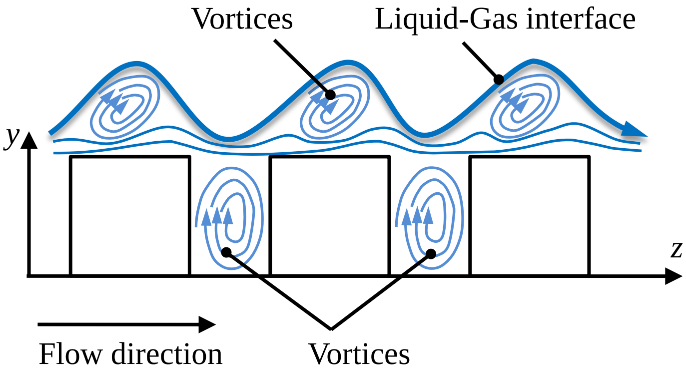

Figure 2.8. Liquid film streaming along horizontally oriented structures, strong deformation of the liquid film surface, formation of vortices within large waves and within the troughs.

In the literature, it is described that providing the surface with micro-structures destabilizes the flow [34]. This applies strongly to the use of horizontally-oriented structures. The liquid film flow recognizes a considerable destabilization as compared to an unstructured surface [74]. The micro-structure depth and width, the capillary scale that is described by the surface tension, and the gravity are the most significant dimensions governing the film distortion, the film destabilization, and hence its flow dynamics [76, 117]. As shown in Fig. 2.8, the liquid film surface experiences a noticeable static jump (crest) before the entrance to the structure trough [11, 76, 117]. The height and the slope of the micro-structure shape significantly determine the amplitude of the static jump [11].

In flow direction a wake at the surface after the structure appears while liquid mass is collected in the troughs [117, 142]. Close to the concave edge of the structure, the film thickness has its thinnest point.

Owing to the geometry, especially towards the structure crests, a film thickening is also caused in the case of large waves [113]. The rougher the surface is, the larger the mean film thickness can be [33]. Compared to that, a contradictory behavior is observed that the amplitude and the slope of the micro-structure can lead to a reduction of the film thickness. Due to the increased contact time between liquid and solid, more waves can appear [113]. Large contact times increase friction at the solid-liquid interface and the occurrence of strong velocity variations. However, in another study, a reduction of the number of large amplitude waves and the formation of solitary waves which are involved in films falling along unstructured surfaces has been reported [142]. Consequently, the fluctuation of the velocity induces liquid distortions causing pressure variations along the wall and hence again influence the flow field [137]. Since liquid accumulates in the troughs, vortices are caused between the structures which lead to the heterogeneity of the flow domain in the region near the structure. This liquid accumulation exhibits noticeable recirculation regions which promote the enhancement of convective heat transfer from the wall to the liquid [142]. However, some studies reported that the heat transfer rate in films flowing over micro-structured surfaces can be lower than on unstructured surfaces [44, 45]. Another effect of micro-structures is that the thermal and hydrodynamic entry distances and the critical Reynolds number for the transition of the flow from laminar to turbulent can be decreased by increasing the wall roughness [33]. The transition occurs when propagating disturbances transfer into non-linear waves [11]. However, using a steeper geometry for the design of micro-structures, a higher value for the critical Reynolds number for transition can be obtained and hence the destabilization of steady flows can be avoided [11]. As the turbulent state of flow is reached, the heat transfer rate is expected to rise.

Fluids with high Pr_L incorporate a strong decrease of the thickness of the thermal boundary layer, which is one of the major reasons for the intensification of heat transfer at unstructured surfaces [16, 123]. In case of structured surfaces, for small Pr_L, the heat transfer enhancement is induced in the region of the structure crest and requires significant effort to achieve strong intensification similar to the unstructured surface [16]. This can be attributed to the fact that micro-structures for fluids with low Pr_L do not intensify the turbulent convection [90]. The relative sizes of the micro-structure (h_struc), the viscous sublayer thickness δ_ν and the thermal boundary layer thickness δ_λ determine the heat transfer enhancement [90]:

For $Pr_\mathrm{L} \sim 1 \rightarrow \delta_\nu = \delta_\lambda \rightarrow$ pressure drop and heat transfer intensifies with increase in roughness. In the case of $Pr_\mathrm{L} \gg 1 \rightarrow \delta_\nu > \delta_\lambda$ the following conditions can exist:

- $h_\mathrm{struc} < \delta_\lambda \rightarrow$ an increase in flow friction and heat transfer will not occur
- $\delta_\nu > h_\mathrm{struc} > \delta_\lambda \rightarrow$ heat transfer will increase and the pressure drop will remain constant
- $h_\mathrm{struc} > \delta_\nu > \delta_\lambda \rightarrow$ heat transfer and pressure drop will increase

At $Pr_\mathrm{L} \ll 1 \rightarrow \delta_\nu < \delta_\lambda$ the following conditions can exist:

- $h_\mathrm{struc} < \delta_\nu \rightarrow$ heat transfer and pressure drop will not increase
- $\delta_\lambda > h_\mathrm{struc} > \delta_\nu \rightarrow$ pressure drop will increase while heat transfer will be not enhanced
- $h_\mathrm{struc} > \delta_\lambda > \delta_\nu \rightarrow$ heat transfer and pressure drop will increase

As an appropriate condition to achieve the optimal heat transfer coefficient, it is suggested to use a micro-structure height which is three times larger compared to the thickness of the viscous sublayer [90]. Furthermore, the surface wettability behavior of liquids can be controlled using various micro-structure geometries that affect the static contact angle. They can introduce the action of fluctuating capillary forces caused by pressure fluctuations, resulting in the formation of ridges and pinches of step-downs and step-ups, respectively. This mechanism homogeneously spreads the liquid film over the surface, so the occurrence of liquid break-up and resulting hot spots can be prevented [62, 76].

Tubes with longitudinal grooves or flutes are currently used in heat exchangers [112]. Micro-V-grooves lead to an increase in heat transfer due to high evaporation rates [19]. Exemplarily, the liquid flow within a V-groove is shown in Fig. 2.9. In the center of the V-groove, a liquid valley forms incorporating a main axial flow depending on the liquid load and on the interplay of the boundary layer development and the surface tension [112]. High pressure is present in the vicinity of the solid-liquid-gas interface, which gradually reduces towards the center of the flow. This leads to the promotion of a secondary flow from the groove crest to the trough [112]. The main axial flow is stronger than the secondary flow that exists in the vicinity of evaporating contact line. This might be one of the reasons for the increase of heat transfer. However, it has been shown that the secondary flow is also an important factor in the heat transfer mechanism [16]. On approaching the wetting front region, the axial flow becomes less active [112]. As long as the secondary flow is present, the flow in the center can achieve a higher velocity [112]. In fluids with very low surface tension, the secondary flow is suppressed owing to the reduced or even non-existence of the inward pressure gradient [112]. The liquid film thins due to the larger velocity of the liquid in the center synchronously pulling the liquid which is closer to the wall [112].

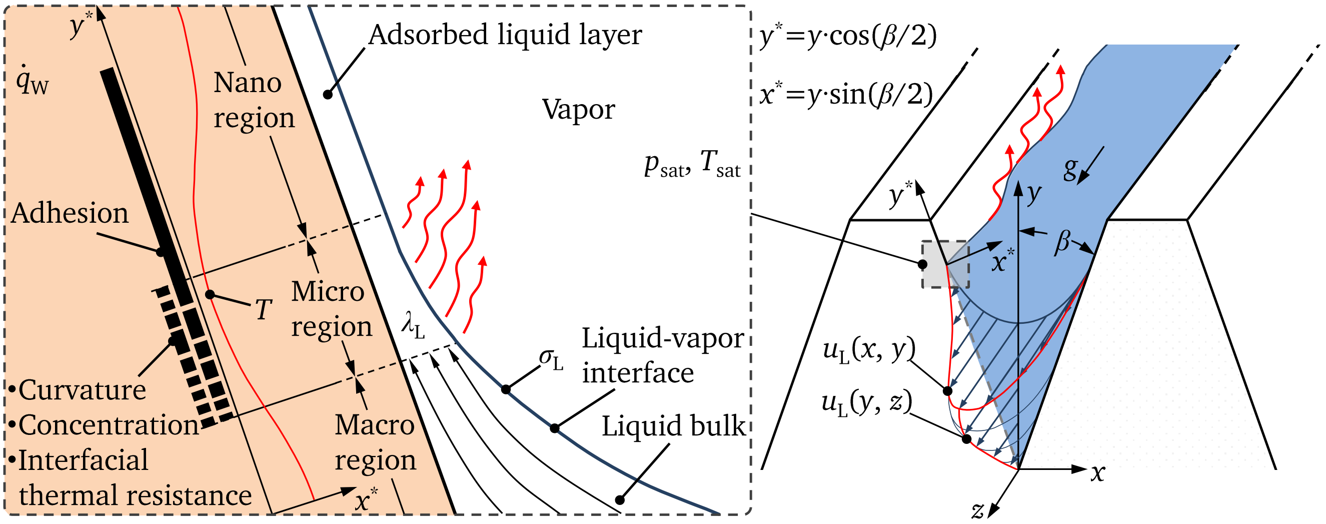

Figure 2.9. Liquid film flow along longitudinal grooved structure, three-phase contact line model within the nano-, micro-, and macro-region (adopted from [81]).

Small liquid loads on micro-structures leads to partially wetted zones incorporating the formation of the three-phase contact line and hence the micro-region (see Fig. 2.9). In this condition, the heat and mass transfer performance can be dramatically raised by high liquid evaporation rates existing locally within the apparent solid-liquid-vapor phase boundary region [62, 127]. The micro-region is located between the adsorbed film that covers the dry region of the wall and the macroscopic visible inward bend meniscus [130]. In this region, an ultra-thin liquid layer with large temperature variations is present where the shortest path through which heat can be transferred effectively is provided [112, 127, 129]. Macroscopically, this region can be seen as the three-phase contact line. Its length can be enlarged with the micro-structuring, and hence the heat transfer rates can be affected [127]. Similarly, higher heat fluxes also lead to a stronger expansion of the contact line length [109, 127]. A large amount of heat input increases the wall temperature and causes a growth of the apparent contact angle [2]. In gravity-driven films, this heat transfer mechanism in the micro-region is additionally supported with the film flow waviness [46].

In the case of partially wetted or flooded micro-structures, the Marangoni convection is also leading to heat transfer enhancement [62]. The variation in film thickness along the micro-structure causes sharp gradients of the temperature at the liquid-gas interface and hence in surface tension [62, 155]. This non-isothermal condition promotes thermocapillary stresses forcing the flow patterns in the form of vortices that enhance the heat transfer through mixing [62]. Liquid is forced to flow towards regions of higher surface tension [155]. There is an interdependence between the Marangoni convection and the liquid evaporation in the micro-region [62]. It is reported that the flow behavior of liquid in gravity- and gas-driven films induced by Marangoni convection is controlled by the heat and mass transfer occurring in the vicinity of the three-phase contact line [62].

Through the application of pyramid structures which represent a combination of horizontal and longitudinal geometries, retaining turbulence is promoted, which leads to heat transfer enhancement [139]. At similar operating parameters, the heat transfer coefficients on pyramid structured surfaces can be more than 70 % higher as compared to spherical shapes [139]. Since a pyramid represents a geometrical combination of horizontal and longitudinal grooves, it can be assumed that the thermo-hydrodynamic transport mechanisms are also combined. However, each transport mechanism has its own state of dominance. Between the wall and the gas, a long-range sensitive intermolecular interaction exists, which can lead to the formation of a small pinch and hence to the rupture of the film close to the concave corner of the step-down [76]. However, when the sizes of roughness elements decrease and come to a condition where they merge together, the state of the liquid film flow can be almost compared to the film flow on an unstructured surface [33].

Although significant progress has been achieved recently in understanding the complex mechanisms of heat transport in wavy shear-driven films on micro-structured walls, a complete understanding of these mechanisms has not yet been achieved, especially for the walls with complex three-dimensional topography.

2.4 Objectives of the thesis

The cooling process in thin film flows is rather complex, and wide-ranging knowledge about the physical mechanisms is necessary for the mathematical reconstruction of the film flow process. Each of the entailed mechanisms described by many scientific investigations represent an individual research area. Depending on the flow conditions, the thermo-hydrodynamic transport mechanisms in thin gravity- and gas-driven films can change from one to another above-mentioned transport modes or exhibit several simultaneously. Starting from first disturbances, the film flow can develop from a laminar to a wavy-turbulent flow. Disturbances cause an initial formation of ripples which develop further to 2D or 3D waves with capillary waves propagating ahead. Although numerous scientific investigations have been performed to determine the hydrodynamics and heat transfer in gravity-driven and gas-driven films, the knowledge of the complex transport mechanisms in conjunction with the enhancement of the convective heat transfer in laminar and turbulent wavy two-phase flows is still not sufficient. Contradictions are existing in terms of the determination of governing heat transfer mechanisms in shear-driven liquid films.

In some of the publications the substrate film (inter-wave thin liquid layer) is mentioned as the reason for the increase in heat transfer. This is attributed to the smaller thermal resistance of the thin liquid layer. However, other scientific groups have stated that vortices which are generated within the waves are the dominating mechanism. These intensify the internal mixing between hot and cold liquid and contribute to the enhancement of heat transfer. Contrary, in other investigations it is argued that waves have very minor or even no influence on heat transfer. Several papers are dedicated to the description of heat transfer enhancement and the correlation between the film hydrodynamics. However, most of those studies were performed on shear-driven films, where both the fluids were hydrodynamically developed and the liquid film thermally developing. Here either laminar or turbulent film flow regimes were investigated. Very less number of work comprise the film flow within the transition from laminar to turbulent and this within the thermo-hydrodynamic developed regime.

This work focuses on the research of hydrodynamics and convective heat transfer in thermally and hydrodynamically developing annular liquid film flows driven by gravity and by a co-currently flowing turbulent gas stream. More insight into the intricate thermo-hydrodynamic phenomenon is to be achieved. Especially, answers to the question whether waves have a contribution to heat transfer enhancement should be given by identifying flow regimes in shear-driven liquid films.

The objective of the present work is to experimentally investigate the thermo-hydrodynamic transport phenomena during thermally and hydrodynamically developing gravity-driven and gas-driven films flow along unstructured and structured walls. The first goal of this study is to investigate the hydrodynamics and heat transfer in a thin film flowing along an unstructured wall using a high-speed imaging technique and temperature sensors. Through high-speed photography, film flow regimes were identified by determining the film waviness using standard deviation of the liquid-gas interface and the wave frequencies. Thereby, the effect of shear stress and liquid mass flow rate was determined. Furthermore, the measurement of wall temperature distributions and the calculation of the heat transfer coefficients at varying liquid mass flow rate and shear stress was performed. The mechanisms dominating the heat transfer enhancement were interpreted with the film waviness. Additionally, the experimentally obtained heat transfer coefficients were compared with theoretical approaches and measured data from the literature. Furthermore, correlations are developed for the heat transfer coefficients measured at the unstructured surface.

The second goal of this work is the study of the effect of surface topography on the overall process. Therefore, micro-structures with systematically conceptualized geometries were chosen and the film waviness, film rupturing, and rewetting phenomena are to be discussed at varying fluid flow rates. For the latter, high-speed infrared thermography technique was used. Further, to evaluate the effect of surface topography on the heat transfer, the wall temperature distribution at the micro-structured surfaces were detected, the heat transfer coefficients determined and compared with those obtained by the unstructured surface. Film flow regimes were identified and the corresponding heat transfer mechanisms discussed. Moreover, the present work incorporates experimental data for the validation of the results of mathematical modeling work performed simultaneously at the same institute.

3

Experimental Methodology

In this chapter, starting with the idea based on an existing application, the concept of the experimental setup is introduced. Following this, the working principle of the experimental setup along with its peripheral devices is presented. The methodologies used for the design of micro-structures adopted in this study are reported and their geometries are characterized. At the end of this chapter, the experimental parameters and their ranges are presented.

3.1 Basic idea/concept

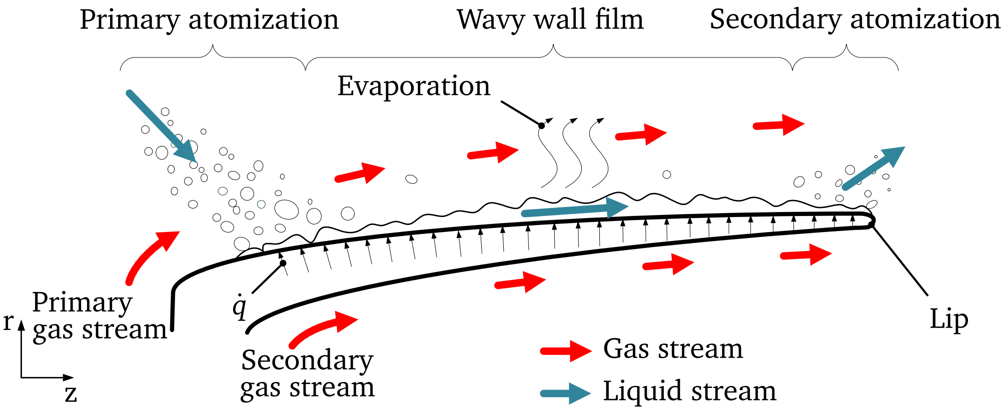

Figure 3.1. Two-phase flow within an airblast atomizer used in LPP combustors [57] (modified).

The idea for the design of the flow channel is inspired by the two-phase flow configuration which exists in an LPP airblast atomizer injection system as presented in Fig. 3.1. In Sec. 1.1, three main regions have been determined where the liquid fuel is primary atomizing, evaporating, and undergoing secondary atomization into the compressed hot air.

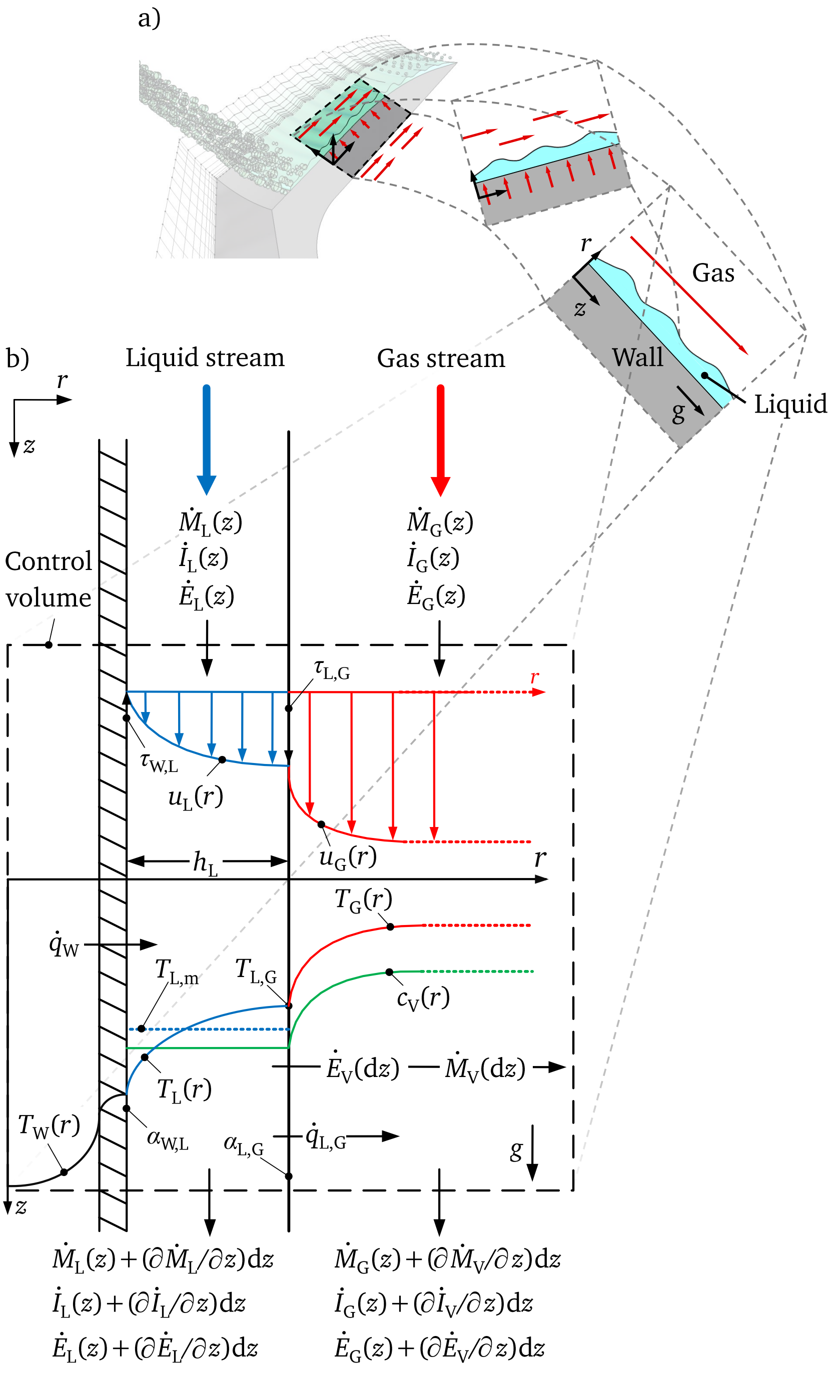

Figure 3.2. Schematic representation of transport mechanisms within an airblast atomizer: a) 2D cutout of an airblast atomizer system, b) Temperature and velocity distribution within the wall, liquid film, and gas stream.

A wall film is created due to the spray impingement in the primary atomization region. This region is followed by the domain incorporating a hydrodynamically and thermally developing thin liquid film flow. The liquid film is sheared by the gas stream and destabilized due to strong pressure gradients along the liquid-gas interface. This leads to a rather strong deformation of the liquid layer and hence to a wavy state of flow. While the liquid film accelerates towards the outlet of the injector, it partially evaporates into the gas. Finally, in the region of secondary atomization, droplets are entrained from the thin liquid film owing to strong interaction between liquid and gas stream. Further downstream on the edge of the wall, the residual liquid layer ruptures into liquid ligaments. The ligaments are atomized into drops, which are eventually transported to the combustion chamber by the gas stream [18, 128]. Since the focus of the present study is to understand the shear-driven thin liquid film flow encountered in such an LPP combustor, the primary and secondary atomization regions are not included in the experimental setup. Only a detailed quantitative and qualitative study of the transport mechanisms within the liquid film flow sheared by a gas stream has been considered. The transport mechanisms and the resulting measurable parameters such as velocity, temperature, and vapor concentration within the two-phase flow configuration were determined using a control volume as illustrated in Fig. 3.2a. The mass ($\dot{M}_\mathrm{L}$, $\dot{M}_\mathrm{G}$), the momentum ($\dot{I}_\mathrm{L}$, $\dot{I}_\mathrm{G}$), and the energy ($\dot{E}_\mathrm{L}$, $\dot{E}_\mathrm{G}$) are exchanged between the wall, liquid, and the gas streams due to strong interaction induced by a gas stream co-currently flowing over the liquid film (see Fig. 3.2b). Furthermore, the wall film receives thermal energy from the heated wall. The heated wall is stationary ($u_W = 0$) while the liquid is streaming relatively to it driven by a gas flowing with a higher relative velocity. The shear forces acting at the wall-liquid and the liquid-gas interfaces are denoted by $\tau_{W,L}$ and $\tau_{L,G}$, respectively. Due to the fact that $\tau_{W,L}$ is responsible for the deceleration of the liquid film and $\tau_{L,G}$ for the acceleration, the velocity profiles denoted by $u_L(r)$ and $u_G(r)$ of both the fluids result. The higher the gas velocity is, the stronger the film is sheared and adopts a higher velocity. The velocity profiles will develop in flow direction and change their distribution until an equilibrium of momentum is reached. As a result, the boundary layer thicknesses $\delta_{W,L}$ and $\delta_{L,G}$ will also develop depending on the viscosities μ_L and μ_G and the velocity gradients $\partial u_L/\partial r$ and $\partial u_G/\partial r$ within the boundary layer region. Beyond these fluid dynamic parameters, the state of the fluid flow is also important. Compared to a laminar liquid flow, a wavy turbulent liquid film flow exhibits closed streamlines and can include capillary separated eddies and hence a vorticity [32]. The vorticity in the liquid film can cause a better mixing and lead to an enhancement of heat transfer [126]. The heat is transferred from the wall to the liquid by convection.

Besides the convective mode of heat transfer, evaporation of liquid may play an important role. In this case, the humidity in the gas phase is important. In the case of an unsaturated gas flow, the difference between the saturation pressure p_{sat} and the partial pressure p_{H2O} of liquid which corresponds to the vapor concentration in the gas stream is the driving force of liquid evaporation. This mechanism comprises the simultaneous heat $\dot{E}_V$ and mass transfer $\dot{M}_V$ into the gas phase. With further increase of liquid temperature at constant absolute pressure of the system, the evaporation intensifies and passes over to vaporization. Recapitulating, the understanding of these transport mechanisms enhancing heat transfer in laminar and turbulent wavy two-phase flows is up to now inadequate owing to their complexity. An experimental flow channel has been conceptualized to investigate the thermo-hydrodynamic transport mechanism between a thin liquid film and a gas stream. To study this, physical and technical requirements regarding the configuration of an annular two-phase flow system coming across in industrial systems mentioned in chapter 2 have been taken into account. Within the flow channel, the following conditions should be ascertained:

- thermally and hydrodynamically developing liquid and gas flows are generated,
- the liquid and gas inlet temperatures and the absolute pressure are adjustable,
- the liquid film is heated by a controllable, well-defined heat flux from the wall,
- the accessibility of measurement techniques for the observation of the film dynamics and heat transfer is ensured,
- a large range of gas and liquid mass flow rates is guaranteed.

In consideration of these facts, the conceptual design of the flow channel has been incrementally carried out. Initially, simplifications have been considered for the configuration of the two-phase flow domain shown in Fig. 3.3a. Firstly, the two-phase flow domain was confined by a wall (see Fig. 3.3b). Since the primary atomization is not investigated, the application of the liquid layer onto the wall was realized

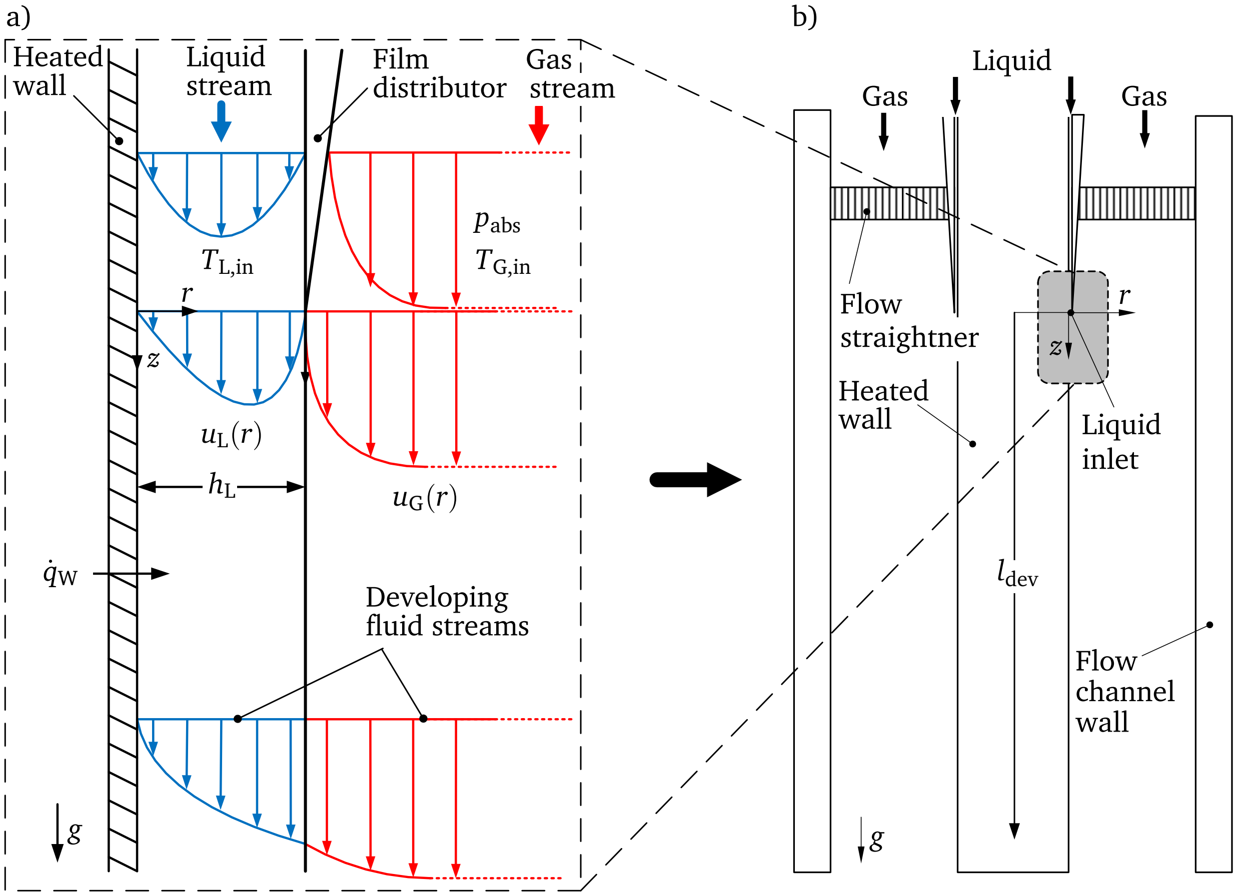

Figure 3.3. Development of the experimental flow channel: a) Configuration of two-phase flow domain, b) Rough concept of flow channel.

with a film distributor. The initial film thickness has to be within a predecided range. The flow direction of both the fluids and the wall was designed vertical, parallel to the direction of the gravitational force. For the quantitative and qualitative study of the film flow dynamics, the shadowgraphy method (SG) and the infrared thermography (IR) were used. Since only a 2D projection of an object can be recorded with the shadowgraphy method, a cylindrical heated wall was used. For the investigations of the heat transfer, a heating cartridge and thermocouples were embedded into the wall. The length of the wall and the length of the flow channel was appropriately chosen to ensure that both the liquid film and the gas stream propagate within the hydrodynamically and thermally developing regime. For the calculations of the developing length, the following equations for a falling film were adopted. According to Keyhani et al. [97], the length of the hydrodynamic development length of a liquid film falling along a tube is

$$l_{\mathrm{hyd}} = 1000 h_{\mathrm{L}} = 1000 \left(\frac{3 {\nu_{\mathrm{L}}}^2 Re_{\mathrm{L}}}{g} \right)^{\frac{1}{3}} . \tag{3.1}$$

Kabov et al. [24] proposed the following expression for the thermal development length of a falling film

$$l_{\mathrm{therm}} = 0.139 \left(\frac{{\nu_{\mathrm{L}}}^2}{g} \right)^{\frac{1}{3}} Pr_{\mathrm{L}} {Re_{\mathrm{L}}}^{\frac{4}{3}} . \tag{3.2}$$

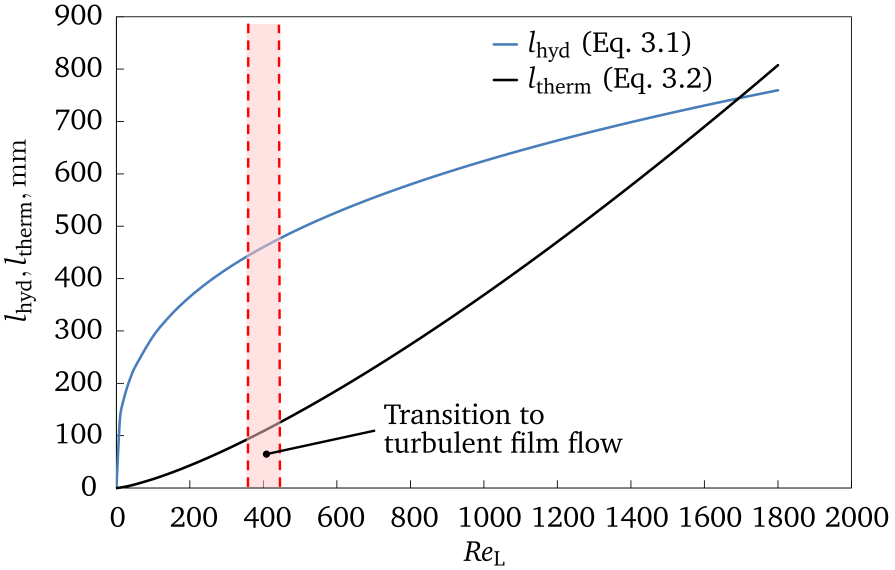

Figure 3.4. Propagation of the hydrodynamically and thermally development length of falling liquid films for $Pr_\mathrm{L} = 6.13$.

As shown in Fig. 3.4, the length from which a liquid film can be considered as hydrodynamically and thermally fully developed expands with increasing Reynolds number or film thickness. However, a region of transition from laminar to turbulent flow exists between $Re_\mathrm{L} = 400 - 450$ [95, 120]. The hydrodynamic developing length of the film flow can be shorter in the case of a wavy film flow as compared to a film streaming with a rather smooth free surface [30]. The thermal development length also decreases by the generation of waves [89]. It can be expected that the waviness will be strongly induced by interfacial shear forces generated through a co-current gas stream acting at the liquid-gas interface. To apply the liquid film onto the surface of the tube, a film distributor was designed which was positioned co-axially with the tube and forming the liquid inlet as shown in Fig.3.5.

The length of the channel for liquid inlet inside the film distributor was considered with $28\,\mathrm{mm}$ (see Fig. 3.5a). At $z = 0$, the liquid enters the flow channel with a parabolic velocity profile $u_\mathrm{L}(r)$. However, at low Re_L the liquid film pins at the edge of the film distributor and contracts as shown in Fig. 3.5a. This can be due to the acceleration generated by gravitation and to the shear stress induced through the action of the gas stream. The liquid velocity increases and concurrently the film thickness decreases. This region of contraction is defined as the inlet transition region. Along the flow direction, the film layer develops further. At high liquid Reynolds numbers, this contraction does not appear (see Fig. 3.5b). In both cases, the film flow develops hydrodynamically and thermally over the full length of the evaporator tube determined with Eqs. 3.1 and 3.2. The contraction can affect the length of thermo-hydraulic development of the liquid film and hence the overall heat transfer process. How strong the influence of liquid contraction on the heat transfer is, was not investigated.

In order to fulfill the accessibility need for the visualization techniques, planar glass windows were included in the flow channel wall. Planar glasses also minimize reflection and refraction of light used for shadowgraphy and infrared radiation. Deionized water and compressed dry air are used as the working fluids. The experimental setup and the flow channel are described in detail in the following subsections.

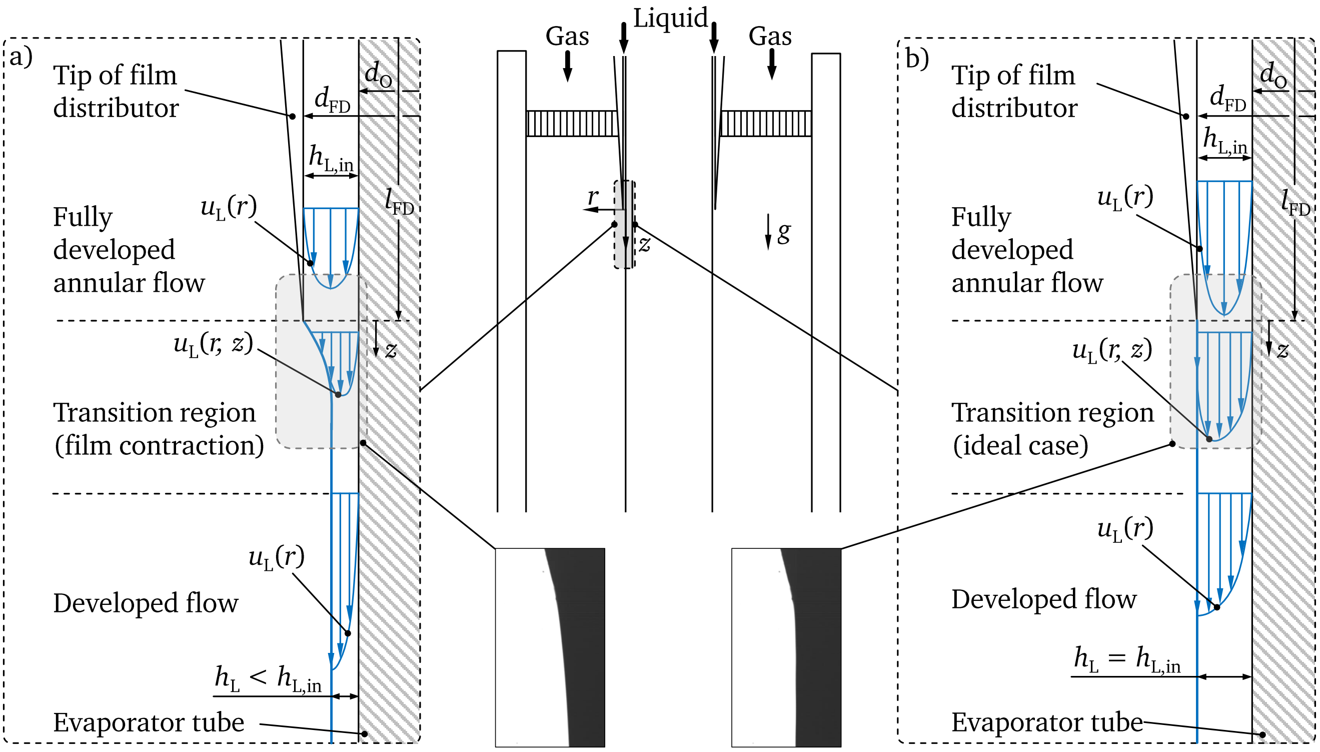

Figure 3.5. State of the liquid flow within and at the outlet of the film distributor: a) Liquid film contraction due to lower liquid mass flow rate insufficiently filling the annulus within the film distributor, b) Liquid film initialization at higher mass flow rates.

3.2 Schematic layout

In Figure 3.6 an overview of the experimental setup for the investigation of hydrodynamics and heat transfer in gravity and gas-driven liquid films is shown in the form of a flow chart. The experimental setup operates with gas (air) and liquid (deionized water) flow loops. Two high-performance compressors[1] ($p_{\max} = 13\,\mathrm{bar}$) suck in air from the surroundings, compressing and then pushing it through a dehumidifier[2] to condense the moisture. The dry gas is stored in a pressure vessel up to an absolute pressure of $13\,\mathrm{bar}$. The stored air is extracted from this vessel, while the compressor ensures that the tank pressure is maintained constant. During the operation of the test section, the gas mass flow rate and the operating pressure in the test section is controlled manually. This is achieved by isenthalpically discharging the compressed air through a pressure release valve, the simultaneous monitoring of its mass flow rate by a thermal mass flow meter, and the adjustment of a back pressure valve in the outflow line. The air extracted from the pressure vessel is preheated in a tube bundle heat exchanger by utilizing heat of the outflow at the channel exit. The preheated air is further heated to the desired temperature in an air heater with electrical input. The relative humidity $X_G = 2\,\% - 4\,\%$ of the gas is kept constant and measured before entering the flow channel with a humidity sensor[3]. The gas flows into the flow channel, exchanging heat and momentum with the liquid film. After exiting the flow channel, it passes through a

---

[1] GA 75, Atlas Copco, Essen/Germany
[2] HD 1110, Hankinson, Canonsburg/USA
[3] HMT 333, Vaisala, Vantaa/Finland

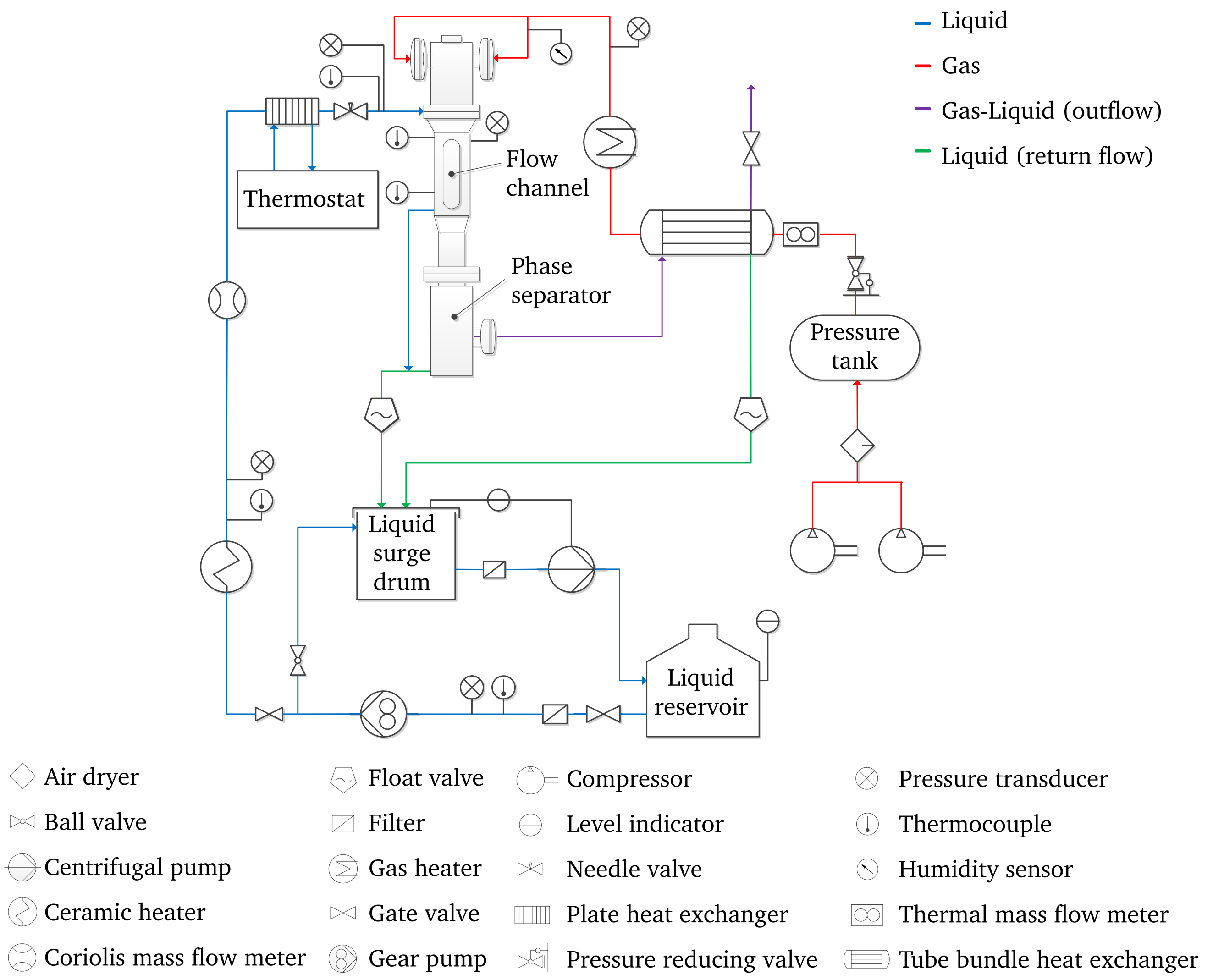

Figure 3.6. Process flow diagram of experimental setup.

phase separator. Subsequently the outflow transfers its residual heat to the inflowing gas while passing the tube bundle heat exchanger.

The liquid is stored in a stainless steel vessel. A variable frequency controlled gear pump is used to transport the filtered liquid towards the flow channel. Firstly, it passes an electrically operating ceramic heater bundle in which it can be preheated. The liquid mass flow rate is determined using a Coriolis mass flow meter downstream of the fluid heater. Subsequently, by means of a plate heat exchanger which is coupled with a high-performance thermostat, the liquid is heated to the final desired temperature. The liquid then flows concurrently with the gas stream into the flow channel and is released into the phase separator. In a float valve attached to the phase separator, the liquid is collected and drained into a surge drum. The accumulated liquid in the surge drum is sucked through a filter by a centrifugal pump and is fed back to the liquid reservoir. The centrifugal pump is switched on by the signal of a second level indicator measuring the liquid height at a preset value inside the surge drum.

3.3 Flow channel

The flow channel has been designed to closely recreate the gas-driven film evaporation conditions of the LPP airblast atomizer. In addition to this aspect, the configuration also considers the boundaries set by the properties of materials used, the accessibility of high resolution measurement techniques, and the available manufacturing capability in the institute's workshop. Over the period of development, the realization of the basic concept discussed in Sec. 3.1 resulted as the geometrical shape presented in detail in Figs. 3.7 and 3.8. The relevant parts of the flow channel, their dimensions, and the operating parameters of the experimental setup are listed in Table 3.1. Most of the parts of the flow channel were made of stainless steel of the compounding 1.4541 (Type AISI 321). Graphite gaskets with plain and tanged metal reinforcements were used to seal the flow channel at its connecting junctures. Depending on the liquid mass flow rate $\dot{M}_{\mathrm{L}}$, the range of the liquid temperature $T_{\mathrm{L,in}}$ was restricted by the heating capacity of the ceramic heater and the thermostat. Similarly, the temperature $T_{\mathrm{G,in}}$ of the gas flow was limited by the gas heater capacity and the gas mass flow rate $\dot{M}_{\mathrm{G}}$.

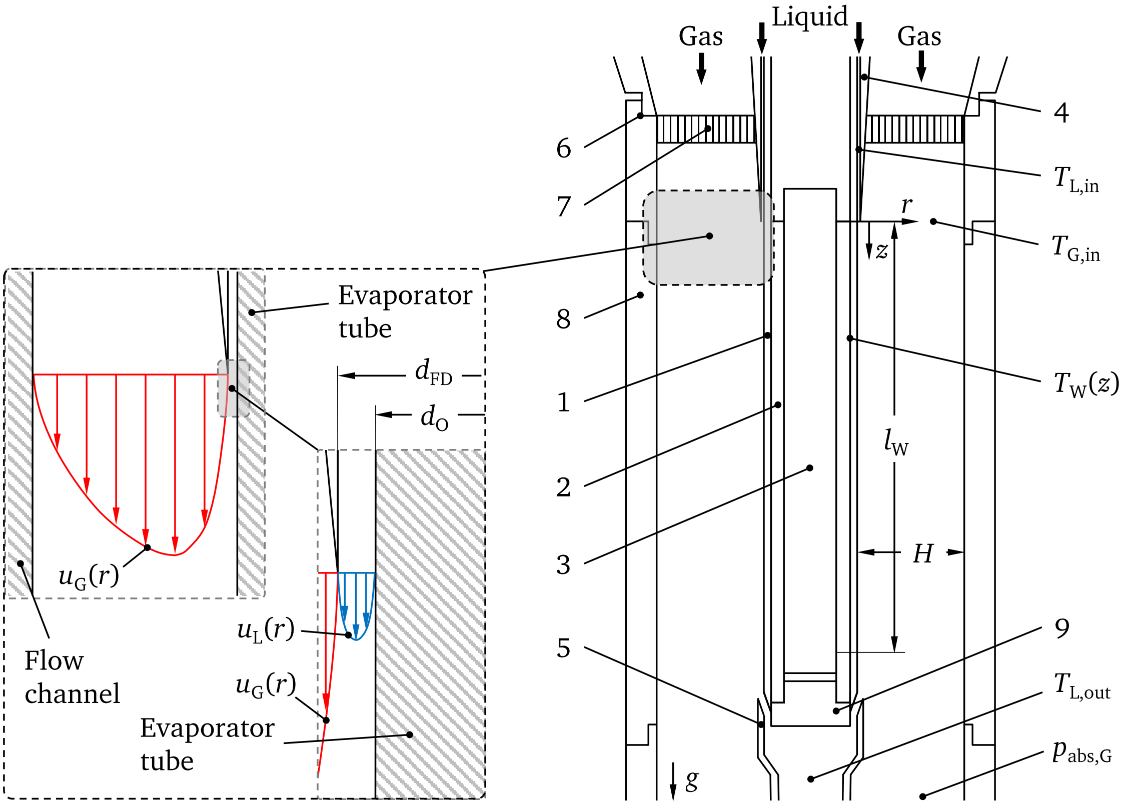

Figure 3.7. Longitudinal cut of the flow channel. In the insets, exemplarily qualitative velocity profiles of gas and liquid streams are shown.

A vertically aligned evaporator tube (1), which is made of copper, represents the core element of the the flow channel (6) (see Fig. 3.7). The tube is positioned in the channel's center and thereby an annular octagonal cross section is formed. At the channel inlet, the gas flows in and streams through a flow straightener (7), such that any radial or peripheral inhomogeneity of the gas flow field is avoided. The liquid simultaneously exits from a slot of a width of $425 \pm 25\,\mu\mathrm{m}$ provided by a film distributor (4) concentrically positioned to the tube. The liquid after exiting the film distributor forms a uniform thin film on the evaporator tube. The distance between the tube and the film distributor was adjusted by using a spacer ring positioned in the liquid outlet.

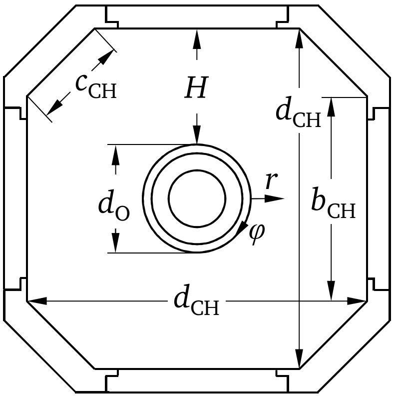

Figure 3.8. Cross section of flow channel at $z = 10\,\mathrm{mm}$.

After the adjustment procedure, the spacer was removed and the liquid flow was initiated to check for the uniform distribution of liquid.

Table 3.1. Left: list of relevant parts of flow channel, center: characteristic dimensions of flow channel, right: operating parameters of experimental setup

No.	**Item**	**Dimension**			**Parameter**		
1	Evaporator tube	d_{CH}	$= 60$	mm	$T_{\mathrm{G,in}}$	$= 293 - 723$	K
2	Sleeve	b_{CH}	$= 40$	mm	$T_{\mathrm{L,in}}$	$= 298 - 358$	K
3	Heating cartridge	c_{CH}	$= 14.1$	mm	$p_{\mathrm{abs,G,max}}$	= max. 12	bar
4	Film distributor	d_{O}	$= 19$	mm	$\dot{M}_{\mathrm{G}}$	$= 0.0125 - 0.2216$	$\mathrm{kg s^{-1}}$
5	Drainage	d_{FD}	$= 19.85$	mm	$\dot{M}_{\mathrm{L}}$	$= 0.00417 - 0.0417$	$\mathrm{kg s^{-1}}$
6	Flow channel	l_{W}	$= 90$	mm	$\dot{q}_{\mathrm{W}}$	= max. 37.2	$\mathrm{W cm^{-2}}$
7	Flow straightener				X_{G}	$= 2 - 4$	%
8	Glass window						
9	Sealing plug						

The first contact between the gas and the liquid stream occurs at the axial position $z = 0$. The gas stream concurrently accelerates the liquid film towards the exit of the flow channel and ahead to the drainage (5). Once the liquid film reaches the end of the evaporator tube, it is collected inside the drainage and extracted out of the flow channel. At the end of the evaporator tube, a sealing plug (9) prevents the intrusion of liquid and gas into the core of the tube. While the liquid is sheared along the surface of the evaporator tube, it is heated by using a high-performance heating cartridge (3) mounted inside the tube. With an AC power supply, a preset heat flow density $\dot{q}_{\mathrm{W}}$ on the wall is applied. Due to manufacturing and assembly constraints, the inlet temperature of the liquid $T_{\mathrm{L,in}}$ is measured with a thermocouple dipped into the liquid at the axial coordinate $z = -15\,\mathrm{mm}$. With a second thermocouple inside the collected liquid within the drainage, the outlet liquid temperature $T_{\mathrm{L,out}}$ is recorded. In order to provide optical access to the liquid film flow, glass windows (8) are assembled at the channel. The inlet temperature of

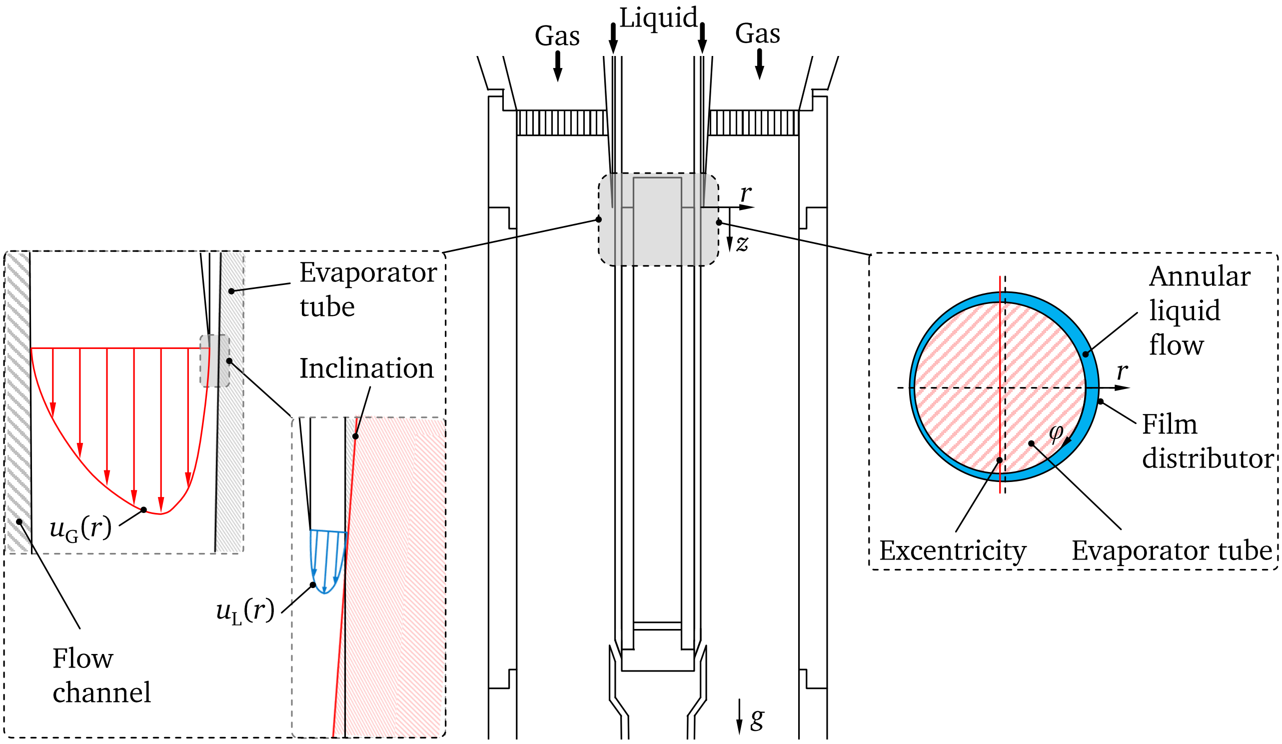

Figure 3.9. Inhomogeneity of film distribution due to inclination and eccentric orientation of the evaporator tube inside the flow channel.

the gas $T_{\mathrm{G,in}}$ is detected in the gas stream at $z = 0$. Inside the evaporator tube, a copper sleeve (2) is integrated along with thermocouples to measure the axial distribution of the wall temperature.

During the design and the assembly procedure of the flow channel, great attention was paid to the exact configuration of the evaporator tube together with the film distributor. The vertical orientation of the tube was aligned using a water-level bubble. The concentric position within the film distributor was adjusted with three radially mounted fine-threaded screws. To keep a constant distance between the tube and the film distributor, a stainless steel ring was used. The difference between the inner diameter of the ring and the outer diameter d_{O} of the evaporator tube was $10\,\mu\mathrm{m}$. Similar tolerance was maintained with its outer diameter and the inner diameter d_{FD} of the film distributor. The ring was sleeved over the evaporator tube into the film distributor. To make sure that a constant distance between the evaporator tube and the film distributor is maintained over the perimeter, the stainless steel ring was rotated a full circle around its axis. If necessary, the evaporator tube was radially relocated using either of the radially mounted fine-threaded screws. Nevertheless, due to the manufacturing, assembling, and measurement tolerances, perfect alignment of the evaporator tube in the center of the film distributor was not possible. As shown in Fig. 3.9, both of the cases can lead to a heterogeneous distribution of the liquid film at the inlet. More liquid on one side may lead to the formation of three-dimensional waves even at low liquid Reynolds numbers (see Fig. 7.1).

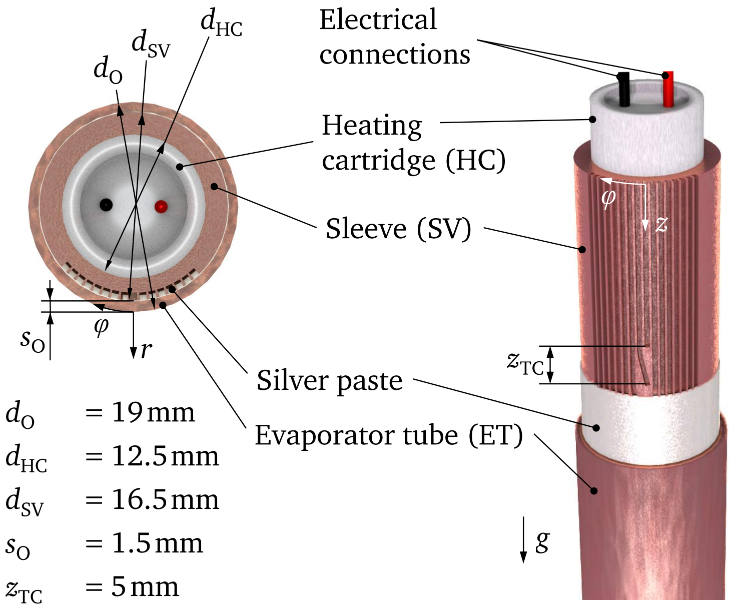

Figure 3.10. Configuration of the evaporator tube for unstructured and micro-structured surfaces containing the sleeve for thermocouples and the heating cartridge [82] (modified).

The details of the evaporator tube are shown in Fig. 3.10. Principally, the evaporator tube bundle incorporates the evaporator tube itself, a sleeve, and a heating cartridge. A commercially available high-performance heating cartridge[4] with a maximum power of $2000\,\mathrm{W}$ was chosen. The outer diameter d_{HC} of the heating cartridge was $12.5\,\mathrm{mm}$ with a heated length of $l_{\mathrm{W}} = 90\,\mathrm{mm}$. To determine the axial wall temperature distribution and for determining the heat transfer rates between the heated wall and the liquid flow, 16 thermocouples were embedded at $\varphi = 0$ into the copper sleeve as shown in Fig. 3.10. The sleeve has an outer diameter of $d_{\mathrm{SV}} = 16.5\,\mathrm{mm}$.

The implementation of the thermocouples was executed as follows. At the outer cylindrical surface of the sleeve accurate grooves with squared cross section and a depth of $s_{\mathrm{TC}} = 0.6\,\mathrm{mm}$ were previously micro-milled. The heating cartridge was covered with liquid silver paste, to reduce the thermal resistance. Subsequently the heating cartridge was pushed into the sleeve. After inserting each thermocouple into the rectangular grooves, they were bounded with thin wires wrapping over the circumference of the sleeve. This stage was necessary to ensure the thermocouples not to stuck out from the grooves. Once all the thermocouples were mounted and their measuring tips were positioned, the heating cartridge was turned on to heat up the sleeve. During the heating process, the temperature by the wall of the sleeve was measured using the embedded thermocouples. The input power of the heating cartridge was controlled to obtain a constant temperature over the wall which was equal to the melting temperature of the solder. Subsequently, all grooves were filled with solder and the thermocouples were completely dipped in the solder. After the soldering, the heating cartridge was turned off and the sleeve slowly cooled down in the surrounding air. The remaining waste solder was then removed and the surface of the sleeve was polished with fine abrasive paper to achieve a smooth surface.

---

[4] FIREROD, Watlow, Kronau/Germany

In Figure 3.11, a longitudinal cut of the tube bundle including the most important parts such as the

- evaporator tube (1),
- thermocouple sleeve (2),
- heating cartridge (3),
- and plug (4)

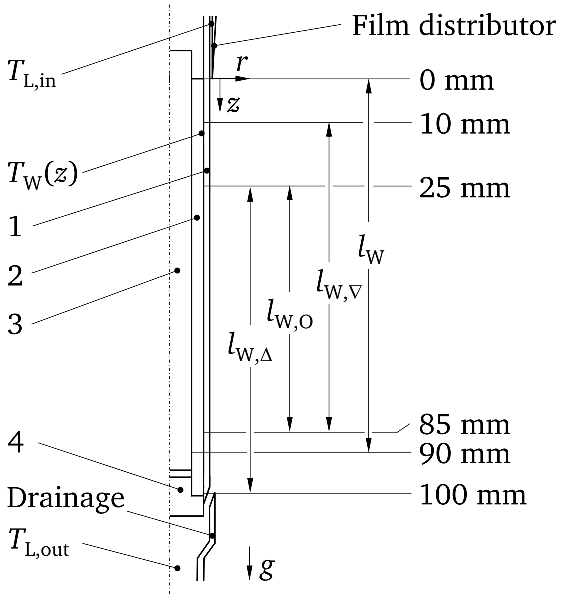

Figure 3.11. Longitudinal cut of tube bundle: Location of temperature measurements inside the wall with embedded thermocouples for unstructured, ∇-grooved and Δ-structured surfaces.

is presented. For all three types of surfaces used in this study, the lengths $l_{\mathrm{W,O}}$, $l_{\mathrm{W},\nabla}$, and $l_{\mathrm{W},\Delta}$, at which the wall temperatures along the z-direction were measured, are designated. Initially, the start and end positions for the lengths of wall temperature measurements in the tube bundles with unstructured and Δ-structured surfaces had been declared to be at $z = 25\,\mathrm{mm}$ and $z = 100\,\mathrm{mm}$. However, in the case of the unstructured surface, only 13 thermocouples out of 16 which were soldered into the wall of the sleeve could be used due to mechanical damage of the thermocouples during the assembling of the tube bundle. Hence, the measurement length $l_{\mathrm{W,O}}$ was $60\,\mathrm{mm}$ long and ranged between $z = 25\,\mathrm{mm}$ to $85\,\mathrm{mm}$. The length $l_{\mathrm{W},\Delta}$ to measure the wall temperature distribution in the Δ-structured tube was $75\,\mathrm{mm}$. After performing the first experiments with unstructured and Δ-structured surfaces, it was decided to move the starting position of the measurement length for the ∇-grooved surface as far as possible upstream. This was intended to help to gain information of the wall temperature distribution closer to the liquid inlet. Consequently, the measurement length of $l_{\mathrm{W},\nabla} = 75\,\mathrm{mm}$ at the ∇-grooved surface reached from $z = 10\,\mathrm{mm}$ to $z = 85\,\mathrm{mm}$.

The polished surface of the sleeve was then coated with silver paste for the reduction of thermal resistance. To complete the tube bundle assembly, the evaporator tube was heated up and was then shrunken onto the sleeve. A sealing plug (see Fig. 3.7) was screwed into the sleeve to prevent the flow of fluid through the tube bundle.

Between the sealing plug and the heating cartridge an air gap of $2\,\mathrm{mm}$ was maintained to minimize the axial heat conduction. Consequently, all thermocouples which were used had a distance of $s_{\mathrm{O}} = 1.5\,\mathrm{mm}$ from the liquid-wall interface. During the assembly, the cables of the thermocouples and the heating cartridge were led through the top of the flow channel using an extension tube connected upstream at the evaporator tube. Finally, the cables were connected to the data acquisition system and to the power supply unit[5]. In the image 3.12b, parallel arranged scratches running in φ-direction can be noticed. The orientation of the striation-like scratches can be accommodated to the manufacturing with lathe in which the tube was rotated at the z-axis. During this process, the form of the cutting edge could have led

---

[5] GEN300-8-D, TDK-Lambda Germany GmbH, Achern-Germany

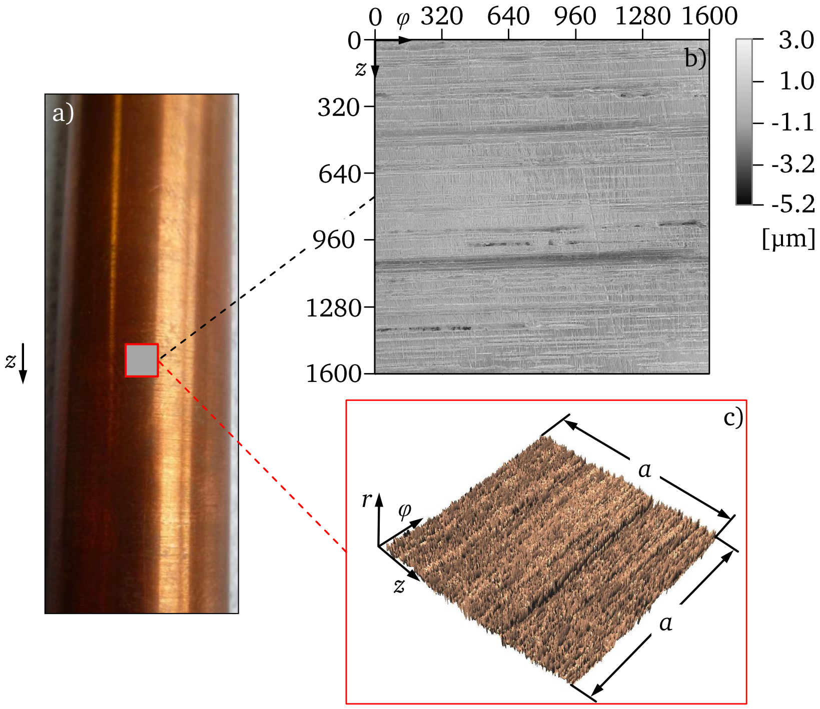

Figure 3.12. Unstructured surface: a) Image taken with single-lens reflex camera after manufacturing with lathe, b) 2D image scanned by using confocal microscope, c) 3D isometric reconstruction through post-processing after surface scanning.

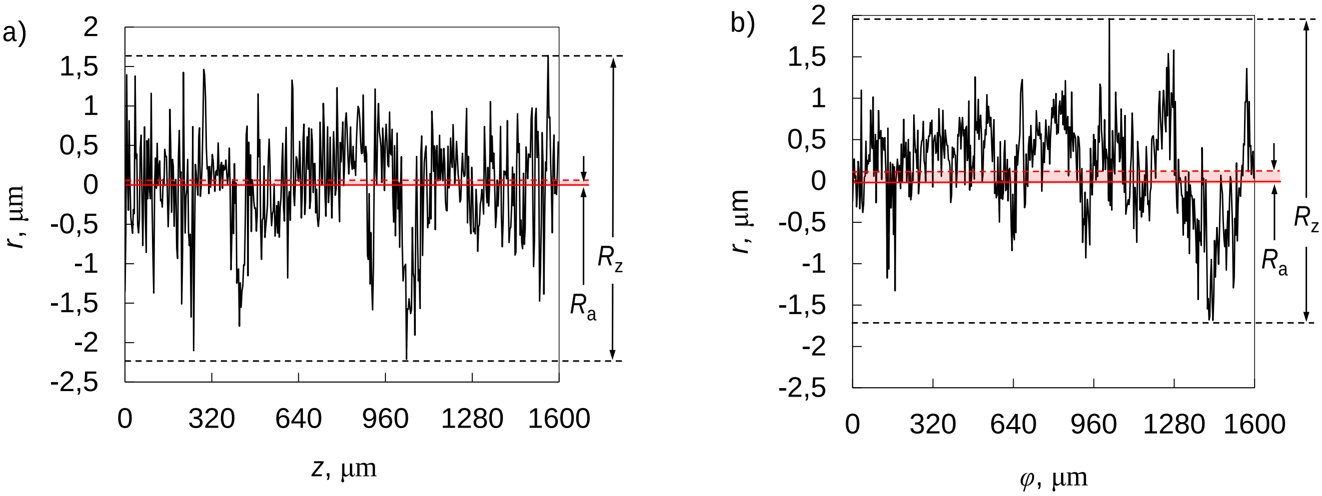

Figure 3.13. Roughness profiles of unstructured surface: a) Profile at $\varphi = 800\,\mu\mathrm{m}$, b) Profile at $z = 800\,\mu\mathrm{m}$.

to the formation of chips. However, a few longitudinal scratches arranged almost parallel to the z-axis can be identified. The 3D reconstruction (see Fig. 3.12c) of the surface scan qualitatively displays the micro-corrugations at the surface. As examples, quantitative measurement results regarding the profile of surface roughness are provided by the plots shown in Figs. 3.13a and 3.13b. The arithmetic mean values of the profile ordinates R_a for both cases are in the range of $\pm 0.1 - 0.2\,\mu\mathrm{m}$, which is rather small compared to the maximum height $R_z = 3.6 - 3.9\,\mu\mathrm{m}$. Based on multiple scans, the mean of R_z was calculated $3\,\mu\mathrm{m}$.

3.4.1 V-grooved surface (∇-structure)

The ∇-grooved surface was chosen because a heat transfer enhancement can be obtained through the rupture of the film and hence by the three-phase contact line formation [46, 85, 130]. The increase of the three-phase contact line length increases the heat flux dissipation remarkably [127]. Besides this aspect, longitudinally oriented grooves can stabilize the liquid film flow [62] and thus can avoid surface dryout. In addition, shear force acting at the liquid film surface can additionally prevent the formation of film rupture. However, the geometrical dimensions at which film rupture occurs for particular interfacial shear stress had to be predetermined.

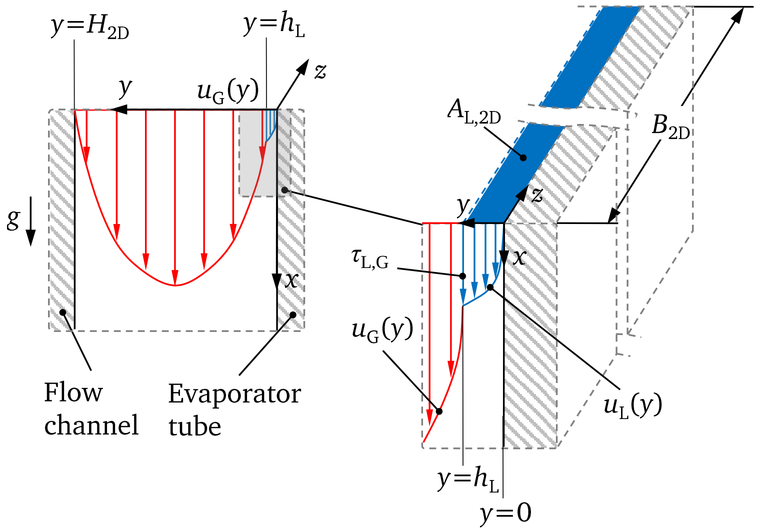

Figure 3.14. Schematic of 2D model of a shear-driven liquid film under the influence of gravity flowing in a rectangular channel with Cartesian coordinates.

With these requirements, an approximation with an analytical 2D model according to [49] was carried out in Matlab. The calculations have been used to design grooves with ∇ geometry in terms of achieving film rupture for the gas and liquid mass flow rates which could be adjusted in the experiments. For the 2D model, a flow channel with a rectangular flow cross section with a height H_{2D} and a much larger width B_{2D} was considered (see Fig. 3.14). A laminar and fully developed liquid film flow was initiated at the inlet. For both the fluids, the velocity profiles have been set as co-current parallel streams, or superimposition of Couette flow with a pressure drop and gravity-driven flow. The other assumptions are:

- streamlines are parallel to x-direction,
- waveless gas-liquid interface,
- both the flows are stationary and laminar.

The following equations have been used for the velocity profiles of the gas and the liquid flow fields:

$$u_{\mathrm{G}}(y)=\frac{1}{\mu_{\mathrm{G}}}\left(\left(\rho_{\mathrm{G}}g-\frac{\partial p}{\partial x}\right)\left(h_{\mathrm{L}}\left(y-H_{\mathrm{2D}}\right)-\frac{y^2-{H_{\mathrm{2D}}}^2}{2}\right)+\tau_{\mathrm{L,G}}\left(y-h_{\mathrm{L}}\right)\right)\quad , \tag{3.3}$$

$$u_{\mathrm{L}}(y)=\frac{1}{\mu_{\mathrm{L}}}\left(\left(\rho_{\mathrm{L}}g-\frac{\partial p}{\partial x}\right)\left(h_{\mathrm{L}}y-\frac{y^2}{2}\right)+\tau_{\mathrm{L,G}}y\right)\quad . \tag{3.4}$$

Here, h_{L} and $\tau_{\mathrm{L,G}}$ are the liquid film thickness and the interfacial shear force between liquid and gas, respectively. The interfacial shear stress $\tau_{\mathrm{L,G}}$ and the pressure gradient $\partial p/\partial x$ could be determined by using the expressions

$$\tau_{\mathrm{L,G}}=2\frac{H_{\mathrm{2D}}-h_{\mathrm{L}}}{H_{\mathrm{2D}}{h_{\mathrm{L}}}^2}\left(\mu_{\mathrm{L}}\mathit{\Gamma}_{\mathrm{L}}-\left(\rho_{\mathrm{L}}-\rho_{\mathrm{G}}\right)g\frac{{h_{\mathrm{L}}}^3}{3}-\mu_{\mathrm{G}}\mathit{\Gamma}_{\mathrm{G}}\frac{{h_{\mathrm{L}}}^3}{\left(H_{\mathrm{2D}}-h_{\mathrm{L}}\right)^3}\right)\quad , \tag{3.5}$$

$$\frac{\partial p}{\partial x}=\rho_{\mathrm{G}}g-\mu_{\mathrm{G}}\mathit{\Gamma}_{\mathrm{G}}\frac{3}{\left(H_{\mathrm{2D}}-{h_{\mathrm{L}}}^3\right)}-\frac{3}{H_{\mathrm{2D}}{h_{\mathrm{L}}}^2}\mu_{\mathrm{L}}\mathit{\Gamma}_{\mathrm{L}}+\frac{h_{\mathrm{L}}}{H_{\mathrm{2D}}}\left(\rho_{\mathrm{L}}-\rho_{\mathrm{G}}\right)g+\frac{3}{H_{\mathrm{2D}}}\mu_{\mathrm{G}}\mathit{\Gamma}_{\mathrm{G}}\frac{h_{\mathrm{L}}}{\left(H_{\mathrm{2D}}-h_{\mathrm{L}}\right)^3}\quad . \tag{3.6}$$

Conditions of constant gas and liquid flow rates yielded the formulas:

$$\dot{V}_{\mathrm{L}}=\int_0^{h_{\mathrm{L}}}\int_0^{B_{\mathrm{2D}}}u_{\mathrm{L}}(y)\,dydz\quad , \tag{3.7}$$

$$\dot{V}_{\mathrm{G}}=\int_0^{H_{\mathrm{2D}}}\int_0^{B_{\mathrm{2D}}}u_{\mathrm{G}}(y)\,dydz\quad . \tag{3.8}$$

Here, is $\partial p/\partial x=$ constant. Since the height of the film thickness h_{L} is expected to be much smaller than height H_{2D} of the gas flow field, the integration limit $\int_0^{H_{\mathrm{2D}}}$ has been used in Eq. 3.8 instead of the limit $\int_h^{H_{\mathrm{2D}}}$. Substituting u_{G} and u_{L} from Eqs. 3.3 and 3.4 into Eqs. 3.7 and 3.8 and integrating over dy leads to the specific gas and liquid flow rates per unit channel width:

$$\mathit{\Gamma}_{\mathrm{L}}=\frac{1}{\mu_{\mathrm{L}}}\left(\rho_{\mathrm{L}}g\frac{{h_{\mathrm{L}}}^3}{3}-\frac{{h_{\mathrm{L}}}^3}{3}\frac{\partial p}{\partial x}+\tau_{\mathrm{L,G}}\frac{{h_{\mathrm{L}}}^2}{2}\right), \tag{3.9}$$

$$\mathit{\Gamma}_{\mathrm{G}}=\frac{1}{\mu_{\mathrm{G}}}\left(\rho_{\mathrm{G}}g\left(\frac{{H_{\mathrm{2D}}}^3}{3}-\frac{h_{\mathrm{L}}{H_{\mathrm{2D}}}^2}{2}\right)-\frac{\partial p}{\partial x}\left(\frac{{H_{\mathrm{2D}}}^3}{3}-\frac{h_{\mathrm{L}}{H_{\mathrm{2D}}}^2}{2}\right)-\tau_{\mathrm{L,G}}\frac{{H_{\mathrm{2D}}}^2}{2}\right)\quad . \tag{3.10}$$

The pressure drop, interfacial stress, and the film thickness have been calculated for the experimental flow channel height H and the provided gas and liquid flow rates. The calculations were done by solving the two-phase flow equations in the channel at constant temperature and without free-surface deformations (negligence of contact angle). For varying gas and liquid flow rates, the resulting cross section $A_{\mathrm{L,2D}}$ was determined. Subsequently, the area $A_{\mathrm{L,2D}}$ was placed as $A_{\mathrm{L},\nabla}$ in a ∇-groove geometry as shown in Fig. 3.15. Since this geometry should be manufactured on the surface of a tube, the height of a single groove h_{∇}, the apex angle β_{∇} and the number of grooves n_{∇} were variable parameters.

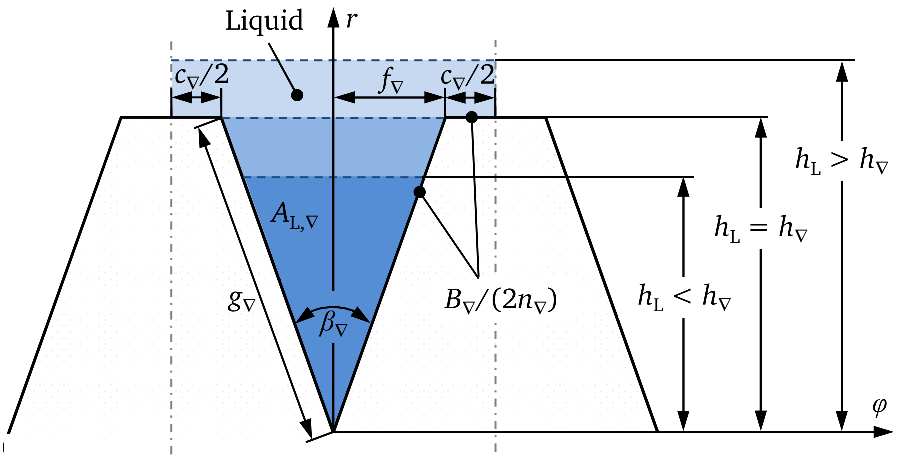

Figure 3.15. 2D sketch of liquid flow cross section in the ∇-grooved geometry.

It has to be mentioned here that the formation of a meniscus such as in real conditions has not been taken into account. The wetted length B_∇ in the 2D model (see Fig. 3.15) for film rupture has been calculated as

$$B_\nabla = n_\nabla \left(c_\nabla + 2g_\nabla\right) \quad , \tag{3.11}$$

with the crest width

$$c_\nabla = \frac{d_\mathrm{O}\pi}{n_\nabla} 2f_\nabla \quad , \tag{3.12}$$

and the length

$$f_\nabla = h_\nabla \tan\frac{\beta_\nabla}{2} \quad , \tag{3.13}$$

additionally with

$$g_\nabla = \frac{h_\nabla}{\cos\frac{\beta_\nabla}{2}} \quad . \tag{3.14}$$

Comparing the height of the liquid-gas interface with the groove height, three possible physical states were identified:

- $h_\mathrm{L} < h_\nabla \rightarrow$ partial wetting,
- $h_\mathrm{L} = h_\nabla \rightarrow$ onset of partial wetting,
- $h_\mathrm{L} > h_\nabla \rightarrow$ fully flooded structure area.

Particularly at the maximum liquid flow rate combined with the minimum gas flow rate or even without gas flow a film rupture in the ∇-groove is unlikely. Hence, these configurations constituted a limitation for the ∇-groove geometry design. Nevertheless, the calculations were executed for all gas and liquid mass flow rates (see Tab. 3.1) in the experimental setup. It was found that for the given experimental flow parameters, the predicted geometry configuration for the ∇-groove is with $n_\nabla = 70$, $\beta_\nabla = 60\,^\circ$ and $h_\nabla = 650\,\mu\mathrm{m}$.

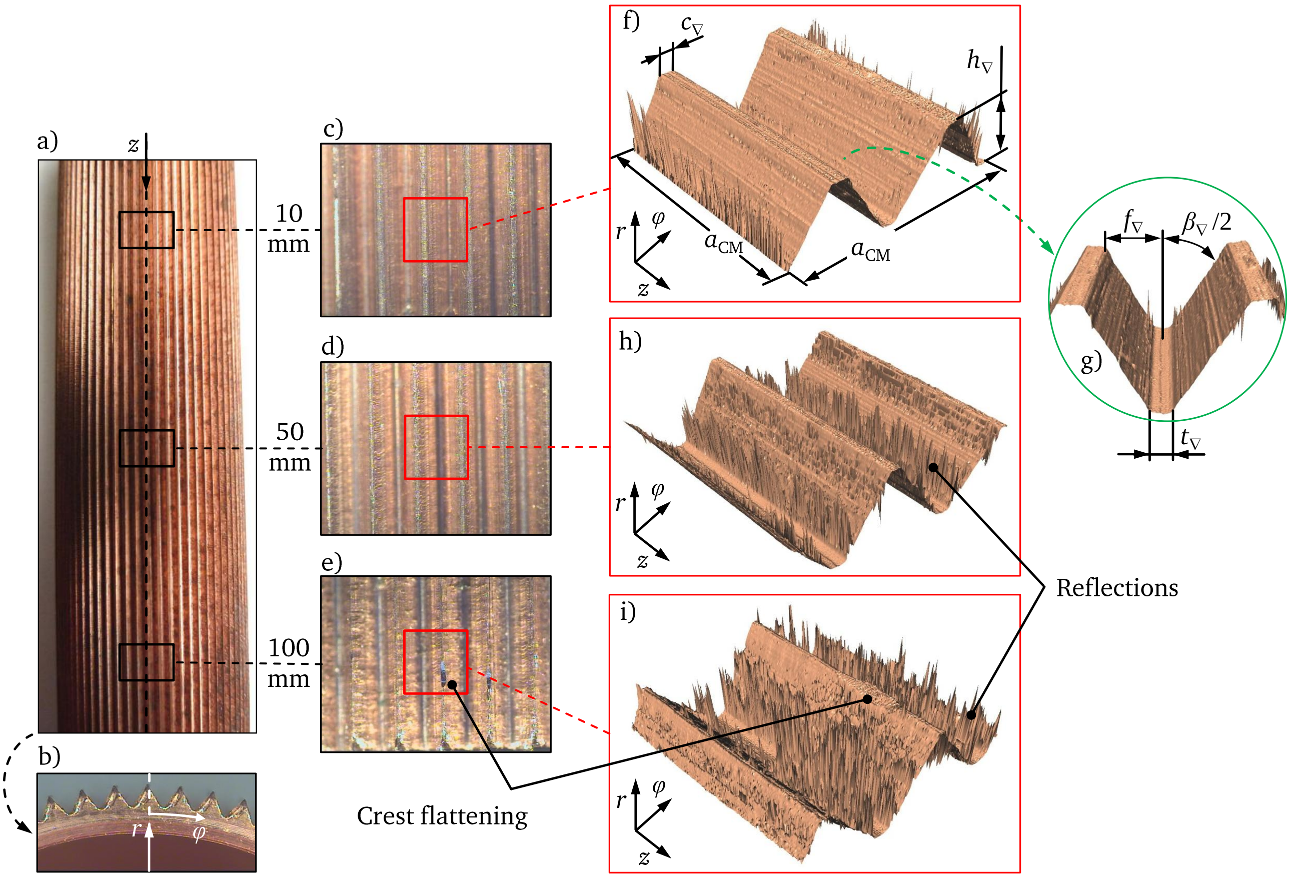

Figure 3.16. ∇-grooved surface: a) Image taken with single-lens reflex camera after manufacture, b)–e) Images made by using stereo microscope, f)–i) 3D isometric reconstruction through post-processing after scanning surface with confocal microscope.

To manufacture the ∇-grooves at the tube surface, the ultra-precision machine was used. With a $60\,^\circ$ graver, 70 longitudinal ∇-grooves were cut in the wall of the tube as illustrated in Fig. 3.16a. Since the manufacturing technology has production tolerances and deviations, the geometrical shape of the cut ∇-groove was roughly examined with a stereo microscope with a field of view of $2.2 \times 2.8\,\mathrm{mm}^2$. The faces of the ∇-grooves seem pretty smooth (see Figs. 3.16b, c, d, e) and it could be concluded that their geometrical parameters conform to the predicted values. A closer microscopic observation carried out at the axial positions $z = 10\,\mathrm{mm}$ (see Fig. 3.16f), $z = 50\,\mathrm{mm}$ (see Fig. 3.16h) and $z = 100\,\mathrm{mm}$ (see Fig. 3.16i) reveals that the ∇-grooves triangular shape is slightly different compared to the mathematical model. Instead of a spiky trough, a portion of flat platform can be seen in the trough of the groove as demonstrated in Fig. 3.16g. This can be ascribed to the flat cutter tip of the graver, which could not exactly reproduce the ideal geometry. The sharp peaks in the image are strong reflections of the LED light coming from the confocal microscope[6]. The reason for this appearance can be attributed to micro-

---

[6] µsurf explorer, NanoFocus AG, Oberhausen/Germany

corrugations on the faces leading to light reflection and resulting in incorrect information concerning the surface property. These reflections increase with increasing z due to increase of micro-corrugations.

The reason for the axial growth of micro-corrugations can be the one-sided fixation of the tube in the mechanical chuck provided inside the milling machine and the resulting vibrations during the milling procedure. This effect could not be avoided, since the length of the tube was close to the size limitation for mountable parts inside the micro-milling machine. Furthermore, the apex angle β_∇, the crest width c_∇ and the trough width t_∇ vary for the locations $z = 10\,\mathrm{mm}$, $50\,\mathrm{mm}$ to $100\,\mathrm{mm}$. This can be explained by the vibrations generated during the manufacturing process and possibly because of the fact that the copper material can be plastically deformed. In Fig. 3.16i a crest flattening happened downstream towards the end of the tube is shown. The shape of the ∇-groove is exemplarily shown in Fig. 3.17 for the position $z = 10\,\mathrm{mm}$.

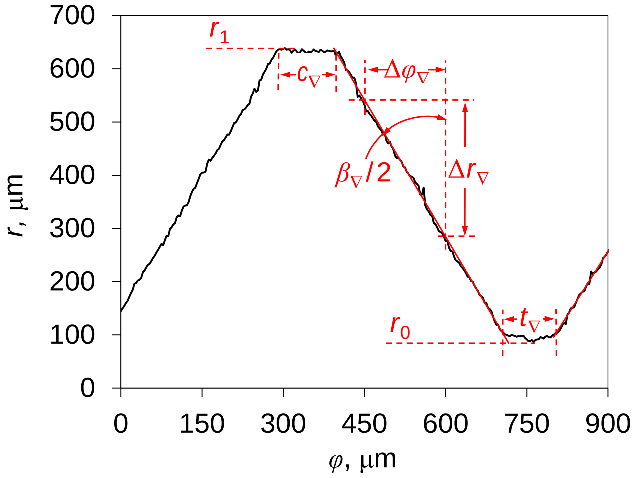

Figure 3.17. Profile of the ∇-grooved surface along φ-direction at $z = 10\,\mathrm{mm}$.

The typical triangular form is depicted together with the characteristic flat trough as mentioned. As relevant geometrical dimensions the structure height h_∇, the crest width c_∇ and the trough width t_∇ are directly measured as differences Δr_∇ and $\Delta\varphi_\nabla$. The measurements were carried out at the coordinates $z_i = 10\,\mathrm{mm}$, $50\,\mathrm{mm}$, and $100\,\mathrm{mm}$ and for each at the angular positions $0\,^\circ$, $90\,^\circ$, $180\,^\circ$ and $270\,^\circ$. The apex angle β_∇ is calculated with the formula

$$\beta_\nabla = 2\arctan\frac{\Delta\varphi_\nabla}{\Delta r_\nabla}. \tag{3.15}$$

For all geometrical dimensions, mean values are calculated. Due to the V-grooves at the wall, the surface area increased compared to the unstructured tube. Here, a surface increase factor is introduced through the expression

$$\eta_\nabla = \frac{U_\nabla}{U_\mathrm{O}}, \tag{3.16}$$

where U_∇ and U_O are the perimeters of the ∇-grooved and the unstructured tube, respectively. U_O was calculated with $d_\mathrm{O}\pi$ and $U_\nabla = B_\nabla$. The overall ∇-groove cross section $\bar{A}_\nabla$ in was determined by the equation:

$$\bar{A}_\nabla = n_\nabla \bar{h}_\nabla \bar{f}_\nabla. \tag{3.17}$$

The mean values (labelled with a bar) of relevant geometric dimensions are listed in Tab. 3.2.

The microscopic measurements reveal that the geometrical dimensions of the ∇-grooves milled on the tube surface differ with the prescribed dimensions. The source for these deviations can be the effects

Table 3.2. Mean values of geometric dimensions of the ∇-grooved surface.

Dimension		
$\bar{h}_\nabla$	=	$610 \pm 10\,\mu\text{m}$
$\bar{c}_\nabla$	=	$55\,\mu\text{m}$
$\bar{t}_\nabla$	=	$96\,\mu\text{m}$
$\bar{U}_\nabla$	=	$105.2 \cdot 10^{-3}\,\text{m}$
$\bar{A}_\nabla$	=	$207\,\text{mm}^2$
$\bar{\beta}_\nabla$	=	$51\,^\circ$
$\bar{\eta}_\nabla$	=	1.76

during the milling process explained on page 41. However, the mean groove height $\bar{h}_\nabla$ and the apex angle $\bar{\beta}_\nabla$ have been adequately manufactured in the frame of possibilities.

3.4.2 Pyramid surface (Δ-structure)

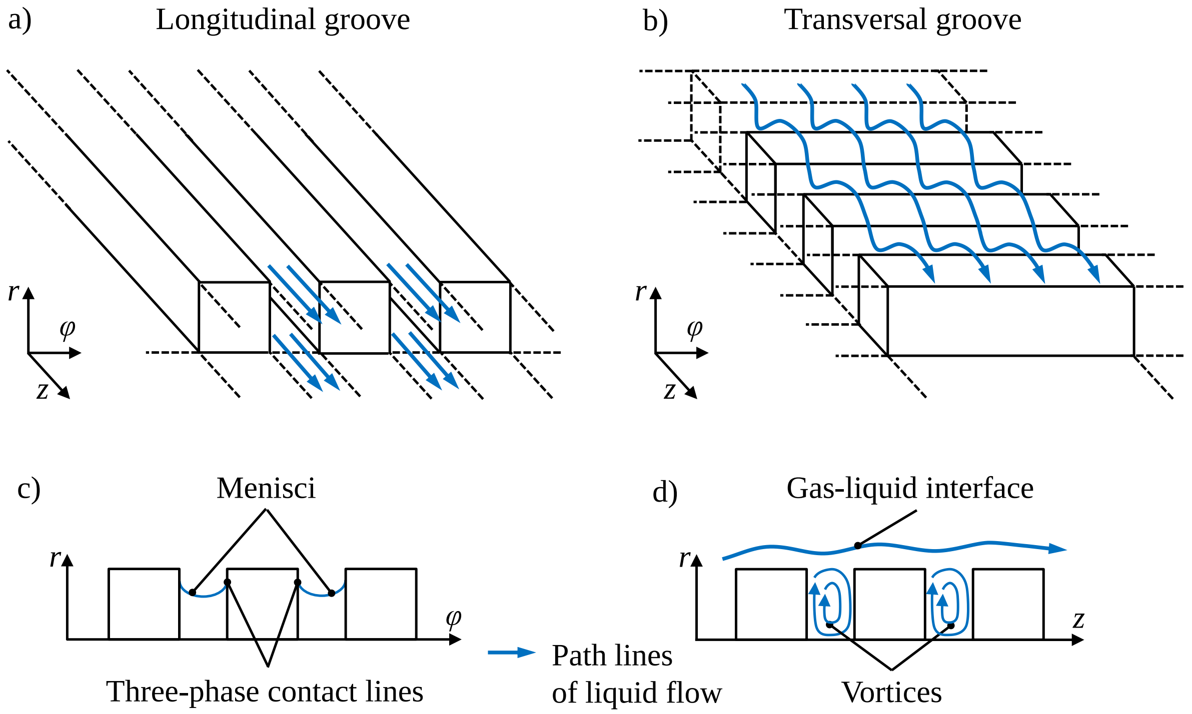

Figure 3.18. Model of rectangular grooves: a) Longitudinally oriented, b) Transversally oriented, c) Three-phase contact line formation in longitudinal grooves, d) Generation of vortices in transversal grooves.

The second structure was designed in consideration of the findings that micro-grooves oriented perpendicularly to the flow direction of the liquid cause additional enhancement of heat transfer [23, 126, 137, 146]. Compared to a longitudinal structured surface exemplarily shown in Fig. 3.18a where under partially wetted conditions menisci are formed and the three-phase contact line appears (see Fig. 3.18c), transversally oriented obstructions (see Fig. 3.18b) were depicted as baffles and led to the formation of a wavy gas-liquid interface and vortices as illustrated in Fig. 3.18d and hence to the intensification of the mixing within the liquid bulk. To achieve the advantages of both the geometries, a superpositioning of longitudinally and transversally running grooves was chosen (see Fig. 3.19a). The initial geometry was characterized by cubic obstacles. To reduce the pressure loss for the liquid flow and to avoid a permanent rupture of the film behind a single obstacle, the faces of the cubes were chamfered as shown in Fig. 3.19b to promote the rewetting of the tube surface. Thus a geometry comprised of pyramids resulted. In order that the wettability of the surface is ensured, the pyramid geometry was rotated by an angle of $45\,^\circ$ to the r-axis (see Fig. 3.20a).

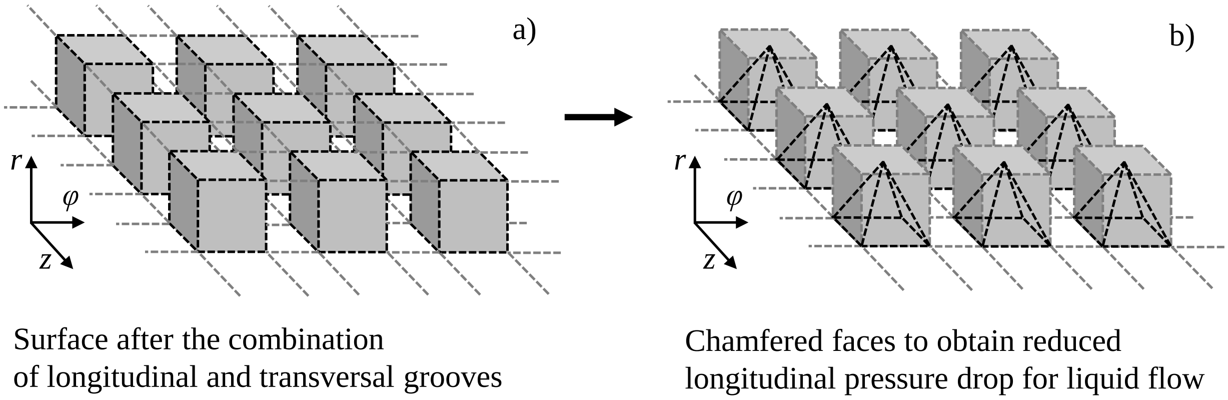

Figure 3.19. Combination of longitudinal and transversal geometry: a) Cubic geometry after combining rectangular longitudinal and transversal grooves, b) Resulting pyramid geometry after chamfering cubic faces.

A structure-free area between the pyramids remained. The path lines in Fig. 3.20b show how the liquid would flow along the pyramids. To utilize the surface fully covered with structures, additional pyramids were positioned to the structure-free area as presented in Figs. 3.21a and 3.21b.

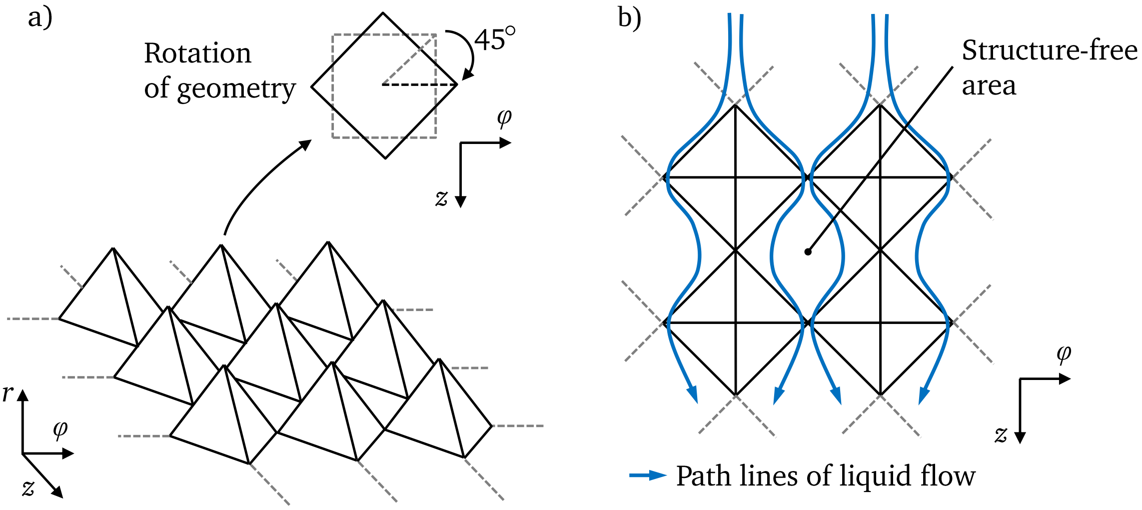

Figure 3.20. Modification of pyramid structure: a) Pyramid geometry rotated $45\,^\circ$, b) Top view of Δ-surface including pathlines of liquid flow.

The current configuration of the pyramids can induce a wavy liquid film flow containing vortices within its bulk in φ and z-direction (see Figs. 3.21c and 3.21d). Under conditions in which the structure is partially wetted, it had been expected that the crests of the pyramids would emerge from the wavy liquid film as demonstrated in Fig. 3.22. The geometric dimensions of the pyramids should be comparable to the ∇-grooved dimensions. Since the mean height $\bar{h}_\nabla$ of the ∇-grooves was determined to be $610 \pm 10\,\mu\mathrm{m}$, the equal mean height $\bar{h}_\Delta$ of the pyramid structure has been chosen. The same requirement is valid for the apex angle $\bar{\beta}_\Delta$ of the Δ-structure. Besides this angle, three more angles δ_Δ, γ_Δ, and ε_Δ have been determined.

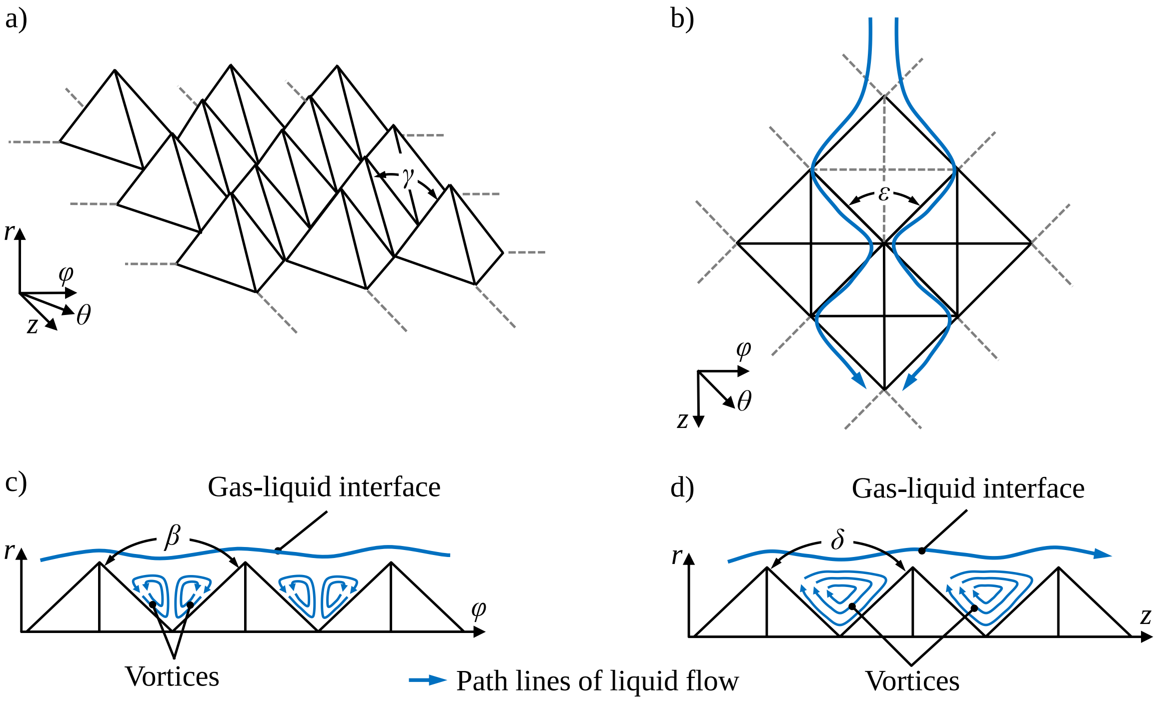

Figure 3.21. Optimization of pyramid structure: a) Δ-surface without structure-free area, b) Top view of Δ-surface including pathlines of liquid flow, c) Vortices within the pyramid troughs in cross-flow direction, d) Vortices within the pyramid troughs in liquid flow direction.

To produce the pyramids onto the surface of an evaporator tube, the ultra-precision milling machine and the knurling tool was used. The latter is based on the method of cold forging. First attempts to mill the Δ-structure on copper probes were unsuccessful. Due to the comparatively soft material copper and because of the vibration during the milling process, Δ-structure was smeared and hence was not conform with the requirements.

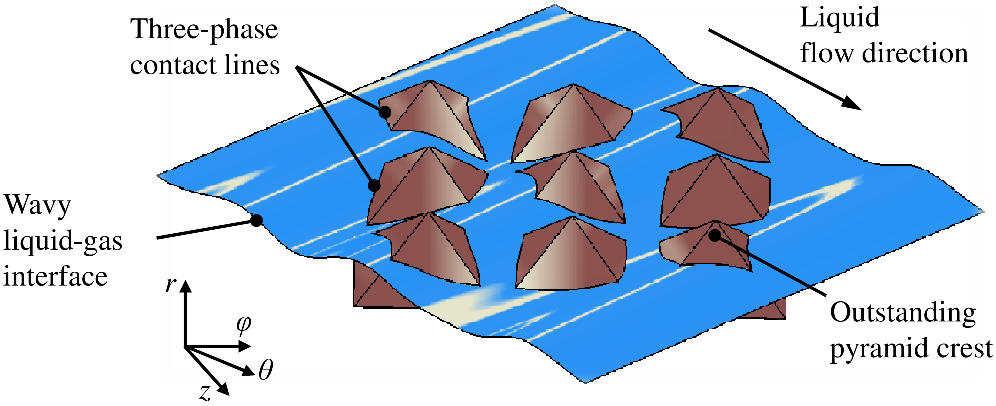

Figure 3.22. Partially wetted Δ-structure.

The trials with the knurling tool were more auspicious. The resulting pyramid structure was visually clear and indicated no smearing. After this preliminary assessment of the manufacturing procedure, the Δ-structure was knurled onto the surface of an unstructured evaporator tube. In Fig. 3.23a the manufactured Δ-structured tube is presented. The closer microscopic observation carried out at the axial positions $z = 10\,\mathrm{mm}$ (see Fig. 3.23e), $z = 50\,\mathrm{mm}$ (see Fig. 3.23i) and $z = 100\,\mathrm{mm}$ (see Fig. 3.23j) reveal that the characteristic shape of the pyramid has been acceptably embossed into the surface. However, a crest denting occurred in z-direction.

This can be explained with a simplified system of a deflecting beam. The copper cylinder was mounted on both sides into the chucks of a lathe as shown in Fig. 3.24. Here, l_{ET} is the overall length of the evaporator tube including the threaded end for mounting. $l_{\triangle}$ is the length where structures are provided and l is the overall length of the cylindrical part. The chucks are represented as fixed bearings, and the load F_{k} from the knurling tool was applied radially on the part. Due to the knurling tool design size impeding the processing of the necessary portion of the evaporator tube length l_{ET}, the area with the Δ-structure starts at $z(l_{\triangle})$. The compression force F_{k} was kept constant along $l_{\triangle}$. Since the bending stiffness of copper is not as large as steel for instance, the resilience of copper comes into account and the cylindrical part deflects. The deflection $W(z)$ is zero at the fixing points of the bearings and increases along the z-axis towards its maximum at the symmetry ($z = 0.5l$).

This effect leads to an unincisive forging of the geometry in the region of the symmetry line. At $z = 0.5l$ of the cylindrical part, only an insufficient amount of copper material could penetrate into the Δ-geometry inside the knurl and hence crater-like crests of the pyramids at these particular locations occurred. In other respects, the Δ-structure has been adequately processed such that the major area of the tube surface is homogeneously covered by pyramids.

In terms of the geometric dimensions, three more angles $\delta_{\triangle}$, $\varepsilon_{\triangle}$, and $\gamma_{\triangle}$ were determined (see Figs. 3.23e, 3.23g, and 3.23h) besides the apex angle $\beta_{\triangle}$. The determination of a single pyramid length $b_{\triangle}$, the width $c_{\triangle}$, and the height $h_{\triangle}$ was carried out with the following steps. Since the field of view of the confocal

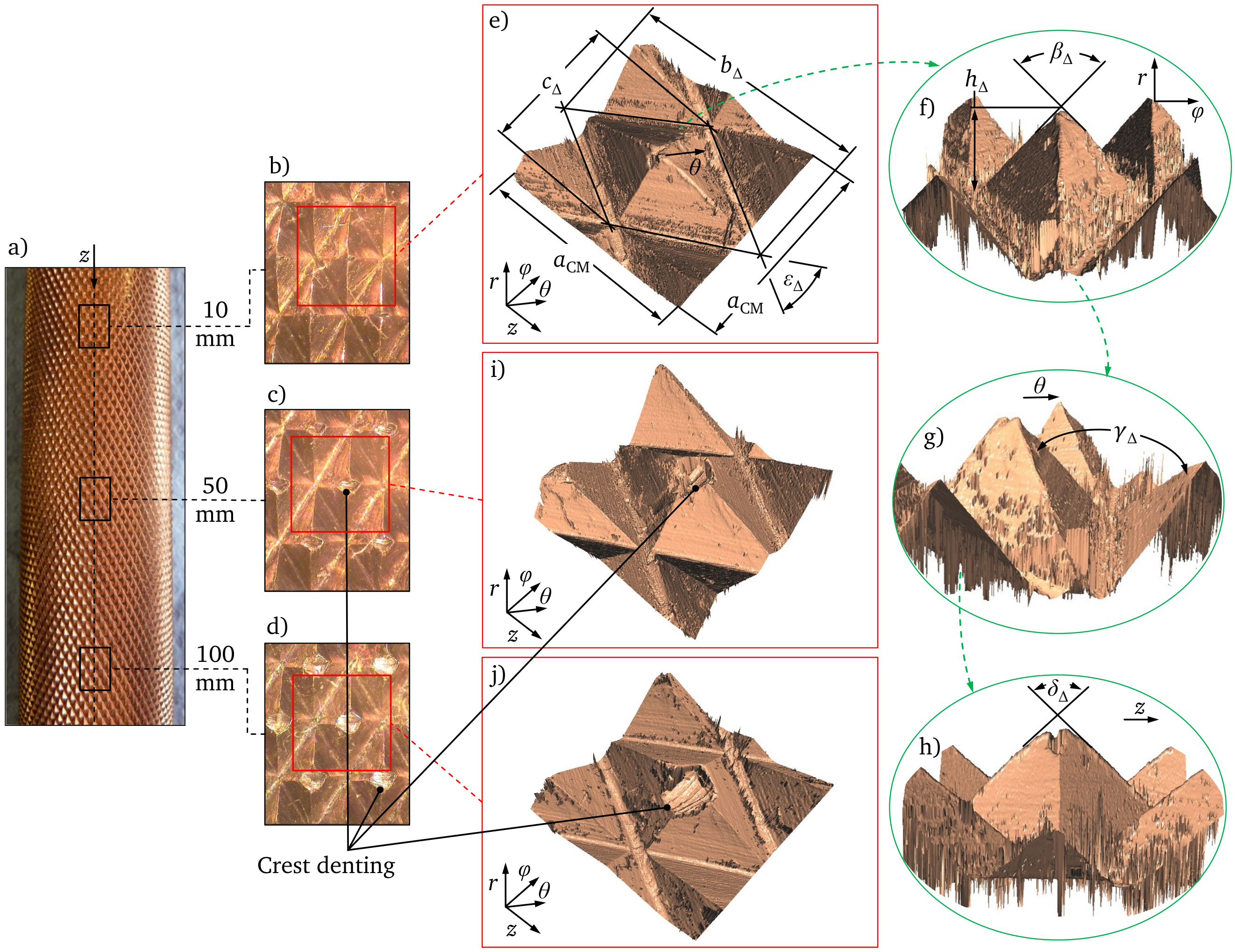

Figure 3.23. Δ-surface: a) Image taken with single-lens reflex camera after manufacture, b)–d) Images made by using stereo microscope, e)–j) 3D isometric reconstruction through post-processing after scanning surface with confocal microscope.

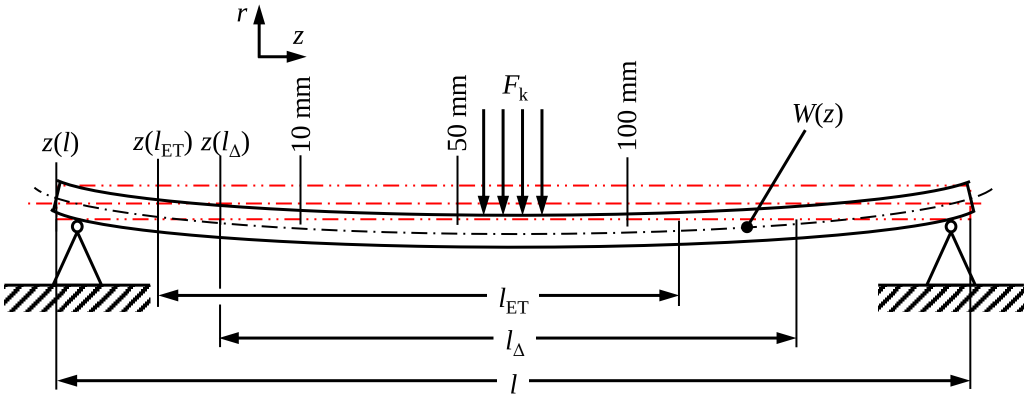

Figure 3.24. Deflection of cylindrical part during knurling process to produce pyramids on the surface.

microscope was not large enough to capture the whole geometry of a single pyramid in z-direction for the preset spatial resolution, the length b_Δ was calculated by using the angle

$$\delta_\Delta = 2\arctan\frac{\Delta z_\Delta}{\Delta r_\Delta}, \tag{3.18}$$

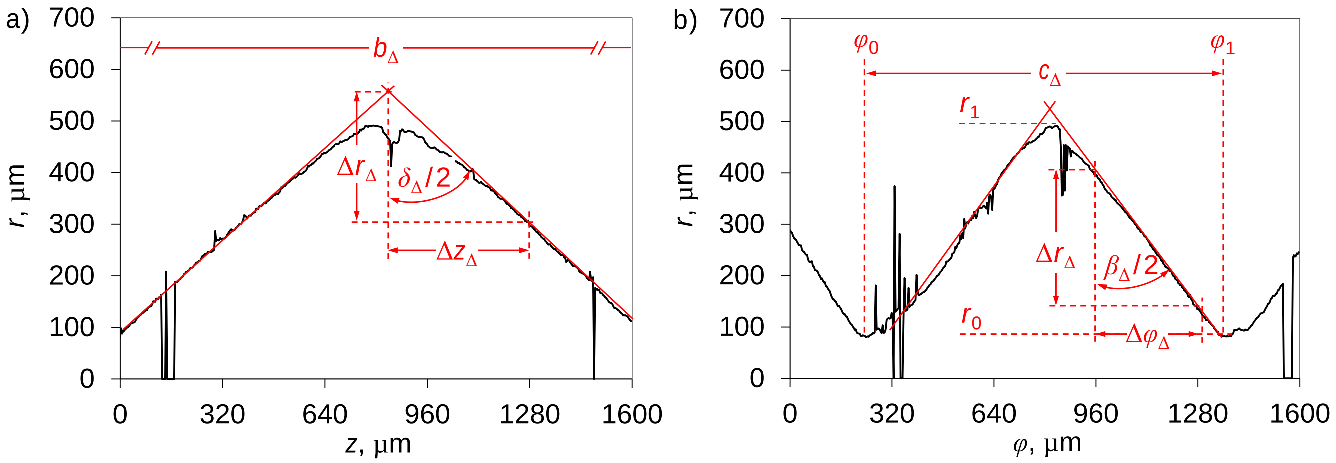

Figure 3.25. Profile of the Δ-surface: a) Along z-direction, b) Along φ-direction.

where Δz_Δ and Δr_Δ were taken by measurements presented exemplarily in Fig. 3.25a and the pyramid height measured as (see Fig. 3.25b)

$$h_\Delta = r_1 - r_0, \tag{3.19}$$

resulting as

$$b_\Delta = 2h_\Delta \tan\frac{\delta_\Delta}{2}. \tag{3.20}$$

The width c_Δ was directly measured (see Fig. 3.25b) as

$$c_\Delta = \varphi_1 - \varphi_0, \tag{3.21}$$

while the angles

$$\beta_\Delta = 2\arctan\frac{\Delta\varphi_\Delta}{\Delta r_\Delta}, \tag{3.22}$$

and

$$\gamma_\Delta = 2\arctan\frac{\Delta\theta_\Delta}{\Delta r_\Delta} \tag{3.23}$$

were elicited again by means of trigonometric functions (see Figs. 3.25b and 3.26a, respectively).

The angle ε_Δ was determined through measurements performed on half of the pyramid as illustrated in Fig. 3.26b and the function:

$$\varepsilon_\Delta = 2\arctan\frac{\Delta\varphi_\Delta}{\Delta z_\Delta}. \tag{3.24}$$

The calculations of the mean geometrical dimensions were performed similar to the calculations done for the ∇-grooved surface. The measurements were carried out at the coordinates $z = 10\,\mathrm{mm}$, $50\,\mathrm{mm}$, $100\,\mathrm{mm}$ and at four angular positions $0\,°$, $90\,°$, $180\,°$, and $270\,°$. For all geometrical dimensions, mean values are calculated. Due to the pyramids on the wall, the surface area increased compared to the unstructured tube. The surface increase factor for the Δ-structured tube was calculated with the expression

$$\bar{\eta}_\Delta = \frac{\bar{A}_\Delta}{\bar{A}_{\Delta 0}}, \tag{3.25}$$

where $\bar{A}_\Delta$ is the sum of the surfaces of manufactured pyramids positioned within a projected area confined by

$$\bar{A}_{\Delta 0} = d_O \pi \bar{b}_\Delta. \tag{3.26}$$

Here $\bar{b}_\Delta$ is the mean length of the pyramids in z-direction. The mean values (labeled with a bar) of relevant geometric dimensions for the Δ-surface are listed in Tab. 3.3.

Table 3.3. Mean values of geometric dimensions of the Δ-surface.

Dimension		
$\bar{h}_\Delta$	$=$	$450.4 \pm 10\,\mu\mathrm{m}$
$\bar{c}_\Delta$	$=$	$1210.1\,\mu\mathrm{m}$
$\bar{b}_\Delta$	$=$	$1778.3\,\mu\mathrm{m}$
$\bar{A}_\Delta$	$=$	$128.9\,\mathrm{mm}^2$
$\bar{\beta}_\Delta$	$=$	$60.1\,°$
$\bar{\delta}_\Delta$	$=$	$126.3\,°$
$\bar{\epsilon}_\Delta$	$=$	$68.5\,°$
$\bar{\gamma}_\Delta$	$=$	$94.2\,°$
$\bar{\eta}_\Delta$	$=$	1.35

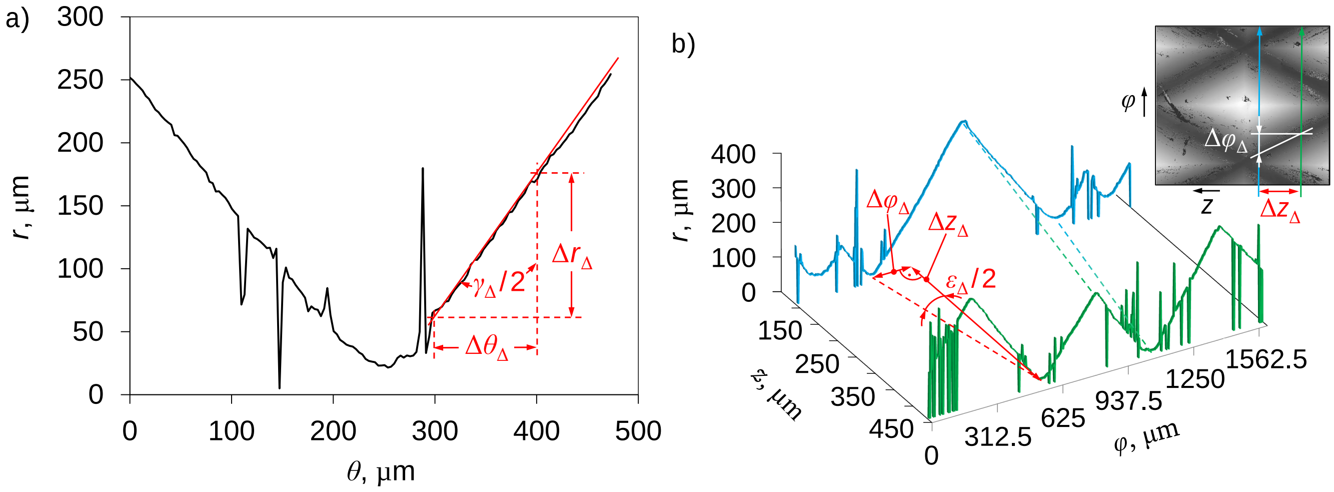

Figure 3.26. Profile of the Δ-surface: a) Along θ-direction, b) Calculation of the angle ϵ with profiles of single pyramids along φ-direction for two different z coordinates.

Regrettably, the mean height $\bar{h}_\Delta$ is smaller compared to the mean height $\bar{h}_\nabla$ of the ∇-grooves and thus $\bar{\eta}_\Delta$ shows an approximate reduction of $23.3\,\%$ compared to $\bar{\eta}_\nabla$. This large difference can be accounted for by the denting effect of the pyramid crests which increases along the z-direction. It has an influence on the calculation of $\bar{A}_\Delta$ (see Fig. 3.27) which could not be ignored.

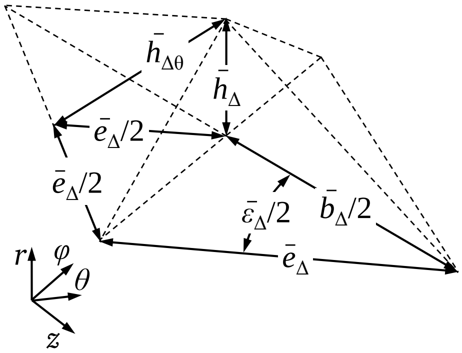

Figure 3.27. Sketch of a pyramid for the calculation of skin surface.

With

$$\bar{h}_{\Delta\theta} = \sqrt{\bar{h}_\Delta^2 + \left(\frac{\bar{e}_\Delta}{2}\right)^2} \tag{3.27}$$

and

$$\bar{e}_\Delta = \frac{\bar{b}_\Delta}{2}\left(\cos\frac{\bar{\varepsilon}_\Delta}{2}\right)^{-1}, \tag{3.28}$$

the calculation for the mean surface can be calculated using the expression

$$\bar{A}_\Delta = 2\bar{h}_{\Delta\theta}\bar{e}_\Delta = 2\sqrt{\bar{h}_\Delta^2 + \left(\frac{\bar{e}_\Delta}{2}\right)^2}\,\bar{h}_\Delta \tan\frac{\bar{\delta}_\Delta}{2}\left(\cos\frac{\bar{\varepsilon}_\Delta}{2}\right)^{-1}. \tag{3.29}$$

Here $\bar{\delta}_\Delta$ and $\bar{\varepsilon}_\Delta$ can be determined from Eqs. 3.18 and 3.24 and . It can be seen that the mean height $\bar{h}_\Delta$ is quadratically influencing the size of the surface of the pyramid.

3.5 Experimental parameters

For the comparison of measurement results between different surfaces and with theoretical and experimental data from the literature, the experimental parameters are formulated in dimensionless form. The geometrical parameters together with flow parameters are presented in Fig. 3.28. The liquid Reynolds number Re_L has been determined with the familiar expression for falling liquid films as

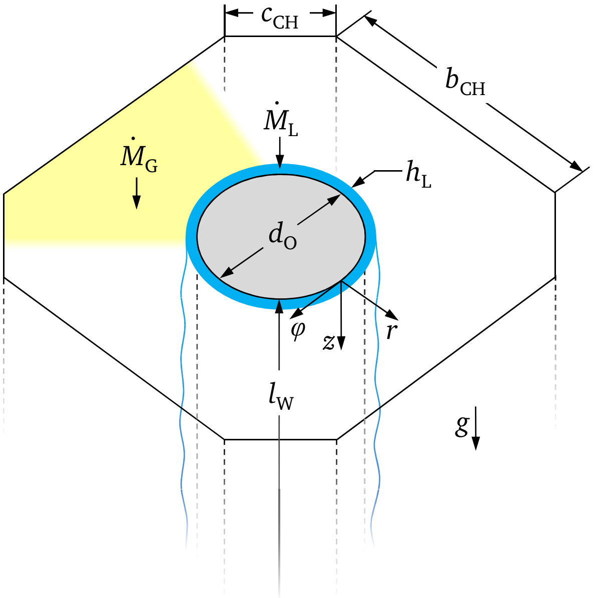

Figure 3.28. Geometrical and flow parameters for the experiments.

$$Re_{\mathrm{L}} = \frac{\Gamma_{\mathrm{L}}}{\mu_{\mathrm{L}}} = \frac{\dot{M}_{\mathrm{L}}}{U_{\mathrm{L}}\mu_{\mathrm{L}}} = \frac{\dot{M}_{\mathrm{L}}}{d_{\mathrm{O}}\pi\mu_{\mathrm{L}}} \quad . \tag{3.30}$$

To facilitate the comparison of two gas flows regarding the hydrodynamic similarity, the gas Reynolds number Re_{G} has been defined as

$$Re_{\mathrm{G}} = \frac{\bar{u}_{\mathrm{G}} d_{\mathrm{hydG}}}{\nu_{\mathrm{G}}} = \frac{\dot{M}_{\mathrm{G}}}{A_{\mathrm{G}}\rho_{\mathrm{G}}} \frac{4A_{\mathrm{G}}}{U_{\mathrm{G}}} \frac{1}{\nu_{\mathrm{G}}} = \frac{4\dot{M}_{\mathrm{G}}}{U_{\mathrm{G}}\mu_{\mathrm{G}}} = \frac{4\dot{M}_{\mathrm{G}}}{(d_{\mathrm{O}}\pi + 4(b_{\mathrm{CH}} + c_{\mathrm{CH}}))\mu_{\mathrm{G}}} \quad . \tag{3.31}$$

The wall heat flux $\dot{q}_{\mathrm{W}}$ has been calculated as

$$\dot{q}_{\mathrm{W}} = \frac{VI}{d_{\mathrm{O}}\pi l_{\mathrm{W}}} \quad , \tag{3.32}$$

where V and I are the voltage and the electrical current adjusted at the power supply of the heating cartridge, respectively.

To analyze the physical interdependence among the prescribed hydrodynamic parameters and to develop correlations concerning the heat transfer depending on gas and liquid Reynolds numbers, a large number of measurements were designed. The main parameters that were varied in the experiments are listed in Tab. 3.4. The gas and liquid inlet temperatures in the experiments on unstructured and Δ-structured surfaces were kept constant at $293\,\mathrm{K}$ and $298\,\mathrm{K}$. For the ∇-grooved surface measurements which were performed at higher ambient temperatures due to weather conditions, the gas and liquid inlet temperatures were $303\,\mathrm{K}$ and $298\,\mathrm{K}$. The dynamic viscosities μ_{L} and μ_{G} were determined indirectly by measuring the fluid inlet temperatures $T_{\mathrm{L,in}}$, $T_{\mathrm{G,in}}$ and the absolute pressure p_{abs}. The absolute pressure in the flow channel was kept constant at $3\,\mathrm{bar}$ for all measurements.

Table 3.4. Design of experimental parameters varied in this study.

<table>
<tr><th colspan="2">Parameter</th><th>unstructured surface</th><th>∇-grooved surface</th><th>Δ-structured surface</th></tr>
<tr><td>$T_{\mathrm{G,in}}$</td><td>K</td><td>293</td><td>303</td><td>293</td></tr>
<tr><td>$T_{\mathrm{L,in}}$</td><td>K</td><td colspan="3">298</td></tr>
<tr><td>p_{abs}</td><td>bar</td><td colspan="3">3</td></tr>
<tr><td>Re_{G}</td><td>–</td><td>$0 - 10^5$</td><td>$2.5 \cdot 10^4 - 8.5 \cdot 10^4$</td><td>$10^4 - 7 \cdot 10^4$</td></tr>
<tr><td>Re_{L}</td><td>–</td><td colspan="3">$80 - 800$</td></tr>
<tr><td>$\dot{q}_{\mathrm{W}}$</td><td>Wcm^{-2}</td><td colspan="3">$0, 15$</td></tr>
</table>

3.6 Closure

Through the methodological procedure and the feasibility aspects regarding material properties and the accessibility for measurement techniques, the experimental flow channel and overall setup has been designed. For the study of the influence of different surface topographies on hydrodynamics and heat transfer, two evaporator tubes, one with longitudinal ∇-grooves and another with a Δ-structure was designed and manufactured. Finally, a range of experimental parameters was chosen.

4

Data Acquisition and Measurement Methods

The data acquisition system used for the measurements is introduced in Section 4.1. The measurement techniques and instrumentation used for the record of process parameters, fluid properties, and temperature distribution in the evaporator tubes are described in Sections 4.2 and 3.4. High-speed black and white and infrared cameras are used for the visualization of the flow dynamics and the wetting characteristics. These were introduced in Section 4.3. A hot-wire anemometer used for determining the gas velocity field is described in Section 4.4.

4.1 Data acquisition system

In Figure 4.1, a line diagram of the data acquisition system (DAQ) and the connections of measurement devices is shown. During the experiments, all relevant parameters, except the high-speed camera records, were monitored and triggered by the system design software LabVIEW© from National Instruments (NI). Two separate modules, one to send analog output (AO) signals and a second to receive analog input (AI) signals, were used. In Table 4.1 the NI peripheral devices are listed. The properties (p_i, T_i) and process parameters ($\dot{M}_i$) were detected with input signals of pressure sensors, thermocouples, and mass flow meters. The data was acquired for each measurement over 10 seconds with a frequency of $f_{\mathrm{DAQ}} = 1\,\mathrm{kHz}$. Two different types of output signals were used. A signal variable between $0 - 10\,\mathrm{V}$ was used to regulate a gear pump via a frequency converter and hence the liquid mass flow rate. A single $5\,\mathrm{V}$ signal was used to trigger a high-speed black and white camera (HSC) connected with its frame grabber (FG) to visualize the liquid hydrodynamics. To investigate the liquid flow pattern and film rupture, a high-speed infrared camera (IRC) was installed and triggered with a single signal ($5\,\mathrm{V}$) sent via its own software. Besides these, a hot-wire anemometer (HWA) probe was used to measure the gas velocity distribution in the channel. Its data was also recorded using LabVIEW. In the following sections, the deployed measurement techniques are briefly described.

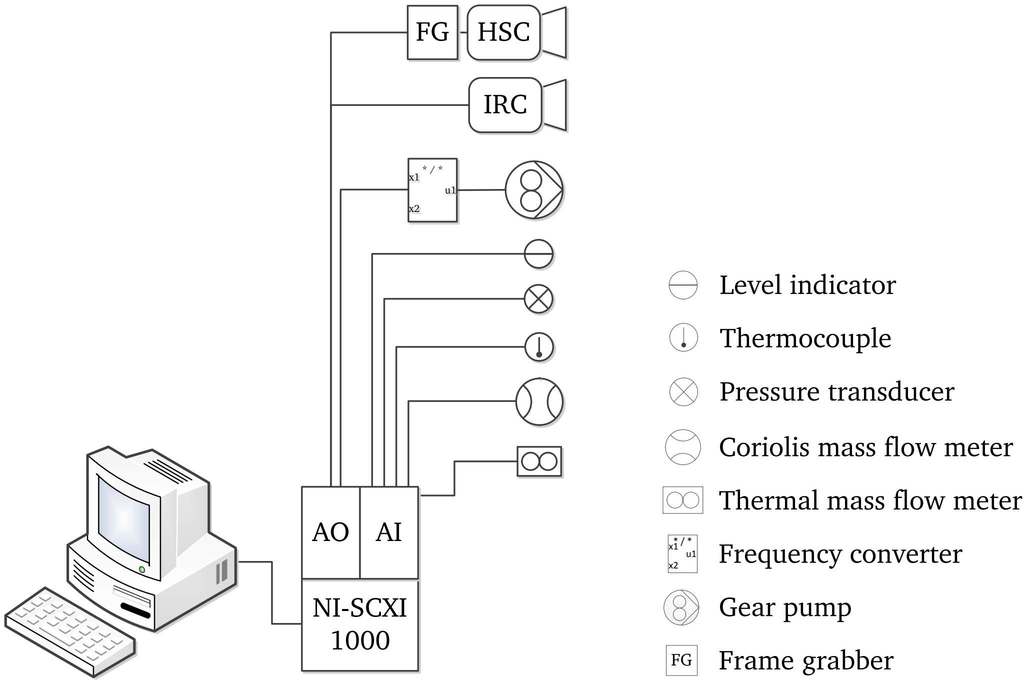

Figure 4.1. Simple circuit diagram of data acquisition system.

Table 4.1. National Instruments peripheral devices.

Module	
PCI-6289	18-bit, $500\,\mathrm{kS/s}$ (multichannel), $625\,\mathrm{kS/s}$ (1-channel), 32 analog inputs
SHC68-68-EP	Shielded I/O cable
SCXI-1000	4-slot chassis houses any SCXI modules
SCXI-1102B	32-channel amplifier module, $200\,\mathrm{Hz}$ bandwidth
SCXI-1303	Thermocouple output measurement with in-built cold junction compensation

4.2 Pressures, temperatures, and mass flow rates of gas and of liquid flows

To measure the evaporator tube temperature and the temperature of both the fluids flowing in the loops and inside the flow channel, type-K sheath thermocouples[1] were applied. According to the American Society of Testing and Materials [134], type-K thermocouples are recommended for a temperature range from $-250\,°\mathrm{C}$ to $1260\,°\mathrm{C}$ which were chosen for the experimental investigations. Some had diameters of $0.5\,\mathrm{mm}$ and other $1\,\mathrm{mm}$ and were designed according to IEC 584-3 with a responding time of $t = 150\,\mathrm{ms}$. The thermocouples were connected via Lemo couplings to the amplifier module SCXI-1102B at the NI system. To measure the system pressure in both of the flow loops, multiple pressure transducers[2] were

---

[1] Electronic Sensors, Heilbronn/Germany

[2] dTRANS p30, model 404366, JUMO GmbH & Co. KG, Fulda/Germany

used in the setup. The pressure sensors used an integrated piezoresistive measuring cell [48] embedded inside the transducer; measurement accuracy is $\pm 0.05\,\mathrm{bar}$. In the gas supply line approaching the flow channel, an absolute pressure transducer was assembled (see Figure 3.6). Another absolute pressure transducer was assembled within the flow channel at an axial position right after the liquid drainage (see Figure 3.7). Preliminary tests have revealed that a pressure drop of $0.1\,\mathrm{bar}$ arises along the flow channel when gas runs through at $Re_\mathrm{G} = 10^5$ ($p_\mathrm{abs} = 3\,\mathrm{bar}$, $T_\mathrm{G,in} = 293\,\mathrm{K}$). With a third transducer assembled in the liquid line at the inlet to the flow channel, the absolute pressure of the inflow was recorded. As was expected that $p_\mathrm{abs,G,in}$ and $p_\mathrm{abs,L,in}$ are almost equal during the tests. For the calculation of the dynamic viscosities μ_G and μ_L (for Re_G and Re_L), $p_\mathrm{abs,G,in}$ and $T_\mathrm{G,in}$ and $T_\mathrm{L,in}$, were used. The mass flow rates $\dot{M}_\mathrm{G}$ and $\dot{M}_\mathrm{L}$ of the gas and liquid flow were measured by using a thermal mass flow meter[3] and a Coriolis mass flow meter[4], respectively. The maximum flow rates which can be measured are $\dot{M}_\mathrm{G,max} = 800\,\mathrm{kg/h}$ and $\dot{M}_\mathrm{L,max} = 2.5\,\mathrm{kg/min}$, respectively. The measurement error of the thermal mass flow meter is $\pm 1.5\,\%$ of the measured value, while the Coriolis mass flow meter has an accuracy of $\pm 0.15\,\%$ of the measured value.

4.3 Measurement of film flow dynamics and visualization of film flow pattern

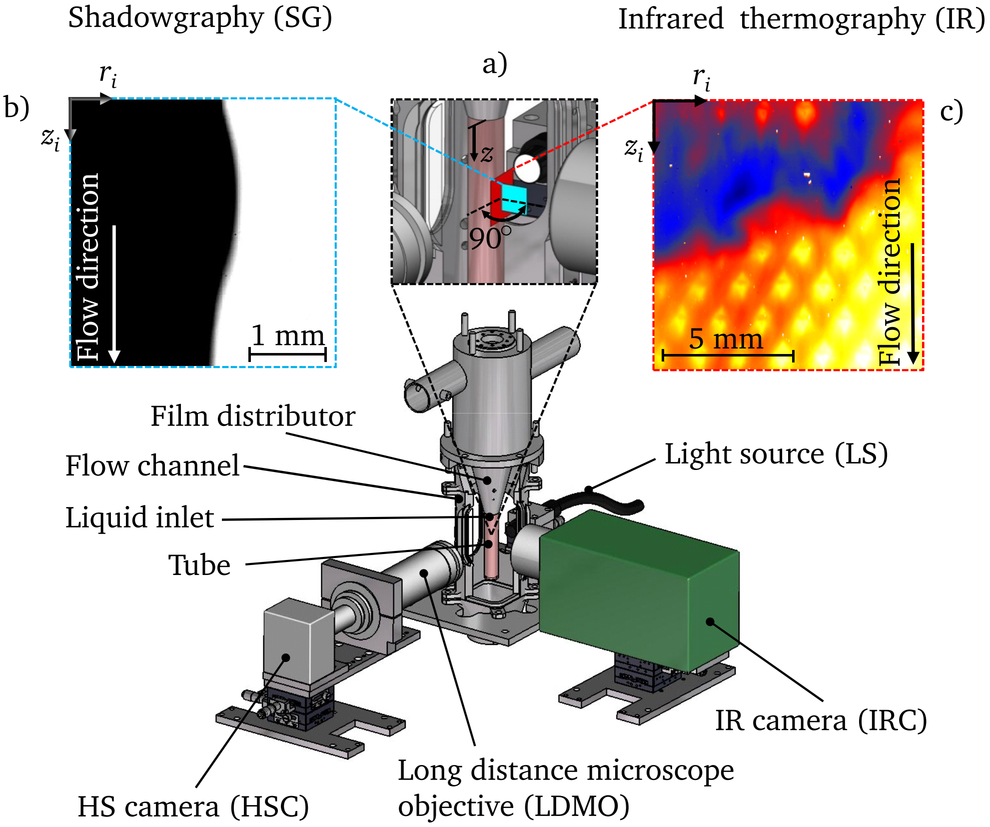

Figure 4.2. Sketch of the configuration of high-speed camera (HSC) and infrared camera (IRC) to observe the dynamics and the flow pattern of the film flow.

---

[3] T-MASS 65F, Endress + Hauser Messtechnik GmbH + Co. KG, Weil am Rhein/Germany

[4] Promass 80A, Endress + Hauser Messtechnik GmbH + Co. KG, Weil am Rhein/Germany

The film dynamics can be characterized by the number of waves N within a duration t and by the standard deviation σ of the film thickness. In order to investigate the dynamics of the film and the film rupture on structure surfaces, the shadowgraphy [61, 63] and the infrared thermography were used. In Figure 4.2, the setup of the high-speed camera (HSC) and the infrared camera (IRC) is exhibited. On predefined planes in liquid flow direction (see detail in Figure 4.2a), both devices have been aligned with an angle of $90\,^\circ$ to each other, focusing on the film flow. The black and white high-speed camera was focused tangentially to the liquid flow as shown in Figure 4.2b, and 2D images were obtained containing a portion of the tube and liquid film (in black color) and a white colored domain representing the gas flow. The gas-liquid interface is indicated by a wavy motion of the intersecting black and white colors. The HSC images were later evaluated quantitatively. Figure 4.2c shows the example of a 2D image of the film flow on a Δ-surface. The IRC was focused perpendicularly to the film flow direction, and frontal images were recorded. The use of the infrared images was to qualitatively interpret the results of the heat transfer measurements and to determine the wetting events of the liquid flowing on different micro-structures.

4.3.1 Shadowgraphy method

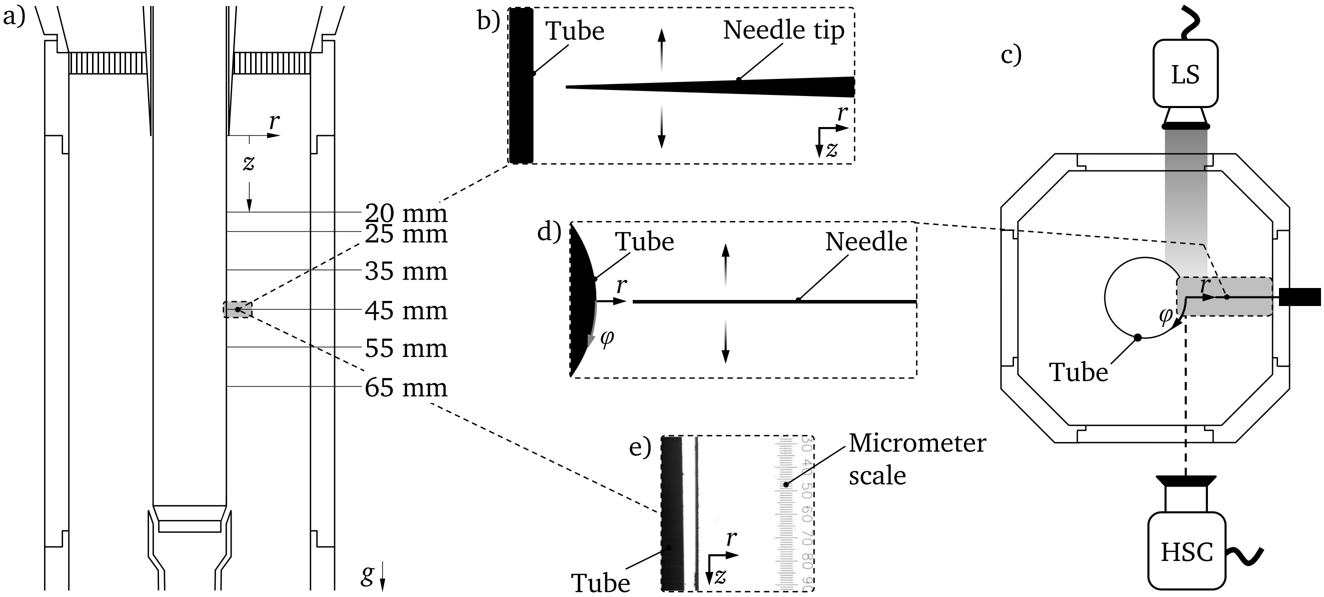

Figure 4.3. Setting of shadowgraphy technique: a) z-positions of high-speed records, b) Needle tip adjustment towards tube surface, c) Top view of the configuration of high-speed camera (HSC) and collimated white light source (LS), d) Top view of needle position, e) Micrometer scale for determination of spatial resolution in field of view.

In this subsection, the setup of the high-speed camera and its focusing procedure is explained. The shadowgraphy measurements were performed at positions $z = 20\,\mathrm{mm}$ to $65\,\mathrm{mm}$ as shown in Figure 4.3a. A high-speed camera[5] with an external frame grabber and a maximum spatial resolution of 512 pixel $\times$ 512 pixel at $f_{\mathrm{SG}} = 2000\,\mathrm{Hz}$ was used. To have enough working distance and an accurate spatial resolution,

---

[5] Fastcam Ultima 512, Photron USA Inc., San Diego/USA

a long-distance microscope objective[6] (LDMO) provided with variable zoom was mounted at the camera. The camera was mounted on a platform with micrometer accuracy three-axis linear translation stages. The focusing of the camera was performed without a gas or liquid flow and with one glass window dismounted. First, the z-positions were marked by using a washable marker. By using a collimated white light source with its axis congruently positioned to the axis of the HSC, the tube surface was identified tangentially (see Figure 4.3c). Then, the HSC was focused roughly with a modest size of field of view (FOV_{SG}) onto the backlit tube surface. Subsequently, a needle mounted in a micrometer travel stage with an accuracy of $\pm 10\,\mu\text{m}$ was positioned at the particular z-position congruently on the r-axis at $\varphi = 0$ to the tube surface as shown in Figures 4.3a and 4.3b. It was moved towards the marked point on the wall of the tube until its tip could be seen within the FOV_{SG}. At the maximum zoom of the LDMO, the needle tip was just about touching the wall. To make sure that the camera FOV_{SG} was at $\varphi = 0$, the needle was tangentially moved along φ-axis as illustrated in Figure 4.3d. When the tip of the needle perpendicularly touched the wall within the FOV_{SG} and its edges were not seen sharply, the camera was adjusted onto it such that a very sharp live image of the needle tip could be seen. Following this, the needle was replaced by a micrometer glass scale as demonstrated in Figure 4.3e. The glass scale was sharply positioned into the FOV_{SG} of the camera, and a single image was taken. With the micrometer scale in the single image and the number of pixels (512×512) the spatial resolution κ_{SG} of the FOV_{SG} could be determined. The depth of field DOF_{SG} of the LDMO configuration was estimated to be $5\,\mu\text{m}$.

As shown in Figure 4.4, in the case of the micro-structured surfaces the FOV_{SG} of the high-speed camera was adjusted at the crest of the ∇-structure and the Δ-structure. The field of view in this investigation was set to $\text{FOV}_{\text{SG}} = 3.84\,\text{mm} \times 3.84\,\text{mm}$ with a spatial resolution of $\kappa_{\text{SG}} = 7.5^2\,\mu\text{m}^2/\text{pix}$.

Figure 4.4. Position of FOV_{SG} for the shadowgraphy records: a) At the unstructured surface, b) At the structured surfaces.

4.3.2 Confocal chromatic technique

To determine the accuracy of the shadowgraphy method, a confocal chromatic sensor[7] (CHR) was used [62, 131]. The measurement range of the sensor is $600\,\mu\text{m}$ with a spatial resolution of $20\,\text{nm}$ in z-direction. The spot diameter is $4\,\mu\text{m}$ with a maximum measurement error of $\leq 1\,\mu\text{m}$. The validation of the accuracy of the shadowgraphy measurements was performed only on a falling film flowing along the unstructured surface. Since the sensor working distance of $6.5\,\text{mm}$ was predefined due to its lens configuration and its size, the sensor-side glass window was removed to focus accurately onto the surface of the tube. On the unstructured surface, a washable black point is marked on the surface of the tube

---

[6] Leica Camera AG, Solms/Germany

[7] CHRocodile E, Precitec GmbH & Co. KG, Gaggenau-Bad Rotenfels/Germany

at half of the FOV height of the HSC, which was focused at $z = 25\,\mathrm{mm}$. Subsequently, the CHR sensor is mounted perpendicular to the HSC axis shown in Figure 4.5 and its measuring spot was focused on the black point. The data acquisition of the high-speed camera and the CHR sensor are simultaneously triggered. At a frequency of $f_{\mathrm{CHR}} = 2000\,\mathrm{Hz}$, film thickness measurements were carried out for a falling film with $Re_{\mathrm{L}} = 200$ for two seconds.

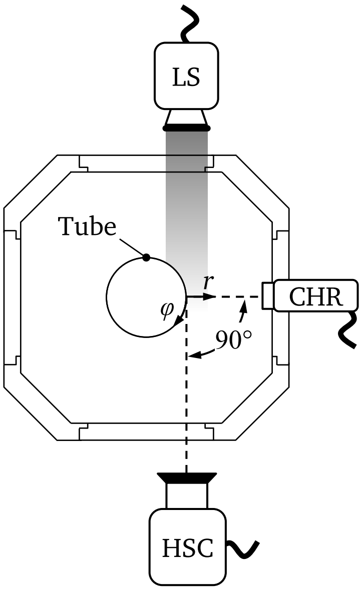

Figure 4.5. Configuration of high-speed camera with confocal chromatic sensor to validate the accuracy of the shadowgraphy measurement.

4.3.3 Infrared imaging technique

Since the shadowgraphy method is applied on a 2D plane tangentially oriented to the tube radius, the flow pattern and the rewetting behavior of the liquid in the case of local disruption cannot be visualized with this method. To observe these phenomena, an infrared camera (IRC) was targeted frontally to monitor the liquid film flowing on the surface of the tube. The IR recordings were only made at the position $z = 45\,\mathrm{mm}$ and only during the measurements with the micro-structured surfaces. Due to the curved surface of the tube, the wavy liquid film and the geometry of the micro-structures, the quantitative thermography was impossible. However, the infrared camera was used to observe qualitatively the film flow and understand the onset of critical conditions at which dry patches on the heated wall occur. For this investigation, a high-speed infrared camera[8] with a range of wave length of $3.4\,\mu\mathrm{m} - 5.1\,\mu\mathrm{m}$ was installed at the flow channel. The camera includes a cadmium-quicksilver-telluride detector which can detect infrared radiation within the range of wavelength $3.4\,\mu\mathrm{m}$ to $5.1\,\mu\mathrm{m}$. The field of view, the spatial resolution, and the frame rate were $\mathrm{FOV}_{\mathrm{IR}} = 9.14\,\mathrm{mm} \times 9.14\,\mathrm{mm}$, $\kappa_{\mathrm{IR}} = 40.82^2\,\mu\mathrm{m}^2/\mathrm{pix}$, and $f_{\mathrm{IR}} = 1000\,\mathrm{Hz}$, respectively. To focus the IRC, the same method as with the high-speed b/w camera was used. The needle was fixed in a second translation stage as shown in Figure 4.6a and was inclined such that the light used for the shadowgraphy was not disturbed. The needle was carefully aligned along the

---

[8] CMT 256M HS, DCG Systems GmbH, Erlangen/Germany

r- and φ-coordinates such that its tip did not touch the surface of the tube and it could be seen sharply in the field of view of the HSC (see Fig. 4.6b).

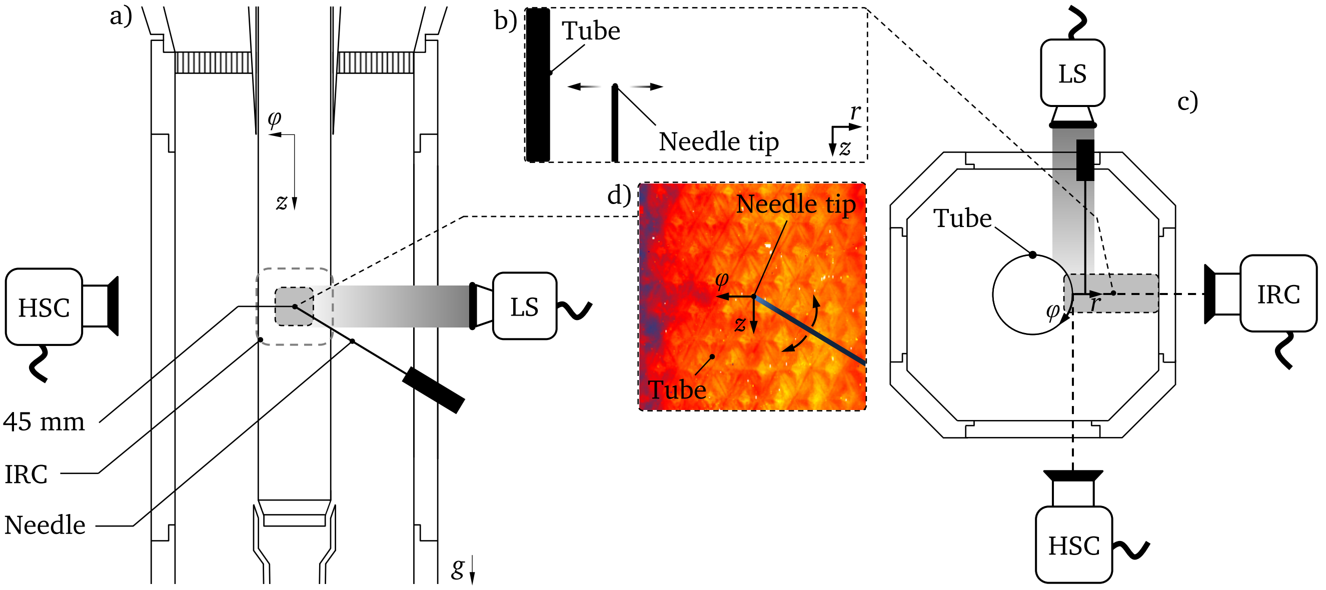

Figure 4.6. Configuration of high-speed black and white (HSC) and infrared camera (IRC) to synchronously observe the flow patterns and local rupture of film at the position $z = 45\,\mathrm{mm}$.

Subsequently, the IRC was mounted on to a platform with micrometer accuracy two-axis linear translation stages and positioned at $90\,^{\circ}\mathrm{C}$ (see Figure 4.6c). During the focusing of the IRC, the heater power was adjusted such that good contrast was seen in the IR images, which helped in distinguishing between wall and needle. During the heating-up procedure a distance of $50\,\mu\mathrm{m}$ between the needle and the crest of a single ∇-groove and between the needle and a single pyramid was kept. This distance was measured through the live images of the HSC. In Figure 4.7a and 4.7b the location of the $\mathrm{FOV_{IR}}$ is shown. The temperature of the tube was increased to $330\,\mathrm{K}$. Consequently, a difference between the radiation intensities of the tube surface and the needle itself was found .

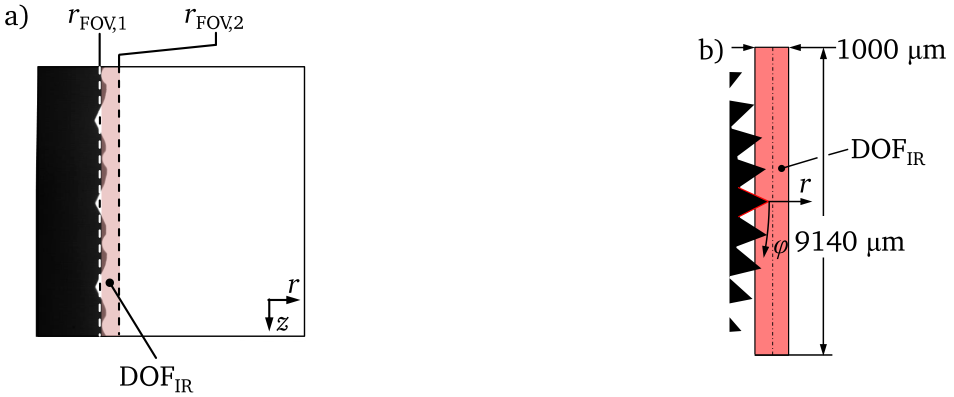

Figure 4.7. Focusing of the field of view of the infrared camera on to the micro-structured surfaces: a) Δ-structured surface, b) ∇-grooved surface.

Accordingly, the IRC was carefully moved along the r- and φ-axis to sharply focus onto the tip of the needle as displayed in Figure 4.6d. In Figure 4.6d the needle is exemplarily shown in front of the tube with Δ-structured surface in the FOV_{IR} of the infrared camera. Besides the spatial resolution κ_{IR} of the IRC, the FOV_{IR} has a limited depth of field (DOF_{IR}) in which the radiation of objects is detected. The determination of the DOF_{IR} was carried out similar to the HSC. After the depth of field was determined, the IRC was moved back to the position r_1. Once the needle tip was sharply seen, the IRC was moved the distance of $50\,\mu m$ towards the tube to exactly focus on the micro-structure (see Figure 4.7b). Then, the needle was carefully removed and the opening for optical access at the side of the light source was provided with a quartz glass window. On the side of the IRC, a calcium fluoride (CaF_2) glass window was mounted to finally close the flow channel. The CaF_2 glass had a IR transmissivity of approximately $95\,\%$ for the wavelengths between $0.2\,\mu m$ and $7\,\mu m$. Hence, the detection of the radiation emitted from the tube surface and the liquid film was ensured. The calibration of the infrared camera was performed with falling liquid film flow (see Section 5.3).

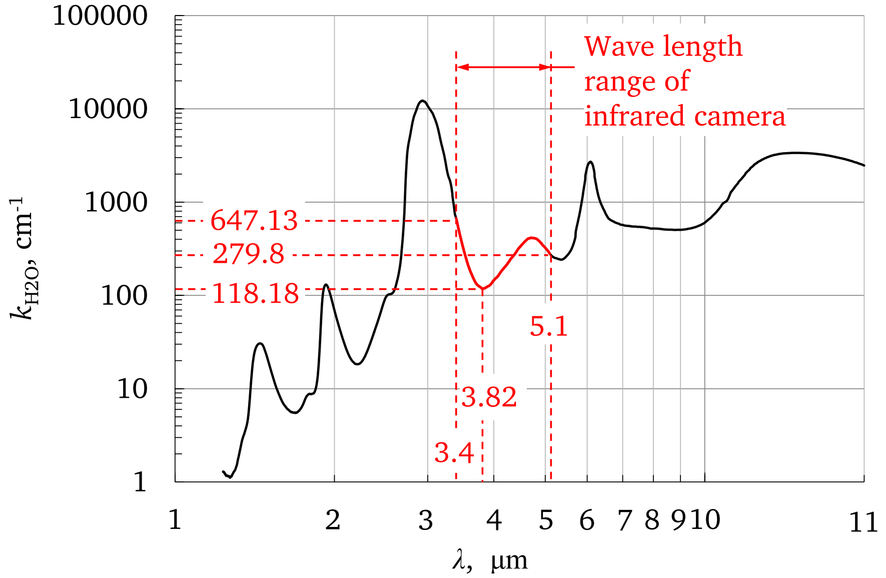

Figure 4.8. Absorption coefficient for water [145].

Since the liquid film is heated by the tube, it can be assumed that the wall temperature is higher than the temperature at the surface of the liquid. Besides the radiation of the liquid film, the wall can emit radiation as well. However, in the presence of a fluid (water) which absorbs the radiation rather in particular wave length range, radiation emitted from the wall does not reach the IRC. This attenuation depends on the intensity I_0 leaving the tube surface, the substance-specific absorption coefficient k_{H2O}, and the length of the path (here film thickness h_L). The wall radiation that reaches the IR camera can be mathematically written as [138]:

$$I_{IR} = I_0 \cdot \exp\left(-k_{H2O} h_L\right) \quad . \tag{4.1}$$

The absorption coefficient k_{H2O} of water depends on the wave length and is shown in Figure 4.8. For the wave length range of the camera ($3.4\,\mu m - 5.1\,\mu m$) The absorption of water is weak at $\lambda = 3.82\,\mu m$ with $k_{H2O,min} = 118.18\,cm^{-1}$ in the range of wave length required by the infrared camera. The maximum reduction of transmission occurs at $\lambda = 3.4\,\mu m$ with $k_{H2O,max} = 647.13\,cm^{-1}$. The influence of the film thickness on the rate of radiation intensity is displayed in Figure 4.9. The transmission decays exponentially with the film thickness h_{L}. The Beer-Lamberts law predicts that about $63.22\,\%$ of the radiation for $\lambda = 3.82\,\mu\mathrm{m}$ emitted from the hot wall will be absorbed by a liquid layer with a thickness of $84.61\,\mu\mathrm{m}$. For a falling film at $Re_{\mathrm{L}} = 80$, as per Nusselt theory, the film thickness is $278.45\,\mu\mathrm{m}$. For this film thickness, only $3.72\,\%$ of the wall radiation will reach the IRC. With increasing Re_{L}, the falling film thickness increases and the transmission rate decreases. However, a gas-driven liquid film thickness strongly varies with time due to various dynamic effects and an unknown proportion of wall radiation is captured by the IRC. Since Equation 4.1 assumes an ideal case of a smooth film and neglects radiation emitted by the surrounding towards the liquid film, it is not safe to conclude that the IRC records the liquid film surface temperature. Therefore, a qualitative interpretation rather than a quantitative evaluation of the IR records was carried out.

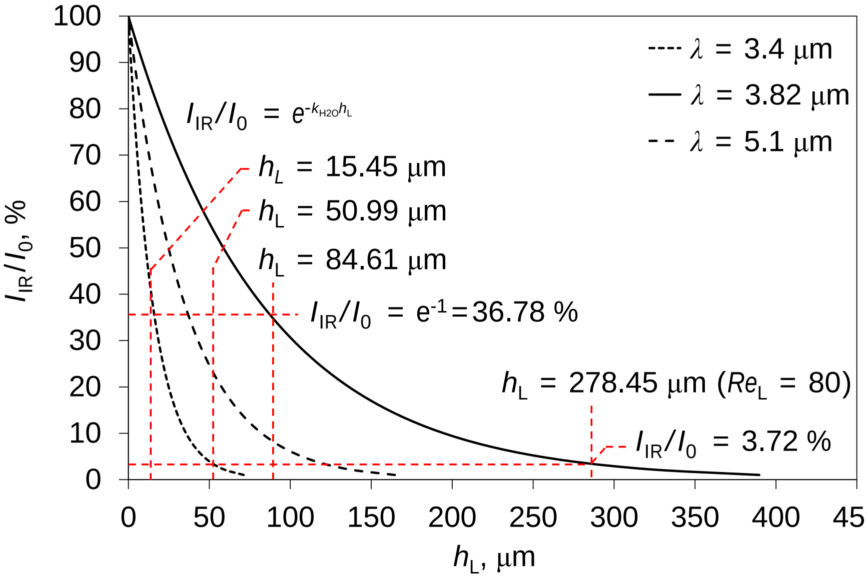

Figure 4.9. Rate of radiation intensity I_{IR}/I_0 vs. film thickness h_{L} for $\lambda = 3.4\,\mu\mathrm{m}$, $3.82\,\mu\mathrm{m}$, and $5.2\,\mu\mathrm{m}$.

4.4 Gas velocity profile measurement

The gas velocity inside the flow channel was measured using the hot-wire anemometry technique from Dantec Dynamics© as displayed in Figure 4.10. The purpose of the measurements was to determine the radial gas velocity profiles for determining the shear stresses on the dry wall and hence to use that information for the comparison with data taken from the literature. The measuring probe was a constant temperature anemometer (CTA) for 1D measurements. The material of the probe wire was tungsten covered with a layer of platinum. Its diameter was $5\,\mu\mathrm{m}$ with a length of $1.25\,\mathrm{mm}$ and was inserted into a long probe support. To detect the signal, the probe was connected to the data acquisition interface[9]. The interface was connected through an A/D converter[10] device to a notebook to acquire the data with a provided LabVIEW program[11]. The measurements were done without liquid flow for $Re_{\mathrm{G}} = 10^4$, $4 \cdot 10^4$,

---

[9] StreamLine CTA Pro Anemometer, Dantec Dynamics A/S, Skovlunde/Denmark

[10] NI USB-X-6361, National Instruments Germany, Munich/Germany

[11] LabVIEW Toolbox for CTA, Dantec Dynamics A/S, Skovlunde/Denmark

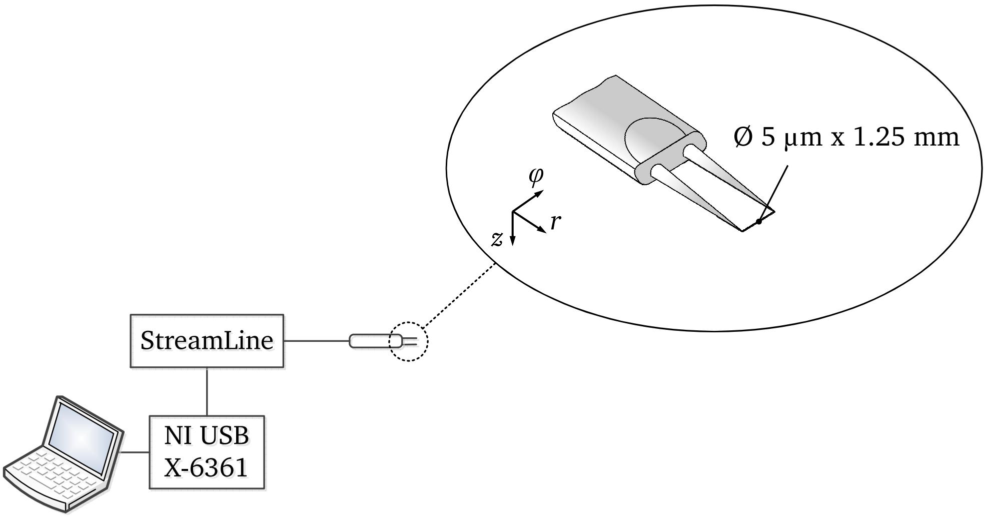

Figure 4.10. Hot-wire anemometry measurement system.

$7 \cdot 10^4$, and 10^5 at the axial distances $z = 15\,\mathrm{mm}$, $25\,\mathrm{mm}$, $35\,\mathrm{mm}$, and $45\,\mathrm{mm}$ (see Figure 4.11). At each distance, the probe tip was positioned radially starting close to the tube surface at $r = 0.1\,\mathrm{mm}$ and moved radially outwards with a step of $\Delta r = 0.5\,\mathrm{mm}$. The hot-wire probe was positioned using the methods explained in Section 4.3.1. After focusing the injection needle, on the position $\varphi = 0$, it was replaced by the hot wire probe. Then, the probe was carefully moved toward the tube surface until its wire could be seen on the live image of the high-speed camera.

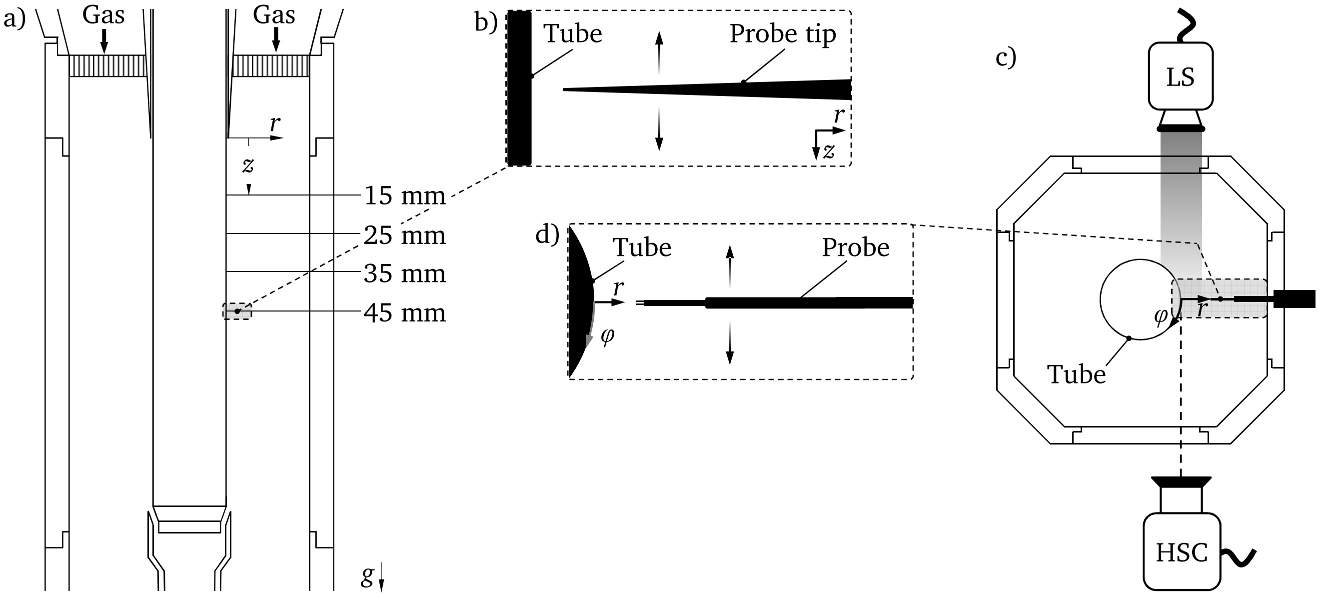

Figure 4.11. Setting of hot-wire probe: a) z-positions of velocity profile measurements, b) Probe tip adjustment towards tube surface, c) Top view of the configuration of high-speed camera (HSC) and collimated white light source (LS), d) Top view of probe position.

The distance of $\Delta r = 0.1\,\mathrm{mm}$ between the probe's tip and the surface of the tube was then adjusted. At each z-position, this procedure had to be carried out. The velocity measurements were performed for two seconds with a frequency of $10\,\mathrm{kHz}$ at each r- and z-location. Since in the experiments the gas temperature was not varied, a temperature compensation of the hot-wire probe was not performed.

4.5 Closure

The detailed description of the data acquisition system and measurement techniques used in this work to investigate the hydrodynamics and heat transfer in gas-driven film flows was explained. The configuration of the thermocouples and the resulting length for the wall temperature measurements were presented. The method of the implementation of the shadowgraphy, infrared thermography, and confocal sensing technique and hot-wire anemometry was explained.

5

Data Analysis and Calibration Procedure

In this chapter, the mathematical approach for heat transfer data reduction is detailed. A semi-analytical model for such two-phase flow is derived in this thesis and is presented in Section 5.1.4. Film dynamics data has been extracted by post-processing the images obtained by shadowgraphy and infrared thermography. The image analysis procedure and statistical treatment of the temporal film thickness data are explained in Section 5.2. The post-processing of the hot-wire measurements data is presented in Section 5.4.

5.1 Heat transfer analysis

During the experiments the following process parameters were measured for the heat transfer analysis:

- wall temperature T_{W} in z-direction,
- liquid inlet $T_{\mathrm{L,in}}$ and outlet $T_{\mathrm{L,out}}$ temperature,
- wall heat flux $\dot{q}_{\mathrm{W}}$,
- the relative humidity X_{G} of the gas phase at the inlet.

The heat and mass transfer between the liquid and gas phase has not been determined. Only the convective heat transfer between the wall and the liquid film has been analyzed using the measured data. Taking the measured values, new correlations for the convective heat transfer in gas-driven liquid films have been developed for all three surface topographies. The approach to achieving the correlations is elucidated in Section 5.1.3. Semi-analytical mathematical models have been derived for the two-phase flow and their prediction will be compared with the experimental data in Chapter 7. Beyond that, the experimentally determined Nusselt numbers Nu have been compared with the Nusselt number Nu_{GRN} predicted through solving the Graetz-Nusselt model (see Section 5.1.4). Hereby, it was intended to point to the enhancement of heat transfer by inducement of waves and to differentiate the effect of the hydrodynamic development.

5.1.1 Dimensionless wall temperature

To describe the wall temperature distribution along the direction of the liquid flow, the measured wall temperatures were transformed into dimensionless form. The expression for the non-dimensional wall temperature distribution is given as

$$\vartheta(z_i) = \frac{T_{\mathrm{W}}(z_i) - T_{\mathrm{L,in}}}{\overline{T}_{\mathrm{W}} - T_{\mathrm{L,in}}} \quad . \tag{5.1}$$

$\overline{T}_{\mathrm{W}}$ is the averaged wall temperature over the heated length calculated as

$$\overline{T}_{\mathrm{W}} = \frac{1}{n} \sum_{i=1}^{n} T_{\mathrm{W}}(z_i) \quad . \tag{5.2}$$

Here, n is the number of measurement points considered, which is equal to the number of thermocouples embedded in the wall. For the comparison of the wall temperature distributions between the surfaces, the dimensionless length

$$\tilde{z} = \frac{z}{l_{\mathrm{W}}} \tag{5.3}$$

is calculated, with the heated length $l_{\mathrm{W}} = 90\,\mathrm{mm}$.

In first evaluations, it was found that the absolute wall temperature distribution $T_{\mathrm{W}}(z)$ at each surface has a maximum as illustrated in Figure 5.1. For the unstructured and ∇-grooved surfaces, the wall temperature decreases starting from the position $z = 65\,\mathrm{mm}$ and $z = 75\,\mathrm{mm}$, respectively. For the Δ-structured surface, a negative gradient of the wall temperature exists from $z = 80\,\mathrm{mm}$ onward. This can be attributed to the axial heat conduction in flow direction, since the heater tube and the sleeve for the thermocouples were manufactured from copper. The axial heat conduction could not be justified; as a result, the temperature data up to $z = 60\,\mathrm{mm}$ (unstructured surface), $z = 70\,\mathrm{mm}$ (∇-grooved surfaces) and $z = 75\,\mathrm{mm}$ (Δ-structured surface) is used for heat transfer calculations.

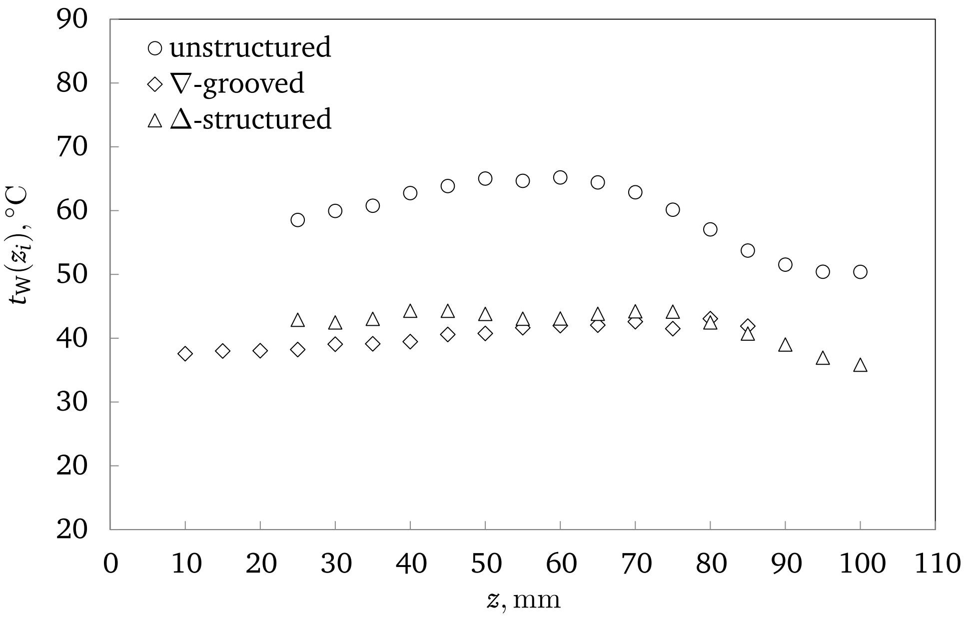

Figure 5.1. Measured local wall temperature distribution in liquid flow direction for all surfaces at $Re_{\mathrm{L}} = 400$, $Re_{\mathrm{G}} = 4 \cdot 10^4$, and $\dot{q}_{\mathrm{W}} = 15\,\mathrm{W/cm^2}$.

5.1.2 Heat transfer coefficient

Since the design of the flow channel configuration used in this study ensured measurements of limited numbers of process parameters such as $T_{\mathrm{L,in}}$, $T_{\mathrm{L,out}}$, $T_{\mathrm{G,in}}$, $T_{\mathrm{W}}(z_{\mathrm{i}})$, and p_{abs}, firstly the overall convective heat transfer coefficient $\overline{\alpha}_{\mathrm{W,LG}}$ existing between the heated wall and the two-phase flow was calculated as

$$\overline{\alpha}_{\mathrm{W,LG}} = \frac{\dot{q}_{\mathrm{W}}}{\overline{T}_{\mathrm{W}} - T_{\mathrm{L,in}}} \quad . \tag{5.4}$$

$\dot{q}_{\mathrm{W}}$ is equal to the power of the cartridge heater and was determined with Eq. 3.32. The Nusselt number *Nu* is defined by the equation

$$Nu = \frac{\dot{q}_{\mathrm{W}} l_{\mathrm{hyd}}}{\lambda_{\mathrm{L}} \left(\overline{T}_{\mathrm{W}} - T_{\mathrm{L,in}}\right)} \quad . \tag{5.5}$$

Since the temperature profiles decayed due to heat conduction towards $z = 100\,\mathrm{mm}$ (especially in case of the unstructured surface), the overall dimensionless heat transfer coefficient *Nu* was determined using $l_{\mathrm{hyd,O}} = 60\,\mathrm{mm} - 25\,\mathrm{mm} = 35\,\mathrm{mm}$ for the unstructured surface, $l_{\mathrm{hyd},\nabla} = 70\,\mathrm{mm} - 10\,\mathrm{mm} = 60\,\mathrm{mm}$ for the ∇-grooved surface, and $l_{\mathrm{hyd},\Delta} = 75\,\mathrm{mm} - 25\,\mathrm{mm} = 50\,\mathrm{mm}$ for the Δ-structured surfaces.

5.1.3 Development of correlations for the average Nusselt number

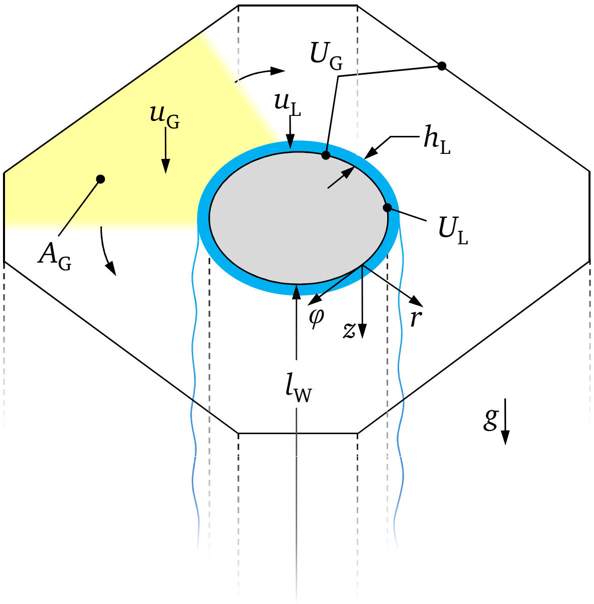

Figure 5.2. Characteristic dimensions for the determination of the influence of geometry.

In this section, the dimensional analysis [64] is introduced and the mathematical approach for the correlations for Nusselt numbers developed in this study is presented. The correlations are developed only for the gas-driven film flow measurements performed at the unstructured surface, since the effect of surface topography needs to be further investigated by varying the chosen geometrical shape. For the development of correlations, the Buckingham Π-Theorem has been used. With this theorem, each physical problem containing n number of parameters afflicted with units and m number of SI basic units used can be reduced into a system with $n - m$ dimensionless Π-terms [22, 88]. Admittedly, the exact functional relations have to be determined through experiments. The influencing parameters have been sorted into properties, experimental parameters, and geometrical dimensions (see Figure 5.2). These are listed in Table 5.1.

Table 5.1. List of influencing parameters for the dimensional analysis.

Symbol	**Quantity**	**Basic unit**[1]
	Properties	
$c_{p,\mathrm{L}}$	Specific heat capacity of liquid	$\left[\mathrm{L}^2\mathrm{T}^{-2}\Theta^{-1}\right]$
$c_{p,\mathrm{G}}$	Specific heat capacity of gas	$\left[\mathrm{L}^2\mathrm{T}^{-2}\Theta^{-1}\right]$
λ_L	Thermal conductivity of liquid	$\left[\mathrm{MLT}^{-3}\Theta^{-1}\right]$
λ_G	Thermal conductivity of gas	$\left[\mathrm{MLT}^{-3}\Theta^{-1}\right]$
ρ_L	Density of liquid	$\left[\mathrm{ML}^{-3}\right]$
ρ_G	Density of gas	$\left[\mathrm{ML}^{-3}\right]$
ν_L	Kinematic viscosity of liquid	$\left[\mathrm{L}^2\mathrm{T}^{-1}\right]$

---

[1] Basic units are used according to Buckingham Π-Theorem

ν_G	Kinematic viscosity of gas	$\left[\mathrm{L}^2\mathrm{T}^{-1}\right]$
	Heat transfer and flow parameters/condition	
V	Voltage	$\left[\mathrm{ML}^2\mathrm{T}^{-3}\mathrm{I}\right]$
I	Electrical current	$[\mathrm{I}]$
ΔT	Temperature difference $\overline{T}_W - T_{L,in}$	$[\Theta]$
u_L	Mean velocity of liquid	$\left[\mathrm{LT}^{-1}\right]$
u_G	Mean velocity of gas	$\left[\mathrm{LT}^{-1}\right]$
	Geometry	
A_G	Cross section for gas flow	$\left[\mathrm{L}^2\right]$
h_L	Film thickness	$[\mathrm{L}]$
l_W	Heated length on the evaporator tube	$[\mathrm{L}]$
U_L	Wetted perimeter for liquid flow (see Eq. 3.30)	$[\mathrm{L}]$
U_G	Wetted perimeter for gas flow (see Eq. 3.31)	$[\mathrm{L}]$

All in all $n = 18$ influencing parameters with $m = 5$ basic units were determined resulting in 13 Π-groups. According to the Buckingham Π-Theorem, the influencing parameters have been brought into the form of multiplication, where Π is a non-dimensional quantity:

$$\Pi = c_{p,\mathrm{L}}{}^a \cdot c_{p,\mathrm{G}}{}^b \cdot \rho_\mathrm{L}{}^c \cdot \rho_\mathrm{G}{}^d \cdot \nu_\mathrm{L}{}^e \cdot \nu_\mathrm{G}{}^f \cdot V^g \cdot I^h \cdot \lambda_\mathrm{L}{}^i \cdot \lambda_\mathrm{G}{}^j \cdot u_\mathrm{L}{}^k \cdot u_\mathrm{G}{}^l \cdot \Delta T^m \cdot U_\mathrm{L}{}^n \cdot U_\mathrm{G}{}^o \cdot A_\mathrm{G}{}^p \cdot h_\mathrm{L}{}^q \cdot l_\mathrm{W}{}^r \tag{5.6}$$

Subsequently, the basic dimensions were inserted in Eq. 5.6:

$$\begin{aligned}\Pi = &\left(\frac{\mathrm{L}^2}{\mathrm{T}^2\cdot\Theta}\right)^a \cdot \left(\frac{\mathrm{L}^2}{\mathrm{T}^2\cdot\Theta}\right)^b \cdot \left(\frac{\mathrm{M}}{\mathrm{L}^3}\right)^c \cdot \left(\frac{\mathrm{M}}{\mathrm{L}^3}\right)^d \cdot \left(\frac{\mathrm{L}^2}{\mathrm{T}}\right)^e \cdot \left(\frac{\mathrm{L}^2}{\mathrm{T}}\right)^f \cdot \left(\frac{\mathrm{M}\cdot\mathrm{L}^2\cdot\mathrm{I}}{\mathrm{T}^3}\right)^g \ldots\\ &\ldots\cdot(\mathrm{I})^h \cdot \left(\frac{\mathrm{M}\cdot\mathrm{L}}{\mathrm{T}^3\cdot\Theta}\right)^i \cdot \left(\frac{\mathrm{M}\cdot\mathrm{L}}{\mathrm{T}^3\cdot\Theta}\right)^j \cdot \left(\frac{\mathrm{L}}{\mathrm{T}}\right)^k \cdot \left(\frac{\mathrm{L}}{\mathrm{T}}\right)^l \cdot (\Theta)^m \cdot (\mathrm{L})^n \cdot (\mathrm{L})^o \ldots\\ &\ldots\cdot\left(\mathrm{L}^2\right)^p \cdot (\mathrm{L})^q \cdot (\mathrm{L})^r\end{aligned} \tag{5.7}$$

and the following expression results:

$$\begin{aligned}\Pi = &\mathrm{L}^{(2a+2b-3c-3d+2e+2f+2g+i+j+k+l+n+o+2p+q+r)} \cdot \mathrm{T}^{(-2a-2b-e-f-3g-3i-3j-k-l)} \ldots\\ &\ldots\cdot \mathrm{M}^{(c+d+g+i+j)} \cdot \Theta^{(-a-b-i-j+m)} \cdot \mathrm{I}^{(g+h)} \quad .\end{aligned} \tag{5.8}$$

To make the above equation dimensionally consistent, the exponents a, b, ... should satisfy the following equations:

$$
\begin{align}
0 &= 2a + 2b - 3c - 3d + 2e + 2f + 2g + i + j + k + l + n + o + 2p + q + r \quad , \tag{5.9}\\
0 &= -2a - 2b - e - f - 3g - 3i - 3j - k - l \quad , \tag{5.10}\\
0 &= c + d + g + i + j \quad , \tag{5.11}\\
0 &= -a - b - i - j + m \quad , \tag{5.12}\\
0 &= g + h \quad . \tag{5.13}
\end{align}
$$

After several rearrangements (see details in Section A.1.1) and substitutions of the equations above, the exponents n, l, c, m, and g can be replaced in Eq. 5.6 with

$$
\begin{aligned}
n &= -e - f - 2h - i - j - o - 2p - q - r \quad , \\
l &= -2a - 2b - e - f - 3h - 3i - 3j - k \quad , \\
c &= -d - h - i - j \quad , \\
m &= a + b + i + j \quad , g = h \quad .
\end{aligned}
$$

Upon summarizing the remaining dimensionless exponents, the following dimensionless products result:

$$
\begin{aligned}
\Pi = {} & \underbrace{\left(\frac{c_{p,\mathrm{L}} \cdot \Delta T}{u_{\mathrm{G}}{}^2}\right)^{a}}_{\pi_1} \cdot \underbrace{\left(\frac{c_{p,\mathrm{G}} \cdot \Delta T}{u_{\mathrm{G}}{}^2}\right)^{b}}_{\pi_2} \cdot \underbrace{\left(\frac{\rho_{\mathrm{G}}}{\rho_{\mathrm{L}}}\right)^{d}}_{\pi_3} \cdot \underbrace{\left(\frac{\nu_{\mathrm{L}}}{u_{\mathrm{G}} \cdot U_{\mathrm{L}}}\right)^{e}}_{\pi_4} \\
& \cdot \underbrace{\left(\frac{\nu_{\mathrm{G}}}{u_{\mathrm{G}} \cdot U_{\mathrm{L}}}\right)^{f}}_{\pi_5} \cdot \underbrace{\left(\frac{V \cdot I}{u_{\mathrm{G}}{}^3 \cdot \rho_{\mathrm{L}} \cdot U_{\mathrm{L}}{}^2}\right)^{h}}_{\pi_6} \cdot \underbrace{\left(\frac{\lambda_{\mathrm{L}} \cdot \Delta T}{\rho_{\mathrm{L}} \cdot u_{\mathrm{G}}{}^3 \cdot U_{\mathrm{L}}}\right)^{i}}_{\pi_7} \\
& \cdot \underbrace{\left(\frac{\lambda_{\mathrm{G}} \cdot \Delta T}{\rho_{\mathrm{L}} \cdot u_{\mathrm{G}}{}^3 \cdot U_{\mathrm{L}}}\right)^{j}}_{\pi_8} \cdot \underbrace{\left(\frac{u_{\mathrm{L}}}{u_{\mathrm{G}}}\right)^{k}}_{\pi_9} \cdot \underbrace{\left(\frac{U_{\mathrm{G}}}{U_{\mathrm{L}}}\right)^{o}}_{\pi_{10}} \cdot \underbrace{\left(\frac{A_{\mathrm{G}}}{U_{\mathrm{L}}{}^2}\right)^{p}}_{\pi_{11}} \cdot \underbrace{\left(\frac{h_{\mathrm{L}}}{U_{\mathrm{L}}}\right)^{q}}_{\pi_{12}} \cdot \underbrace{\left(\frac{l_{\mathrm{W}}}{U_{\mathrm{L}}}\right)^{r}}_{\pi_{13}}
\end{aligned} \tag{5.14}
$$

The resulting products can be combined with each other to obtain well-known dimensionless numbers such as Nu, Re_{L}, Re_{G}, Pr_{L}, and Pr_{G}.

$$
\begin{align}
\frac{\pi_6 \cdot \pi_3}{\pi_7 \cdot \pi_3} &= Nu = \frac{\dot{q} \cdot l_{\mathrm{W}}}{\Delta T \cdot \lambda_{\mathrm{L}}} \tag{5.15}\\
\frac{\pi_3 \cdot \pi_9 \cdot \pi_{12}}{\pi_3 \cdot \pi_4} &= Re_{\mathrm{L}} = \frac{\dot{M}_{\mathrm{L}}}{U_{\mathrm{L}} \cdot \mu_{\mathrm{L}}} \tag{5.16}\\
\frac{\pi_3 \cdot \pi_9 \cdot \pi_{11}}{\pi_3 \cdot \pi_5 \cdot \pi_9 \cdot \pi_{10}} &= Re_{\mathrm{G}} = \frac{4 \cdot \dot{M}_{\mathrm{G}}}{U_{\mathrm{G}} \cdot \mu_{\mathrm{G}}} \tag{5.17}
\end{align}
$$

$$\frac{\pi_1 \cdot \pi_4}{\pi_7} = Pr_{\mathrm{L}} = \frac{\mu_{\mathrm{L}} \cdot c_{p,\mathrm{L}}}{\lambda_{\mathrm{L}}} \tag{5.18}$$

$$\frac{\pi_2 \cdot \pi_5 \cdot \pi_3}{\pi_8} = Pr_{\mathrm{G}} = \frac{\mu_{\mathrm{G}} \cdot c_{p,\mathrm{G}}}{\lambda_{\mathrm{G}}} \tag{5.19}$$

The following terms can be used to identify additional dimensionless numbers concerning property, process parameter and geometry:

$$\pi_3 = \frac{\rho_{\mathrm{G}}}{\rho_{\mathrm{L}}} \quad , \pi_9 = \frac{u_{\mathrm{L}}}{u_{\mathrm{G}}} \quad , \pi_{10} = \frac{U_{\mathrm{G}}}{U_{\mathrm{L}}} \quad , \pi_{11} = \frac{A_{\mathrm{G}}}{{U_{\mathrm{L}}}^2} \quad , \pi_{12} = \frac{h_{\mathrm{L}}}{U_{\mathrm{L}}} \quad , \pi_{13} = \frac{l_{\mathrm{W}}}{U_{\mathrm{L}}} \tag{5.20}$$

Hence, the dimensional analysis predicts that Nu is a function of the following parameters:

$$Nu = f\left(Re_{\mathrm{L}}, Re_{\mathrm{G}}, Pr_{\mathrm{L}}, Pr_{\mathrm{G}}, \frac{\rho_{\mathrm{G}}}{\rho_{\mathrm{L}}}, \frac{u_{\mathrm{L}}}{u_{\mathrm{G}}}, \frac{U_{\mathrm{G}}}{U_{\mathrm{L}}}, \frac{A_{\mathrm{G}}}{{U_{\mathrm{L}}}^2}, \frac{h_{\mathrm{L}}}{U_{\mathrm{L}}}, \frac{l_{\mathrm{W}}}{U_{\mathrm{L}}}\right) \tag{5.21}$$

As far as Re_{L} and Re_{G} have been varied solely in the experiments and the rest of the process parameters, fluid properties, and geometric dimensions have been kept constant, the following mathematical form for the correlation can be used:

$$Nu_{\mathrm{C}} = a \cdot {Re_{\mathrm{L}}}^b \cdot {Re_{\mathrm{G}}}^c \tag{5.22}$$

All other influencing parameters which have not been changed are included in the coefficient a:

$$a = f\left(Pr_{\mathrm{L}}, Pr_{\mathrm{G}}, \frac{\rho_{\mathrm{G}}}{\rho_{\mathrm{L}}}, \frac{u_{\mathrm{L}}}{u_{\mathrm{G}}}, \frac{U_{\mathrm{G}}}{U_{\mathrm{L}}}, \frac{A_{\mathrm{G}}}{{U_{\mathrm{L}}}^2}, \frac{h_{\mathrm{L}}}{U_{\mathrm{L}}}, \frac{l_{\mathrm{W}}}{U_{\mathrm{L}}}\right).$$

The coefficient a and the exponents b and c were determined applying an already available algorithm in Matlab called Simplex [105]. The algorithm is appropriate for non-linear optimization problems without solving derivatives and operates in accordance to the Gaussian method of least squares. The general equation which has to be minimized with the algorithm is

$$f_{Nu} = \sqrt{\sum \left(Nu_{\mathrm{C}} - a \cdot {Re_{\mathrm{L}}}^b \cdot {Re_{\mathrm{G}}}^c\right)^2} \tag{5.23}$$

5.1.4 Theoretical approaches used for the interpretation of experimental results

Single-phase annular flow

The measured heat transfer rates were compared with the heat transfer coefficients for a single phase (air) flow through the flow channel (see Fig. 5.3). Generally, the heat transfer induced by temperature gradients at the thermal boundary layer of a fluid flowing along a heated wall can be characterized with

$$Nu_{\mathrm{G}} = \frac{\alpha_{\mathrm{G}} l_{\mathrm{W}}}{\lambda_{\mathrm{G}}} \quad . \tag{5.24}$$

For a gas flow through an annular channel at $Re_{\mathrm{G}} \geq 10^4$, where the effect of cooling takes place at the surface of the evaporator tube characterized with d_{O}, the following correlation according to [52] is used to determine Nu_{G}:

$$\begin{aligned} Nu_{\mathrm{G}}(d_{\mathrm{O}}) &= 0.75 \cdot Nu_{\mathrm{G}}(d_{\mathrm{hyd,G}}) \cdot \left(\frac{d_{\mathrm{O}}}{d_{\mathrm{CH}}{}^{*}}\right)^{-0.17} \\ &= 0.75 \cdot \left[\frac{\frac{\xi_{\mathrm{G}}}{8} Re_{\mathrm{G}} Pr_{\mathrm{G}}}{1 + 12.7\sqrt{\frac{\xi_{\mathrm{G}}}{8}}\left(Pr_{\mathrm{G}}{}^{\frac{2}{3}} - 1\right)} \cdot \left(1 + \left(\frac{d_{\mathrm{hyd,G}}}{l_{\mathrm{W}}}\right)^{\frac{1}{3}}\right)\right] \cdot \left(\frac{d_{\mathrm{O}}}{d_{\mathrm{CH}}{}^{*}}\right)^{-0.17} \quad . \end{aligned} \tag{5.25}$$

Properties were evaluated at inlet conditions. ξ_{G} is the friction coefficient of the gas stream at the tube and channel wall. The velocity profile of a fluid streaming through an annular duct deviates from the velocity profile in a circular tube. Hence, the friction coefficient ξ_{G} in an annular duct depends on the diameter ratio $a_{\mathrm{i,o}} = (d_{\mathrm{in}}/d_{\mathrm{out}})$ which has been calculated according to [51] with

$$\xi_{\mathrm{G}} = \left[1.8 \log_{10}\left(Re_{\mathrm{G}}{}^{*}\right) - 1.5\right]^{-2} \quad . \tag{5.26}$$

with

$$Re_{\mathrm{G}}{}^{*} = Re_{\mathrm{G}} \frac{\left[1 + \left(\frac{d_{\mathrm{O}}}{d_{\mathrm{CH}}{}^{*}}\right)^2\right] \ln \frac{d_{\mathrm{O}}}{d_{\mathrm{CH}}{}^{*}} + \left[1 - \left(\frac{d_{\mathrm{O}}}{d_{\mathrm{CH}}{}^{*}}\right)^2\right]}{\left[1 - \left(\frac{d_{\mathrm{O}}}{d_{\mathrm{CH}}{}^{*}}\right)^2\right] \ln\left(\frac{d_{\mathrm{O}}}{d_{\mathrm{CH}}{}^{*}}\right)} \quad . \tag{5.27}$$

Because the theory assumes only circular annular geometry while the flow channel cross section in this work has an octagonal shape, the outer wall of the annular geometry is replaced by an equivalent circle with the same perimeter of the octagonal shape. This leads to an equivalent circle with the diameter

$$d_{\mathrm{CH}}{}^{*} = \frac{4\left(b_{\mathrm{CH}} + c_{\mathrm{CH}}\right)}{\pi} \quad . \tag{5.28}$$

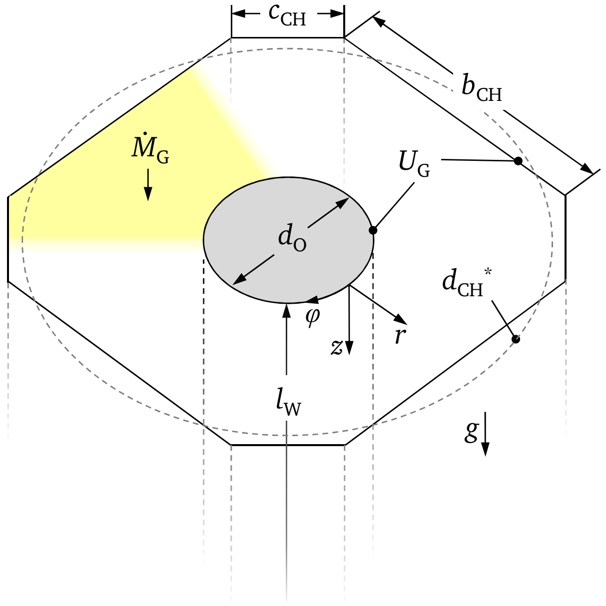

Figure 5.3. Geometric dimensions for the gas flow domain.

Re_{G} was determined with Eq. 3.31 while the hydraulic diameter $h_{\mathrm{hyd,G}}$ is given as

$$d_{\mathrm{hyd,G}} = \frac{4A_{\mathrm{G}}}{U_{\mathrm{G}}} = \frac{4\left[{d_{\mathrm{CH}}}^2 - \left(\frac{{d_{\mathrm{O}}}^2\pi}{4} + {c_{\mathrm{CH}}}^2\right)\right]}{d_{\mathrm{O}}\pi + 4\left(b_{\mathrm{CH}} + c_{\mathrm{CH}}\right)} \quad . \tag{5.29}$$

The Prandtl number Pr_{G} was calculated as

$$Pr_{\mathrm{G}} = \frac{c_{p,\mathrm{G}}\mu_{\mathrm{G}}}{\lambda_{\mathrm{G}}} \quad . \tag{5.30}$$

Graetz-Nusselt model

To determine the effect of the waviness within the thermo-hydrodynamic developing regime on heat transfer, the heat transfer coefficients based on the experiments are compared with analytic calculations for average heat transfer coefficients in gravity-driven films using the classical Graetz-Nusselt model. This approach was first investigated by Graetz [53, 54] and later by Nußelt [107]. In [152] the Graetz-Nusselt model was used in application to falling liquid film flowing down heated inclined grooved plates. As is known, the Graetz-Nusselt model assumes a hydrodynamic developed flow, a smooth liquid-gas interface, and straight path lines of velocity components and neglects vortices within the liquid bulk. Since in the experiments the liquid film thickness is very small compared to the diameter d_{O} and the width of the annuli $(d_{\mathrm{CH}} - d_{\mathrm{O}})/2$, this model has been adopted onto a 2D sector cut out with a negligible thickness in φ-direction as presented in Fig. 5.4.

Also the influence of the wall on the flow channel ($r = H$) was not taken into account, due to the large distance from the liquid film flow. For the process parameters and fluid properties, the parameters of the film flow configuration existing in the experimental flow channel are used. In this approach, a falling liquid film flowing down along a wall is used. The tube wall is considered as sufficiently long such that

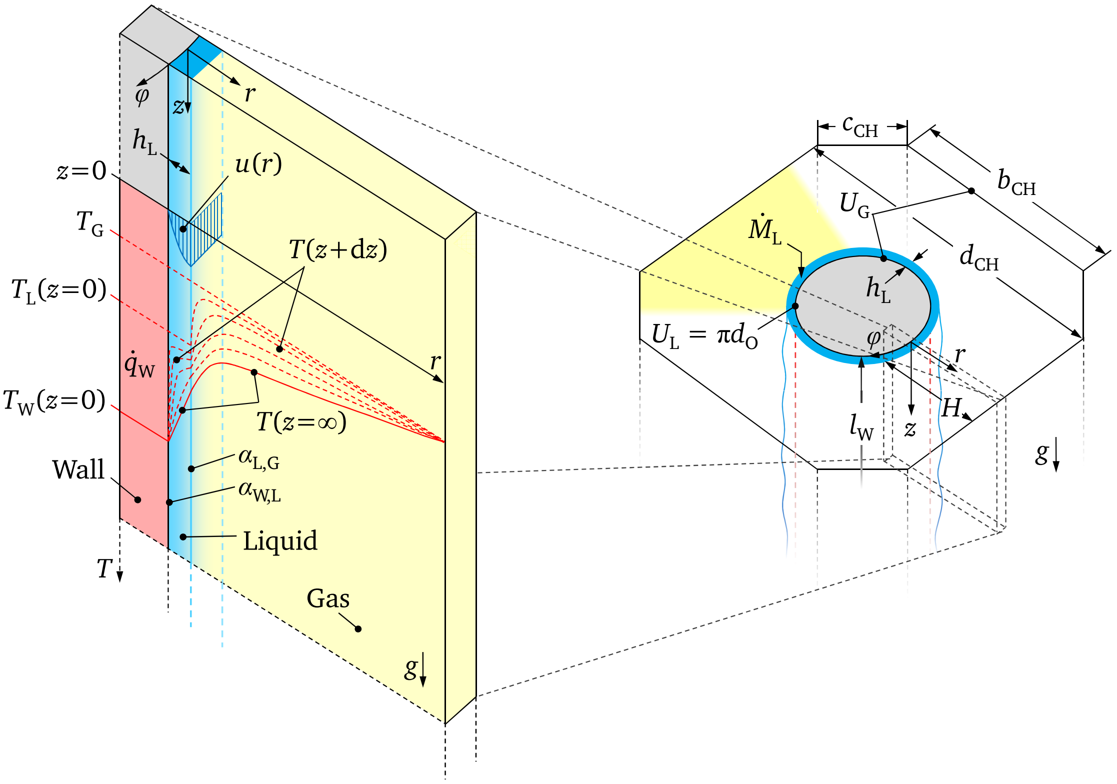

Figure 5.4. Simplified model to perform calculations for heat transfer, flow domain for liquid and gas streams.

the liquid film is hydrodynamically developed before it enters a heated zone at $z = 0\,\mathrm{mm}$. At this location, the velocity profile u_r of the liquid film has a half parabolic shape and the fluid temperatures T_L and T_G at $z = 0$ are assumed to be constant ($\partial T_L/\partial r = \partial T_G/\partial r = 0$). Far from the heated wall, the temperature T_G of the gas phase is considered as the free stream temperature. Along the heated length, constant heat flux $\dot{q}_W$ boundary condition has been assumed. The temperature profiles in the liquid starts developing once the liquid film flows along the heated region. The temperature development within the liquid bulk depends on the kinematic viscosity μ_L and its thermal conductivity λ_L described as a ratio in Pr_L. Hereby, the theory assumes that at $z = \infty$ the temperature distribution within the liquid film reaches a linear form $\partial T_L/\partial r$ as indicated in Fig. 5.4. The heat transfer between the liquid and gas phase is determined by the heat transfer coefficient α_{LG}. All properties of the liquid are assumed to be independent from temperature as well. Firstly, in context to the present liquid film flow configuration the dimensionless coordinates and velocity were defined as

$$\tilde{z} = \frac{z}{h_L} \quad , \tag{5.31}$$

$$\tilde{r} = \frac{r}{h_L} \quad , \tag{5.32}$$

$$\tilde{u}_L = \frac{u_L \cdot \nu_L}{{h_L}^2 \cdot g} \quad . \tag{5.33}$$

As velocity field for the hydrodynamic developed film flow the following formula was used:

$$\tilde{u}_{\mathrm{L}}(\tilde{r}) = -\frac{\tilde{r}^2}{2} + \tilde{r} \quad . \tag{5.34}$$

The velocity component in radial direction is not considered. The liquid Reynolds number as defined in the work was

$$Re_{\mathrm{L,GRN}} = \frac{1}{\nu_{\mathrm{L}}} \int_0^{h_{\mathrm{L}}} \tilde{u}_{\mathrm{L}} d\tilde{r} = \frac{g h_{\mathrm{L}}{}^3}{3 \nu_{\mathrm{L}}{}^2} = \frac{Re_{\mathrm{L}}}{3} \quad . \tag{5.35}$$

Additional dimensionless parameters are

$$Pe_{\mathrm{L}} = Re_{\mathrm{L}} \cdot Pr_{\mathrm{L}} = \frac{g \cdot h_{\mathrm{L}}{}^3}{\nu_{\mathrm{L}}{}^2} \frac{c_{\mathrm{p,L}} \cdot \mu_{\mathrm{L}}}{\lambda_{\mathrm{L}}} = \frac{g \cdot h_{\mathrm{L}}{}^3}{\nu_{\mathrm{L}}} \frac{c_{\mathrm{p,L}} \cdot \rho_{\mathrm{L}}}{\lambda_{\mathrm{L}}} \quad , \tag{5.36}$$

and

$$Bi = \frac{\alpha_{\mathrm{L,G}} \cdot h_{\mathrm{L}}}{\lambda_{\mathrm{L}}} \quad . \tag{5.37}$$

The dimensionless temperature difference was defined as

$$\vartheta = \frac{T_{\mathrm{L}}(r,z) - T_{\mathrm{L}}(r, z \to \infty)}{\Delta T} \quad . \tag{5.38}$$

Here is

$$T_{\mathrm{W}} = \dot{q}_{\mathrm{W}} \left(\frac{h_{\mathrm{L}} - r}{\lambda_{\mathrm{L}}} + \frac{1}{\alpha_{\mathrm{L,G}}} \right) + T_{\mathrm{G}} \quad . \tag{5.39}$$

and

$$\Delta T = \frac{\dot{q}_{\mathrm{W}} \cdot h_{\mathrm{L}}}{\lambda_{\mathrm{L}}} \quad . \tag{5.40}$$

It was assumed that the liquid film at the wall acts as a flat plate cooled due to forced convection generated through its motion within a static air. In other words, gas flows longitudinally along a vertically aligned steady flat plate. With this approach, the Reynolds number for the gas flow was calculated with the assumption $u_{\mathrm{L}} = u_{\mathrm{G}}$ as:

$$Re_{\mathrm{G}}(u_{\mathrm{L}}) = \frac{u_{\mathrm{L}} \cdot l_{\mathrm{W}}}{\nu_{\mathrm{G}}} \quad . \tag{5.41}$$

The characteristic length l_{W} is the tube length of $0.035\,\mathrm{m}$. The average liquid velocity u_{L} was determined with

$$u_{\mathrm{L}} = \frac{\dot{M}_{\mathrm{L}}}{\rho_{\mathrm{L}} \cdot d_{\mathrm{O}} \cdot \pi \cdot h_{\mathrm{L}}} \quad . \tag{5.42}$$

The liquid film thickness h_{L} was expressed according to the Nusselt theory [108] through

$$h_{\mathrm{L}} = \left(\frac{3 \nu_{\mathrm{L}} \dot{M}_{\mathrm{L}}}{\rho_{\mathrm{L}} g d_{\mathrm{O}} \pi} \right)^{\frac{1}{3}} \quad . \tag{5.43}$$

The calculations resulted in $Re_{\mathrm{G}}(u_{\mathrm{L}}) < 10^5$ and $0.6 < Pr_{\mathrm{G}} < 2000$. Accordingly, the correlation for forced convective heat transfer in a fluid longitudinally passing a flat plate with laminar boundary layer flow was used to determine $\alpha_{\mathrm{L,G}}$ [83, 116, 135]:

$$Nu_{\mathrm{G,lam}} = \frac{\alpha_{\mathrm{L,G}} \cdot l_{\mathrm{W}}}{\lambda_{\mathrm{G}}} = 0.664 \cdot \left(Re_{\mathrm{G}}(u_{\mathrm{L}})\right)^{\frac{1}{2}} \cdot Pr_{\mathrm{G}}{}^{\frac{1}{3}} \quad . \tag{5.44}$$

The energy equation for hydrodynamically developed flow on the far high Péclet numbers ($Pe_{\mathrm{L}} \gg 1$) has the following form:

$$Pe_{\mathrm{L}} u_{\mathrm{L}} \frac{\partial \vartheta}{\partial \tilde{z}} = \frac{\partial^2 \vartheta}{\partial \tilde{r}^2} \quad . \tag{5.45}$$

The following boundary conditions were used:

$$\vartheta \left(\tilde{z} = 0, \tilde{r} \right) = \Theta + \tilde{r} - 1 - \frac{1}{Bi} \quad , \tag{5.46}$$

$$\left. \frac{\partial \vartheta}{\partial r} \right|_{\tilde{r}=0} = 0 \quad , \tag{5.47}$$

$$\frac{\partial \vartheta}{\partial \tilde{r}} + Bi \vartheta = 0, \ \tilde{r} = 1 \quad . \tag{5.48}$$

Herein

$$\Theta = \frac{\lambda_{\mathrm{L}} (T_0 - T_{\mathrm{G}})}{\dot{q}_{\mathrm{W}} h_{\mathrm{L}}} \quad . \tag{5.49}$$

With the method of separation of the variables

$$\vartheta \left(\tilde{z}, \tilde{r} \right) = \varsigma \left(\tilde{z} \right) \psi \left(\tilde{r} \right) \quad , \tag{5.50}$$

the following solution for $\varsigma \left(\tilde{z} \right)$ was obtained:

$$\varsigma\left(\tilde{z}\right) = A \cdot exp^{\left(-\Lambda\left(Pe_{\mathrm{L}} \cdot \tilde{z}\right)^{-1}\right)} \quad , \tag{5.51}$$

where A is a constant to be determined later.

For determination of Λ and $\psi\left(\tilde{r}\right)$, the eigenvalue problem was solved, which is comprised of the homogeneous ordinary differential equation:

$$\psi'' + \psi\Lambda^2 u_{\mathrm{L}} = 0 \quad , \tag{5.52}$$

and homogeneous boundary conditions:

$$\left.\frac{\partial\psi}{\partial r}\right|_{\tilde{r}=0} = 0 \quad , \tag{5.53}$$

$$\frac{\partial\psi}{\partial\tilde{r}} + Bi\psi = 0, \tilde{r} = 1 \quad . \tag{5.54}$$

The temperature field had the following form:

$$\vartheta\left(\tilde{z}, \tilde{r}\right) = \sum_{s=1}^{\inf} A_{\mathrm{s}} exp^{\left(-\Lambda\left(Pe_{\mathrm{L}} \cdot \tilde{z}\right)^{-1}\right)} \psi_{\mathrm{s}}\left(\tilde{r}\right) \quad . \tag{5.55}$$

The constants A_{s} were determined from the boundary condition at $x = 0$:

$$\vartheta\left(\tilde{z} = 0, \tilde{r}\right) = \Theta + \tilde{r} - 1 - \frac{1}{Bi} = \sum_{s=1}^{\inf} A_{\mathrm{s}}\psi_{\mathrm{s}}\left(\tilde{r}\right) \quad , \tag{5.56}$$

which lead to:

$$A_{\mathrm{s}} = \frac{\int_0^1 \left(\Theta + \tilde{r} - 1 - \frac{1}{Bi}\right)\psi_{\mathrm{s}} u_{\mathrm{L}} d\tilde{r}}{\int_0^1 {\psi_{\mathrm{s}}}^2 u_{\mathrm{L}} d\tilde{r}} \quad . \tag{5.57}$$

5.2 Shadowgraphy images

In order to determine the dynamics of the liquid film flow, it was necessary to extract the motion of the net liquid domain from the images generated with the shadowgraphy measurements (see Sec. 4.3). For this purpose, the following method was used. To capture the net liquid film domain, it was necessary that the location of the wall-gas (W,G) and the liquid-gas (L,G) interface is captured by the high-speed camera. Before starting each shadowgraphical measurement sequence, a reference image of the dry tube surface was saved. The wall and the liquid is presented in black while the transparent gas domain has a white color (see Figure 5.5a). Subsequently, the reference image and all images in the sequences with the liquid film flow were binarized. Thereby, the color images are transferred into images incorporating gray scales. Through the RGB information of a single pixel a gray scale value is calculated. Using a standard threshold value of 132 for the gray scale value, the wall-gas and the liquid-gas interface could be determined in the reference image and the sequence images. Therefore, a scanning algorithm was applied on the images. As demonstrated with white dashed lines in Figure 5.5b, in each z_i-level the coordinates of pixels which represent the transition from black to white were detected along increasing r-values. Hence the coordinates of $r_{\mathrm{W,L}}$ and $r_{\mathrm{L,G}}$ of the wall-liquid and the liquid-gas interfaces are determined in the reference image and the sequence images, respectively.

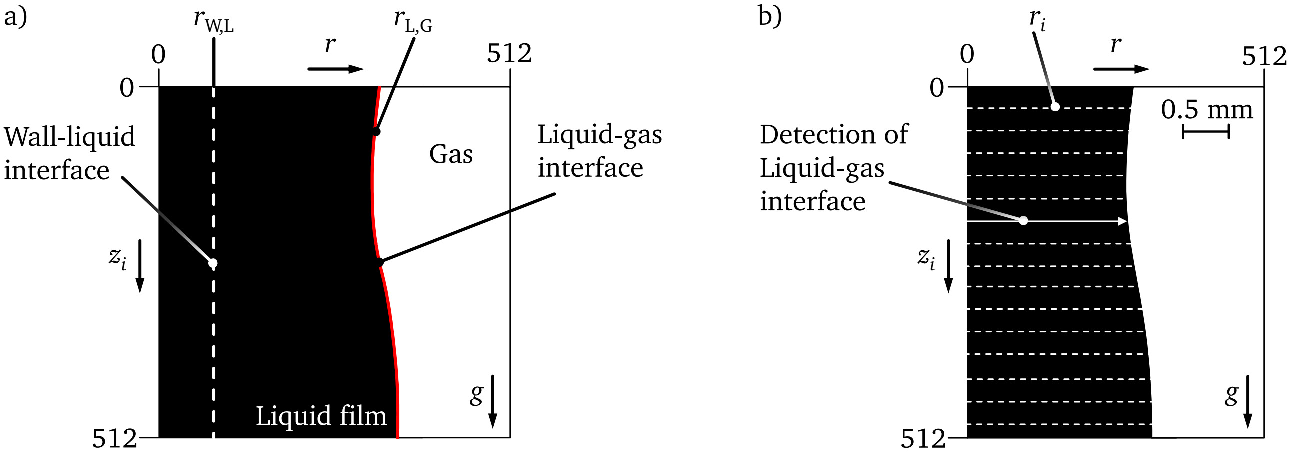

Figure 5.5. Processing of images created with shadowgraphy technique: a) Image including heated wall, liquid film and gas phase domain, b) Detection of liquid-gas interface.

The net liquid film domain at a position i is defined as

$$r_i = r_{\mathrm{L,G}} - r_{\mathrm{W,L}} \quad . \tag{5.58}$$

5.2.1 Standard deviation of liquid-gas interface

The waviness of the liquid film flow can influence the transport of heat from the wall to the liquid bulk [31, 42]. In this context, the temporal variation of the liquid-gas interface can play an important role in terms of heat transfer enhancement. These interfacial fluctuations have been calculated using the standard deviation σ_{L} as a measure of the waviness of the film flow. σ_{L} has been calculated using the pixel coordinates identified with the method described in Section 5.2 multiplied with the spatial resolution of $\kappa_{\mathrm{SG}} = 7.5^2\,\mu\mathrm{m}^2/\mathrm{pix}$ as follows:

$$\sigma_{\mathrm{L}} = \sqrt{\kappa_{\mathrm{SG}}}\,\frac{\sum_{j=1}^{m}\sqrt{\frac{1}{n-1}\sum_{i=1}^{n}\left(r_{ij}-\bar{r}_j\right)^2}}{m} \quad , \tag{5.59}$$

with

$$\bar{r}_j = \frac{1}{n}\sum_{i=1}^{n} r_i \quad . \tag{5.60}$$

Here, $m = 2048$ is the number of images recorded in a single sequence and $n = 512$ is the number of pixels in an image.

5.2.2 Wave frequency

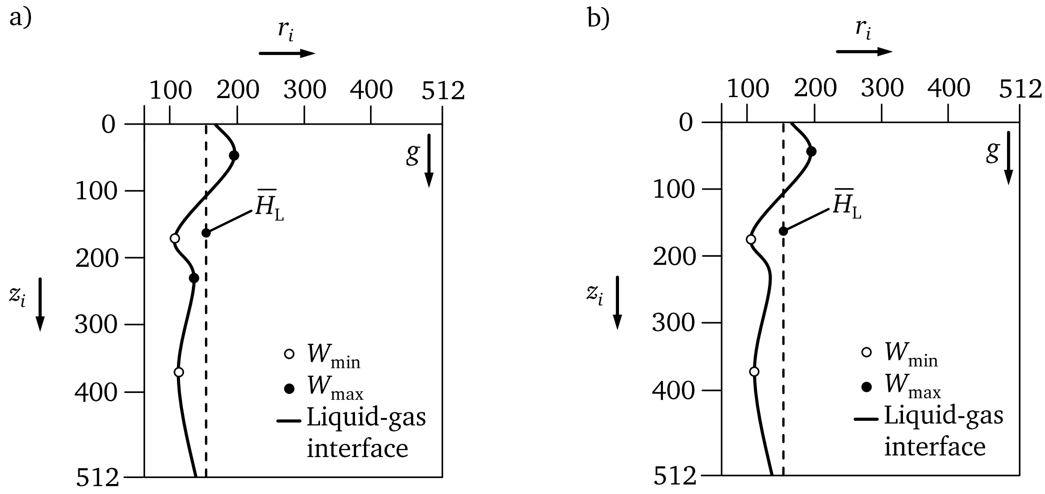

a) W_{min}

#	r_i	z_i
1	105	175
2	110	370

a) W_{max}

#	r_i	z_i
1	195	45
2	142	223

b) W_{min}

#	r_i	z_i
2	105	175
3	110	370

b) W_{max}

#	r_i	z_i
1	195	45

Figure 5.6. a) Detection of local minima and maxima of liquid-gas interface, b) After elimination of coordinates of local minima and maxima according to case distinction.

Another parameter describing the waviness of a liquid-gas interface is the number of waves detected over a certain period of time. For the calculation of the wave frequencies, a wave front detection and a front matching algorithm have been adopted. In the following, the wave detection algorithm is described. Firstly, Gaussian filter is applied to the images such that a smooth liquid-gas interface was obtained. In the algorithm, it has been assumed that the translatory motion of the waves is in the $+z$-direction (see Figure 5.6a). To ascertain the crest and the trough of a wave which represent a local maximum W_{max} and a local minimum W_{min}, a scan of the signal was performed

With this scan the local maxima W_{max} and the local minima W_{min} of the liquid-gas interface were determined in each image. After locating those points, their coordinates z_i and r_i were stored. To distinguish the start and the end of the wave front, the mean film thickness $\overline{H}_L$ for the sequence based on the mean film thicknesses $\bar{h}_{Lj}$ in the single images was calculated with

$$\overline{H}_{\mathrm{L}} = \sqrt{\kappa_{\mathrm{SG}}}\frac{1}{m}\sum_{j=1}^{m}\overline{r}_j \quad . \tag{5.61}$$

By analyzing the r-coordinates of $W_{\max}$ and $W_{\min}$ with $\overline{H}_{\mathrm{L}}$, the following cases have been differentiated in the actual image m:

- $r(W_{\max}) > r(\overline{H}_{\mathrm{L}})$
  $\longrightarrow$ start of a wave front W_{s} is detected,
- $r(W_{\min}) < r(\overline{H}_{\mathrm{L}})$
  $\longrightarrow$ end of a wave front W_{e} is detected,
- $r(W_{\max}) < r(\overline{H}_{\mathrm{L}})$ and $r(W_{\min}) > r(\overline{H}_{\mathrm{L}})$
  $\longrightarrow$ the corresponding inflection points have been eliminated (see Fig. 5.6b).

The remaining $W_{\min}$ and if necessary $W_{\max}$ were analyzed to find out their order, i.e. to determine the start and end of the wave front. Therefore a loop was used to scan the signal from $z = 512$ to $z = 0$. The localized $W_{\min}$ were compared to each other and the smaller one chosen as the starting point W_{s} of the wave. Similarly, the ending point W_{e} of the wave was found out by analyzing the $W_{\max}$ in order to the highest value. In cases as shown exemplarily in Fig. 5.7 where an intermediate $W_{\min,1\text{-}2}$ between two local maximum ($W_{\max,1}$ and $W_{\max,2}$) is identified, the following two criteria are used:

- for $r(W_{\min,1\text{-}2}) - r(\overline{H}_{\mathrm{L}}) = 10\,\mathrm{pix}$
  $\longrightarrow$ a single wave is detected in the image,
- for $r(W_{\min,1\text{-}2}) - r(\overline{H}_{\mathrm{L}}) = -10\,\mathrm{pix}$
  $\longrightarrow$ two successively propagating waves are detected.

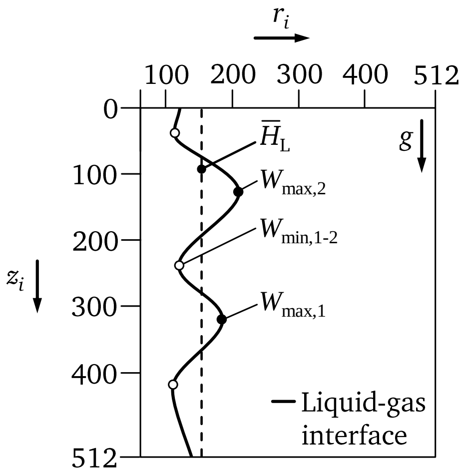

Figure 5.7. Liquid-gas interface characterized by two successive propagating waves.

Due to the translatory motion, wave fronts can be fully visible in several images or are only partially detected in two images. In order to avoid a multiple count of the wave fronts, a simple front matching algorithm has been developed to determine the number of waves n_{w} accurately. The algorithm interrelates the wave fronts existing in the actual image j with the wave front detected in the image j+1. To imagine this situation, a first wave front is detected by identifying the $W_{\mathrm{s}j}$ and $W_{\mathrm{e}j}$ in image j as shown in Fig. 5.8a. In the second image j+1 (see Fig. 5.8b) this wave front will not be counted anymore. The counting only starts when the local minimum, i.e. $W_{\mathrm{s}j+1}$, of the following wave front appears in the image.

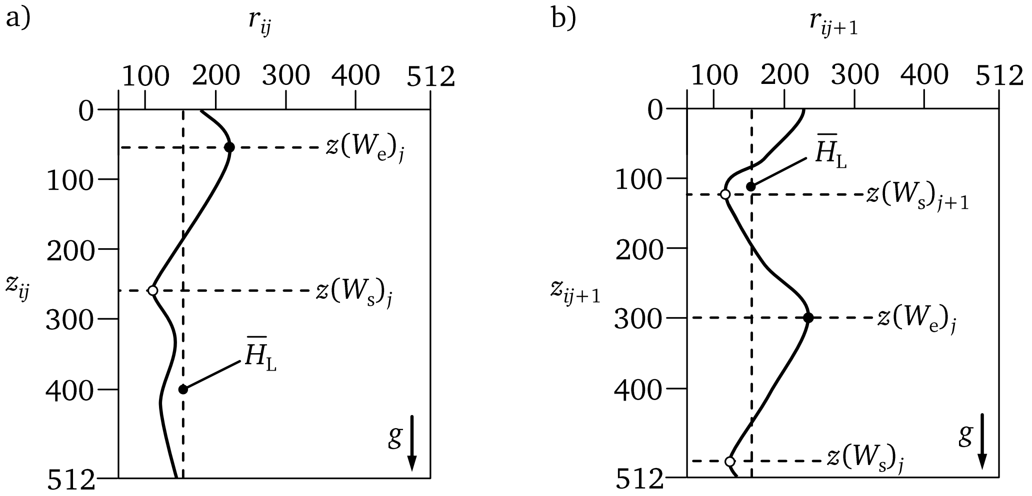

Figure 5.8. a) Detection of first wave in image j, b) Propagated first wave and visible $W_{\mathrm{s}j+1}$ of succeeding wave in image $m+1$.

Finally, the wave frequency f_w was calculated based on the expression

$$f_\mathrm{w} = \frac{n_\mathrm{w}}{t} \quad . \tag{5.62}$$

5.3 Infrared images

The infrared images incorporate pixel-wise intensities corresponding to the radiation of objects focused on (see on next page left half of Fig. 5.9). As explained in Section 4.3.3, a qualitative evaluation of the images was intended in order to interpret the flow pattern and to identify the rupture of the liquid film. Therefore, an in-situ calibration of the infrared camera was not performed.

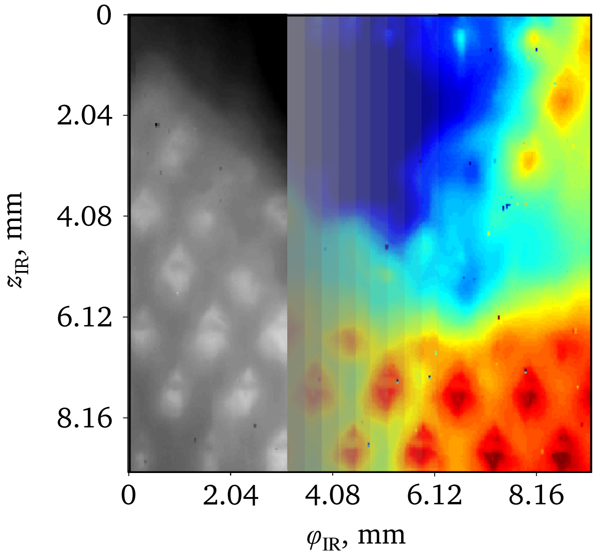

Figure 5.9. Illustration of combination of an image incorporating radiation intensities (gray and RGB)

5.4 Gas flow field measurements and shear stress calculation

The gas flow field measurements inside the experimental flow channel were carried out for $Re_{\mathrm{G}} = 10^4 - 10^5$ at $p_{\mathrm{abs}} = 3\,\mathrm{bar}$ and $T_{\mathrm{G,in}} = 293\,\mathrm{K}$. The calibration of the hot-wire anemometer system was done by using a calibrator built in-house (see Figure 5.10). For calibrating the hot-wire probe, it is assembled inside the calibrator together with a $3\,\mathrm{mm}$ pitot tube[2]. The measurement tips of both sensors were aligned at the same location within the main gas stream inside the calibrator. The pitot tube was coupled to a highly accurate differential pressure sensor[3] and a signal conditioner unit[4] to display the pressure. The pressure sensor could measure a maximum pressure of $1333.\overline{2}\mathrm{Pa}$.

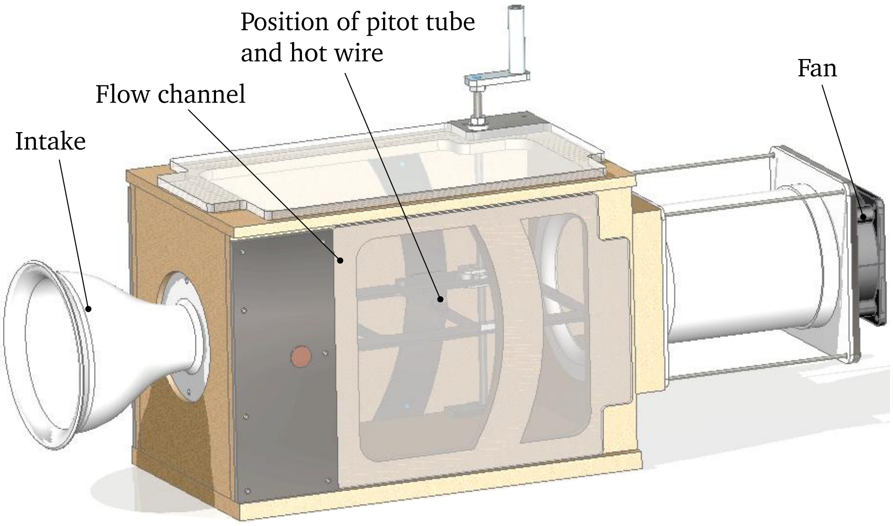

Figure 5.10. Flow channel built in-house at the Institute of Fluid Mechanics and Aerodynamics Technische Universität Darmstadt for the calibration of hot-wire anemometers.

---

[2] Type 628, Lambrecht GmbH, Göttingen/Germany
[3] Type 698A, MKS Instruments, Andover/USA
[4] Type 670B, MKS Instruments, Andover/USA

Using a suction fan, an air flow within the calibrator is generated. However, with this device, calibration can only be done at $1\,\mathrm{bar}$ absolute. The gas temperature was kept constant at $293\,\mathrm{K}$. Starting with the lowest possible rotation speed of the fan, 23 calibration points were defined. The data acquisition rate of the hot-wire anemometer probe was adjusted to $f_{\mathrm{HWA}} = 10\,\mathrm{kHz}$. At each step, the corresponding differential pressures measured with the pitot tube were acquired synchronously with the hot-wire signal over 10 seconds. After the data acquisition procedure, the gas velocity was calculated through the Bernoulli equation

$$u_{\mathrm{G,cal}} = \sqrt{\frac{2\Delta p}{\rho_{\mathrm{G}}}} \quad , \tag{5.63}$$

with

$$\Delta p = p_{\mathrm{dyn,cal}} = p_{\mathrm{abs,cal}} - p_{\mathrm{stat,cal}} \quad . \tag{5.64}$$

Here the density of the gas flow was taken at $1\,\mathrm{bar}$ absolute and at $293\,\mathrm{K}$. The hot-wire output voltage V_{HWA} is calibrated against the velocity data of the pitot tube using the King's Law [138]:

$$V_{\mathrm{HWA,cal}} = \sqrt{A + B \cdot u_{\mathrm{G,cal}}{}^{n}} \quad , \tag{5.65}$$

However, the calibration of the hot-wire anemometer had to be corrected, since the measurements in the experimental channel for gas-driven films were carried out at an absolute pressure of $3\,\mathrm{bar}$. Hence, a pressure correction was performed. This correction coefficient C, implemented in Equation 5.66, is determined by performing flow measurements inside the flow channel of the experimental setup at $p_{\mathrm{abs}} = 3\,\mathrm{bar}$ and $T_{\mathrm{G,in}} = 293.15\,\mathrm{K}$ with the pitot tube and the hot-wire anemometer.

$$V_{\mathrm{HWA,cal}} = \sqrt{C\left(A + B u_{\mathrm{G,cal}}{}^{n}\right)} \quad . \tag{5.66}$$

The resulting constants and exponent after calibration for that particular hot-wire probe were

- $A = 1.5491 \cdot V^2$,
- $B = 0.7946 \cdot V^2 m^{-0.5} s^{0.5}$,
- $C = \rho_{\mathrm{G,1bar}} / \rho_{\mathrm{G,3bar}} \approx \frac{1}{3}$,
- $n = 0.5$.

where $\rho_{\mathrm{G,1bar}} = 1.189\,\mathrm{kgm^{-3}}$ corresponds to $1\,\mathrm{bar}$ and $\rho_{\mathrm{G,3bar}} = 3.577\,\mathrm{kgm^{-3}}$ corresponds to $3\,\mathrm{bar}$ at $293\,\mathrm{K}$. The actual gas velocity u_{G} based on the voltage measured with the hot-wire was determined through

$$u_{\mathrm{G}} = \left(\frac{1}{B} \left(\frac{{V_{\mathrm{HWA}}}^2}{C} - A \right) \right)^{\frac{1}{n}} \quad . \tag{5.67}$$

The shear stress at the wall-gas interface was calculated according to the formula

$$\tau_{\mathrm{W,G}} = \mu_{\mathrm{G}} \frac{\partial u_{\mathrm{G}}}{\partial r} = \mu_{\mathrm{G}} \frac{u_{\mathrm{G,n}} - u_{\mathrm{G,n\text{-}1}}}{r_{\mathrm{n}} - r_{\mathrm{n\text{-}1}}} \quad . \tag{5.68}$$

The gradient $\partial u_{\mathrm{G}}/\partial r$ was determined using the values of the gas velocities measured in the region close to the dry surface of the evaporator tube. The dynamic viscosity μ_{G} was taken at $T_{\mathrm{G,in}}$ and p_{abs}.

5.5 Closure

Summarizing this chapter, the calculations concerning the heat transfer and film dynamics analysis were introduced. Using the Buckingham Π-Theorem, the influencing parameters for the convective heat transfer in annular gas-driven liquid film flows were determined and the form and the method of the correlations developed are explained. For distinguishing the governing mechanisms, theoretical models for heat transfer in single-phase flows and the classical Graetz-Nusselt model used for the heat transfer comparison were derived. In order to investigate the standard deviation of the film thickness and the wave frequencies, the procedure for the post-processing of the images recorded with the shadowgraphy method was demonstrated using examples. IR image post-processing methods and calibration method for hot-wire were presented.

6

Error Analysis and Uncertainty Estimation

This chapter reports the method used for analyzing the systematic errors for each directly measured parameter and the estimation of uncertainties of indirectly calculated values. Errors specified by the manufacturers of peripheral devices and errors determined through the in-house calibration procedure for thermocouples are presented for each process parameter and fluid property. The resulting uncertainty in heat transfer calculations is presented. The uncertainties for the shadowgraphy method and the infrared records in terms of standard deviation, wave frequency, and pixel-wise temperature in IR images are reported. At the end, the calibration procedure for the hot-wire anemometer and the corresponding uncertainty calculation for the velocities measured are explained.

6.1 Error calculation method and identification of parameters with uncertainties

The uncertainty for all the parameters have been determined using the Gaussian law of error propagation. With this method, the uncertainty of a function F can be estimated by incorporating measurement uncertainties of individual influencing factors. A function $F = f\left(x_1, x_2, x_3, ..., x_\mathrm{n}\right)$ with the measurement variables $x_1, x_2, x_3, ..., x_\mathrm{n}$ and their errors $\Delta x_1, \Delta x_2, \Delta x_3, ..., \Delta x_\mathrm{n}$ consequently has a measurement uncertainty ΔF. This can be described with the expression

$$\Delta F = \sqrt{\left(\frac{\partial F}{\partial x_1} \cdot \Delta x_1\right)^2 + \left(\frac{\partial F}{\partial x_2} \cdot \Delta x_2\right)^2 + \left(\frac{\partial F}{\partial x_3} \cdot \Delta x_3\right)^2 + ... + \left(\frac{\partial F}{\partial x_\mathrm{n}} \cdot \Delta x_\mathrm{n}\right)^2}. \tag{6.1}$$

Table 6.1. List of errors of quantities for the measurements and the heat transfer calculations

Quantity	**Symbol**	**Error**	**Equation/Source**
Inlet temperature of liquid	$\Delta T_{\mathrm{L,in}}$	$\pm 0.92\,\mathrm{K}$	Eq.6.2
Inlet temperature of gas	$\Delta T_{\mathrm{G,in}}$	$\pm 0.92\,\mathrm{K}$	Eq.6.2
Local wall temperature	$\Delta T_{\mathrm{W}}(z_{\mathrm{i}})$	$\pm 0.92\,\mathrm{K}$	Eq.6.2
Mean wall temperature	$\Delta \overline{T}_{\mathrm{W}}$	$\pm 0.92\,\mathrm{K}$	Eq. 6.7
Absolute pressure	Δp_{abs}	$\pm 0.05\,\mathrm{bar}$	Data sheet supplier
Voltage	ΔV	$0.05\,\% \pm 0.1\,\mathrm{V}$	Data sheet supplier
Current	ΔI	$0.05\,\% \pm 0.001\,\mathrm{A}$	Data sheet supplier
Relative humidity	ΔX_{G}	$0.2 - 0.4\,\%$ (at $298\,\mathrm{K}$)	DKD calibrated
Outer diameter of evaporator tube	Δd_{O}	$\pm 10\,\mu\mathrm{m}$	MT
Outer diameter of flow channel	Δd_{CH}	$\pm 10\,\mu\mathrm{m}$	MT
Width inside flow channel	Δb_{CH}	$\pm 10\,\mu\mathrm{m}$	MT
Edge length inside flow channel	Δc_{CH}	$\pm 10\,\mu\mathrm{m}$	MT
Charactersitic dimension	Δl_{W}	$\pm 10\,\mu\mathrm{m}$	MT
Heated length at evaporator tube	Δl_{W}	$\pm 10\,\mu\mathrm{m}$	MT
Mass flow rate of liquid	$\Delta \dot{M}_{\mathrm{L}}$	$\pm 2.0\,\%$ of MV	Eq. 6.3
Mass flow rate of Gas	$\Delta \dot{M}_{\mathrm{G}}$	$\pm 2.5\,\%$ of MV	Eq. 6.5
Thermal conductivity of liquid	$\Delta \lambda_{\mathrm{L}}$	$\pm 0.05\,\%$	[135]
Thermal conductivity of gas	$\Delta \lambda_{\mathrm{G}}$	$\pm 0.05\,\%$	[135]
Density of liquid	$\Delta \rho_{\mathrm{L}}$	$\pm 0.05\,\%$	[135]
Density of gas	$\Delta \rho_{\mathrm{G}}$	$\pm 0.05\,\%$	[135]
Kinematic viscosity of liquid	$\Delta \nu_{\mathrm{L}}$	$\pm 0.05\,\%$	[135]
Kinematic viscosity of gas	$\Delta \nu_{\mathrm{G}}$	$\pm 0.05\,\%$	[135]
Dynamic viscosity of liquid	$\Delta \mu_{\mathrm{L}}$	$\pm 0.05\,\%$	[135]
Dynamic viscosity of gas	$\Delta \mu_{\mathrm{G}}$	$\pm 0.05\,\%$	[135]
Wall heat flux	$\Delta \dot{q}_{\mathrm{W}}$	$\pm 0.19 - 0.49\,\%$ of MV	Eq. 6.9

The values of uncertainties for the present analysis are given in Table 6.1. On the next pages, the uncertainty calculations regarding experimental parameters and heat transfer are reported. The uncertainty evaluation for heat transfer results is performed in accordance with a confidence of 95%.

6.2 Process properties and experimental parameters

During the calibration and the experiments, all thermocouples were connected to the peripheral devices of the NI system listed in Tab. 6.2. For the calibration, a platinum resistance sensor (PT100) coupled to a hand-held thermometer[1] was used. The thermocouples and the PT100 sensor were bounded together with thin copper wire and were dipped into a thermostat bath[2] filled with liquid thermal oil. The measuring tip of each thermocouple was located at the measuring point of the PT100. It was calibrated over a range against the accuracy of the PT100 of $\pm 0.5\,\mathrm{K}$. The error introduced in the thermocouple measurement by the DAQ system is given in Table 6.2. The overall uncertainty in temperature measurement by the thermocouples is $\pm 0.92\,\mathrm{K}$.

Table 6.2. Specification of NI peripheral devices for temperature measurements.

Module	**Accuracy**
PCI-6289 + SCXI-1102B	$\pm 0.76\,\mathrm{K}$ over full range
SCXI-1303	$\pm 0.5\,\mathrm{K}$ over full range
SHC68-68-EP	–
SCXI-1000	–

Temperature, T

$$\frac{\Delta T_i}{T_i} = \sqrt{\left(\frac{\Delta T_{\mathrm{PCI6289+SCXI1102B}}}{T_{\mathrm{PCI6289+SCXI1102B}}}\right)^2 + \left(\frac{\Delta T_{\mathrm{SCXI1303}}}{T_{\mathrm{SCXI1303}}}\right)^2 + \left(\frac{\Delta T_{\mathrm{PT100}}}{T_{\mathrm{PT100}}}\right)^2 + \left(\frac{\Delta T_{\mathrm{poly}}}{T_{\mathrm{poly}}}\right)^2} \ . \tag{6.2}$$

Mass flow rate of liquid, $\dot{M}_{\mathrm{L}}$

Table 6.3. Parameters determining the accuracy of $\dot{M}_{\mathrm{L}}$.

Parameter	**Symbol**	**Accuracy**
Device error	$\Delta(\Delta\dot{M}_{\mathrm{L}})$	$\pm 0.15\,\%$
Signal transformation error	$\Delta\dot{M}_{\mathrm{L,NI}}$	$\pm 0.03\,\%$
Standard deviation	$\Delta\dot{M}_{\mathrm{L},\sigma}$	$\pm 0.005 - 2.00\,\%$

The following equation was used for the overall error of mass flow meter measurements:

$$\frac{\Delta\dot{M}_{\mathrm{L}}}{\dot{M}_{\mathrm{L}}} = \sqrt{\left(\frac{\Delta(\Delta\dot{M}_{\mathrm{L}})}{\Delta\dot{M}_{\mathrm{L}}}\right)^2 + \left(\frac{\Delta\dot{M}_{\mathrm{L,NI}}}{\dot{M}_{\mathrm{L,NI}}}\right)^2 + \left(\frac{\Delta\dot{M}_{\mathrm{L},\sigma}}{\dot{M}_{\mathrm{L},\sigma}}\right)^2} \ . \tag{6.3}$$

The uncertainty of $\pm 3.78 \cdot 10^{-7} - 3.78 \cdot 10^{-5}\mathrm{kgs}^{-1}$ over the full range was determined.

---

[1] CTH6500, WIKA Alexander Wiegand SE & Co. KG, Klingenberg/Germany

[2] CTB9430, WIKA Alexander Wiegand SE & Co. KG, Klingenberg/Germany

Reynolds number of liquid, Re_{L}

$$Re_{\mathrm{L}} = \frac{\dot{M}_{\mathrm{L}}}{d_{\mathrm{O}}\pi\mu_{\mathrm{L}}}$$

$$\begin{aligned} \Delta Re_{\mathrm{L}} &= \sqrt{\left(\frac{\partial Re_{\mathrm{L}}}{\partial \dot{M}_{\mathrm{L}}}\Delta\dot{M}_{\mathrm{L}}\right)^2 + \left(\frac{\partial Re_{\mathrm{L}}}{\partial d_{\mathrm{O}}}\Delta d_{\mathrm{O}}\right)^2 + \left(\frac{\partial Re_{\mathrm{L}}}{\partial \mu_{\mathrm{L}}}\Delta\mu_{\mathrm{L}}\right)^2} \\ &= \sqrt{\left(\frac{1}{d_{\mathrm{O}}\pi\mu_{\mathrm{L}}}\Delta\dot{M}_{\mathrm{L}}\right)^2 + \left(\frac{-\dot{M}_{\mathrm{L}}}{d_{\mathrm{O}}{}^2\pi\mu_{\mathrm{L}}}\Delta d_{\mathrm{O}}\right)^2 + \left(\frac{-\dot{M}_{\mathrm{L}}}{d_{\mathrm{O}}\pi\mu_{\mathrm{L}}{}^2}\Delta\mu_{\mathrm{L}}\right)^2} \quad . \end{aligned} \tag{6.4}$$

The error for the liquid Reynolds number is estimated to be less than $\pm 1\,\%$. Owing to the fact that the ∇-groove's and Δ-structure's height $\bar{h}_{\nabla}$ and $\bar{h}_{\Delta}$ are negligibly small compared to the perimeter U_{L} of the used evaporator tubes, for both the micro-structures Re_{L} were based on the diameter d_{O} of the unstructured tube.

Mass flow rate of gas, $\dot{M}_{\mathrm{G}}$

Table 6.4. Parameters determining the accuracy of $\dot{M}_{\mathrm{G}}$.

Quantity	Symbol	Accuracy
Device error	$\Delta(\Delta\dot{M}_{\mathrm{G}})$	$\pm 1.5\,\%$
Signal transformation error	$\Delta\dot{M}_{\mathrm{G,NI}}$	$\pm 0.03\,\%$
Standard deviation	$\Delta\dot{M}_{\mathrm{G},\sigma}$	$\pm 0.005 - 2.0\,\%$

The following expression was used to determine the error of gas flow rate detection:

$$\frac{\Delta\dot{M}_{\mathrm{G}}}{\dot{M}_{\mathrm{G}}} = \sqrt{\left(\frac{\Delta(\Delta\dot{M}_{\mathrm{G}})}{\Delta\dot{M}_{\mathrm{G}}}\right)^2 + \left(\frac{\Delta\dot{M}_{\mathrm{G,NI}}}{\dot{M}_{\mathrm{G,NI}}}\right)^2 + \left(\frac{\Delta\dot{M}_{\mathrm{G},\sigma}}{\dot{M}_{\mathrm{G},\sigma}}\right)^2} \quad . \tag{6.5}$$

The uncertainty of $\pm 5.52 \cdot 10^{-6} - 5.52 \cdot 10^{-4}\mathrm{kgs}^{-1}$ over the full range was determined.

Reynolds number of gas, Re_{G}

$$Re_{\mathrm{G}} = \frac{4\dot{M}_{\mathrm{G}}}{(d_{\mathrm{O}}\pi + 4(b_{\mathrm{CH}} + c_{\mathrm{CH}}))\mu_{\mathrm{G}}}$$

$$\Delta Re_{\mathrm{G}} = \sqrt{\begin{array}{c} \left(\frac{\partial Re_{\mathrm{G}}}{\partial \dot{M}_{\mathrm{G}}}\Delta\dot{M}_{\mathrm{G}}\right)^2 + \left(\frac{\partial Re_{\mathrm{G}}}{\partial d_{\mathrm{O}}}\Delta d_{\mathrm{O}}\right)^2 + \left(\frac{\partial Re_{\mathrm{G}}}{\partial b_{\mathrm{CH}}}\Delta b_{\mathrm{CH}}\right)^2 \cdots \\ \cdots + \left(\frac{\partial Re_{\mathrm{G}}}{\partial c_{\mathrm{CH}}}\Delta c_{\mathrm{CH}}\right)^2 + \left(\frac{\partial Re_{\mathrm{G}}}{\partial \mu_{\mathrm{G}}}\Delta\mu_{\mathrm{G}}\right)^2 \end{array}} \quad . \tag{6.6}$$

with

$$\left(\frac{\partial Re_{\mathrm{G}}}{\partial \dot{M}_{\mathrm{G}}}\Delta \dot{M}_{\mathrm{G}}\right)^2 = \left(\frac{4}{\left(d_{\mathrm{O}}\pi + 4\left(b_{\mathrm{CH}} + c_{\mathrm{CH}}\right)\right)\mu_{\mathrm{G}}}\Delta \dot{M}_{\mathrm{G}}\right)^2 \quad ,$$

$$\left(\frac{\partial Re_{\mathrm{G}}}{\partial d_{\mathrm{O}}}\Delta d_{\mathrm{O}}\right)^2 = \left(\frac{-4\dot{M}_{\mathrm{G}}\pi}{\left(d_{\mathrm{O}}\pi + 4\left(b_{\mathrm{CH}} + c_{\mathrm{CH}}\right)\right)^2\mu_{\mathrm{G}}}\Delta d_{\mathrm{O}}\right)^2 \quad ,$$

$$\left(\frac{\partial Re_{\mathrm{G}}}{\partial b_{\mathrm{CH}}}\Delta b_{\mathrm{CH}}\right)^2 = \left(\frac{-16\dot{M}_{\mathrm{G}}}{\left(d_{\mathrm{O}}\pi + 4\left(b_{\mathrm{CH}} + c_{\mathrm{CH}}\right)\right)^2\mu_{\mathrm{G}}}\Delta b_{\mathrm{CH}}\right)^2 \quad ,$$

$$\left(\frac{\partial Re_{\mathrm{G}}}{\partial c_{\mathrm{CH}}}\Delta c_{\mathrm{CH}}\right)^2 = \left(\frac{-16\dot{M}_{\mathrm{G}}}{\left(d_{\mathrm{O}}\pi + 4\left(b_{\mathrm{CH}} + c_{\mathrm{CH}}\right)\right)^2\mu_{\mathrm{G}}}\Delta c_{\mathrm{CH}}\right)^2 \quad ,$$

$$\left(\frac{\partial Re_{\mathrm{G}}}{\partial \mu_{\mathrm{G}}}\Delta \mu_{\mathrm{G}}\right)^2 = \left(\frac{-4\dot{M}_{\mathrm{G}}}{\left(d_{\mathrm{O}}\pi + 4\left(b_{\mathrm{CH}} + c_{\mathrm{CH}}\right)\right)\mu_{\mathrm{G}}^2}\Delta \mu_{\mathrm{G}}\right)^2 \quad .$$

The uncertainty of ± 7 ($Re_{\mathrm{G}} = 10^4$) $- 441$ ($Re_{\mathrm{G}} = 10^5$) corresponding to $\pm 2.48\,\%$ over the full range results.

6.3 Heat transfer

Mean wall temperature, $\overline{T}_{\mathrm{W}}$

Since the thermocouples were embedded in a copper sleeve, the temperature at the wall-liquid interface could not be directly measured (see Fig. 3.10). A rough estimation of the temperature difference between the thermocouple tip and the wall-liquid interface was made. Therefore the wall thickness s_{O} of the evaporator tube and the depth $0.5 s_{\mathrm{TC}} = 0.3\,\mathrm{mm}$ in which the thermocouples were embedded within the micro-milled grooves inside the sleeve was taken into account. Using one-dimensional heat conduction equation for $15\,\mathrm{W cm^{-2}}$

$$\Delta T = \dot{q}_{\mathrm{W}} \frac{\left(s_{\mathrm{O}} + 0.5\, s_{\mathrm{TC}}\right)}{\lambda_{\mathrm{ET}}}$$

with $\lambda_{\mathrm{ET}} = 400\,\mathrm{W m^{-1} K^{-1}}$ for the thermal conductivity of the copper evaporator tube, the temperature difference ΔT was determined to be $0.68\,\mathrm{K}$.

$$\overline{T}_{\mathrm{W}} = \frac{1}{n}\sum_{i=1}^{n} T_{\mathrm{W}}(z_i)$$

The error of the mean wall temperature calculation was determined through

$$\Delta \overline{T}_{\mathrm{W}} = \sqrt{\left(\frac{\partial \overline{T}_{\mathrm{W}}}{\partial T_{\mathrm{W}}(z_i)}\Delta T_{\mathrm{W}}(z_i)\right)^2} = \sqrt{n\left(\frac{1}{n}\Delta T_{\mathrm{W}}(z_i)\right)^2} \quad . \tag{6.7}$$

Dimensionless wall temperature, $\vartheta(z_i)$

$$\vartheta(z_i) = \frac{T_\mathrm{W}(z_i) - T_\mathrm{L,in}}{\overline{T}_\mathrm{W} - T_\mathrm{L,in}}$$

The error for the dimensionless wall temperature ϑ was assessed with

$$\Delta\vartheta(z_i) = \sqrt{\left(\frac{\partial\vartheta(z_i)}{\partial T_\mathrm{W}(z_i)}\Delta T_\mathrm{W}(z_i)\right)^2 + \left(\frac{\partial\vartheta(z_i)}{\partial T_\mathrm{L,in}}\Delta T_\mathrm{L,in}\right)^2 + \left(\frac{\partial\vartheta(z_i)}{\partial\overline{T}_\mathrm{W}}\Delta\overline{T}_\mathrm{W}\right)^2} \quad , \tag{6.8}$$

with

$$\left(\frac{\partial\vartheta(z_i)}{\partial T_\mathrm{W}(z_i)}\Delta T_\mathrm{W}(z_i)\right)^2 = \left(\frac{1}{\overline{T}_\mathrm{W} - T_\mathrm{L,in}}\Delta T_\mathrm{W}(z_i)\right)^2 \quad ,$$

$$\left(\frac{\partial\vartheta(z_i)}{\partial T_\mathrm{L,in}}\Delta T_\mathrm{L,in}\right)^2 = \left[\left(\frac{T_\mathrm{W}(z_i) - T_\mathrm{L,in}}{\left(\overline{T}_\mathrm{W} - T_\mathrm{L,in}\right)^2} - \frac{1}{\overline{T}_\mathrm{W} - T_\mathrm{L,in}}\right)\Delta T_\mathrm{L,in}\right]^2 \quad ,$$

$$\left(\frac{\partial\vartheta(z_i)}{\partial\overline{T}_\mathrm{W}}\Delta\overline{T}_\mathrm{W}\right)^2 = \left(\frac{-\left(T_\mathrm{W}(z_i) - T_\mathrm{L,in}\right)}{\left(\overline{T}_\mathrm{W} - T_\mathrm{L,in}\right)^2}\Delta\overline{T}_\mathrm{W}\right)^2 \quad .$$

Wall heat flux, $\dot{q}_\mathrm{W}$

$$\dot{q}_\mathrm{W} = \frac{VI}{d_\mathrm{O}\pi l_\mathrm{W}}$$

The error for the wall heat flux was determined with

$$\begin{aligned}\Delta\dot{q}_\mathrm{W} &= \sqrt{\left(\frac{\partial\dot{q}_\mathrm{W}}{\partial V}\Delta V\right)^2 + \left(\frac{\partial\dot{q}_\mathrm{W}}{\partial I}\Delta I\right)^2 + \left(\frac{\partial\dot{q}_\mathrm{W}}{\partial d_\mathrm{O}}\Delta d_\mathrm{O}\right)^2 + \left(\frac{\partial\dot{q}_\mathrm{W}}{\partial l_\mathrm{W}}\Delta l_\mathrm{W}\right)^2} \\ &= \sqrt{\left(\frac{I}{d_\mathrm{O}\pi l_\mathrm{W}}\Delta V\right)^2 + \left(\frac{V}{d_\mathrm{O}\pi l_\mathrm{W}}\Delta I\right)^2 + \left(\frac{-VI}{{d_\mathrm{O}}^2\pi l_\mathrm{W}}\Delta d_\mathrm{O}\right)^2 + \left(\frac{-VI}{d_\mathrm{O}\pi {l_\mathrm{W}}^2}\Delta l_\mathrm{W}\right)^2} \quad .\end{aligned} \tag{6.9}$$

The uncertainty of $\pm 9.6 \cdot 10^{-3} - 3.81 \cdot 10^{-2}\,\mathrm{W cm^{-2}}$ corresponding to $\pm 0.19 - 0.12\,\%$ was determined.

Nusselt number, *Nu*

$$Nu = \frac{\dot{q}_\mathrm{W} l_\mathrm{hyd}}{\lambda_\mathrm{L}\left(\overline{T}_\mathrm{W} - T_\mathrm{L,in}\right)}$$

According to Equation 6.1, the error for the Nusselt numbers was determined with

$$\Delta Nu = \sqrt{\begin{matrix}\left(\frac{\partial Nu}{\partial \dot{q}_\mathrm{W}}\Delta \dot{q}_\mathrm{W}\right)^2 + \left(\frac{\partial Nu}{\partial l_\mathrm{hyd}}\Delta l_\mathrm{W}\right)^2 + \left(\frac{\partial Nu}{\partial \lambda_\mathrm{L}}\Delta \lambda_\mathrm{L}\right)^2 \cdots \\ \cdots + \left(\frac{\partial Nu}{\partial \overline{T}_\mathrm{W}}\Delta \overline{T}_\mathrm{W}\right)^2 + \left(\frac{\partial Nu}{\partial T_\mathrm{L,in}}\Delta T_\mathrm{L,in}\right)^2\end{matrix}} \quad , \tag{6.10}$$

with

$$\left(\frac{\partial Nu}{\partial \dot{q}_\mathrm{W}}\Delta \dot{q}_\mathrm{W}\right)^2 = \left(\frac{l_\mathrm{hyd}}{\left(\overline{T}_\mathrm{W} - T_\mathrm{L,in}\right)\lambda_\mathrm{L}}\Delta \dot{q}_\mathrm{W}\right)^2 \quad ,$$

$$\left(\frac{\partial Nu}{\partial l_\mathrm{hyd}}\Delta l_\mathrm{hyd}\right)^2 = \left(\frac{\dot{q}_\mathrm{W}}{\left(\overline{T}_\mathrm{W} - T_\mathrm{L,in}\right)\lambda_\mathrm{L}}\Delta l_\mathrm{hyd}\right)^2 \quad ,$$

$$\left(\frac{\partial Nu}{\partial \lambda_\mathrm{L}}\Delta \lambda_\mathrm{L}\right)^2 = \left(\frac{-\dot{q}_\mathrm{W} l_\mathrm{hyd}}{\left(\overline{T}_\mathrm{W} - T_\mathrm{L,in}\right)\lambda_\mathrm{L}{}^2}\Delta \lambda_\mathrm{L}\right)^2 \quad ,$$

$$\left(\frac{\partial Nu}{\partial \overline{T}_\mathrm{W}}\Delta \overline{T}_\mathrm{W}\right)^2 = \left(\frac{-\dot{q}_\mathrm{W} l_\mathrm{hyd}}{\left(\overline{T}_\mathrm{W} - T_\mathrm{L,in}\right)^2\lambda_\mathrm{L}}\Delta \overline{T}_\mathrm{W}\right)^2 \quad ,$$

$$\left(\frac{\partial Nu}{\partial T_\mathrm{L,in}}\Delta T_\mathrm{L,in}\right)^2 = \left(\frac{\dot{q}_\mathrm{W} l_\mathrm{hyd}}{\left(\overline{T}_\mathrm{W} - T_\mathrm{L,in}\right)^2\lambda_\mathrm{L}}\Delta T_\mathrm{L,in}\right)^2 \quad .$$

6.4 Shadowgraphy visualization

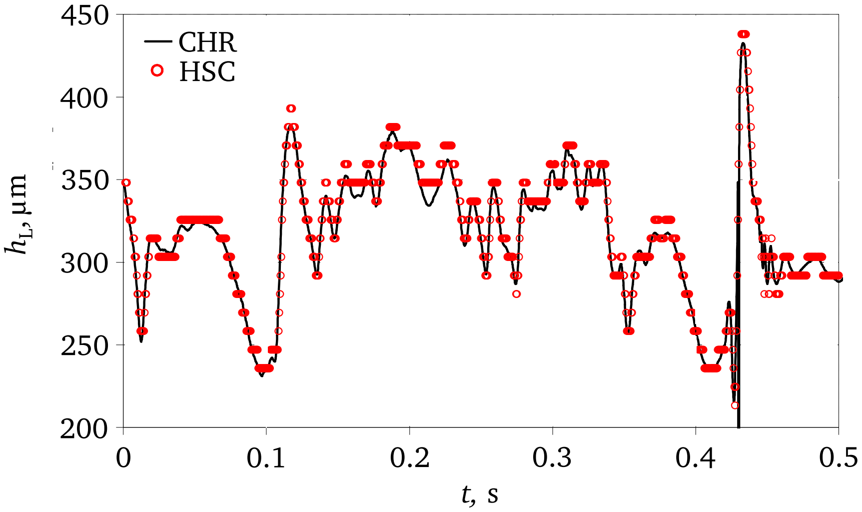

Figure 6.1. Comparison of temporal thickness variation of a falling film at $z = 45\,\mathrm{mm}$ measured with high-speed camera synchronized with confocal chromatic sensor to validate the accuracy of the shadowgraphy measurement.

The measurement error of the shadowgraphy method was determined by performing film thickness measurements at $z = 45\,\mathrm{mm}$ with the high-speed camera synchronized with the confocal chromatic sensor.

During the measurements, the film flow was disturbed intentionally to generate a wavy film flow. For this, a stainless steel wire was immersed into the film perpendicularly to the liquid flow direction at $z = 5\,\mathrm{mm}$. In Fig. 6.1 the temporal variation of the film thickness detected with the CHR and shadowgraphy method is plotted. The shadowgraphy measurements show a very good agreement with the measured values of the CHR sensor. The error of the confocal chromatic sensor is $\leq 1\,\mu\mathrm{m}$ (see Sec. 4.3.2). The uncertainty of $\pm 3\,\mu\mathrm{m}$ of the glass scale (see Fig. 4.3) used to calculate the spatial resolution κ_{SG} had been given by the manufacturer; the deviation of the shadowgraphy measurements were determined to be $\pm 15\,\mu\mathrm{m}$.

6.5 Gas velocity and shear stress

Gas velocity measurement, $u_{\mathrm{G,cal}}$ (V_{HWA})

$$u_{\mathrm{G,cal}} = \sqrt{\frac{2\Delta p}{\rho_{\mathrm{G}}}}$$

$$V_{\mathrm{HWA,cal}} = \sqrt{C\left(A + B u_{\mathrm{G,cal}}{}^{n}\right)}$$

$$u_{\mathrm{G}} = \left(\frac{1}{B}\frac{V_{\mathrm{HWA}}{}^{2}}{C} - A\right)^{\frac{1}{n}}$$

Table 6.5. Specifications concerning the accuracy of pitot tube (628), differential pressure sensor (698A), and signal conditioner unit (670B).

Device	Quantity	Symbol		Accuracy
628	Accuracy	Δp_{628}	=	$\pm 0.38\,\%$ of reading up to gas velocities of $50\,\mathrm{ms}^{-1}$
698A	Accuracy	$\Delta p_{698\mathrm{A}}$	=	$\pm 0.12\,\%$ of reading
670B,l	Display linearity	$\Delta p_{670\mathrm{B,l}}$	=	$< \pm 0.019\,\%$ of full scale
670B,s	Display accuracy span	$\Delta p_{670\mathrm{B,s}}$	=	$\pm 0.267\,\%$ of full scale
670B,z	Display accuracy zero	$\Delta p_{670\mathrm{B,z}}$	=	$\pm 0.067\,\%$ of full scale

The error of the gas flow measurements was calculated as follows:

$$\frac{\Delta\left(\Delta p\right)}{\Delta p} = \sqrt{\begin{aligned}&\left(\frac{\Delta\left(\Delta p_{628}\right)}{\Delta p_{628}}\right)^2 + \left(\frac{\Delta\left(\Delta p_{698\mathrm{A}}\right)}{\Delta p_{698\mathrm{A}}}\right)^2 + \left(\frac{\Delta\left(\Delta p_{670\mathrm{B,z}}\right)}{\Delta p_{670\mathrm{B,z}}}\right)^2 \cdots \\ &\cdots + \left(\frac{\Delta\left(\Delta p_{670\mathrm{B,s}}\right)}{\Delta p_{670\mathrm{B,s}}}\right)^2 + \left(\frac{\Delta\left(\Delta p_{670\mathrm{B,l}}\right)}{\Delta p_{670\mathrm{B,l}}}\right)^2\end{aligned}} \quad , \tag{6.11}$$

further using the expression

$$\begin{aligned}\Delta u_{\mathrm{G,cal}} &= \sqrt{\left(\frac{\partial u_{\mathrm{G,cal}}}{\partial \Delta p}\Delta\left(\Delta p\right)\right)^2 + \left(\frac{\partial u_{\mathrm{G,cal}}}{\partial \rho_{\mathrm{G}}}\Delta \rho_{\mathrm{G}}\right)^2} \\ &= \sqrt{\left(\frac{1}{\rho_{\mathrm{G}}\sqrt{2}\sqrt{\frac{\Delta p}{\rho_{\mathrm{G}}}}}\Delta\left(\Delta p\right)\right)^2 + \left(\frac{-\Delta p}{{\rho_{\mathrm{G}}}^2\sqrt{2}\sqrt{\frac{\Delta p}{\rho_{\mathrm{G}}}}}\Delta \rho_{\mathrm{G}}\right)^2} \quad ,\end{aligned} \tag{6.12}$$

and implementing in

$$\Delta V_{\mathrm{HWA,cal}} = \sqrt{\left(\frac{\partial V_{\mathrm{HWA,cal}}}{\partial u_{\mathrm{G,cal}}}\Delta u_{\mathrm{G,cal}}\right)^2} = \frac{B \cdot C \cdot n \cdot {u_{\mathrm{G,cal}}}^{n-1}}{2\sqrt{C\left(A + B \cdot {u_{\mathrm{G,cal}}}^{n}\right)}}\Delta u_{\mathrm{G,cal}} \quad . \tag{6.13}$$

Finally the error of the gas measurements with the hot wire results in

$$\Delta u_{\mathrm{G}} = \frac{2n \cdot u_{\mathrm{G}}\sqrt{C\left(A + B \cdot {u_{\mathrm{G}}}^{n}\right)}}{B}\Delta V_{\mathrm{HWA,cal}} \quad . \tag{6.14}$$

Shear stress, $\tau_{\mathrm{W,G}}$

$$\tau_{\mathrm{W,G}} = \mu_{\mathrm{G}}\frac{\partial u_{\mathrm{G}}}{\partial r} = \mu_{\mathrm{G}}\frac{u_{\mathrm{G,n}} - u_{\mathrm{G,n\text{-}1}}}{r_{\mathrm{n}} - r_{\mathrm{n\text{-}1}}}$$

The error of shear stress was elaborated with

$$\Delta \tau_{\mathrm{W,G}} = \sqrt{\begin{array}{c}\left(\frac{\partial \tau_{\mathrm{W,G}}}{\partial \mu_{\mathrm{G}}}\Delta \mu_{\mathrm{G}}\right)^2 + \left(\frac{\partial \tau_{\mathrm{W,G}}}{\partial u_{\mathrm{G,n}}}\Delta u_{\mathrm{G,n}}\right)^2 + \left(\frac{\partial \tau_{\mathrm{W,G}}}{\partial u_{\mathrm{G,n\text{-}1}}}\Delta u_{\mathrm{G,n\text{-}1}}\right)^2 \cdots \\ \cdots + \left(\frac{\partial \tau_{\mathrm{W,G}}}{\partial r_{\mathrm{n}}}\Delta r_{\mathrm{n}}\right)^2 + \left(\frac{\partial \tau_{\mathrm{W,G}}}{\partial r_{\mathrm{n\text{-}1}}}\Delta r_{\mathrm{n\text{-}1}}\right)^2\end{array}} \quad . \tag{6.15}$$

$$\begin{aligned}\left(\frac{\partial \tau_{\mathrm{W,G}}}{\partial \mu_{\mathrm{G}}}\Delta \mu_{\mathrm{G}}\right)^2 &= \left(\frac{u_{\mathrm{G,n}} - u_{\mathrm{G,n\text{-}1}}}{r_{\mathrm{n}} - r_{\mathrm{n\text{-}1}}}\Delta \mu_{\mathrm{G}}\right)^2 \quad , \\ \left(\frac{\partial \tau_{\mathrm{W,G}}}{\partial u_{\mathrm{G,n}}}\Delta u_{\mathrm{G,n}}\right)^2 &= \left(\frac{\mu_{\mathrm{G}}}{r_{\mathrm{n}} - r_{\mathrm{n\text{-}1}}}\Delta u_{\mathrm{G,n}}\right)^2 \quad , \\ \left(\frac{\partial \tau_{\mathrm{W,G}}}{\partial u_{\mathrm{G,n\text{-}1}}}\Delta u_{\mathrm{G,n\text{-}1}}\right)^2 &= \left(\frac{-\mu_{\mathrm{G}}}{r_{\mathrm{n}} - r_{\mathrm{n\text{-}1}}}\Delta u_{\mathrm{G,n\text{-}1}}\right)^2 \quad , \\ \left(\frac{\partial \tau_{\mathrm{W,G}}}{\partial r_{\mathrm{n}}}\Delta r_{\mathrm{n}}\right)^2 &= \left(\frac{-\mu_{\mathrm{G}}\left(u_{\mathrm{G,n}} - u_{\mathrm{G,n\text{-}1}}\right)}{\left(r_{\mathrm{n}} - r_{\mathrm{n\text{-}1}}\right)^2}\Delta r_{\mathrm{n}}\right)^2 \quad , \\ \left(\frac{\partial \tau_{\mathrm{W,G}}}{\partial r_{\mathrm{n\text{-}1}}}\Delta r_{\mathrm{n\text{-}1}}\right)^2 &= \left(\frac{\mu_{\mathrm{G}}\left(u_{\mathrm{G,n}} - u_{\mathrm{G,n\text{-}1}}\right)}{\left(r_{\mathrm{n}} - r_{\mathrm{n\text{-}1}}\right)^2}\Delta r_{\mathrm{n\text{-}1}}\right)^2 \quad .\end{aligned}$$

Here the error $\Delta r_{\mathrm{n}} = \Delta r_{\mathrm{n\text{-}1}}$ of the radial coordinate r is $\pm 3\,\mathrm{\mu m}$.

6.6 Closure

In this chapter, the measurement errors are summarized. Using propagation of the uncertainty method, the uncertainties in film thickness, wave frequency, and Nusselt number were reported.

7

Results and Discussion

In this chapter, the results of the high speed shadowgraphy measurements of gravity and gas-driven films flowing at the unstructured, V-grooved and pyramid structured surfaces are discussed. The dimensionless temperature profiles are presented and the heat transfer results are compared. Further, the Nusselt number determined for the unstructured surface is compared with the theoretical approaches and measurements from the literature. For the gas-driven film flow at the unstructured surface, the developed Nusselt number correlations are presented.

7.1 Gravity and gas-driven film flow on unstructured surface

7.1.1 Film waviness

The type of wave can influence the standard deviation calculation and resultantly the wave frequency. Especially, when a 3D wave passes through the field of view of the high speed camera, the wave length measured in the image can be incorrect. A schematic of a 3D wave is shown in Fig. 7.1. The actual wave length is perpendicularly oriented to the meridian axis of the wave. Since the meridian axis is not parallel to the camera view plane, the measured wave length is incorrect. This leads to an increase of the standard deviation and to an decrease of the number of waves per sequence. In the experiments, it has been observed that at very high gas flow rates the skin of the liquid film flow is strongly roughened (see Fig. 7.2). The velocity difference between the liquid and gas stream is very high, and thus the shear force exerted by the gas phase is high. This state of the liquid flow can be supposed as a highly turbulent regime which is characterized by multiple waves. For instance, the shadowgraphy image of the liquid film flow in Fig. 7.2 has two overlapping waves. If waves exist within and outside the $\mathrm{DOF}_{\mathrm{SG}}$, the determined

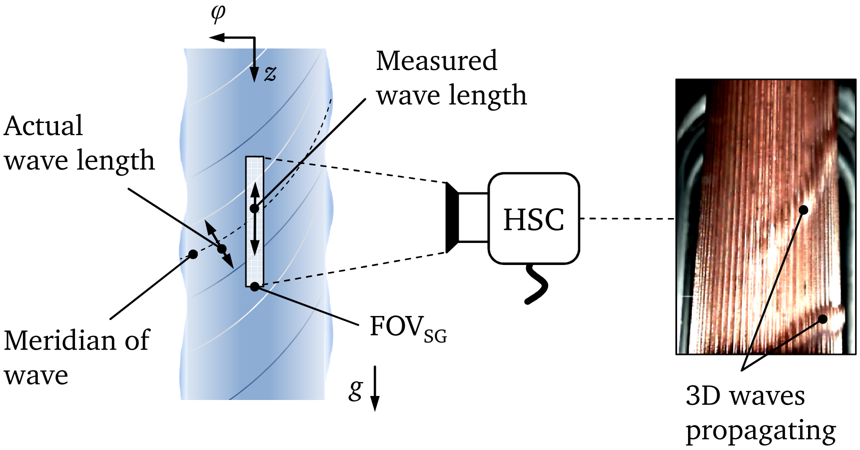

Figure 7.1. 3D waves captured by shadowgraphy measurements propagating along z-axis.

wave parameters are incorrect. It is not possible to estimate the error in this measurement. However, in the following parts of this chapter, these phenomenon shall be given due consideration when discussing the standard deviation and frequency results.

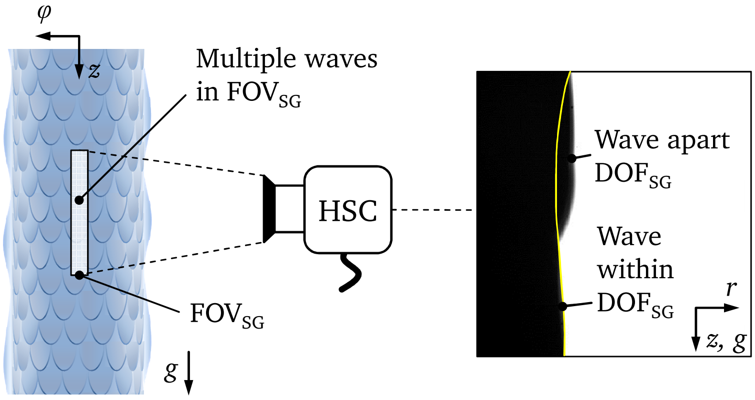

Figure 7.2. 3D shedded liquid film flow leads to overlapping short waves within the shadowgraphy image.

Standard deviation and wave frequency at unstructured surface

In Fig. 7.3 the standard deviation σ_{O} of the film thickness of unheated and heated liquid is displayed for varying gas and liquid mass flow rates at $z = 45\,\mathrm{mm}$. At gas Reynolds numbers of $7 \cdot 10^4$ and 10^5, the standard deviations have to be interpreted with caution due to the shedding of the waves. For particular values images from the high speed sequences are exemplary inserted as insets to describe the interfacial dynamics and the structure of the film surface. For the gravity-driven film flow, σ_{O} is measured around $5 - 10\,\mathrm{\mu m}$. The liquid-gas interface is rather smooth and remains stable. The application of a gas flow with $Re_{\mathrm{G}} = 10^4$ leads to minor change in the standard deviation as compared to gravity-driven film flow (see insert 1 in Fig. 7.3). However, at and beyond $Re_{\mathrm{G}} = 4 \cdot 10^4$, the standard deviation is higher than the gravity-driven liquid film. At $Re_{\mathrm{G}} = 4 \cdot 10^4$, the standard deviation reduces from $50\,\mathrm{\mu m}$ to $25\,\mathrm{\mu m}$ with increase in Re_{L}. In the case of a gravity-driven film, the relative velocity between the liquid film and the surrounding stagnant air increases with increase in Re_{L}. This leads in increase in instability with Re_{L}. On the other hand, in the case of a gas-driven film, the liquid inertia increases while the gas-to-liquid relative

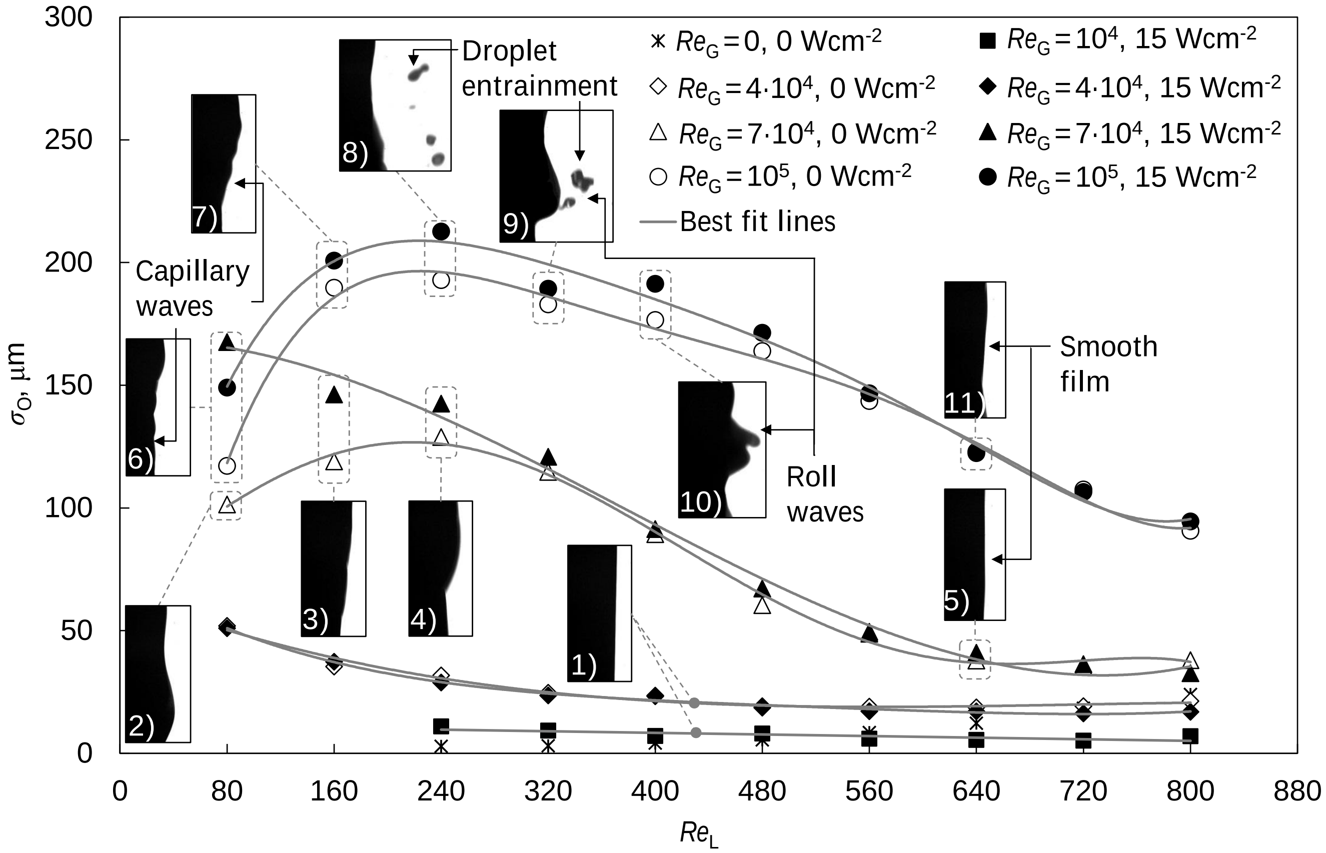

Figure 7.3. Standard deviation σ_O at the unstructured surface with exemplary chosen images of characteristic liquid-gas interfacial structures showing smooth interface, capillary waves, roll waves, and droplet entrainment. Experimental parameters are $Re_L = 80 - 800$, $Re_G = 0 - 10^5$ at $\dot{q}_W = 0$ and $\dot{q}_W = 15\,\mathrm{Wcm^{-2}}$.

velocity decreases with the growth of Re_L. Both increase in liquid inertia and decrease in gas-to-liquid relative velocity leads to a increase in film stability. Applying heat to the liquid film flow does not cause any change in the standard deviation. In the case of higher shear stress ($Re_G = 7 \cdot 10^4$), several effects can be identified. Starting at $Re_L = 80$, σ_O first increases from approximately $100\,\mu\mathrm{m}$ up to $200\,\mu\mathrm{m}$ at $Re_L = 240$ and then gradually decreases to $45\,\mu\mathrm{m}$ for the unheated film flow. The stronger shear stress induced by higher gas velocity overcomes the weak liquid inertial force and causes the formation of waves [70, 91]. As presented in the insert 2 and 3 in Fig. 7.3, waves are formed and propagate along the tube surface. They transform into solitary waves with increased Re_L which overlap each other. This can be seen as a sharp indentation in the wave front region in insert 4. With higher liquid mass flow rates, solitary waves are suppressed [70]. Compared to that, σ_O of the heated film flow is represented with capillary waves moving in the front region of comparable large waves called disturbing waves [4] at $Re_L = 80$ (see insert 6). Additionally, the heat input leads to a reduction of the liquid surface tension which can contribute to the generation of waves through increasing the sensitivity for deformations [13]. As presented in insert 5, higher liquid mass flow rate stabilizes the liquid-gas interface. At $Re_G = 10^5$, the liquid-gas interface deforms significantly, since the liquid film sees stronger shear stress. From $Re_L = 80 - 480$ the heat flux leads to an increase in σ_O while above $Re_L = 480$ this effect reduces.

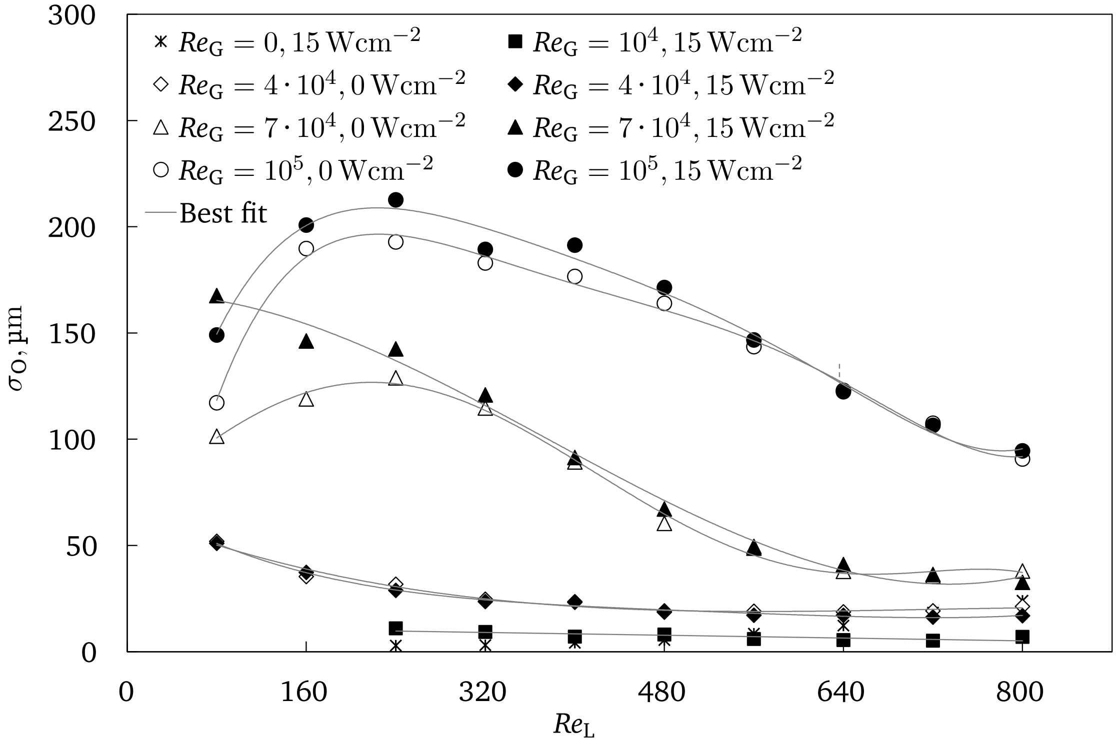

Figure 7.4. Standard deviation σ_O for $Re_L = 80 - 800$, $Re_G = 0 - 10^5$ at $\dot{q}_W = 0$ and $\dot{q}_W = 15\,\mathrm{Wcm^{-2}}$.

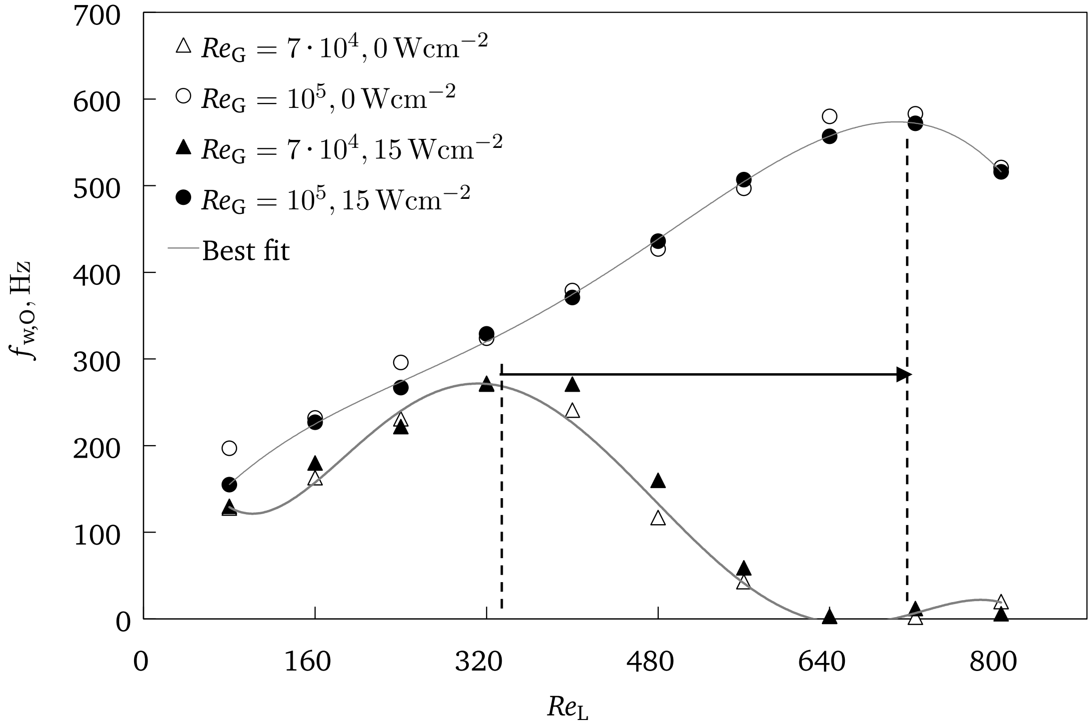

Figure 7.5. Wave frequency $f_{w,O}$ for varying $Re_L = 80 - 800$, $Re_G = 7\cdot10^4, 10^5$ at $\dot{q}_W = 0$ and $\dot{q}_W = 15\,\mathrm{Wcm^{-2}}$.

For $Re_L = 80$ and $Re_L = 160$ still capillary waves could be seen (see insert 7 in Fig. 7.3). The maximum value is at $Re_L = 240$ whereas entrained droplets were observed up to $Re_L = 320$ as shown in insert 8 and 9. This can cause a reduction of the liquid mass load existing on the wall. Additionally, roll waves have been recorded at higher liquid Reynolds number (see insert 10 in Fig. 7.3). Narasimhan et al. [104] has reported that for a horizontal flow, the transition from a smooth film flow to roll waves takes place at $Re_{\mathrm{G}} > 10^4$ (see Fig.2.6) and are suppressed with increasing liquid Reynolds number. However, in the present experiments, roll waves occurred first at $Re_{\mathrm{G}} > 7 \cdot 10^4$. With Fig. 7.4 and Fig. 7.5, σ_{O} and the wave frequency $f_{\mathrm{w,O}}$ for the unheated and heated liquid film can be compared. Frequency values are displayed only for $Re_{\mathrm{G}} = 7 \cdot 10^4$ and $Re_{\mathrm{G}} = 10^5$, since during the data post-processing no frequencies could be determined for $Re_{\mathrm{G}} = 10^4$ and $Re_{\mathrm{G}} = 4 \cdot 10^4$. In case of $Re_{\mathrm{G}} = 7 \cdot 10^4$, the wave frequency detected starts from about $120\,\mathrm{Hz}$, passes through a maximum of $260\,\mathrm{Hz}$ at $Re_{\mathrm{L}} = 320$ and decays almost to $0\,\mathrm{Hz}$ at higher liquid mass flow rates. For the unheated case, the maximum values of the standard deviation and the wave frequency occurs approximately at the same liquid Reynolds number.

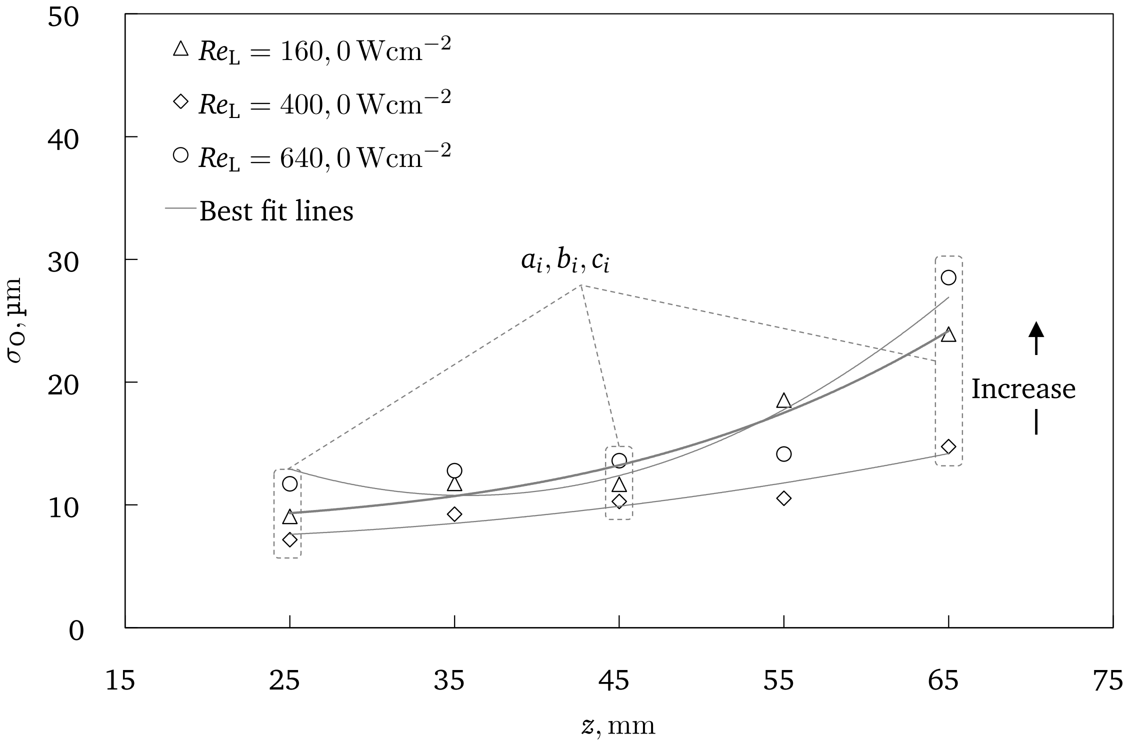

Figure 7.6. Standard deviation σ_{O} of the film thickness of gas-driven liquid films on the unstructured surface as a function of z for $Re_{\mathrm{G}} = 10^4$, $Re_{\mathrm{L}} = 160, 400, 640$, $\dot{q}_{\mathrm{W}} = 0$; values at $z = 25\,\mathrm{mm}, 45\,\mathrm{mm}$, and $65\,\mathrm{mm}$ correspond to image sequences a_i, b_i, and c_i in Fig. 7.7.

According to the corresponding standard deviation values, waves with large amplitudes appear fewer. With increasing Re_{L}, small amplitude waves are generated which travel faster due to the increased film velocity. A further increase of Re_{L} results in a smooth liquid-gas interface and hence a reduction of the number of wave through the smoothing effect [132]. The heat input shows only a minor increasing impact on the wave frequency. At $Re_{\mathrm{G}} = 10^5$, increased number of waves have been recorded compared to $Re_{\mathrm{G}} = 7 \cdot 10^4$ over the full range of Re_{L}. For $Re_{\mathrm{G}} = 10^5$, σ_{O} has its maximum value at $Re_{\mathrm{L}} = 240$, while the maximum wave frequency occurs at $Re_{\mathrm{L}} = 720$ where more high frequent waves appear which is a result of increased Re_{L} [43].

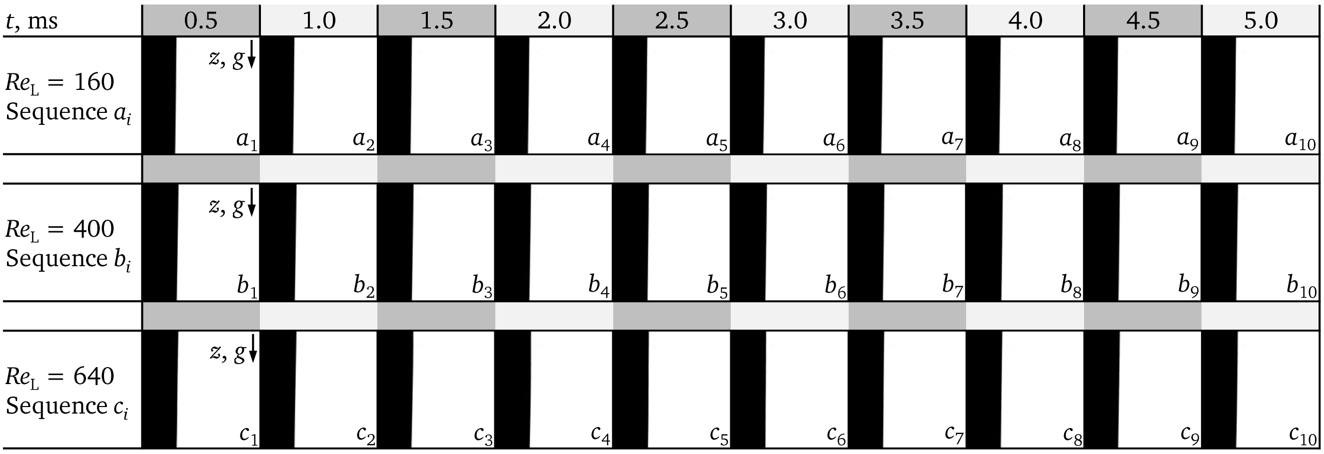

Figure 7.7. Image sequences of gas-driven liquid film flow at the unstructured surface for $Re_L = 160, 400, 640$. Sequences are taken at $Re_G = 10^4$, $Re_G = 4 \cdot 10^4$, and $\dot{q}_W = 0$.

In Fig. 7.6, σ_O of the gas-driven film thickness at $Re_G = 10^4$, varying Re_L and z is displayed. The wall heat flux during the measurements was $q_W = 0$. σ_O increases along the flow direction but decreases with Re_L. The increase along the flow direction is due to the growth of disturbances induced by the interaction with the gas flow. The corresponding high speed imaging sequences in Fig. 7.7 for the σ_O values labeled with a_i, b_i, and c_i reveal a rather smooth and stable film flow.

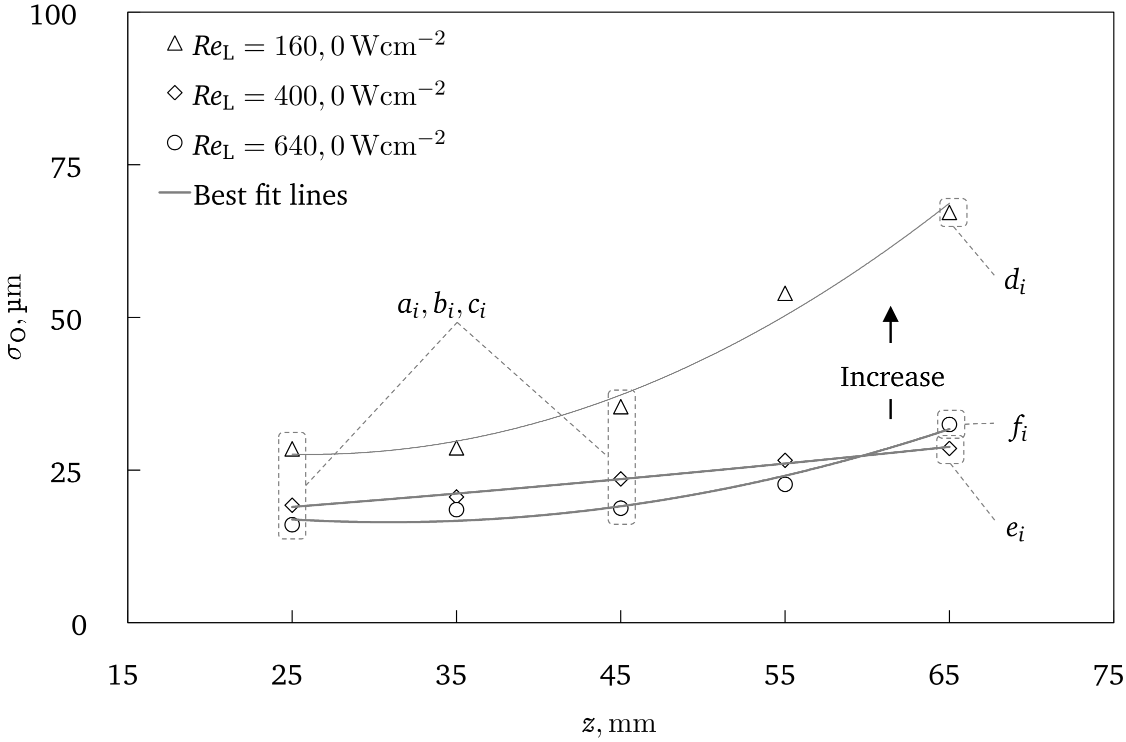

Figure 7.8. Standard deviation σ_O of the film thickness of gas-driven liquid films on the unstructured surface as a function of z for $Re_G = 4 \cdot 10^4$, $Re_L = 160, 400, 640$, $\dot{q}_W = 0$; values at $z = 25\,\mathrm{mm}, 45\,\mathrm{mm}$ correspond to image sequences a_i, b_i, and c_i in Fig. 7.7, values at $z = 65\,\mathrm{mm}$ correspond to image sequences d_i, e_i and f_i in Fig. 7.9.

At increased Re_G, σ_O grows for $Re_L = 160$ while at $Re_L = 400$ and $Re_L = 640$, no significant rise of σ_O can be seen. For the measurement positions $z = 25\,\mathrm{mm}$ and $z = 45\,\mathrm{mm}$ labeled with a_i, b_i, and c_i, the corresponding high speed imaging sequences in Fig 7.7, the film surface remained smooth. Noticeable film deformation was recorded at $z = 65\,\mathrm{mm}$ and $Re_L = 160$ (d_i) which is presented in Fig.7.9. The liquid-gas interface is rather smooth for $Re_L = 400$ and $Re_L = 640$ (e_i, f_i) at the same location as shown in Fig. 7.9.

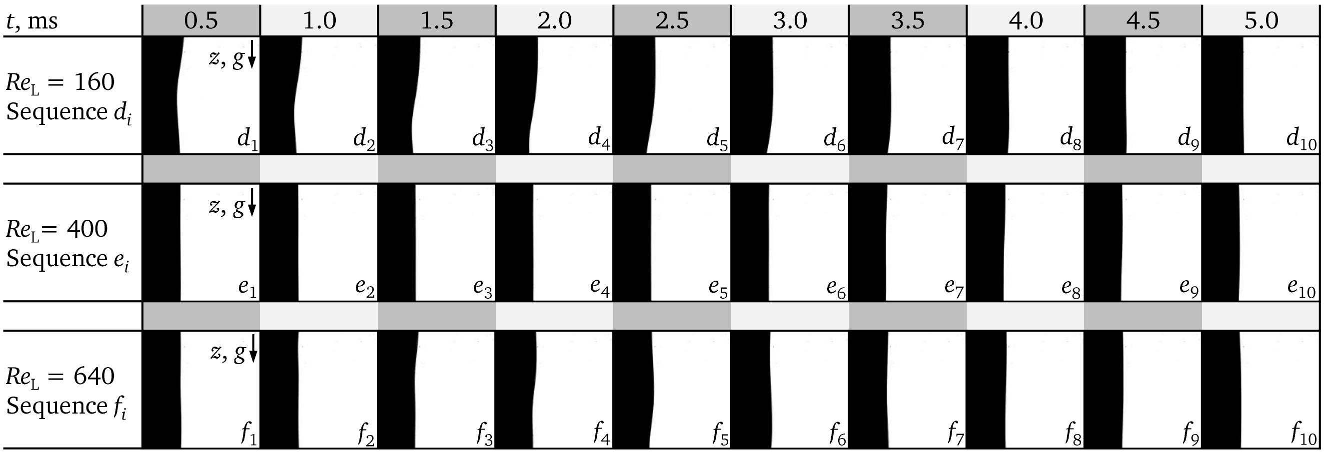

Figure 7.9. Image sequences of gas-driven liquid film flow at the unstructured surface for $Re_L = 160, 400, 640$. Sequences are taken at $Re_G = 4 \cdot 10^4$ and $\dot{q}_W = 0$.

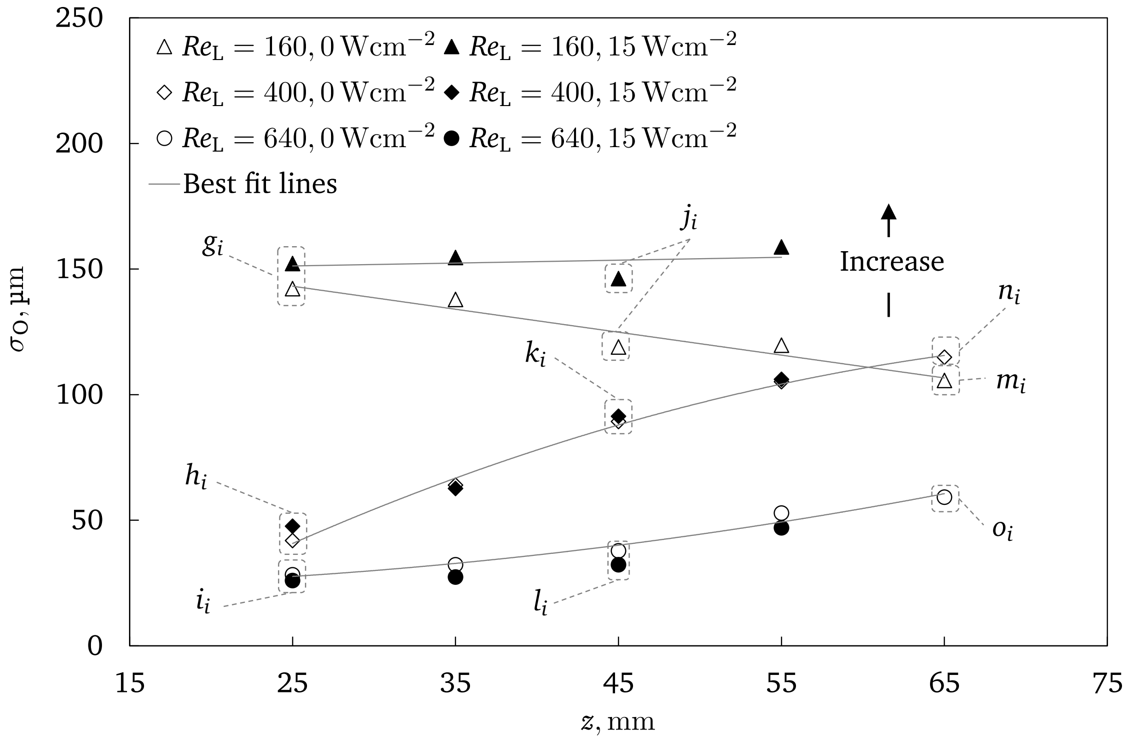

Figure 7.10. Standard deviation σ_O of gas-driven liquid films on the unstructured surface as a function of z for $Re_G = 7 \cdot 10^4$, $Re_L = 160, 400, 640$, $\dot{q}_W = 0, 15\,\mathrm{Wcm^{-2}}$; values at $z = 25\,\mathrm{mm}, 45\,\mathrm{mm}$, and $65\,\mathrm{mm}$ correspond to image sequences $g_i - o_i$ in Fig. 7.12, 7.13, and 7.14.

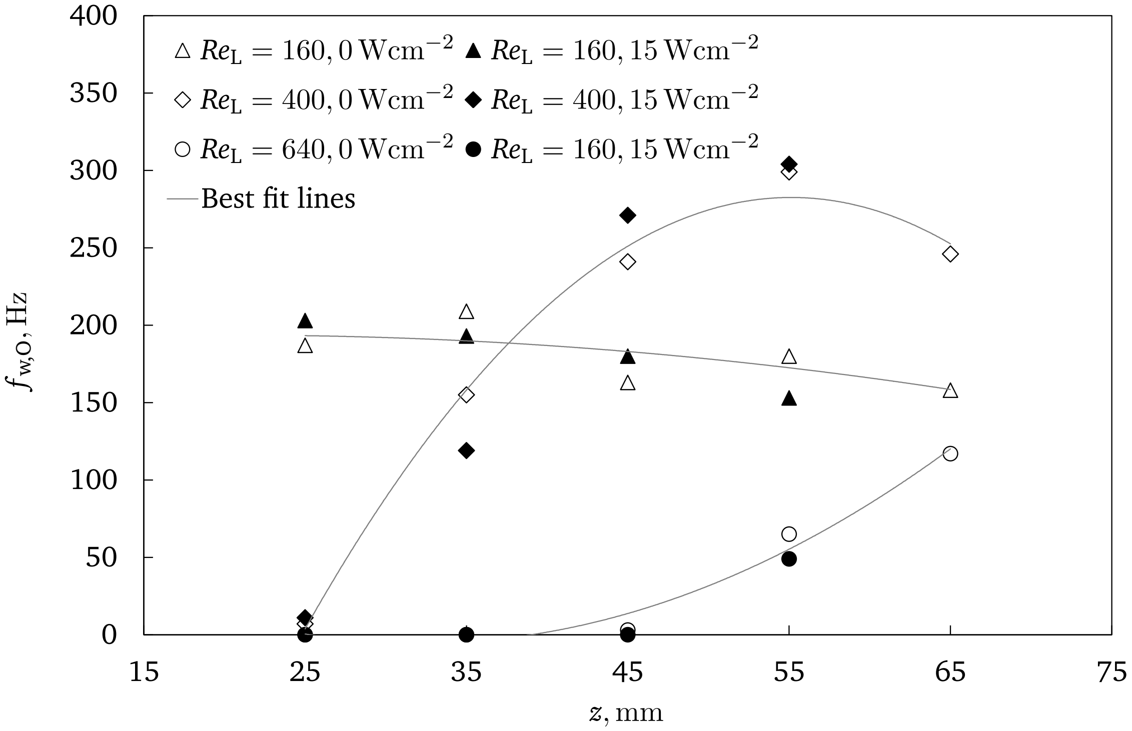

Figure 7.11. Wave frequency $f_{w,O}$ of gas-driven liquid films on the unstructured surface as a function of z for $Re_G = 7 \cdot 10^4$, $Re_L = 160, 400, 640$, $\dot{q}_W = 0, 15\,\mathrm{Wcm^{-2}}$.

The axial variation of σ_O and the wave frequency $f_{w,O}$ for $\dot{q}_W = 0$ and $q_W = 15\,\mathrm{Wcm^{-2}}$ at further increased Re_G and varying Re_L is shown in Fig. 7.10 and Fig. 7.11. At $Re_L = 160$, σ_O increases as compared to $Re_G = 4 \cdot 10^4$. There was no measurement possible during heated wall experiments for the position $z = 65\,\mathrm{mm}$, since the liquid film break-up occurred at that location. The unheated experiments show that σ_O remains rather constant for $Re_L = 160$, while heating of the wall causes a decay towards the end of the tube. Compared to this, the wave frequency decreases along the flow direction and is not significantly influenced by the wall heat flux.

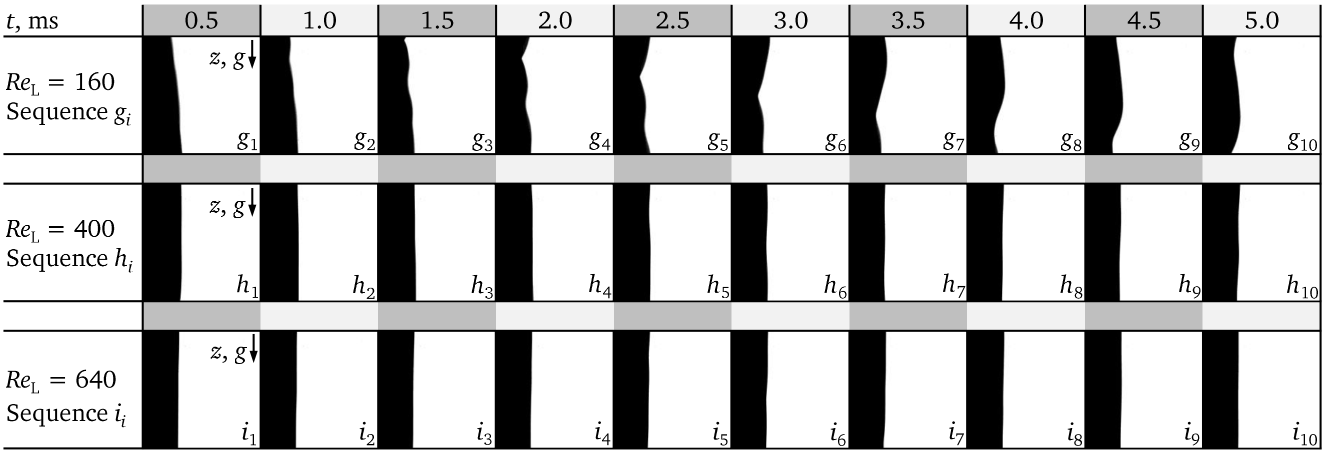

Figure 7.12. Image sequences of gas-driven liquid film flow at the unstructured surface for $Re_L = 160, 400, 640$. Sequences are taken at $z = 25\,\mathrm{mm}$ with $Re_G = 7 \cdot 10^4$ and $\dot{q}_W = 0$.

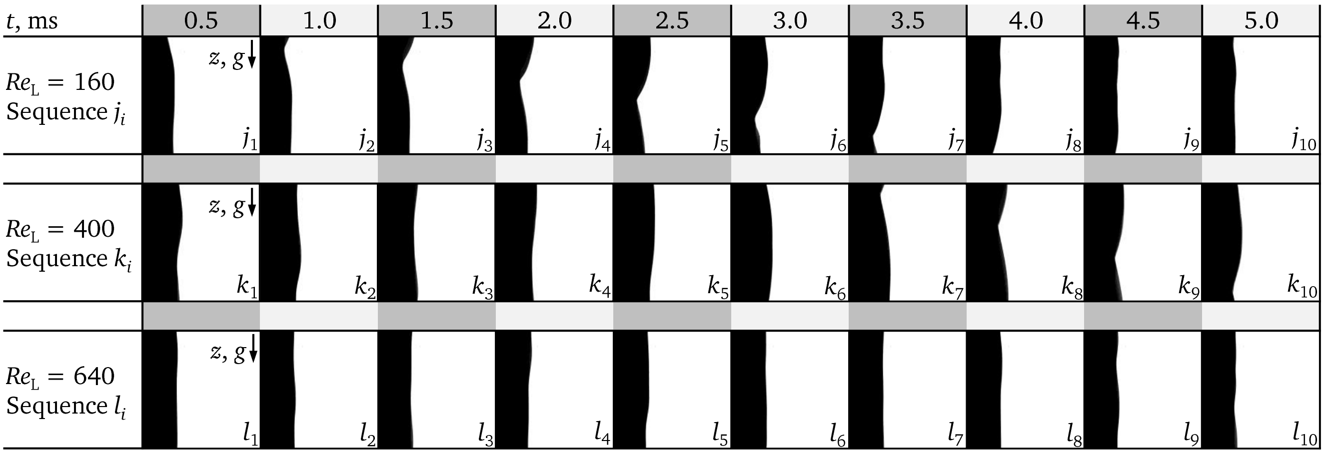

Figure 7.13. Image sequences of gas-driven liquid film flow at the unstructured surface for $Re_L = 160, 400, 640$. Sequences are taken at $z = 45\,\mathrm{mm}$ with $Re_G = 7 \cdot 10^4$ and $\dot{q}_W = 0$.

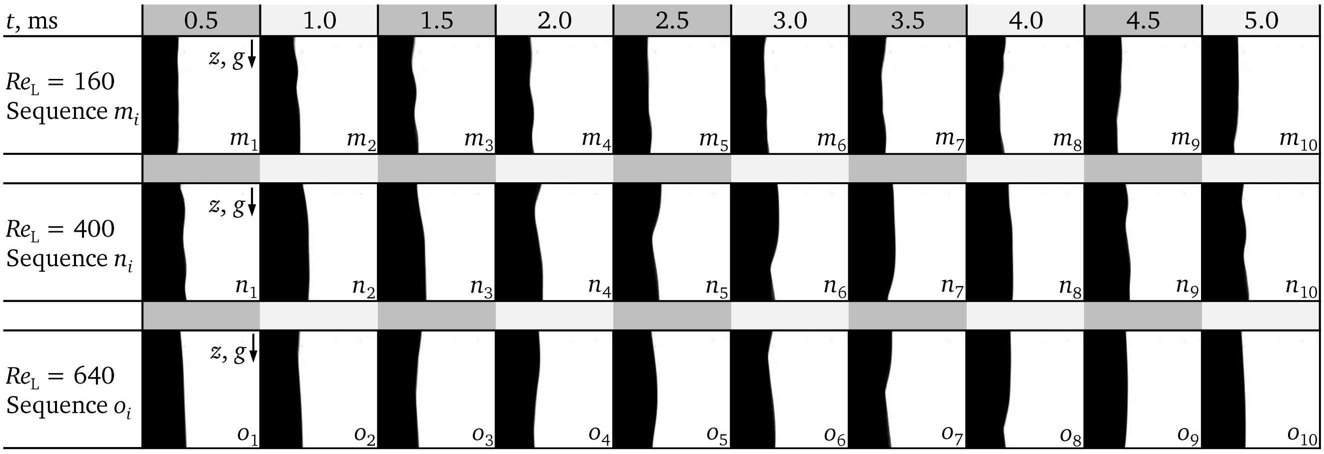

Figure 7.14. Image sequences of gas-driven liquid film flow at the unstructured surface for $Re_L = 160, 400, 640$. Sequences are taken at $z = 65\,\mathrm{mm}$ with $Re_G = 7 \cdot 10^4$ and $\dot{q}_W = 0$.

However, this effect can not be identified for the $Re_L = 400, 640$ measurements. For those, σ_O rises in flow direction; for $Re_L = 640$ the gradient is weaker than for $Re_L = 400$. σ_O and $f_{w,O}$ are suppressed with increasing Re_L from 400 to 640. Nevertheless, the wave frequency increases with z. The high speed records displayed in Figs. 7.12, 7.13, and 7.14 show that the liquid-gas interface transforms from a smooth to a wavy shape for $Re_L = 400$ and $Re_L = 640$. The variation of σ_O and $f_{w,O}$ for $Re_G = 10^5$ are presented in Fig. 7.15 and Fig. 7.16. Values for the heated film measured at $z = 65\,\mathrm{mm}$ are not provided due to film rupture. Over the measurement distance, the standard deviation has an increasing tendency along the flow direction for all Re_L. Similar results has been reported by Kobayashi et al. [132]. The influence of heat cannot be directly distinguished. Similar to the measurements at lower gas Reynolds numbers, higher liquid mass flow rates lead to a reduction of the fluctuations of the liquid-gas interface. However, large waves with capillary ripples in the front are still generated as shown in the sequences p_i, t_i, u_i, and v_i in Figs. 7.17 to 7.19. Similar to σ_O, only minor effect of heating is seen on $f_{w,O}$. At the lowest liquid mass flow rate, the number of waves decrease weakly over the axial direction. The same effect can be seen for the measurements carried out at the liquid Reynolds number of 400.

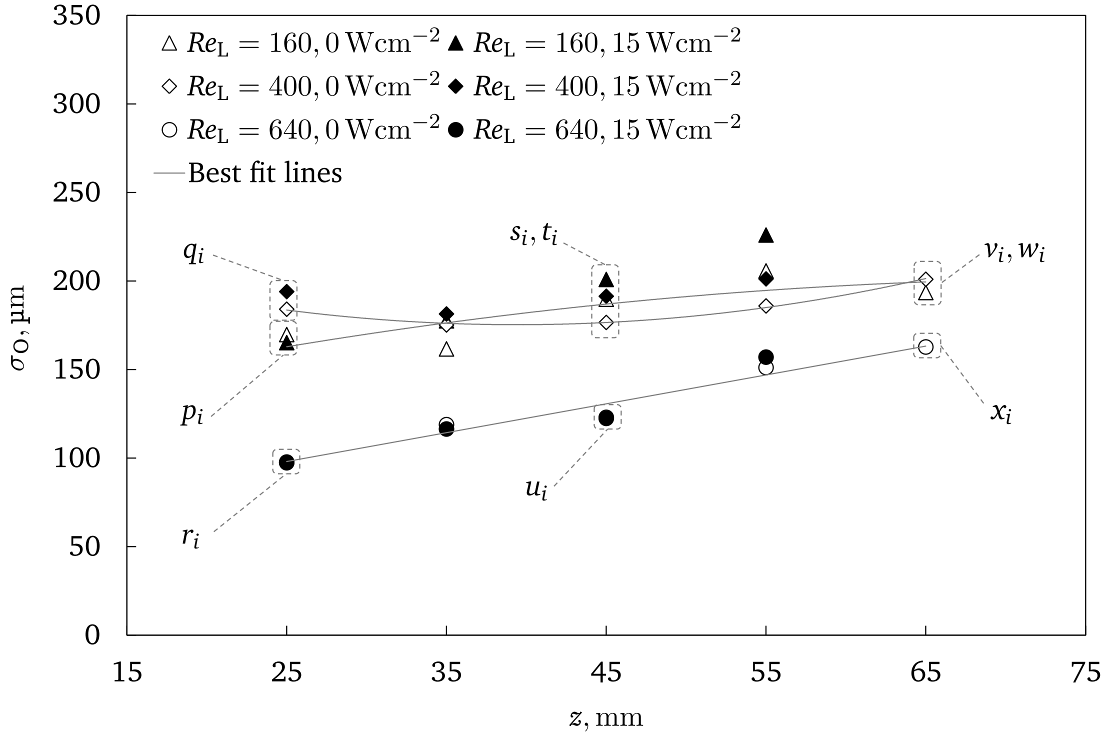

Figure 7.15. Standard deviation σ_O of gas-driven liquid films on the unstructured surface as a function of z for $Re_G = 10^5$, $Re_L = 160, 400, 640$, $\dot{q}_W = 0, 15\,\mathrm{Wcm^{-2}}$; values at $z = 25\,\mathrm{mm}, 45\,\mathrm{mm}$, and $65\,\mathrm{mm}$ correspond to image sequences $p_i - x_i$ in Fig. 7.17, 7.18, and 7.19.

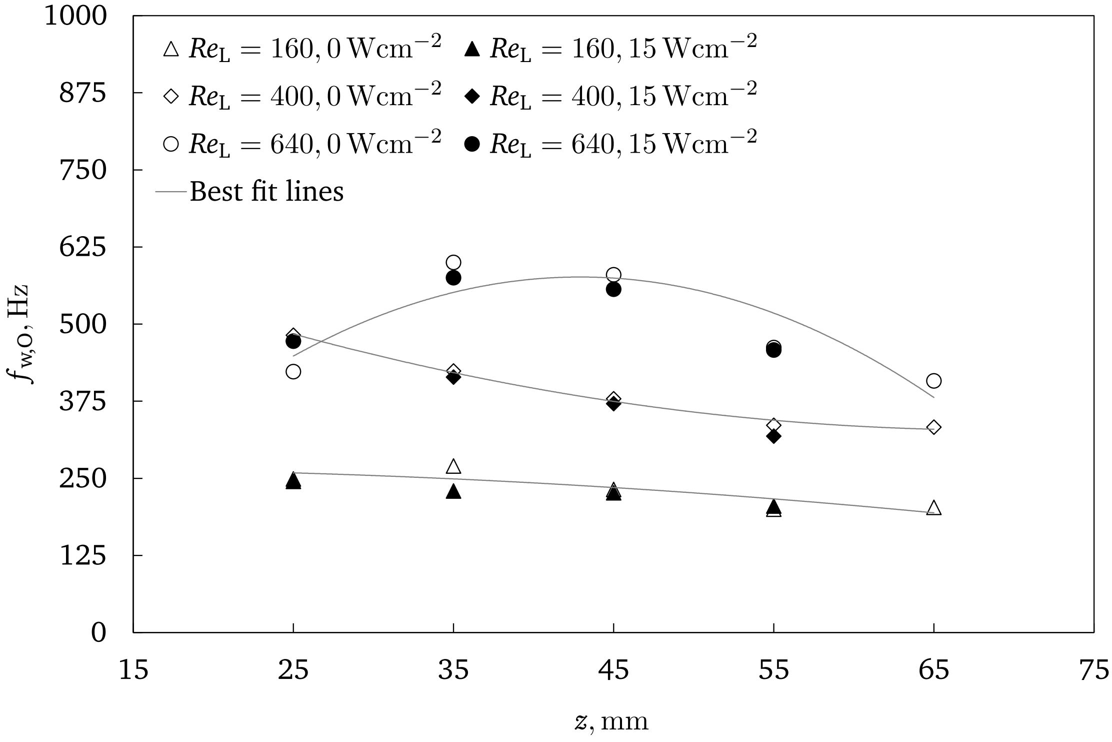

Figure 7.16. Wave frequency $f_{w,O}$ of gas-driven liquid films on the unstructured surface as a function of z for $Re_G = 10^5$, $Re_L = 160, 400, 640$, $\dot{q}_W = 0, 15\,\mathrm{Wcm^{-2}}$.

Regarding the standard deviation results, an inverse trend exists which may can be associated to the increase of liquid mass. Increase of liquid mass flow rate leads to a stabilization of the film, hence the rate of distortion is reduced [132]. However, in the case of $Re_\mathrm{L} = 640$, a maximum frequency appears at $z = 35\,\mathrm{mm}$ which is contradicts the previous explanation and disagrees to the trend of the corresponding σ_O values. Nevertheless, the high speed sequences shown in Figs. 7.17 to 7.19 exhibit no remarkable differences of the interface structure.

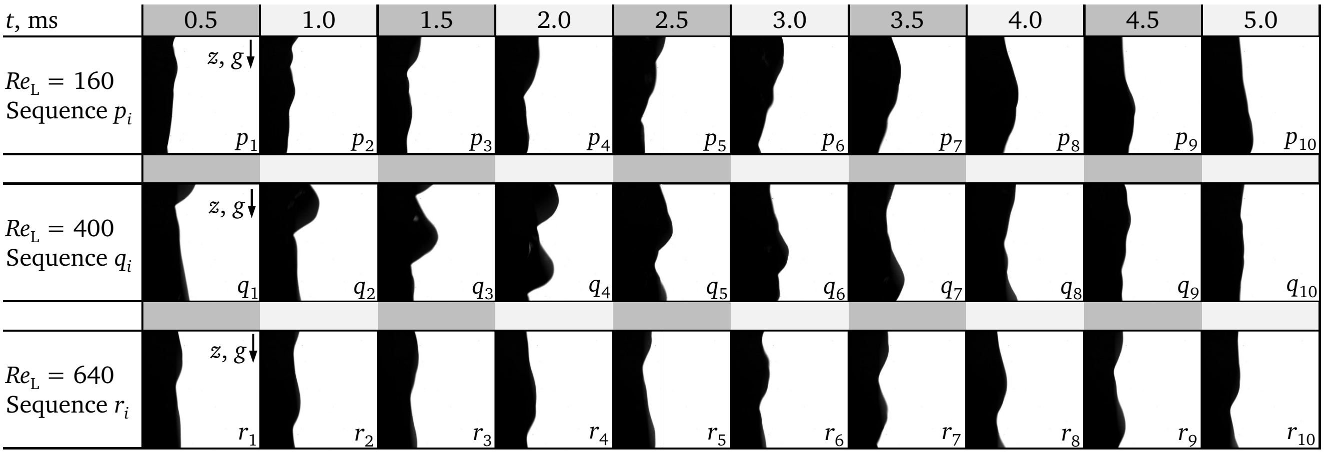

Figure 7.17. Image sequences of gas-driven liquid film flow at the unstructured surface for $Re_\mathrm{L} = 160, 400, 640$. Sequences are taken at $z = 25\,\mathrm{mm}$ with $Re_\mathrm{G} = 10^5$ and $\dot{q}_\mathrm{W} = 0$.

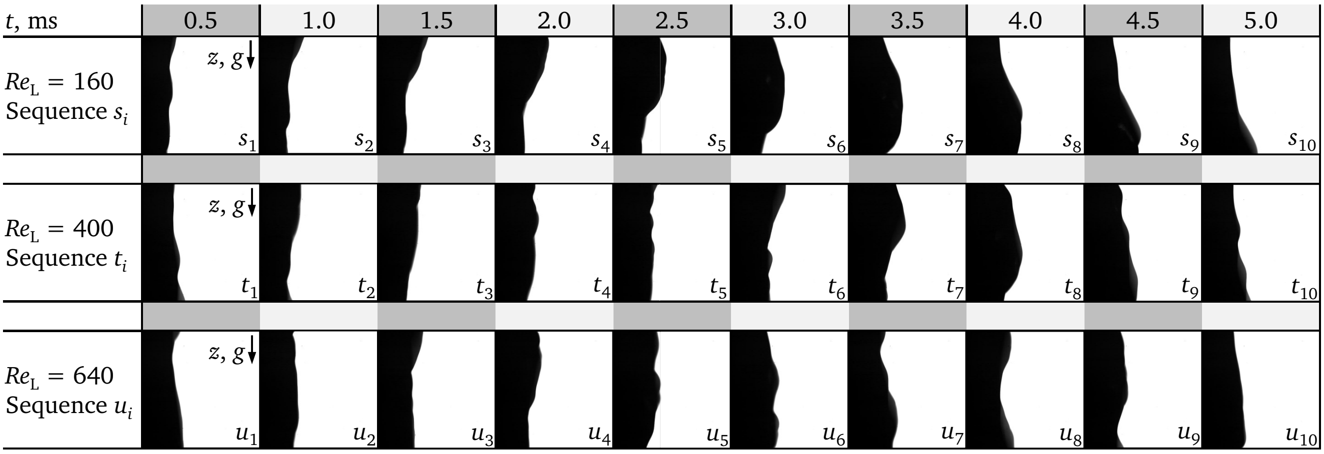

Figure 7.18. Image sequences of gas-driven liquid film flow at the unstructured surface for $Re_\mathrm{L} = 160, 400, 640$. Sequences are taken at $z = 45\,\mathrm{mm}$ with $Re_\mathrm{G} = 10^5$ and $\dot{q}_\mathrm{W} = 0$.

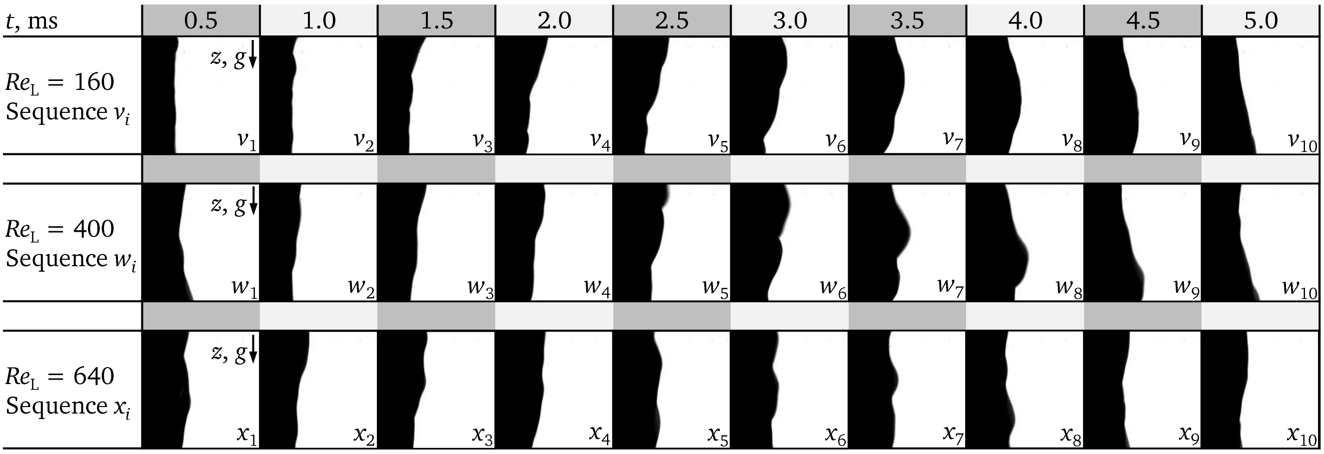

Figure 7.19. Image sequences of gas-driven liquid film flow at the unstructured surface for $Re_L = 160, 400, 640$. Sequences are taken at $z = 65\,\mathrm{mm}$ with $Re_G = 10^5$ and $\dot{q}_W = 0$.

7.1.2 Dimensionless wall temperature distribution

For the heat transfer analysis, the heat conducted axially within the copper tube has not been considered in the calculations. As far as the surface of the tube and the plug installed at the end of the tube was covered with liquid during the experiments, it can be safely assumed that the heat generated by the heating cartridge was fully transferred into the liquid film. To test this assumption, the liquid outlet temperature $T_{L,out}$ has been measured inside the drainage running falling film for $Re_L = 240 - 800$, $p_{abs} = 3\,\mathrm{bar}$ and $T_{L,in} = 278\,\mathrm{K}$. To rectify the assumption that all the heat applied at the tube surface was transferred to the liquid, a simple heat balance calculation concerning the liquid outlet temperature has been performed with

$$T_{L,out} = T_{L,in} + \frac{\dot{q}_W d_O \pi l_W}{\dot{M}_L c_{p,L}} \quad . \tag{7.1}$$

The comparison between the theoretical liquid outlet temperatures and the measured ones are presented in Figure 7.20. As the liquid Reynolds number increases the outlet temperature decreases according to the theory as well as in the experiment. The experimental results match in an rather good agreement with the theoretically predicted temperatures.

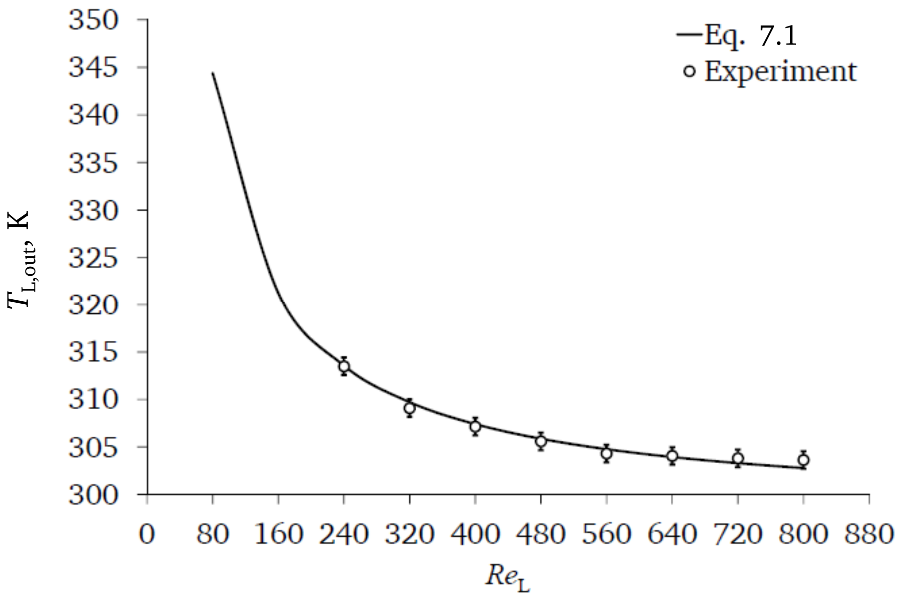

Figure 7.20. Comparison between calculated and measured outlet temperatures of falling liquid film for constant heat flux of $15\,\mathrm{Wcm^{-2}}$ and $T_{\mathrm{L,in}} = 298\,\mathrm{K}$.

Since for the falling film experiments, the temperature differences are about $\pm 0.6\,\mathrm{K}$, the above assumption is justified. In case of a gas-driven liquid film flow, measurements of $T_{\mathrm{L,out}}$ could not be performed, since the liquid film close at the inlet of the drainage was ruptured. In this condition, the measurement tip of the thermocouple was not completely covered with liquid.

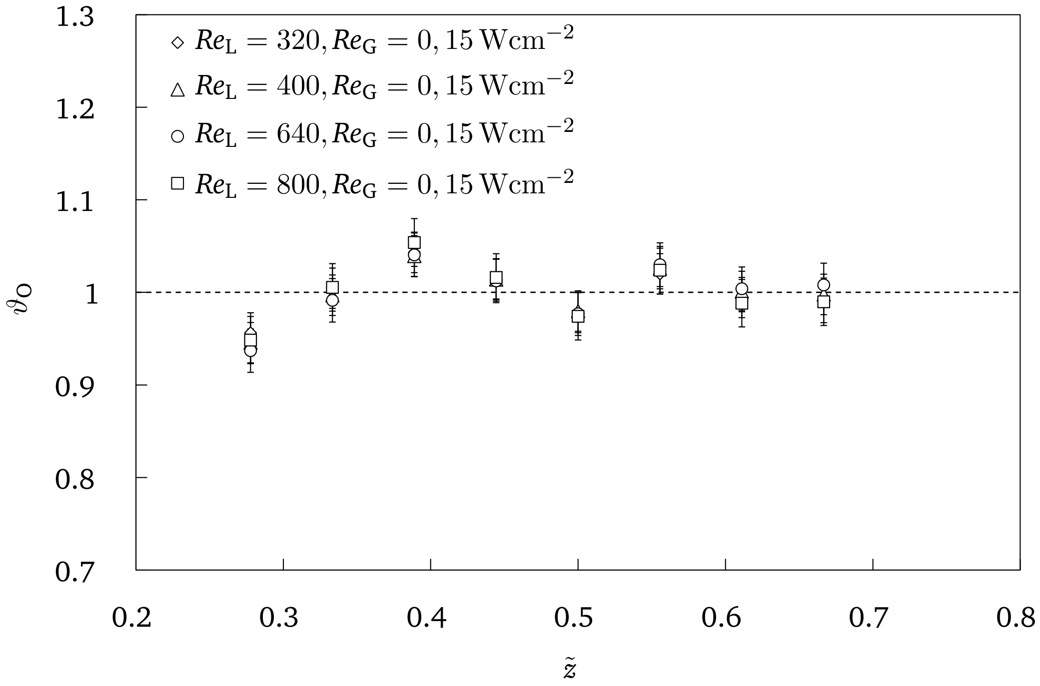

Figure 7.21. Dimensionless temperature ϑ_{O} distribution at the unstructured surface over dimensionless length $\tilde{z}$ for $Re_{\mathrm{L}} = 320, 400, 640, 800$ and $15\,\mathrm{Wcm^{-2}}$ at $Re_{\mathrm{G}} = 0$.

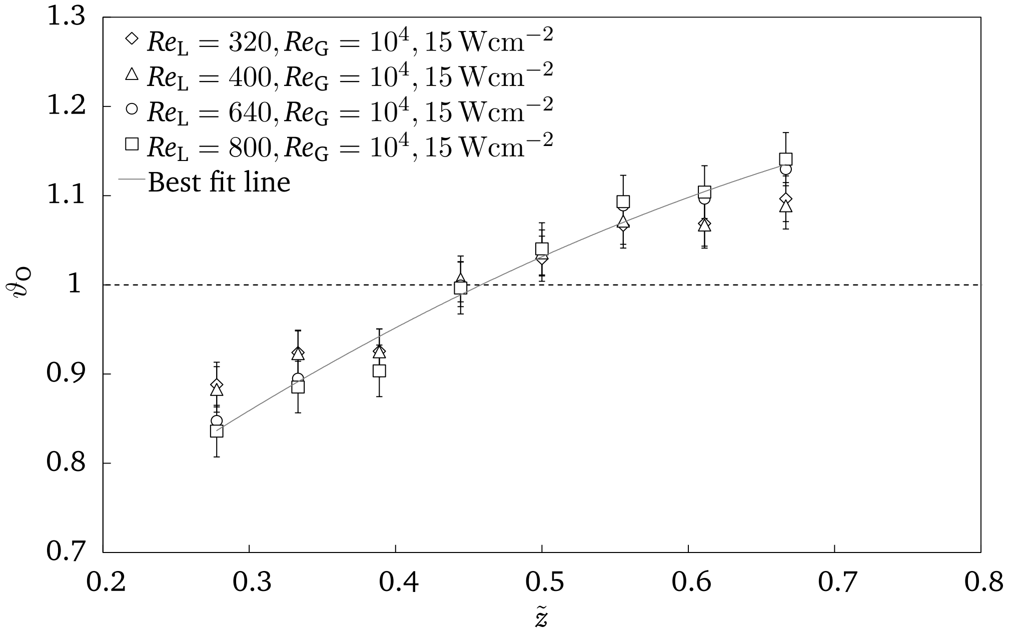

Figure 7.22. Dimensionless temperature ϑ_O distribution at the unstructured surface over dimensionless length $\tilde{z}$ for $Re_L = 320, 400, 640, 800$ and $\dot{q} = 15\,\mathrm{Wcm^{-2}}$ at $Re_G = 10^4$.

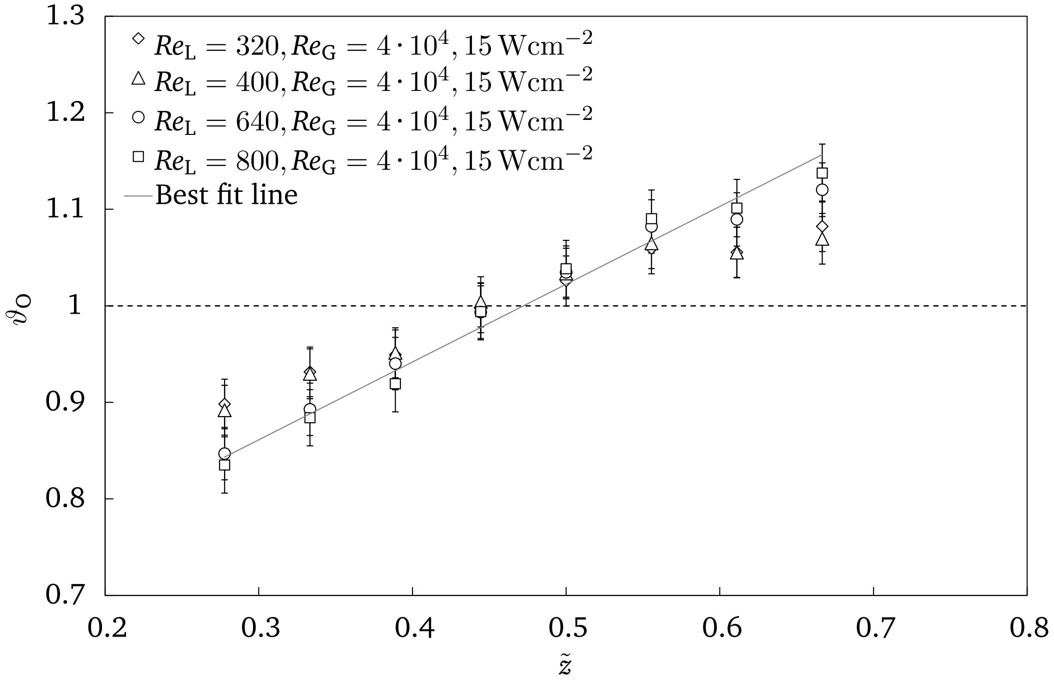

Figure 7.23. Dimensionless temperature ϑ_O distribution at the unstructured surface over dimensionless length $\tilde{z}$ for $Re_L = 320, 400, 640, 800$ and $\dot{q} = 15\,\mathrm{Wcm^{-2}}$ at $Re_G = 4 \cdot 10^4$.

In Fig. 7.21 the distribution of the dimensionless temperature ϑ_O calculated according to Eq. 7.3 at the unstructured surface is shown for a falling film. It can be seen that ϑ_O does not show a monotonous trend along the flow direction. Since boiling did not occur within the liquid film, such a non-monotonous trend is physically incorrect. Surely, this result is an experimental artifact arising due to thermocouple measurement errors such as poor thermal contact. Nevertheless, change in Re_L does not have much effect on ϑ_O, possibly.

By applying shear ($Re_{\mathrm{G}} = 10^4$ and $4 \cdot 10^4$) at the liquid film surface, the dimensionless temperature profile along the tube changes as presented in Fig. 7.22. The gradient of ϑ_{O} increases for the entire liquid Reynolds number range. In spite of the fact that in Fig. 7.23 a four times higher gas Reynolds number was adjusted, a considerable difference between the gradients cannot be distinguished. However, it seems that interfacial shear influences the thermal boundary layer development. Since the heat transfer coefficient is depending on the velocity profile dictated by the external forces such as gravity and in this case the shear stress. This can be described by force balance for a steady laminar gravity- and shear-driven film flow resulting in the velocity distribution:

$$u_{\mathrm{L}} = \frac{\rho_{\mathrm{L}} g}{{}_{\mathrm{L}}} \left(h_{\mathrm{L}} y - \frac{y^2}{2} \right) + \frac{\tau_{\mathrm{L,G}}}{{}_{\mathrm{L}}} y \quad . \tag{7.2}$$

The last term causes a higher liquid velocity while the film thickness decreases according to mass conservation.

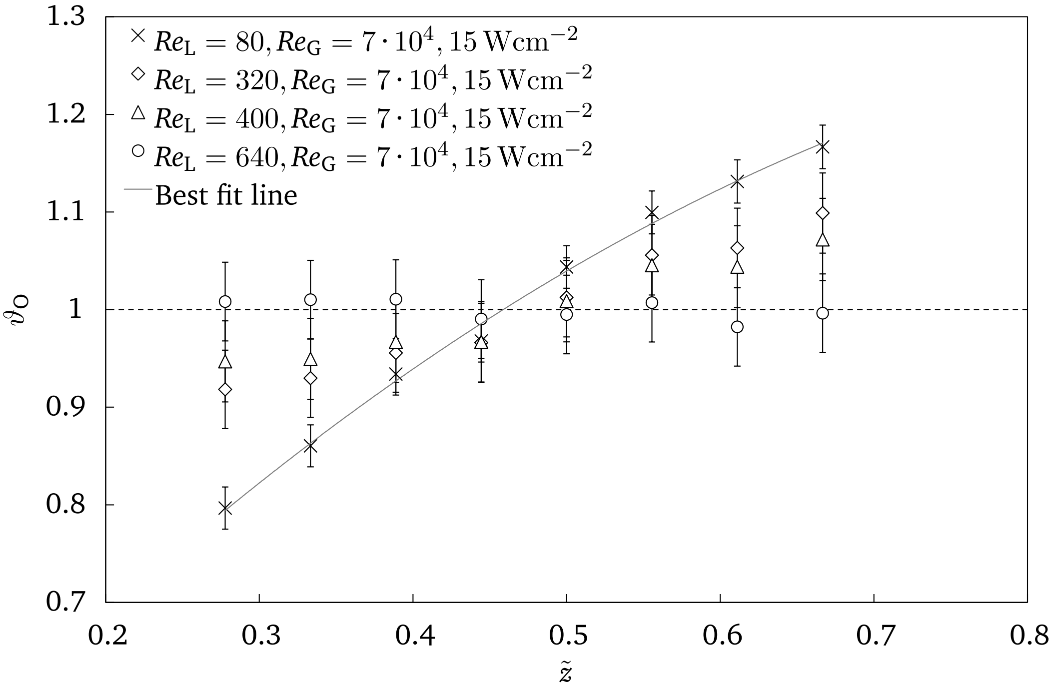

Figure 7.24. Dimensionless temperature ϑ_{O} distribution at the unstructured surface over dimensionless length $\tilde{z}$ for $Re_{\mathrm{L}} = 80, 320, 400, 640$ and $\dot{q} = 15\,\mathrm{W cm^{-2}}$ at $Re_{\mathrm{G}} = 7 \cdot 10^4$.

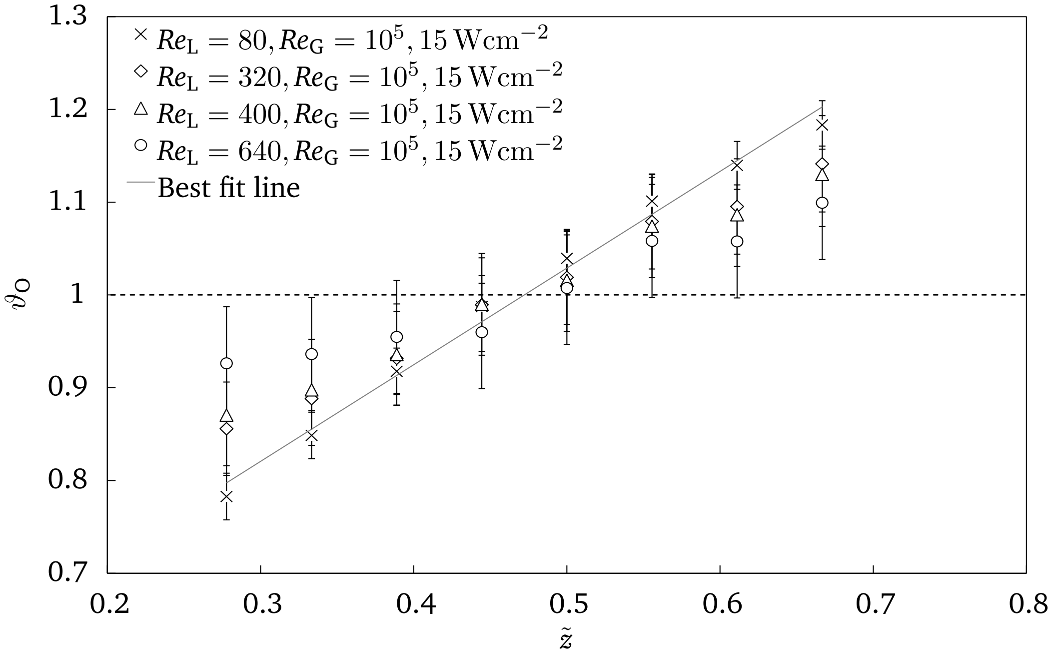

Figure 7.25. Dimensionless temperature ϑ_O distribution at the unstructured surface over dimensionless length $\tilde{z}$ for $Re_L = 80, 320, 400, 640$ and $\dot{q}_W = 15\,\mathrm{Wcm^{-2}}$ at $Re_G = 10^5$.

In Figs. 7.24 and 7.25 the $\vartheta_O(\tilde{z})$ distribution is illustrated for $Re_G = 7 \cdot 10^4$ and 10^5. Both measurement results display increasing gradients of the dimensionless temperature. A remarkable difference compared to values measured at $Re_G = 10^4$ and $4 \cdot 10^4$ is that the gradient is now stronger. This can be attributed to a higher film velocity and additionally to the formation of waves [120] (see Fig. 7.3). However, the maximum gradient takes place at the lowest liquid Reynolds number of 80. This phenomena is not similar to the measurement results displayed in Figs. 7.22 and 7.23. Therefore the governing transport mechanisms are tried to describe as follows.

As per the Fig. 7.3, a higher shear stress on the liquid film cause large amplitude waves (even roll waves) with high frequencies at low Re_L compared to the case with $Re_L = 400$ and 640. In addition, since the high amplitude waves propagate over the distance from $\tilde{z} = 0.27 - 0.72$ (see Figs. 7.10, 7.11, 7.15, and 7.16), it can be supposed that probably a internal mixing mechanism within the liquid bulk holds up almost the entire tube surface. This mechanism induce strong film thinning which promotes the permanent formation of a thin residual film called substrate film [25]. Through this thin layer of liquid, most of the heat is transferred [68]. The waves which travel over this substrate film, transport hot liquid from the wall towards the liquid-gas interface back to the region of the substrate film [32]. This mixing mechanism gives an additional contribution to the intensification of heat transfer and hence causes an enhancement of the local cooling [31, 94, 99]. The gradient of ϑ_O diminishes with larger Re_L. According to the Figs. 7.10, 7.11, 7.15, and 7.16, the mode of waviness switches to high frequent waves with small amplitudes where a suppression of the thinning effect occurs. Although waves are moving over the surface, their contribution to the increase of heat transfer by convective mixing of the liquid bulk is less [68, 148]. Furthermore, the thicker film absorbs the fluctuations which are unable to reach the wall-liquid interface region. This reflects by a reduction of local cooling and is represented by decay of the ϑ_O gradient.

7.1.3 Nusselt number

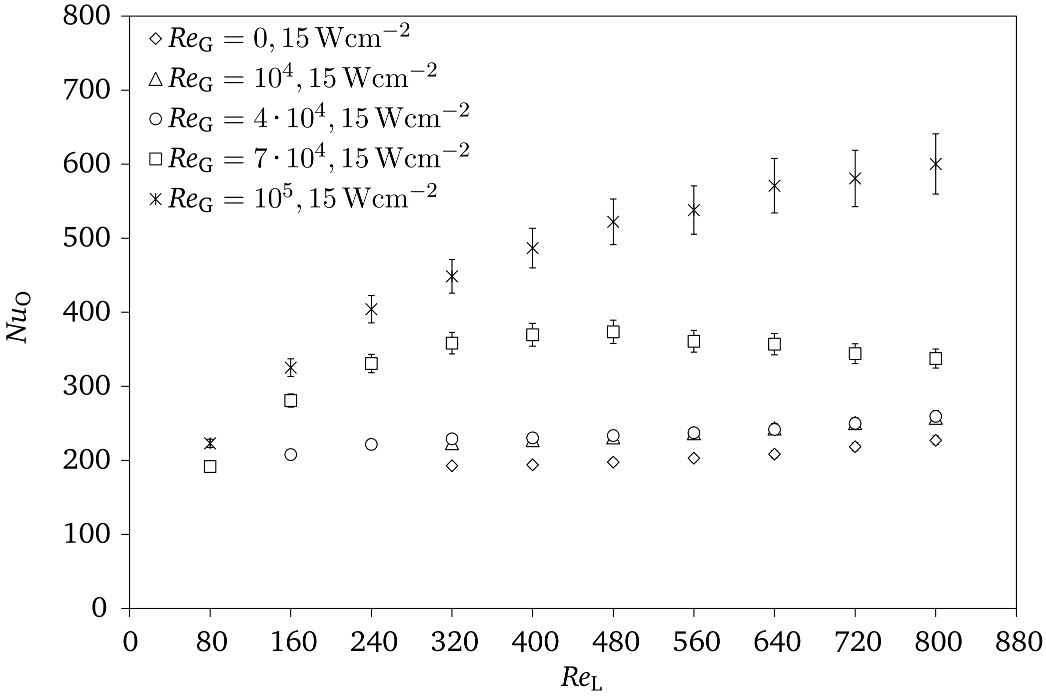

Figure 7.26. Nusselt number Nu_O for gravity- and gas-driven film flow at unstructured surface for $Re_\mathrm{L} = 80 - 800$, $Re_\mathrm{G} = 0 - 10^5$ at $\dot{q}_\mathrm{W} = 15\,\mathrm{Wcm^{-2}}$.

The Nusselt number for gravity and gas-driven liquid film flow on the unstructured surface are shown in Fig. 7.26. Some values for $Re_\mathrm{G} = 0$, 10^4, and $4 \cdot 10^4$ are not present. At these experimental conditions, film rupture occurred due to less amount of liquid. The measurement results were not evaluated as the dry wall temperature exceeded the upper bound of the thermocouple calibration range. For the rest of measurements, no film break-up happened and the measurements could be analyzed. The falling film measurements ($Re_\mathrm{G} = 0$) are taken as reference to elucidate the effect of shear stress on the heat transfer coefficient. The increase of the gas Reynolds number from 10^4 to $4 \cdot 10^4$ show a minor enhancement in heat transfer which has a linear trend. The minor intensification of heat transfer is probably associated with the acceleration of the liquid film without the formation of large waves, e.g. 2D, 3D and roll waves, at the film surface as seen in Fig. 7.27. Also, Re_L has a weak influence and leads to minor increase of the heat transfer coefficient. Further increase of Re_G resulted in a significant rise of Nu_O.

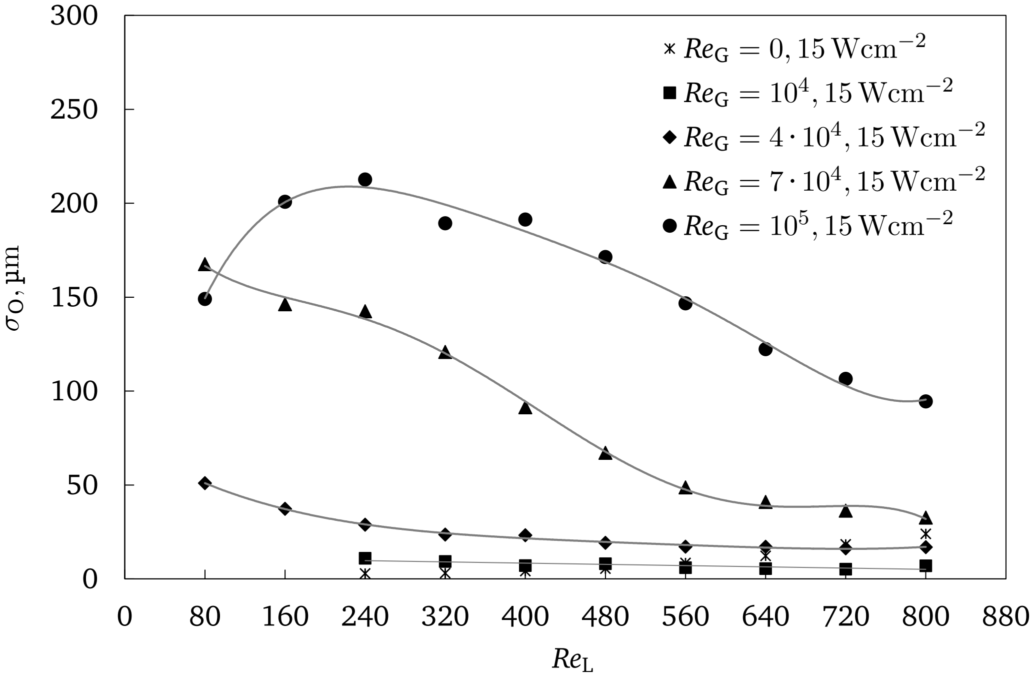

Figure 7.27. Standard deviation σ_O of gravity and gas-driven films on the unstructured surface for $Re_L = 80 - 800$, $Re_G = 0 - 10^5$ at $\dot{q}_W = 15\,\mathrm{Wcm^{-2}}$.

The initial part of increasing Nu_O at $Re_L = 7 \cdot 10^4$ can be explained with several interacting mechanisms. The liquid film is characterized by the existence of large amplitude waves, which generate a strong internal mixing and scoop hot liquid from the substrate film [94]. Periodically destructed and re-established viscous boundary layer accompanied by a skinned thermal boundary layer (Fig. 2.5a and 2.5b) will both lead to an increase in heat transfer coefficient [20]. The second part of the Nu_O development ($Re_L > 480$) is driven by a contrary mechanism where the effect of waviness seems to be reduced. The gas stream might be unable to generate large waves, due to reduction in interfacial shear stress caused by increase in inertia of the liquid film. Similar tendency is incorporated by the Nu_O development for $Re_G = 10^5$ but without a local maximum. The increase in Nu_O for lower Re_L range at $Re_G = 10^5$ is sharper than for $Re_G = 7 \cdot 10^4$ and decreases with increasing liquid mass flow rate. The higher Nusselt numbers for low liquid Reynolds numbers can be accounted for the intensified liquid bulk mixing. By comparing the corresponding σ_O profile shown in Fig. 7.26, a suppression of large waves occurs with greater Re_L. This might influence the slope of the Nu_O development, since waves with large amplitudes can have a strong effect on enhancement of heat transfer. In Fig. 7.26 it is obvious that the heat transfer coefficient decreases starting from $Re_L \sim 240 - 320$, which maybe the result by the effect mentioned before.

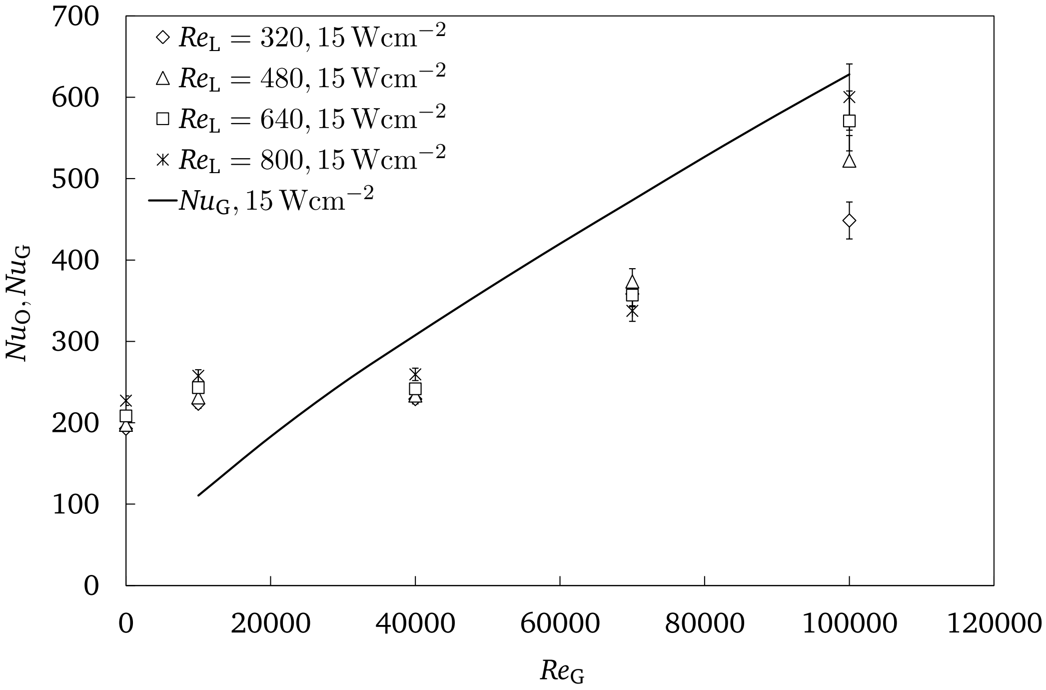

Figure 7.28. Comparison of Nusselt number Nu_O determined experimentally at the unstructured surface for $\dot{q}_W = 15\,\mathrm{Wcm}^{-2}$, varying Re_L and Re_G with Nu_G of single phase (air) flow as described in Sec. 5.1.4.

Using the theoretical approaches introduced in Sec. 5.1.4, the experimental heat transfer coefficients determined for $\dot{q}_W = 15\,\mathrm{Wcm}^{-2}$ are compared in Fig. 7.28 and Fig. 7.29. The first figure contains the validation with the Nusselt number determined with a single phase (air) flow for the same annular configuration and process parameters. It can be seen that Nu_O and Nu_G rise with increasing Re_G. For the latter, the gas velocity increases and consequently the enhancement of the convective heat transfer at the wall-gas interface enhances. Approximately up to $Re_G = 3 \cdot 10^4$ the heat transfer coefficients in the experiments for a gas-driven film is higher than $Nu_G(d_O)$. The gas phase ($Pr_G = 0.715$) is turbulently flowing with a high Re_G, the heat transfer is high. A reason for this difference could be that the definition of the Nusselt number used in this work does not include the heat transferred into the gas phase. With further increase in gas mass flow rate $Re_G > 3 \cdot 10^4$, Nu_G increases and is higher than Nu_O values. This effect reduces when increasing Re_L from 320 to 800. In this case, probably the heat transfer is enhanced through mixing within the liquid bulk. Above $Re_G = 3 \cdot 10^4$ the single phase flow values represent the maximum possible heat transfer coefficients which are by trend followed-up by Nu_O results.

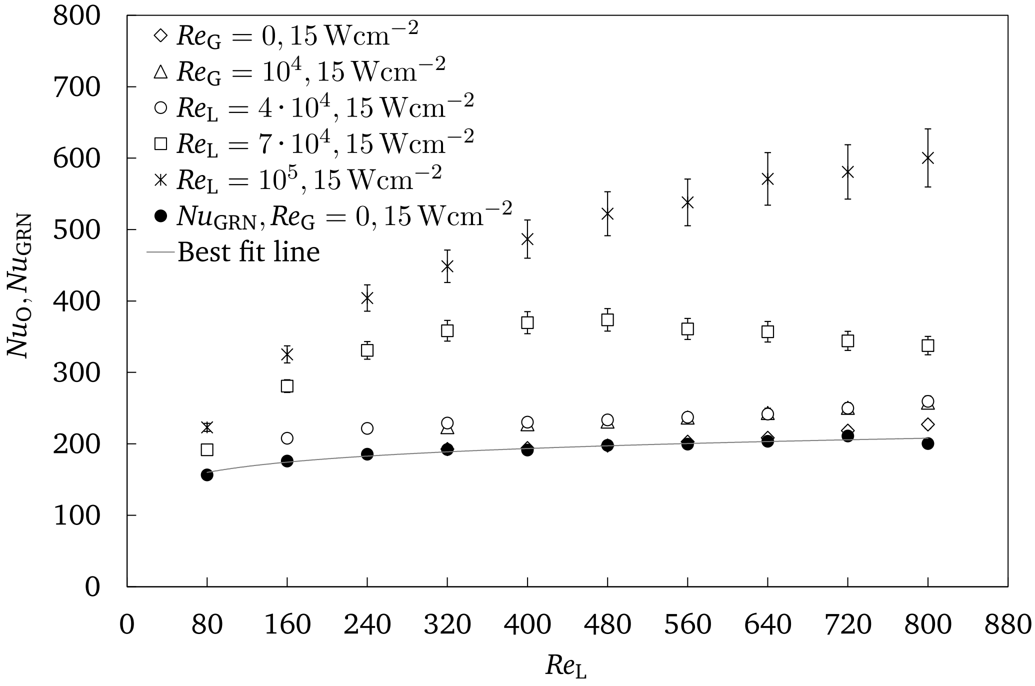

Figure 7.29. Comparison of Nusselt number Nu_{O} determined experimentally at the unstructured surface for $\dot{q}_{\mathrm{W}} = 15\,\mathrm{Wcm}^{-2}$, varying Re_{L} and Re_{G} with Nu_{GRN} of the Graetz-Nusselt model as described in Sec. 5.1.4.

The second diagram (see Fig. 7.29) illustrates the comparison of Nu_{O} with the Nusselt numbers Nu_{GRN} determined by with the Graetz-Nusselt model (see page 73ff). Each Nu_{GRN} value is calculated with the corresponding process values used for the gravity-driven film experiment. Nu_{GRN} increases with growing Re_{L}. The Nusselt number for the falling film experiment agrees well with Nu_{GRN}. The Nusselt numbers for the gas-driven film are larger than Nu_{GRN}. However, the trend of Nu_{O} for $Re_{\mathrm{G}} = 10^4$ and $4 \cdot 10^4$ is similar to that of the Graetz-Nusselt model. The large difference in heat transfer coefficients between gas-driven film and the Graetz-Nusselt model can be described by the simplifications made in the model. Nevertheless, with the comparison the lower limit for heat transfer coefficient for gas driven-films in case of decreasing the shear stress can be determined.

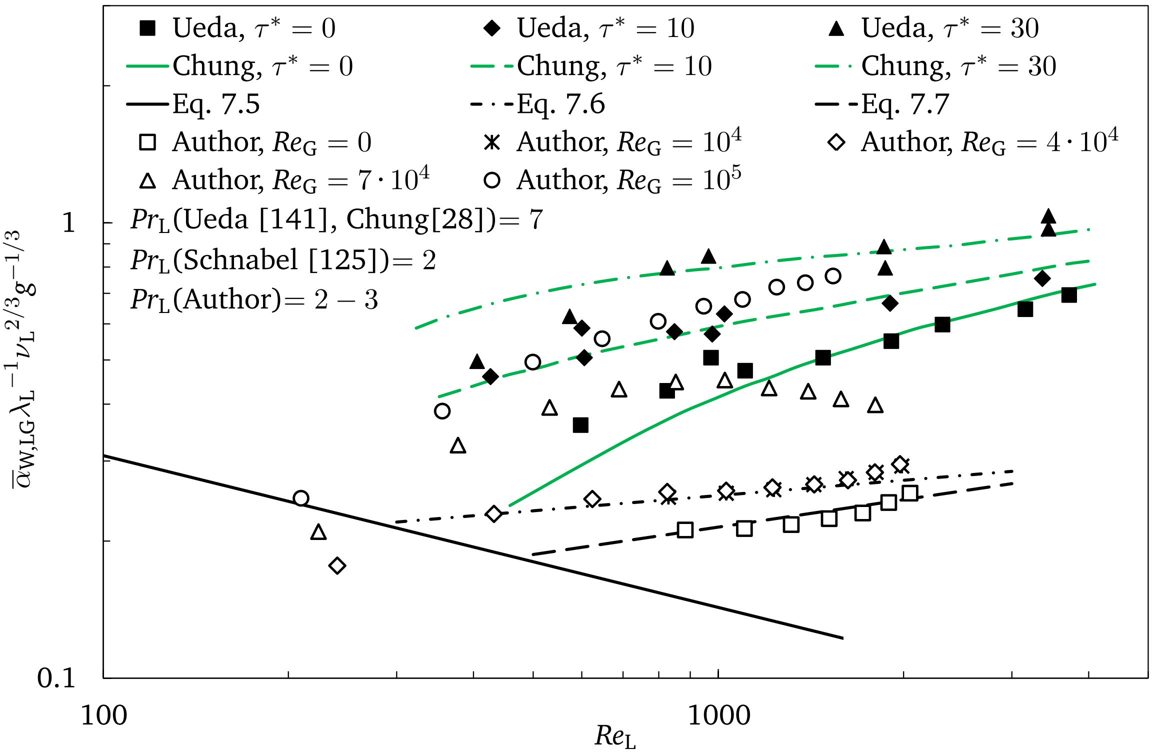

Figure 7.30. Comparison of Nusselt numbers determined experimentally at the unstructured surface for $\dot{q}_\mathrm{W} = 15\,\mathrm{W cm^{-2}}$ for varying Re_L and Re_G with the results of other authors.

To validate the effect of shear stress on the heat transfer, the experimental heat transfer coefficients are compared in a logarithmic diagram shown in Fig. 7.30 with other authors work. The experimental heat transfer coefficients $\overline{\alpha}_\mathrm{W,LG}$ for each experimental process parameter configuration are determined with the mean liquid bulk temperature

$$\overline{T}_\mathrm{L} = \frac{\overline{T}_\mathrm{W} + T_\mathrm{L,in}}{2} \quad . \tag{7.3}$$

and converted with

$$Nu^* = \frac{\overline{\alpha}_\mathrm{W,LG}}{\lambda_\mathrm{L}} \left(\frac{{\nu_\mathrm{L}}^2}{g} \right)^{\frac{1}{3}} \quad . \tag{7.4}$$

The expression ${\nu_\mathrm{L}}^{2/3} g^{-1/3}$ is designated as the viscous length scale [9]. For the comparison, the following heat transfer correlations from the work of Schnabel et al. [125] for heated gravity-driven film flows at different flow stages are taken:

The correlation

$$Nu^{*} = 1.43 {Re_{\mathrm{L}}}^{-\frac{1}{3}} \quad , \tag{7.5}$$

for hydrodynamically and thermally developed laminar film flows. The equation for film flows within the thermal entrance region described by

$$Nu^{*} = 1.1 \left({Re_{\mathrm{L}}}^{\frac{1}{3}} \frac{Pr_{\mathrm{L}}}{l_{\mathrm{hyd}}} \left(\frac{{\nu_{\mathrm{L}}}^{2}}{g} \right)^{\frac{1}{3}} \right)^{\frac{1}{3}} \quad , \tag{7.6}$$

and for film flows transiting to turbulent described by

$$Nu^{*} = 0.0425 {Re_{\mathrm{L}}}^{\frac{1}{5}} {Pr_{\mathrm{L}}}^{0.344} \quad . \tag{7.7}$$

The properties included in the Reynolds number ($\dot{M}_{\mathrm{L}}(d_{\mathrm{O}}\pi\mu_{\mathrm{L}})^{-1}$) and the Prandtl number are determined with the mean liquid bulk temperature. Furthermore, measurement data published by Ueda et al. [141] are used to validate the experimental heat transfer results. In [141], the heat transfer measurements were carried out for the developed film flow (water) in a range of $Re_{\mathrm{L}} = 46.25 - 3500$ and a developed air stream $Re_{\mathrm{G}} = 6 \cdot 10^{3} - 10^{5}$ in a $1880\,\mathrm{mm}$ long tube. The heated length was about $1300\,\mathrm{mm}$ with and area of $0.122\,\mathrm{m}^{2}$. The resulting wall heat flux was approximately equal to $4.1\,\mathrm{W cm}^{-2}$. The liquid inlet temperature was fixed at $294.15\,\mathrm{K}$. However, for the heat transfer calculation the errors are not given.

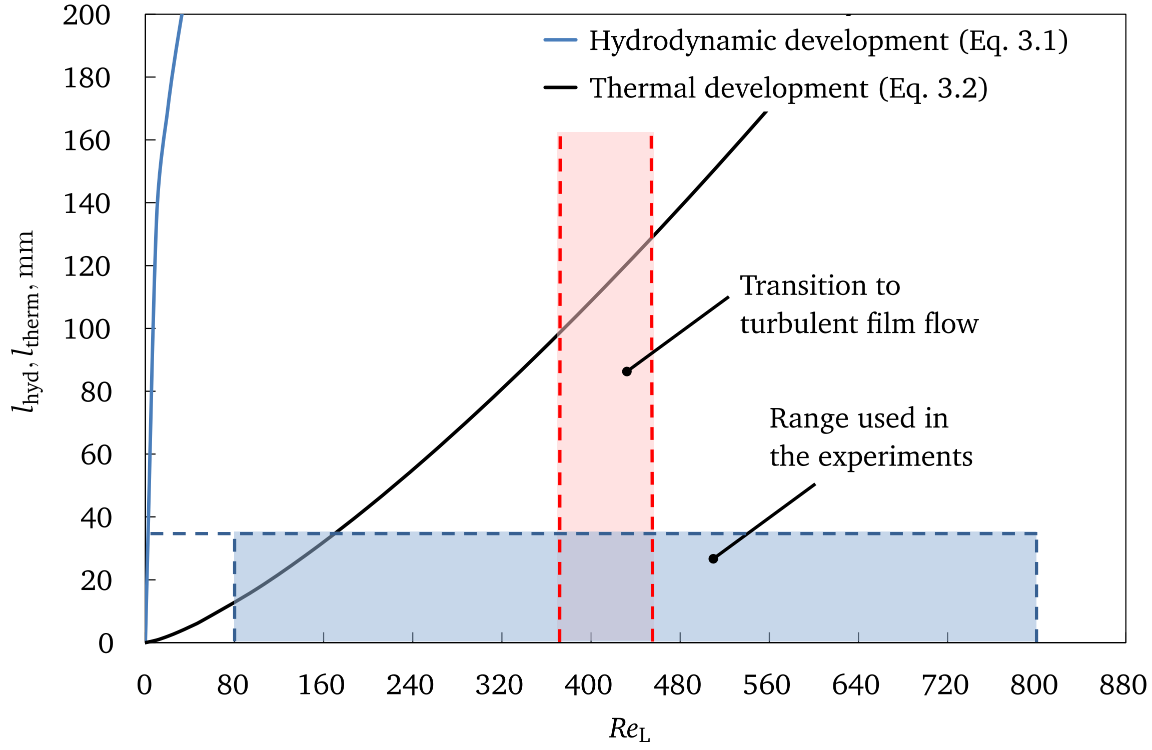

Figure 7.31. Operating regime for gravity-driven film experiment regarding hydrodynamic and thermal development length ($Pr_{\mathrm{L}} = 6.13$).

Additionally, values (green lines) determined with the turbulence model for the prediction of heat transfer coefficients in turbulent falling heated liquid films with interfacial shear developed by Chung et al. are implemented [28]. This model uses a modified version of the semi-empirical turbulence model developed by El-Masri et al. in [103] to replace the eddy viscosity model containing in the unified method suggested by Liu et al. [150]. The detailed steps of the model development will not be further introduced in this chapter and can be taken from [28].

The trend of the heat transfer coefficients determined by the author for gravity-driven and gas-driven films cannot be described with Eq. 7.5, since Nu_{O} depends also on the gas flow. This is indicates that the liquid film flow is neither hydrodynamically nor thermally developed. However, three Nu^* values are below or at the curve defined by Eq. 7.5. Probably these flow conditions are representing a laminar, thermally and hydrodynamically fully developed stage. By analyzing the gravity-driven results, rather good agreement with the correlation described by Eq. 7.7 can be seen. Since this equation is used for the heat transfer calculations for films falling in the transition region region, it can be assumed that this is also valid for the experiment. According to the investigations of Ishigai et al., McAdams, Rohsenow et al., Yüksel et al., the transition from laminar to turbulent gravity-driven film occurs in the range $Re_{\mathrm{L}} = 400 - 450$ [66, 95, 120, 153]. This transition Reynolds number range increases with decreasing Pr_{L} as reported by Mostofizadeh et al. in [101].

Another comparison between the heat transfer results for the gas-driven films and the literature data is displayed for the measurements at $Re_{\mathrm{G}} = 10^4$ and $4 \cdot 10^4$ which follow the Nu^* development predicted by Eq. 7.6 for thermal entrance. As discussed previously, the application of shear stress at the liquid film surface influences the thermo-hydraulic boundary layer development within the liquid bulk. For the liquid Reynolds number range considered in this work, this type of liquid film flow seems to develop hydrodynamically and thermally. The heated length in this work was $l_{\mathrm{W}} = 0.09\,\mathrm{m}$, while the considered hydraulic length $l_{\mathrm{hyd}} = 0.035\,\mathrm{m}$. According to the Eqs. 3.1 and 3.2 (see Fig. 7.31) and the $Re_{\mathrm{L}} = 80 - 800$ (respectively $Re_{\mathrm{L}} = 240 - 1988$ with regard to Fig. 7.30), the gas-driven film first propagates only in the hydrodynamic development regime then with $Re_{\mathrm{L}} > 160$ the thermal boundary layer also develops. Hence the film flows within the thermal entrance regime.

In the case of the heat transfer coefficients for $Re_{\mathrm{G}} = 7 \cdot 10^4$ and 10^5, none of them follow the trend described by the Eqs. 7.5. Moreover, they show a behavior similar to those of the measured values from Ueda et al. and develop according to the prediction proposed by Chung et al. . Ueda et al. have investigated hydrodynamics and heat transfer in a liquid film driven downward by a gas stream. They determined the shear stress $\tau_{\mathrm{L,G}}$ at the liquid-gas interface using momentum equations for the liquid film and the gas core, and measured also the pressure drop over the tube length. The shear stress calculated for the particular gas mass flow rates were then non-dimensionalized through

$$\tau^* = \frac{\tau_{\mathrm{L,G}}}{\rho_{\mathrm{L}} g} \left(\frac{g}{{\nu_{\mathrm{L}}}^2} \right)^{\frac{1}{3}} \quad . \tag{7.8}$$

The Nu^* values for $Re_{\mathrm{G}} = 0, 10^4$, and $4 \cdot 10^4$ lie below the falling film measurements according to [141], since the Prandtl number in the present work was smaller. At $Re_{\mathrm{G}} = 7 \cdot 10^4$ the heat transfer coefficients measured in by the author first develop with an increasing trend between the gas-driven film measurements $\tau^* = 0$ and $\tau^* = 10$ performed by Ueda et al. However, for $Re_L > 1025$ a decay can be identified which is probably the result of the transition from wavy liquid film to a film with a smooth surface (see Fig. 7.27.

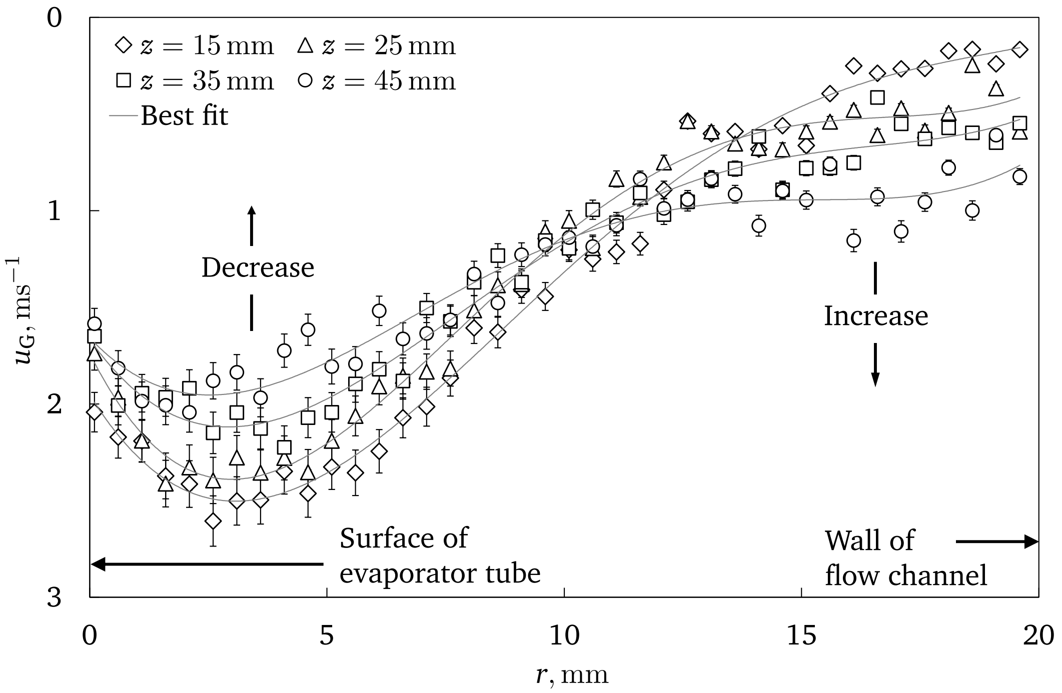

Figure 7.32. Radial distribution of gas velocities u_G at varying axial distances z at $Re_G = 10^4$.

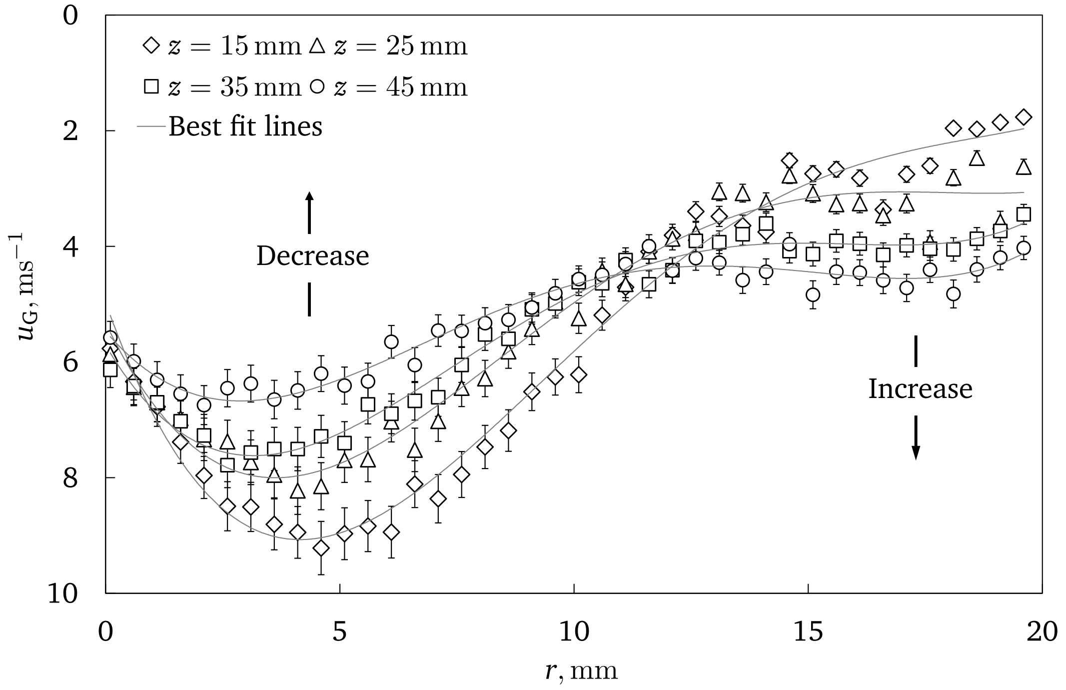

Figure 7.33. Radial distribution of gas velocities u_G at varying axial distances z at $Re_G = 4 \cdot 10^4$.

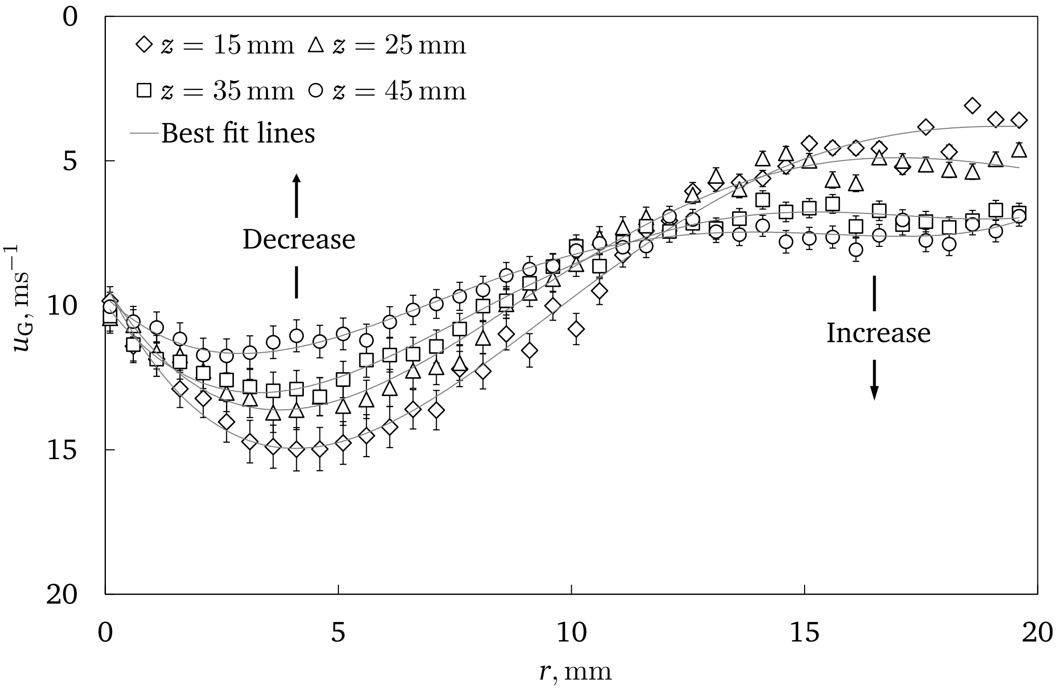

Figure 7.34. Radial distribution of gas velocities u_G at varying axial distances z at $Re_\mathrm{G} = 7 \cdot 10^4$.

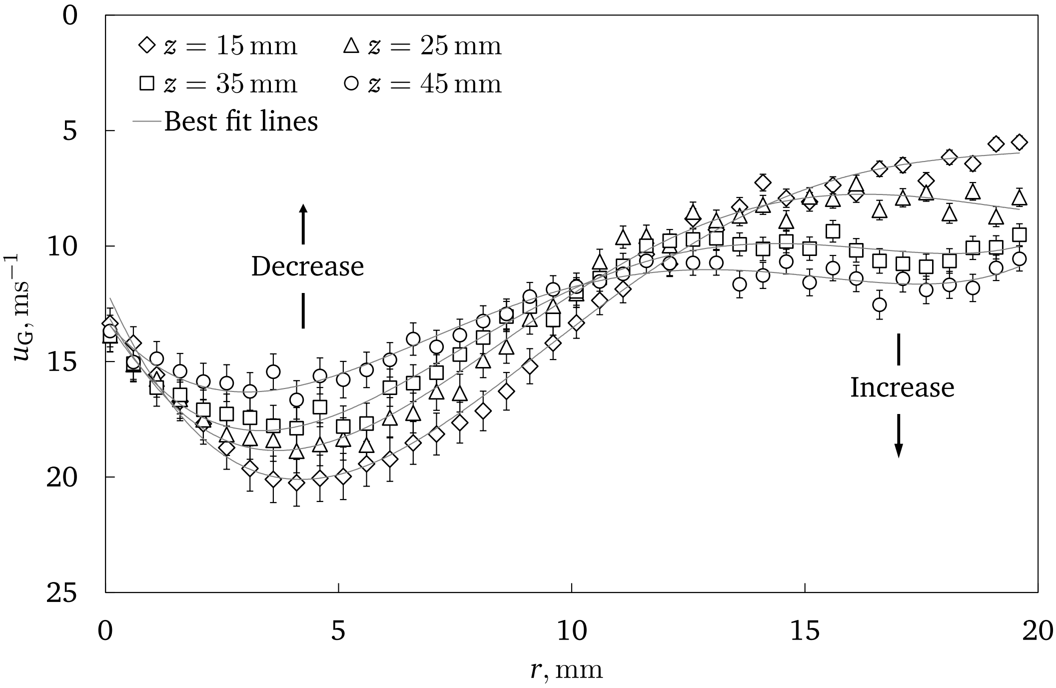

Figure 7.35. Radial distribution of gas velocities u_G at varying axial distances z at $Re_\mathrm{G} = 10^5$.

The decrease tendentiously develop toward the Nu^* values for $Re_\mathrm{G} = 4 \cdot 10^4$ and tends to change into the thermal entrance flow state. The heat transfer coefficients measured at $Re_\mathrm{G} = 10^5$ in this work increase according to the theoretical model of Chung et al. for $\tau^* = 10$. The values are even larger from $Re_\mathrm{L} = 500$ onward and gradually converge to the theoretical prediction for $\tau^* = 30$. To make a justification, to which dimensionless shear stress the experimentally determined heat transfer coefficients for $Re_\mathrm{G} = 7 \cdot 10^4$ and 10^5 correspond, the gas velocity measurements were analyzed as follows.

The Figs. 7.32, 7.33, 7.34, and 7.35 show the axial gas velocity profiles for $Re_\mathrm{G} = 10^4 - 10^5$ measured at the unheated pyramid surface without liquid film flow. For all experimental flow parameters, an asymmetry of the velocity profiles exist. This can be attributed to the flow straightener positioned at about $z = -25\,\mathrm{mm}$ upstream from the liquid outlet. Although the aerodynamics within the flow channel including the flow straightener have been simulated with CFD, large diversion from the CAD-model might have occurred during the manufacturing with the laser sintering machine. A well defined velocity profile such as a parabolic one would be appropriate for the validation of the gas-driven film flows simulated numerically. However, since the velocity gradient at the wall-gas interface will be used for the analysis of the shear stress later, less significance to the profile asymmetry has been given. With increasing gas mass flow rate the local gas velocity measured increase, hence the velocity gradients rise as well. The maximum velocity for each Re_G displaces radially and decreases axially over the measurement location from $z = 15\,\mathrm{mm}$ to $z = 45\,\mathrm{mm}$ as listed in Tab. 7.1.

Table 7.1. Radial displacement and rate of decrease of the maximum gas velocities measured with HWA for $Re_\mathrm{G} = 10^4 - 10^5$.

Re_G	Δr	Δu_G
10^4	$1.0\,\mathrm{mm}$	$0.583\,\mathrm{ms}^{-1}$
$4 \cdot 10^4$	$2.0\,\mathrm{mm}$	$2.76\,\mathrm{ms}^{-1}$
$7 \cdot 10^4$	$1.5\,\mathrm{mm}$	$3.23\,\mathrm{ms}^{-1}$
10^5	$1.0\,\mathrm{mm}$	$3.96\,\mathrm{ms}^{-1}$

Furthermore, all Re_G gas velocity profiles show an increasing trend in the region close to the wall of the flow channel. It can be said, that over the flow direction a balancing of the velocity profiles happens indicating a development of the flow domain. The axial reduction of the maximum velocities can be based on the momentum transfer to the side walls through friction. Hereby strong friction could have happened through the pyramid structured surface while the flow channel wall was ideally smooth. Exemplary, the velocity profiles for varying Reynolds numbers of gas are shown in Fig. 7.36. Starting from $r = 0\,\mathrm{mm}$, the velocities increase for all Re_G up to the position $r = 4.1 - 4.6\,\mathrm{mm}$ and decays further towards the channel wall at $r = 20\,\mathrm{mm}$. Since the molecules at the walls do not move according to the no slip condition, the velocities at $r = 0\,\mathrm{mm}$ and $r = 20\,\mathrm{mm}$ should equal to zero. As per the definition in Eq. 5.68, the shear stress at the dry wall can be strongly affected by the choice of the ratio between gas velocity and the radial distance of the measurement point from the wall. To show the difference in the resulting shear stress values, the radial locations (see Fig. 7.36)

- $\partial r_{1\text{-}0} = 0.1 - 0\,\mathrm{mm}$ (colored in red)
- and $\partial r_{2\text{-}0} = 0.6 - 0\,\mathrm{mm}$ with $r_0 = 0\,\mathrm{mm}$ (colored in blue)

together with their corresponding velocities have been considered. The maximum shear stress exist at the first measurement point close to the wall (see Tab. 7.2). However, since at the wall the no slip condition is valid and the gas velocity is zero, the actual shear stress at the wall-gas interface is probably much higher and could not be resolved appropriately with the HWA. Indeed, the local gas velocity increases as the hot-wire probe has been moved away from the wall, yet the shear stress reduces due to the decrease of $\partial u_{\mathrm{G}}/\partial r$. For further examination, it has been compromised that the local velocities measured at $r = 0.1\,\mathrm{mm}$ should be taken into the calculations for the shear stress determination.

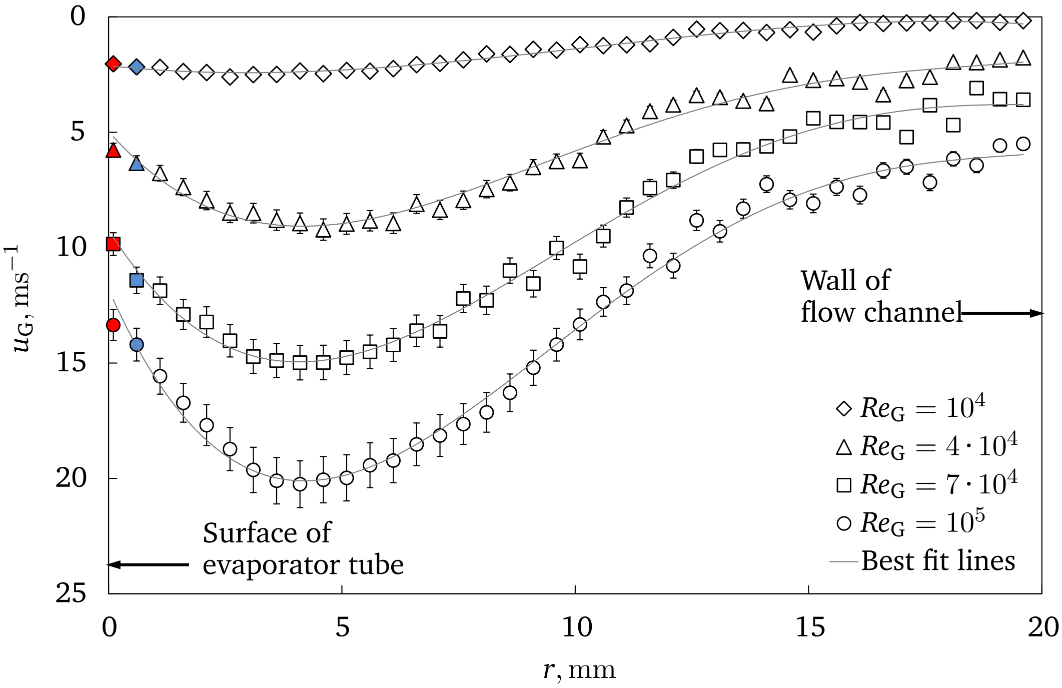

Figure 7.36. Gas velocity profiles measured at the unheated pyramid surface without liquid film flow an axial distance of $z = 15\,\mathrm{mm}$ for varying Re_{G} plotted over the radial coordinate. Velocity values at $r = 0.1\,\mathrm{mm}$ and $r = 0.6\,\mathrm{mm}$ are colored in red and blue, respectively.

Table 7.2. Shear stress $\tau_{\mathrm{W,G}}$ calculated for gas flow velocities measured at $z = 15\,\mathrm{mm}$ for varying Re_{G}.

	$Re_{\mathbf{G}} = 10^4$	$Re_{\mathbf{G}} = 4 \cdot 10^4$	$Re_{\mathbf{G}} = 7 \cdot 10^4$	$Re_{\mathbf{G}} = 10^5$
Radial location	$\tau_{\mathbf{W,G}}$, Nm^{-2}			
$\partial r_{1\text{-}0}$	0.373	1.053	1.798	2.437
$\partial r_{2\text{-}0}$	0.066	0.193	0.347	0.432

In Fig. 7.37 the axial development of the experimentally determined shear stress $\tau_{\mathrm{W,G}}$ is plotted for varying Re_{G} and z. Over the contemplated flow length, for all gas mass flow rates $\tau_{\mathrm{W,G}}$ remains rather constant and rises with increasing Re_{G}. As far as the tube wall does not move, these values can be expected to be smaller, since the liquid film surface is propagating. This cause a decrease of the velocity gradient at the liquid-gas interface and hence a reduction of the interfacial shear stress.

The experimental shear stresses brought into dimensionless form are listed in Tab. 7.3. Here, the density and kinematic viscosity of liquid were taken at $p_{\mathrm{abs}} = 3\,\mathrm{bar}$ and $T_{\mathrm{L,in}} = 298.15\,\mathrm{K}$. While for the heat transfer measurements at $Re_{\mathrm{G}} = 10^5$ a dimensionless shear stress of $10 - 12$ is expected, the calculated one is about $50\,\%$ smaller.

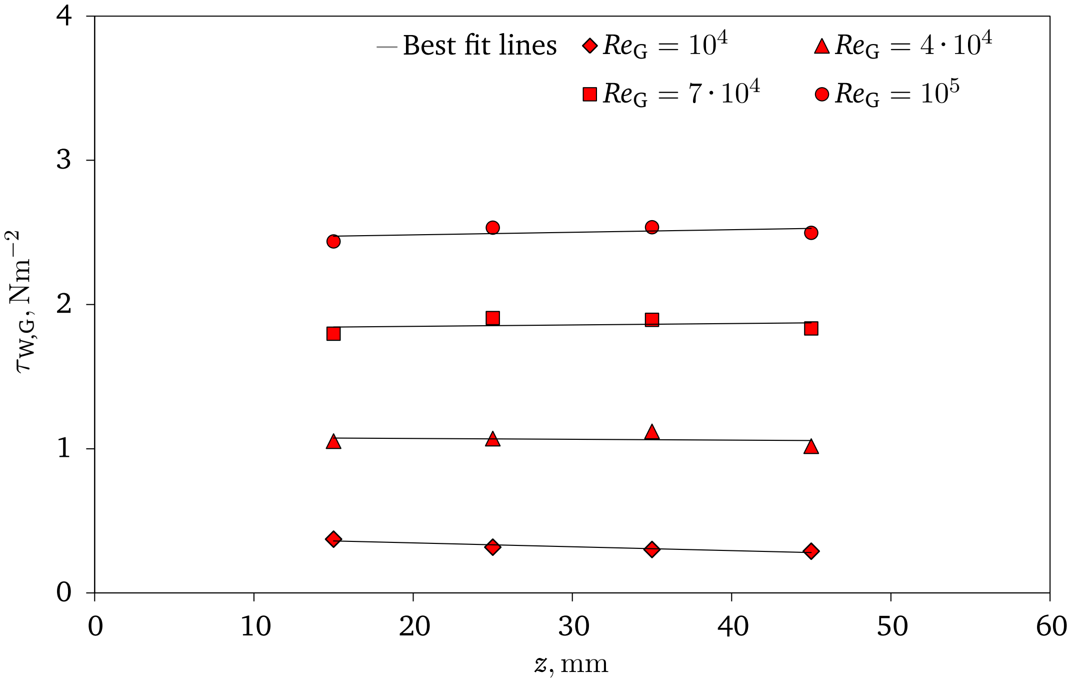

Figure 7.37. Development of $\tau_{W,G}$ determined with gas velocities measured at fixed $r = 0.1\,\mathrm{mm}$ for varying Re_G and z.

One reason for that could be the gas velocity measurements carried out with the hot wire anemometer. Since the hot wire probe was perpendicularly oriented to the tube axis and was immersed radially into the flow channel, the gas flow field could be disturbed unintentionally. Furthermore, at the measuring tip of the hot wire probe, the boundary layer could not be resolved due to the cylindrical shape of the tube. Normally, a flat surface would be an appropriate geometry where a 2D velocity profile is provided in a rectangular channel. In addition, a bifurcated hot wire probe should have been used to minimize the disturbance of the gas flow field.

Table 7.3. Dimensionless shear stress τ^* calculated for gas flow velocities measured averaged over $z = 15\,\mathrm{mm}$ to $45\,\mathrm{mm}$ for varying Re_G.

	$Re_G = 10^4$	$Re_G = 4 \cdot 10^4$	$Re_G = 7 \cdot 10^4$	$Re_G = 10^5$
τ^*	0.88	2.49	4.24	5.75

Another conspicuous result of the comparison with literature are the intersection points of the Nu^* values from the experiments ($Re_G = 4 \cdot 10^4 - 10^5$) with the heat transfer coefficients described by Eq. 7.5 for hydrodynamically and thermally developed gravity-driven films (see Fig. 7.38). The intersection point moves towards decreasing Re_L with increasing τ^*. In the literature the critical Reynolds number at which a falling film transfers from laminar to turbulent flow is reported to be $Re_{L,crit} = 350 - 450$. In this case, when shear is applied on the film surface $Re_{L,crit}$ decreases and an early transition to turbulent flow occurs. This leads to an enhancement of heat transfer which can be attributed to the early onset of instabilities and deformations, which lead to the generation of waves. The latter disturb the thermo-hydrodynamic boundary layers and cause intensification of hot-cold liquid exchange represented as eddies within the bulk liquid. The velocity profile at this stage cannot be simply contemplated with straight path lines or linear velocity profiles as usual in classical theoretical models.

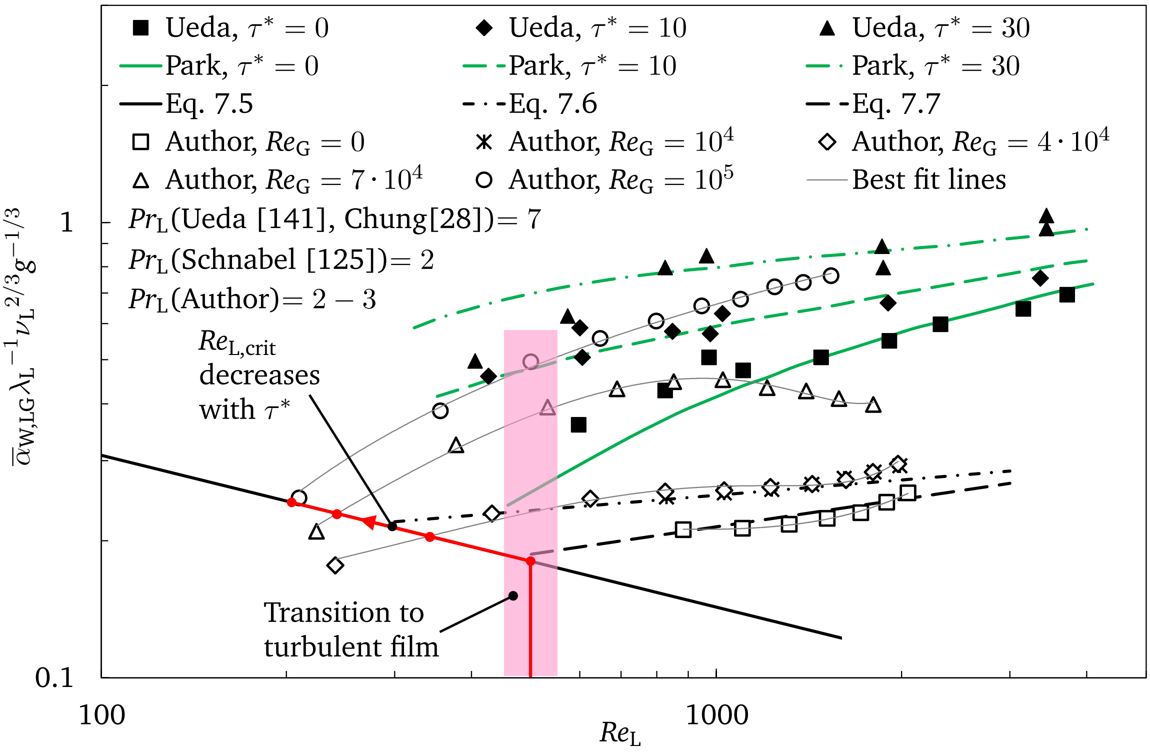

Figure 7.38. Influence of shear stress on the critical liquid Reynolds number for transition from laminar to turbulent film flow.

In Fig. 7.39 the developed correlations are compared with the exerperimental Nusselt numbers. During the development of the correlations, it has been recognized that with a single equation the experimental data cannot be re-calculated. Therefore the area of validity has been divided into $Re_G = 10^4 - 4 \cdot 10^4$ and $Re_G = 7 \cdot 10^4 - 10^5$. The coefficients and exponents of the correlations are presented in Tab. 7.4. Admittedly, the correlations are developed based only on liquid and gas Reynolds number and do not contain the relation to Prandtl number of each fluid. Furthermore the rest of the influencing parameter as determined in Sec. 5.1.3 are also not included as input term. All of these fluid properties and geometric dimensions are considered in the coefficients $a_{C1} = 100$ and $a_{C2} = 0.0004$, respectively. The calculations with the correlation Nu_{C1} show a rather good agreement with the experimental results.

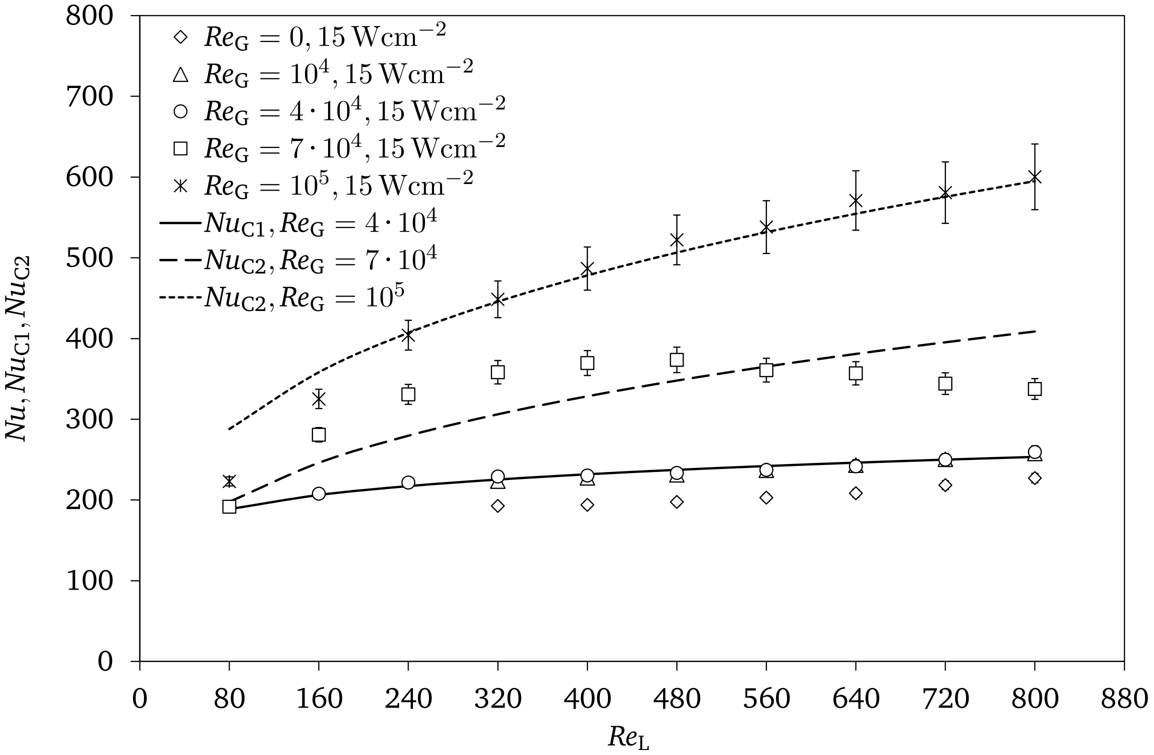

Figure 7.39. Comparison of Nusselt numbers determined through the correlations developed for the unstructured surface measurements in this work with experimental results for $\dot{q}_W = 15\,\mathrm{Wcm^{-2}}$, varying Re_L and Re_G at $T_{L,in} = 298\,\mathrm{K}$.

Through the exponents $b_{C1} = 0.128$ and $c_{C1} = 0.007$ in equation Nu_{C1} in can be seen that the liquid Reynolds number is the governing parameter in this case while Re_G has a minor impact on the values. Contrary, with Nu_{C2} only the trend of the Nusselt numbers for $Re_G = 7 \cdot 10^4$ can be reconstructed. However, the deviation is due to the transition of the liquid film from a wavy into a smooth one. This effect is not considered in the equation. Furthermore the effect of changing fluid properties is also not taken in account. At $Re_G = 10^5$ the correlation Nu_{C2} agrees rather good for the range $Re_L = 240 - 800$. However, at lower liquid Reynolds numbers a disagreement exists. Again here the strong waviness probably cannot be reconstructed by the correlation.

Table 7.4. Developed correlations for the Nusselt number calculation of gas-driven films flowing downwards a heated wall.

	Re_G range	
Nu_{C1}	$Re_G = 10^4 - 4 \cdot 10^4$	$100 Re_L^{0.128} Re_G^{0.007}$
Nu_{C2}	$Re_G = 7 \cdot 10^4 - 10^5$	$0.0004 Re_L^{0.315} Re_G^{1.053}$

The exponents $b_{C2} = 0.315$ and $c_{C2} = 1.053$ reveal that for these kind of film flow Re_G has a the major influence compared to Re_L.

7.2 Gas-driven film flow on micro-structured surfaces: influence of wall topography

7.2.1 Film waviness at ∇-grooved surface

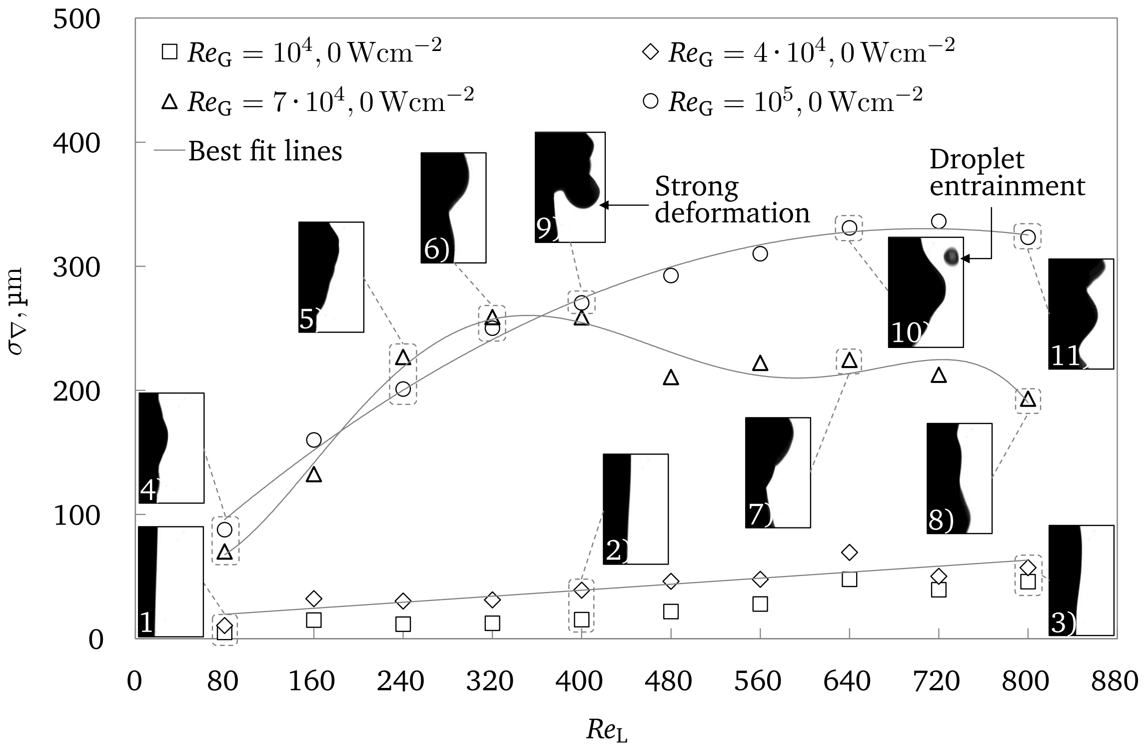

Figure 7.40. Standard deviation σ_∇ of gas-driven liquid films at the ∇-grooved surface with exemplary chosen images of characteristic liquid-gas interfacial structures showing smooth interface, strong deformations, and droplet entrainment. Experimental parameters are $Re_L = 80-800$, $Re_G = 10^4 - 10^5$ at $\dot{q}_W = 0$.

At low Re_L a partial wetting can occur as described in Sec. 3.4.1. For these conditions the liquid-gas interface propagating within the micro-groove through and is not appearing in the high-speed images. This has to be taken in account during the argumentation of the following figures. In Fig. 7.40 the standard deviation σ_∇ of the film thickness of unheated liquid film flowing on the ∇-grooved surface is displayed for varying gas and liquid mass flow rates at $z = 45\,\mathrm{mm}$.

For the gas flow at $Re_G = 10^4$ and $Re_G = 4 \cdot 10^4$, σ_∇ shows a minor increases with rising $\tau_{L,G}$ and Re_L. The development with liquid mass flow rate follows a linear trend. The film surface seem apparently smooth without any disturbances (see inserts 1, 2, and 3). The shear stress at the liquid-gas interface might be weak to deform the liquid film and generate large waves. At $Re_G = 7 \cdot 10^4$ a significant rise in standard deviation appears with a large gradient for $Re_L = 80 - 240$ and a maximum at $Re_L = 320$ (see inserts 4, 5, and 6). The shear stress now overcomes the inertial forces of the liquid film and leads to the formation of an interface incorporating 2D and 3D waves [70, 91]. The liquid mass is pushed out of the structure trough and accelerated towards the tube end. Higher liquid mass flow rate leads to a slight decay of σ_∇ where the deformations are slowly damped [70] but still visible (see inserts 7 and 8).

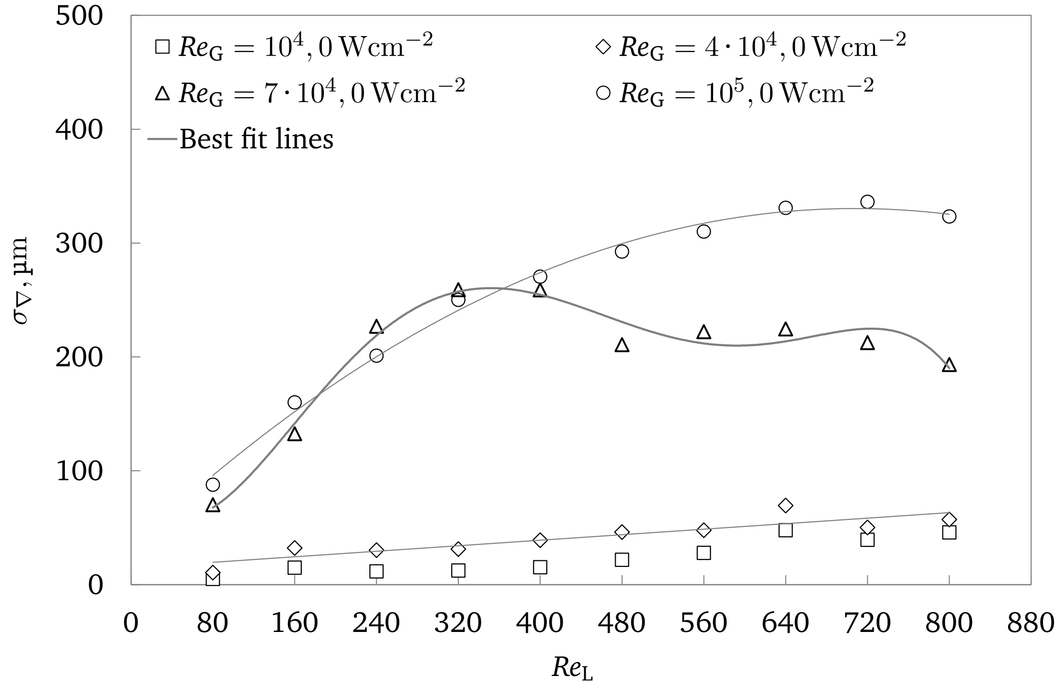

Figure 7.41. Standard deviation σ_∇ of gas-driven liquid films at ∇-grooved surface recorded at $z = 45\,\mathrm{mm}$ for $Re_L = 80 - 800$, $Re_G = 10^4 - 10^5$, $\dot{q}_W = 0$.

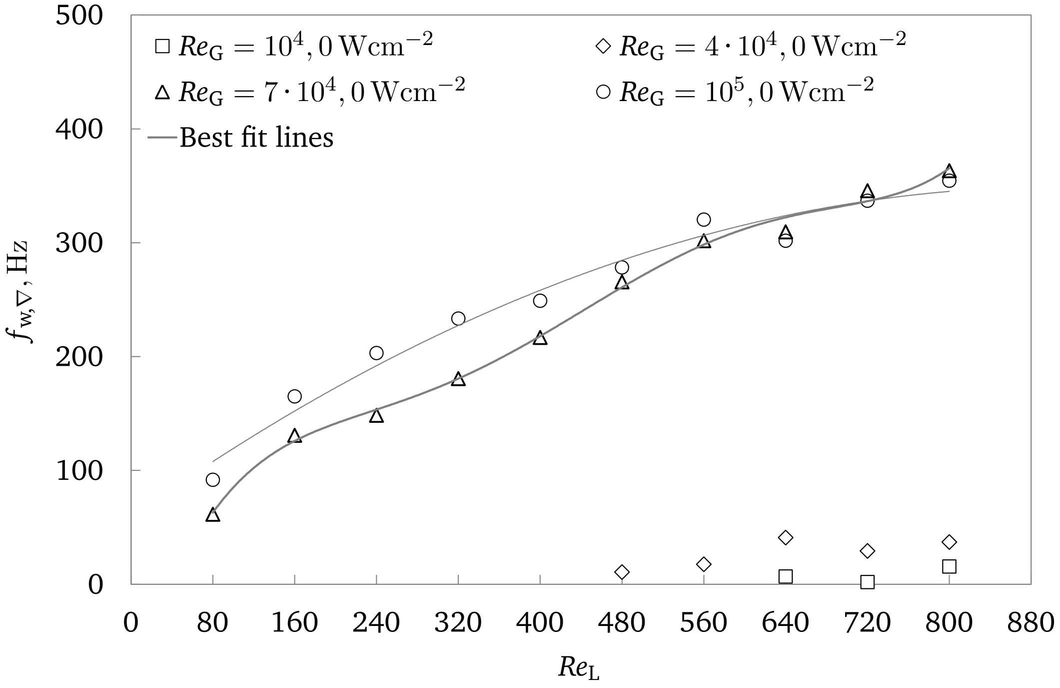

Figure 7.42. Wave frequency $f_{w,\nabla}$ of gas-driven liquid films at ∇-grooved surface recorded at $z = 45\,\mathrm{mm}$ for $Re_L = 80 - 800$, $Re_G = 10^4 - 10^5$, $\dot{q}_W = 0$.

A further increase to $Re_G = 10^5$ results in a permanent rise of σ_∇ over the entire Re_L range. Strong destruction represented by fingering of the liquid film occurs up to the point where droplets are entrained and sinusoidal waves with large amplitudes appear (see inserts 9, 10, and 11). Although liquid films can be stabilized through longitudinally oriented micro-structures [63], the standard deviation shows that the wall topography looses its stabilizing effect on the liquid film which end up in chaotic interface shapes. Thereby, the micro-structure geometry, the surface tension [117], and additionally the shear stress are the most significant dimensions governing the film distortion. Figures 7.41 and 7.42 present σ_∇ and the wave frequency $f_{\mathrm{w},\nabla}$ for the unheated liquid film.

In the case of $Re_\mathrm{G} = 10^4$ and $Re_\mathrm{G} = 4 \cdot 10^4$, less number of waves could be determined solely only for $Re_\mathrm{G} > 400$. $f_{\mathrm{w},\nabla}$ shows a minor increase with Re_L, since the structures become flooded and sufficient mass of liquid is provided. Contrary, for $Re_\mathrm{G} < 480$ the partial wetting phenomena occurred where waves traveled within the troughs and did not emerge from the structure. At $Re_\mathrm{G} = 7 \cdot 10^4$ and $Re_\mathrm{G} = 10^5$ increased number of waves were recorded. Synchronously the standard deviation also increases with increasing fluid Reynolds numbers. This would mean that longitudinal ∇-grooved structures lead to a controlled and stable increase of the waviness [61]. The frequency of waves rises towards larger liquid Reynolds number [43] while the influence of the shear force diminishes.

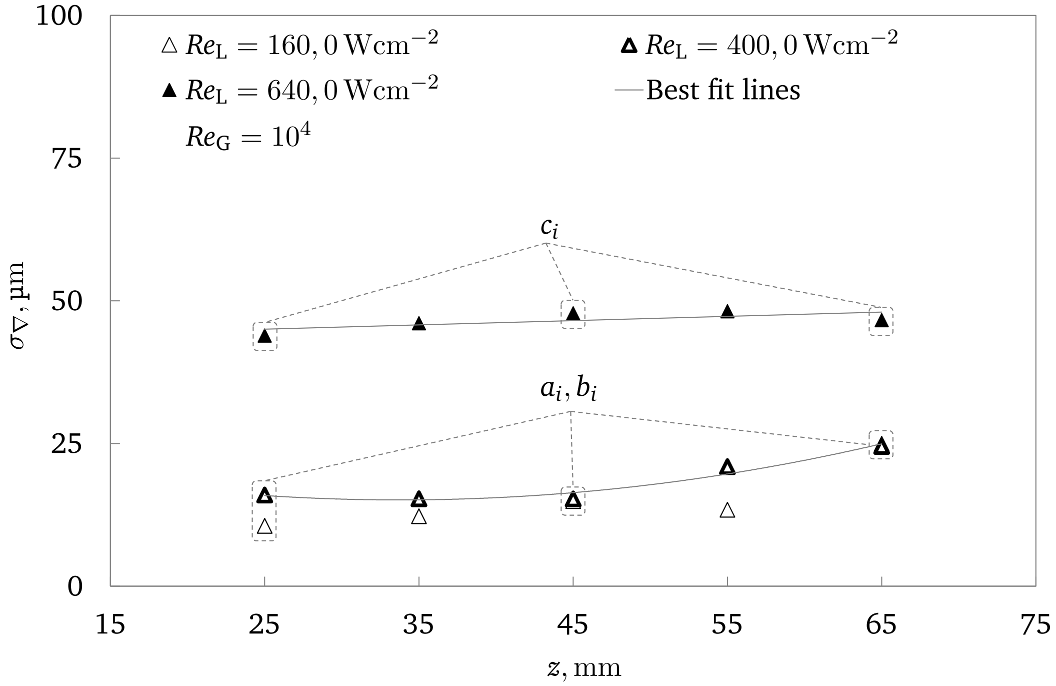

Figure 7.43. Standard deviation σ_∇ of gas-driven liquid films on the ∇-grooved surface as a function of z for $Re_\mathrm{G} = 10^4$, $Re_\mathrm{L} = 160, 400, 640$, $q_\mathrm{W} = 0$; values at $z = 25\,\mathrm{mm}, 45\,\mathrm{mm}$, and $65\,\mathrm{mm}$ correspond to sequences a_i, b_i, and c_i in Fig. 7.44.

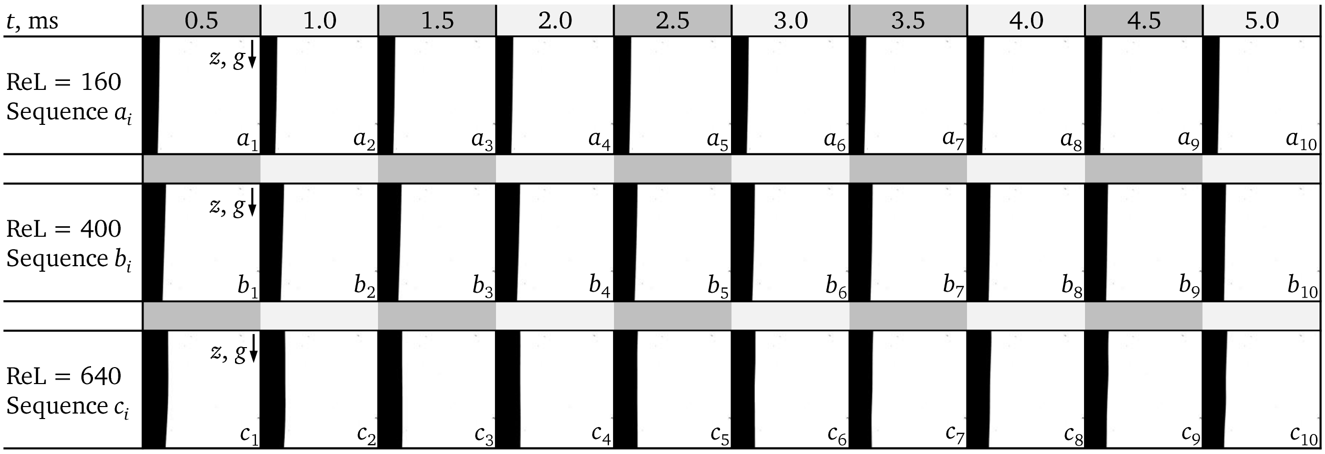

Figure 7.44. Image sequences of gas-driven liquid films at the ∇-grooved surface for $Re_\mathrm{L} = 160, 400, 640$. Sequences are taken at $Re_\mathrm{G} = 10^4$, $Re_\mathrm{G} = 4 \cdot 10^4$, and $\dot{q}_\mathrm{W} = 0$.

The axial development of the standard deviation for the unheated liquid film flow at $Re_\mathrm{G} = 10^4$ for varying Re_L is displayed in Fig. 7.43. Due to the reason of less values, no frequency values are provided. σ_∇ slightly increases with the distance and with the liquid Reynolds number. The increase over z-direction is associated to destabilizing effects which are induced by shear stress at the wall-liquid and liquid-gas interface. However, the high-speed imaging sequences in Fig. 7.44 for values labeled with a_i, b_i, and c_i show a rather steady and stable film flow. Note that in the measurements with $Re_\mathrm{L} = 160$ and probably also $Re_\mathrm{L} = 400$ a partial wetting occurred and therefore the corresponding standard deviations are rather the fluctuations of the dry wall-gas interface instead of liquid-gas interface.

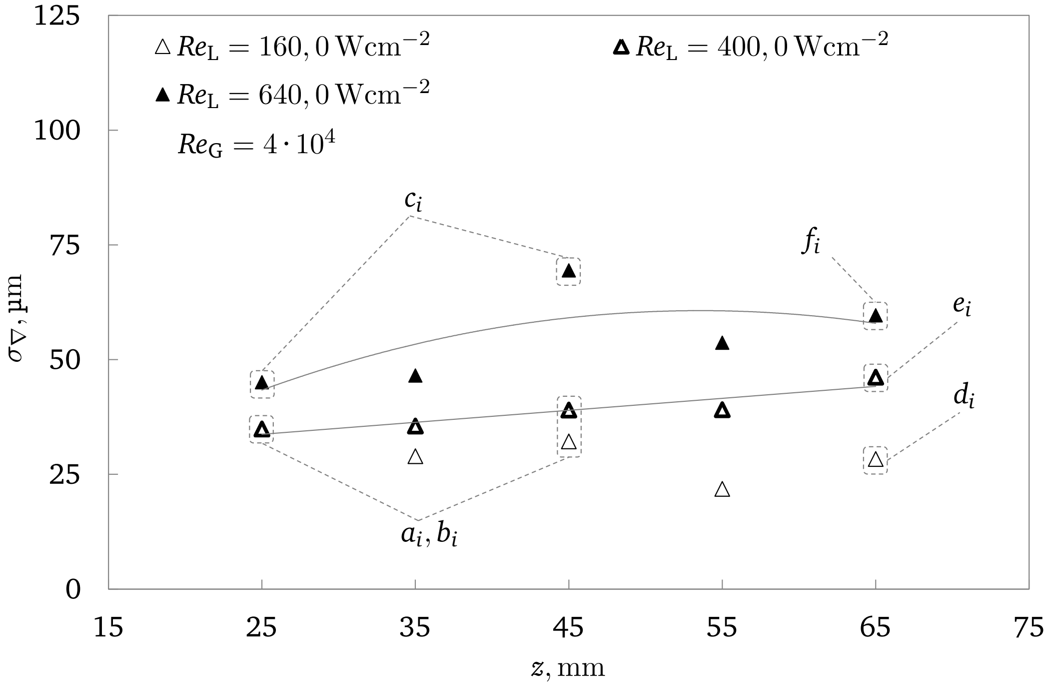

Figure 7.45. Standard deviation σ_∇ of gas-driven liquid films on the ∇-grooved surface as a function of z for $Re_\mathrm{G} = 4 \cdot 10^4$, $Re_\mathrm{L} = 160, 400, 640$, $\dot{q}_\mathrm{W} = 0$; values at $z = 25\,\mathrm{mm}$ and $z = 45\,\mathrm{mm}$ correspond to image sequences a_i, b_i and c_i in Fig. 7.44, values at $z = 65\,\mathrm{mm}$ correspond to image sequences d_i, e_i and f_i in Fig. 7.47.

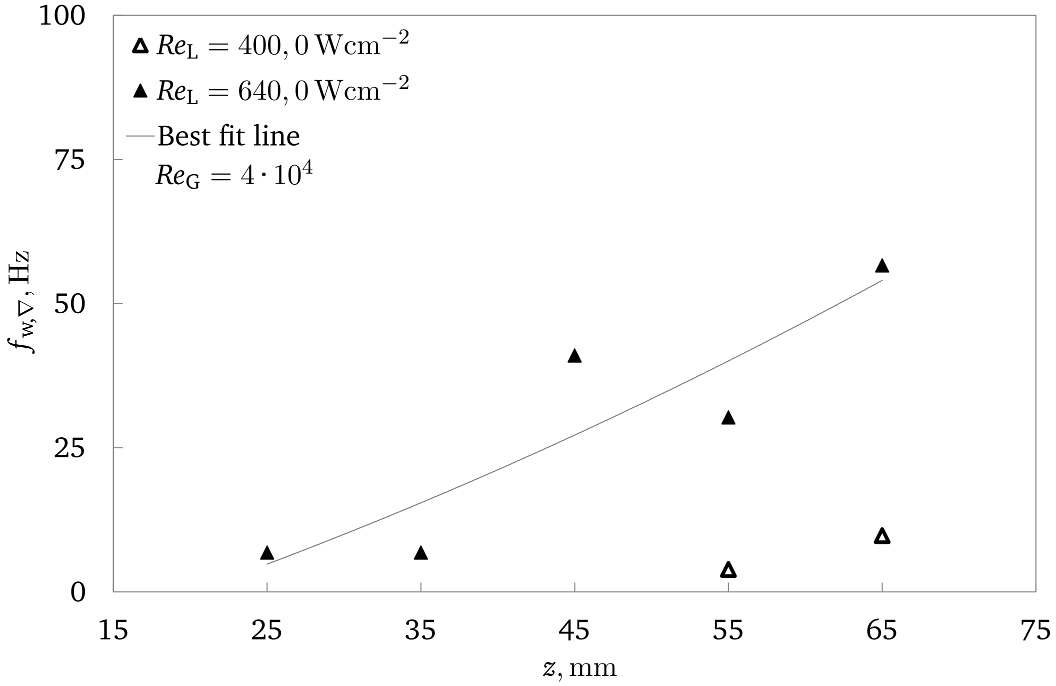

Figure 7.46. Wave frequency $f_{w,\nabla}$ of gas-driven liquid films on the ∇-grooved surface as a function of z for $Re_G = 4 \cdot 10^4$, $Re_L = 160, 400, 640$, $\dot{q}_W = 0$.

In Figs. 7.45 and 7.46, σ_∇ and $f_{w,\nabla}$ for $Re_G = 4 \cdot 10^4$ are demonstrated. With increasing liquid Reynolds number the standard deviation rises locally and axially. As described before, the gas shear stress is not sufficient to achieve large amplitude fluctuations for low liquid mass loads. The liquid film streams inside the micro-grooves and cannot be recorded. As soon as Re_L grows, the liquid fluctuations increase. However, the comparison between the standard deviation and wave frequency for does not reveal a clear relationship. A reasonable data on $f_{w,\nabla}$ could be given only for $Re_G = 640$. With considering large discrepancies, it can be cautiously concluded that an increasing trend over z similar to σ_∇ exists which is related to the filling of troughs with liquid. Even the high-speed records show no significant change of the smooth liquid-gas interface for the particular measurement positions (see Figs. 7.44 and 7.47).

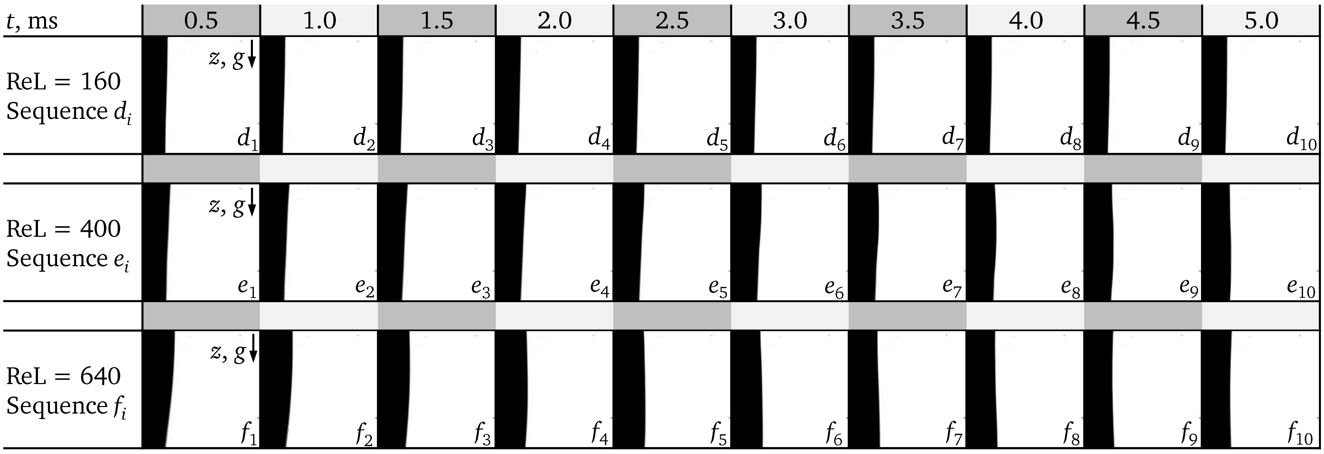

Figure 7.47. Image sequences of gas-driven liquid film flow at the ∇-grooved surface for $Re_L = 160, 400, 640$. Sequences are taken at $Re_G = 4 \cdot 10^4$, $z = 65\,\mathrm{mm}$ and $\dot{q}_W = 0$.

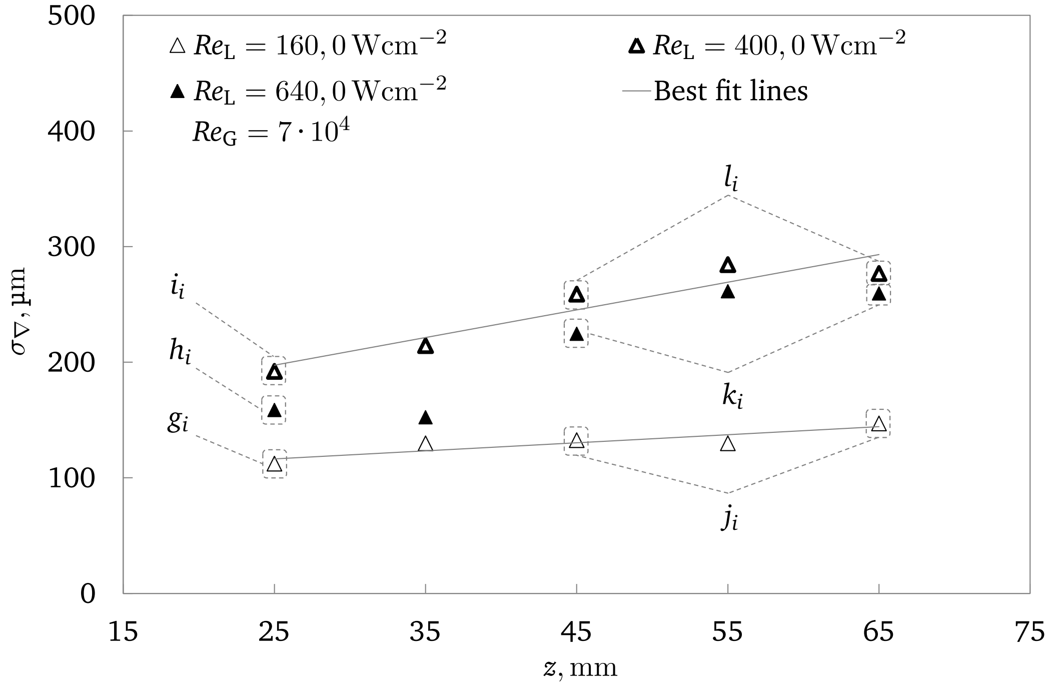

Figure 7.48. Standard deviation σ_∇ of gas-driven liquid films on the ∇-grooved surface as a function of z for $Re_\mathrm{G} = 7 \cdot 10^4$, $Re_\mathrm{L} = 160, 400, 640$, $\dot{q}_\mathrm{W} = 0$; values at $z = 25\,\mathrm{mm}$ correspond to image sequences g_i, h_i and i_i in Fig. 7.50, values at $z = 45\,\mathrm{mm}$ and $z = 65\,\mathrm{mm}$ correspond to image sequences j_i, k_i and l_i in Fig. 7.51.

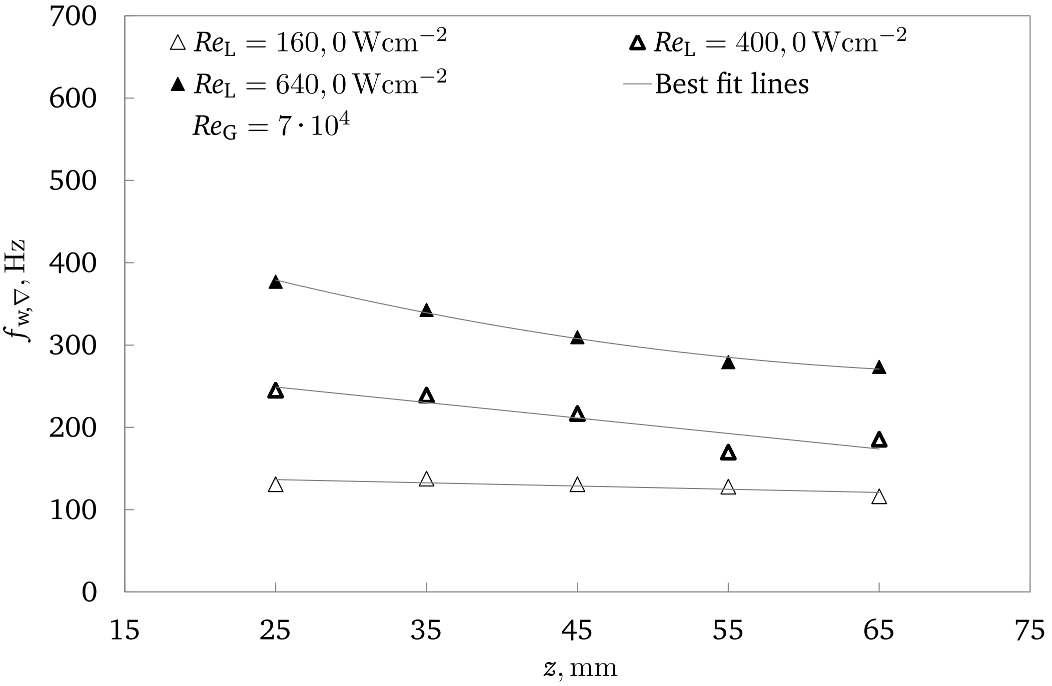

Figure 7.49. Wave frequency $f_{\mathrm{w},\nabla}$ of gas-driven liquid films on the ∇-grooved surface as a function of z for $Re_\mathrm{G} = 7 \cdot 10^4$, $Re_\mathrm{L} = 160, 400, 640$, $\dot{q}_\mathrm{W} = 0$.

At $Re_\mathrm{G} = 7 \cdot 10^4$ and varying Re_L a rather linear dependency of the axial development of σ_∇ and $f_{\mathrm{w},\nabla}$ can bee seen in Figs. 7.48 and 7.49. As the distance grows, the film surface become more fluctuating and involve a decay of the corresponding wave frequency. The larger the liquid film deformations are the smaller the frequency is, since large waves can exhibit small celerity. Both parameters increase by rising the liquid Reynolds number which was also seen in [43, 77]. However the σ_∇ values at $Re_\mathrm{L} = 640$ are smaller than the standard deviation for $Re_\mathrm{L} = 400$. This is either a measurement error during manually saving the data with the wrong name. Or the scooping effect of the acting shear force is not ample. In the high-speed sequences displayed in Fig. 7.50 the partial wetting at low Re_L can be seen in the images $d_1 - d_5$. At $z = 45\,\mathrm{mm}$ and $z = 65\,\mathrm{mm}$ strong emergence of liquid could be identified after analyzing the shadowgraphy images (see exemplary Fig. 7.51).

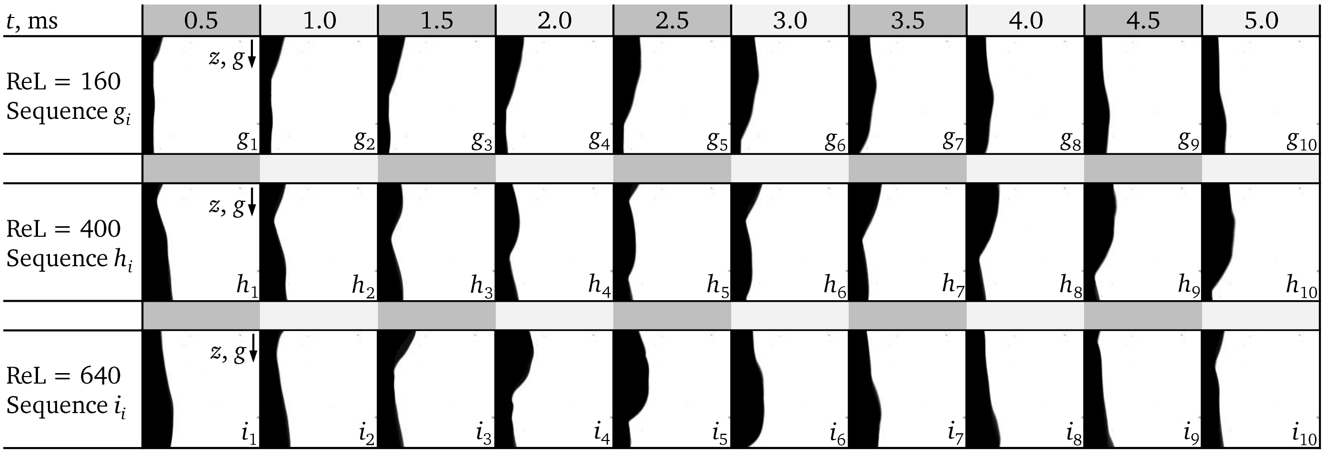

Figure 7.50. Image sequences of gas-driven liquid film flow at the ∇-grooved surface for $Re_\mathrm{L} = 160, 400, 640$. Sequences are taken at $Re_\mathrm{G} = 7 \cdot 10^4$, $z = 25\,\mathrm{mm}$ and $\dot{q}_\mathrm{W} = 0$.

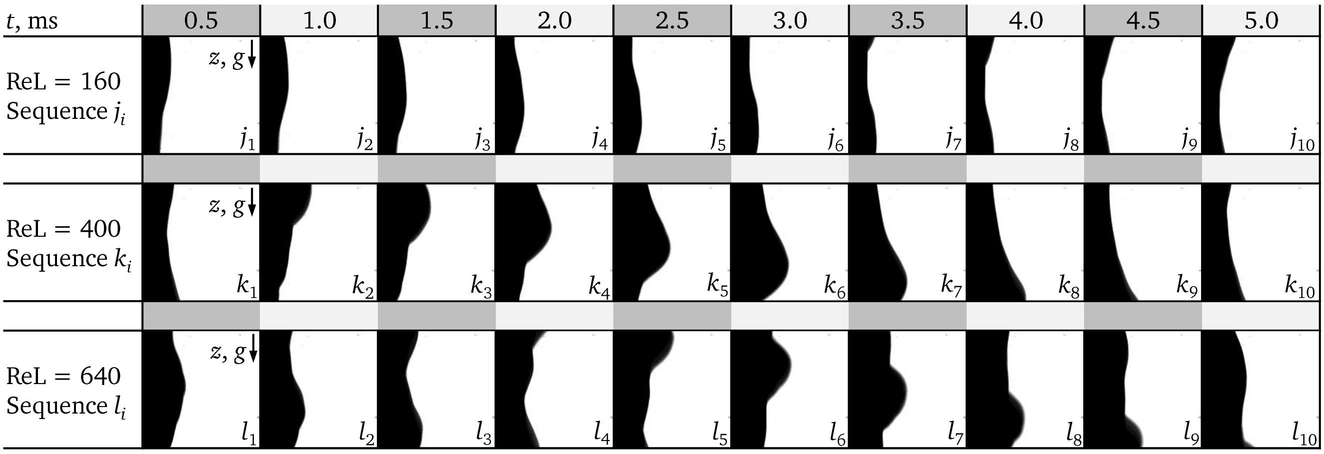

Figure 7.51. Image sequences of gas-driven liquid film flow at the ∇-grooved surface for $Re_\mathrm{L} = 160, 400, 640$. Sequences are taken at $Re_\mathrm{G} = 7 \cdot 10^4$, $z = 45\,\mathrm{mm}, 65\,\mathrm{mm}$ and $\dot{q}_\mathrm{W} = 0$.

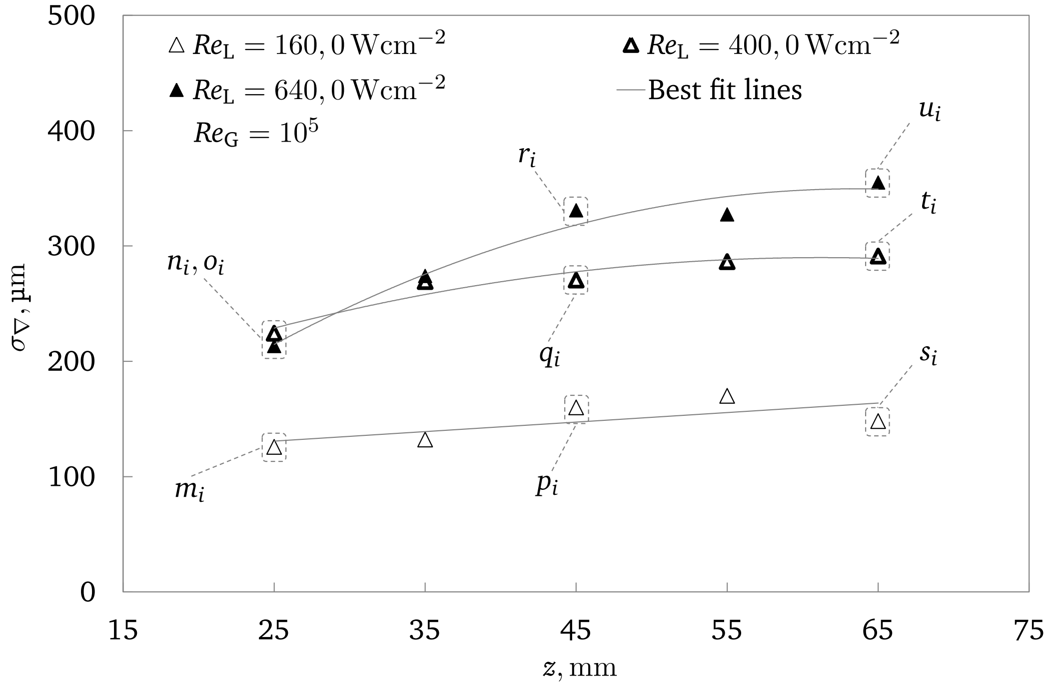

Figure 7.52. Standard deviation σ_∇ of gas-driven liquid films on the ∇-grooved surface as a function of z for $Re_G = 10^5$, $Re_L = 160, 400, 640$, $\dot{q}_W = 0$; values at $z = 25\,\mathrm{mm}$ correspond to image sequences m_i, n_i and o_i in Fig. 7.54, values at $z = 45\,\mathrm{mm}$ correspond to image sequences p_i, q_i and r_i in Fig. 7.55 and values at $z = 65\,\mathrm{mm}$ correspond to image sequences s_i, t_i and u_i in Fig. 7.56.

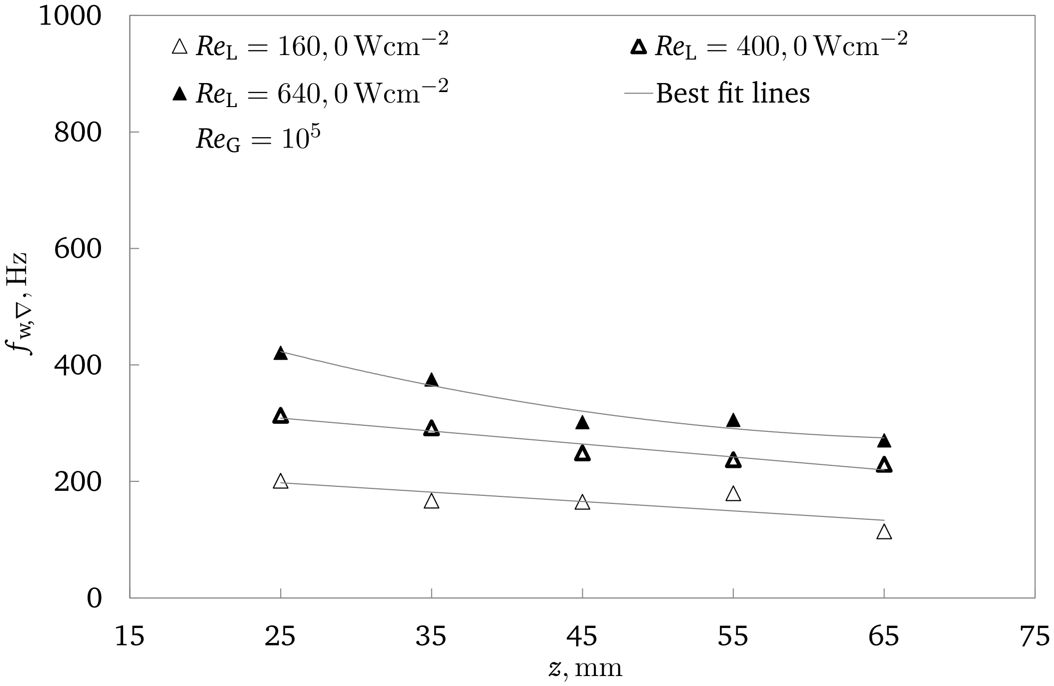

Figure 7.53. Wave frequency $f_{w,\nabla}$ of gas-driven liquid films flow on the ∇-grooved surface as a function of z for $Re_G = 10^5$, $Re_L = 160, 400, 640$, $\dot{q}_W = 0$.

At the highest gas Reynolds number, large standard deviations and large wave frequencies were obtained (see Fig. 7.52 and 7.53) compared to the previous case. Both parameters grow with larger liquid mass flow rate, while σ_{∇} increases and $f_{\mathrm{w},\nabla}$ decays along the flow direction. According to the sequences shown in Figs. 7.54, 7.55, and 7.56 the liquid film surface recognizes first disturbances embossed with ripples at low Reynolds numbers. After rising the liquid mass flow rate, waves with high amplitudes appear which also exhibit fingers (see images $t_2 - t_5$). At $Re_{\mathrm{L}} = 640$ large amplitude waves are present and propagate steadily over the surface. Depending on the strength of the shear stress induced by the gas flow the appearance and shape of waves are determined.

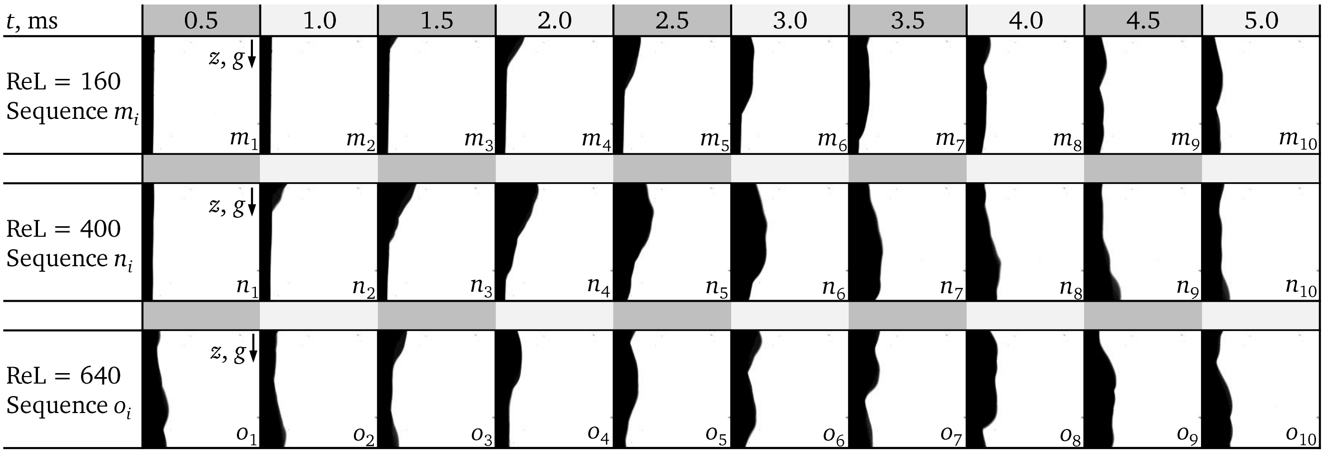

Figure 7.54. Image sequences of gas-driven liquid film flow at the ∇-grooved surface for $Re_{\mathrm{L}} = 160, 400, 640$. Sequences are taken at $Re_{\mathrm{G}} = 10^5$, $z = 25\,\mathrm{mm}$, and $\dot{q}_{\mathrm{W}} = 0$.

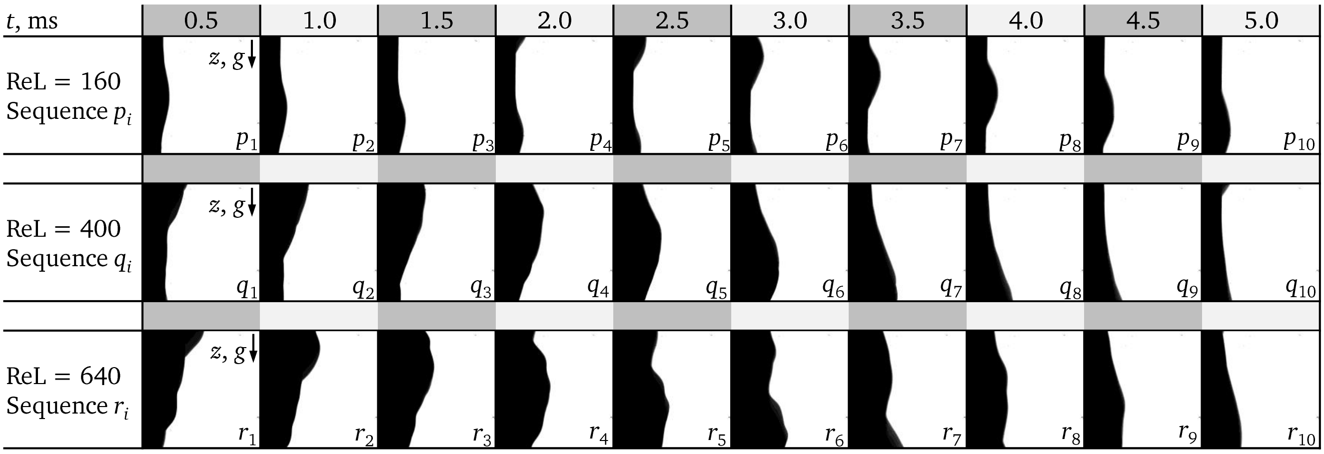

Figure 7.55. Image sequences of gas-driven liquid film flow at the ∇-grooved surface for $Re_{\mathrm{L}} = 160, 400, 640$. Sequences are taken at $Re_{\mathrm{G}} = 10^5$, $z = 45\,\mathrm{mm}$, and $\dot{q}_{\mathrm{W}} = 0$.

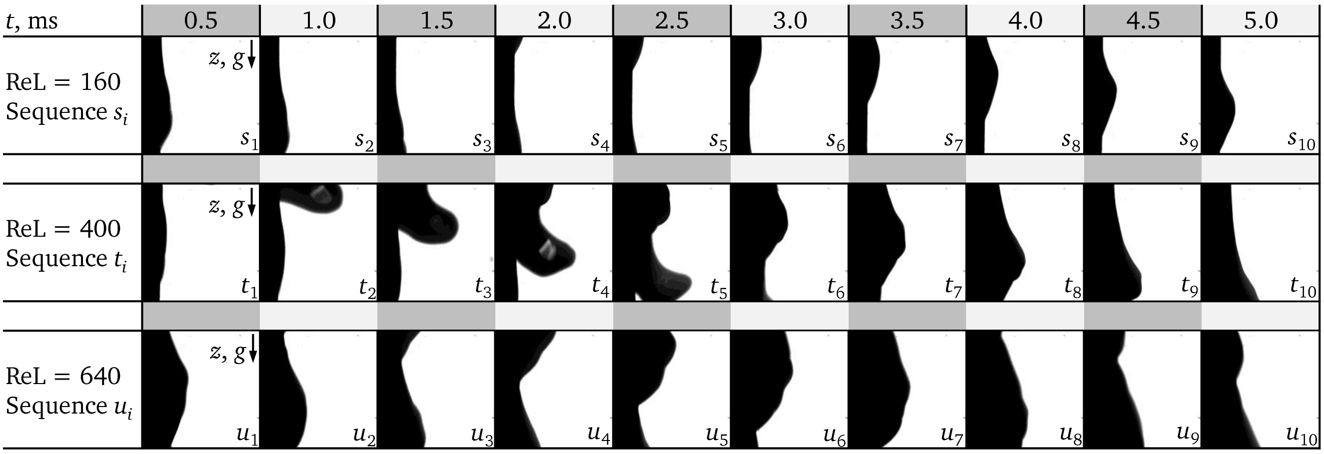

Figure 7.56. Image sequences of gas-driven liquid film flow at the ∇-grooved surface for $Re_\mathrm{L} = 160, 400, 640$. Sequences are taken at $Re_\mathrm{G} = 10^5$, $z = 65\,\mathrm{mm}$, and $\dot{q}_\mathrm{W} = 0$.

7.2.2 Film waviness at Δ-structured surface

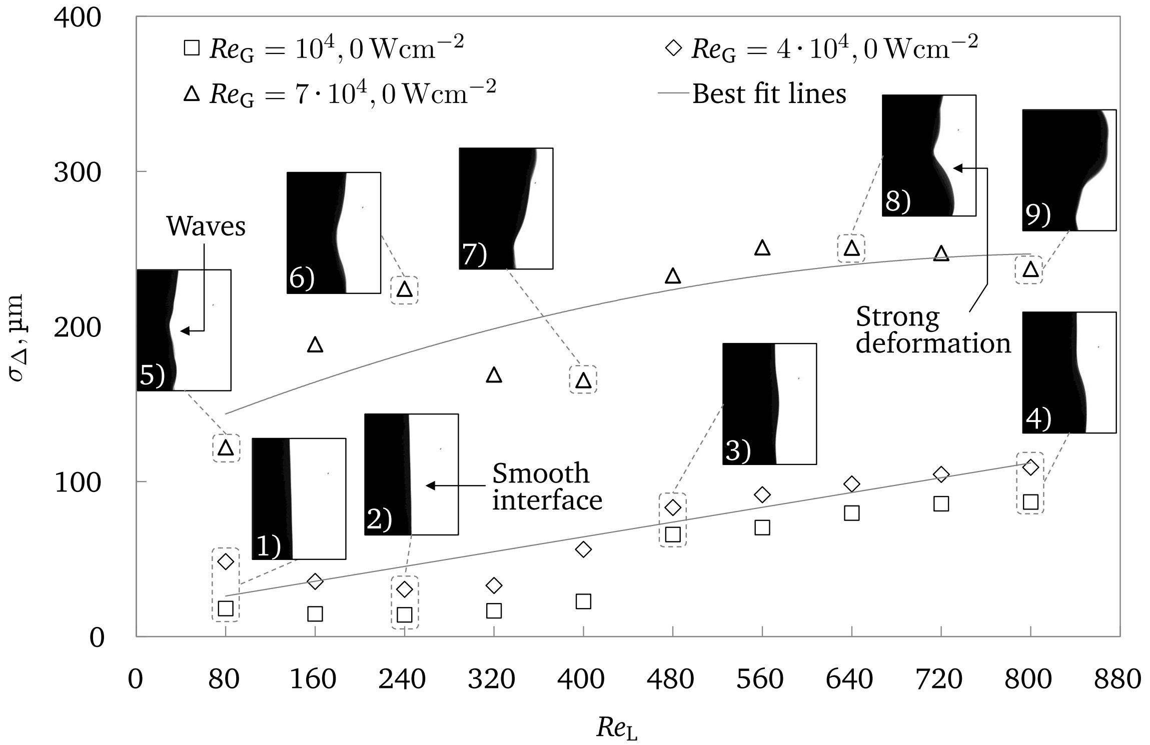

Figure 7.57. Standard deviation σ_Δ of gas-driven liquid films at the Δ-structured surface with exemplary chosen images of characteristic liquid-gas interfacial structures showing smooth interface and strong deformations. Experimental parameters are $Re_\mathrm{L} = 80 - 800$, $Re_\mathrm{G} = 10^4 - 7 \cdot 10^4$ at $\dot{q}_\mathrm{W} = 0$.

The standard deviation of an unheated gas-driven film flowing downward the pyramid structured surface at varying Re_L is illustrated in Fig. 7.57. Over the liquid Reynolds number range the standard deviation has grows by trend. The shear stress cause an increase in σ_Δ for all Re_G. Nevertheless, $Re_\mathrm{G} = 7 \cdot 10^4$ results in the highest σ_Δ values, while a sharp increase was obtained occurring at $Re_\mathrm{L} = 400$ for $Re_\mathrm{G} = 4 \cdot 10^4$ and at $Re_\mathrm{L} = 480$ for $Re_\mathrm{G} = 10^4$.

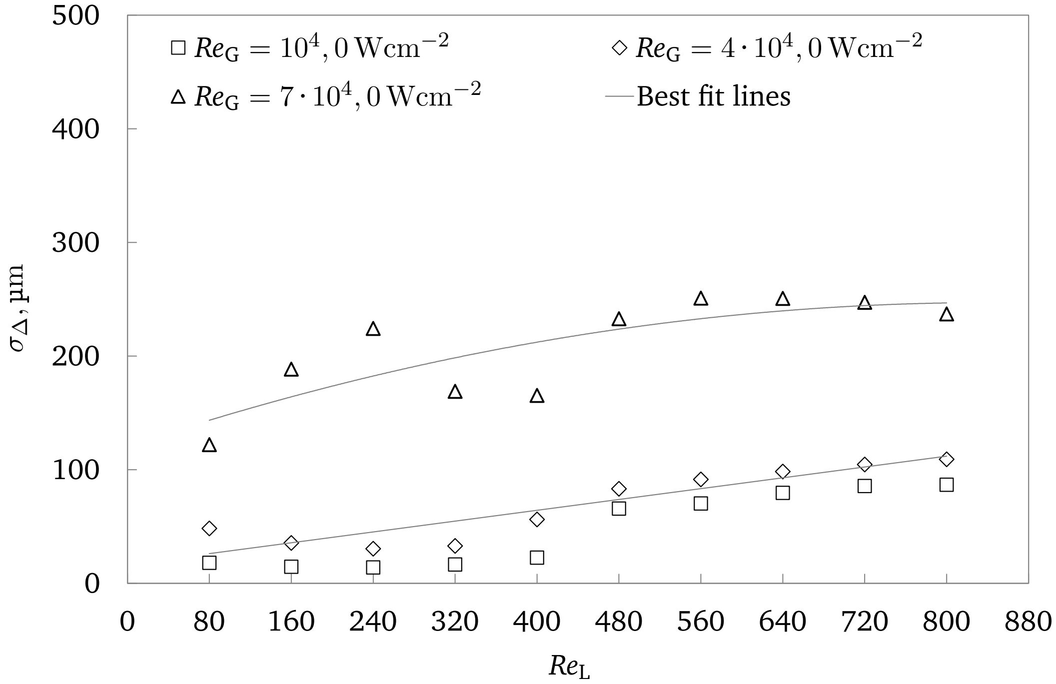

Figure 7.58. Standard deviation σ_Δ of gas-driven liquid films at the Δ-structured surface recorded at $z = 45\,\mathrm{mm}$ for $Re_\mathrm{L} = 80 - 800$, $Re_\mathrm{G} = 10^4 - 7 \cdot 10^4$, $\dot{q}_\mathrm{W} = 0$.

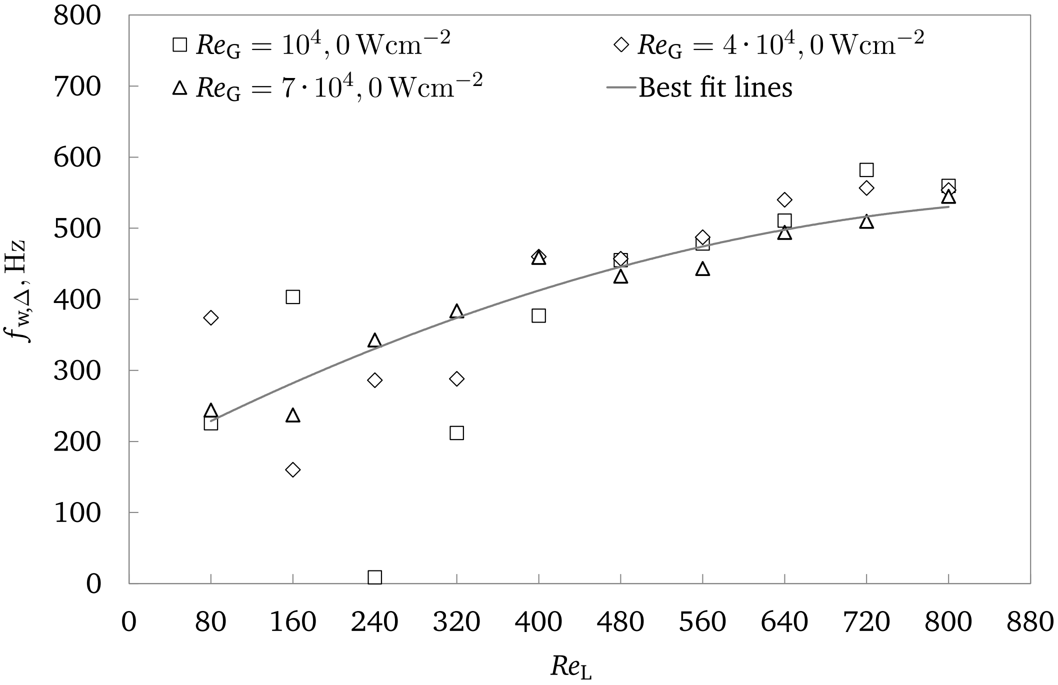

Figure 7.59. Wave frequency $f_{\mathrm{w},\Delta}$ of gas-driven liquid films at the Δ-structured surface recorded at $z = 45\,\mathrm{mm}$ for $Re_\mathrm{L} = 80 - 800$, $Re_\mathrm{G} = 10^4 - 7 \cdot 10^4$, $\dot{q}_\mathrm{W} = 0$.

The rise of σ_Δ is characterized by a immediate change from smooth to wavy liquid-gas interface (see insert 1 to 4). Probably at this point the pyramid structures are fully flooded with liquid, since in partial wetted conditions liquid mass has to scooped up with stronger shear stress. The structure of the liquid film surface at $Re_\mathrm{G} = 7 \cdot 10^4$ develops from small amplitude waves towards large amplitude waves (see inserts 5 to 9). On the basis of the horizontal orientation of the pyramid structures a stronger and maybe earlier destabilization occurs. Thereby the hydrodynamic boundary layer is disturbed significantly. The development of σ_Δ and $f_{\mathrm{w},\Delta}$ at $z = 45\,\mathrm{mm}$ is compared for varying Re_L and Re_G in Figs. 7.58 and 7.59. Concerning the wave frequency, the influence of gas Reynolds number cannot be determined easily. Moreover, similar to the standard deviation, the all frequencies tend to increase with growing Re_L. Larger liquid mass cause more distortion and hence more waves at the film surface. The impact of gas on the number of waves is suppressed by the structure. Since the pyramids cause a higher pressure drop in flow direction, the gas stream sees the surface topography as roughness.

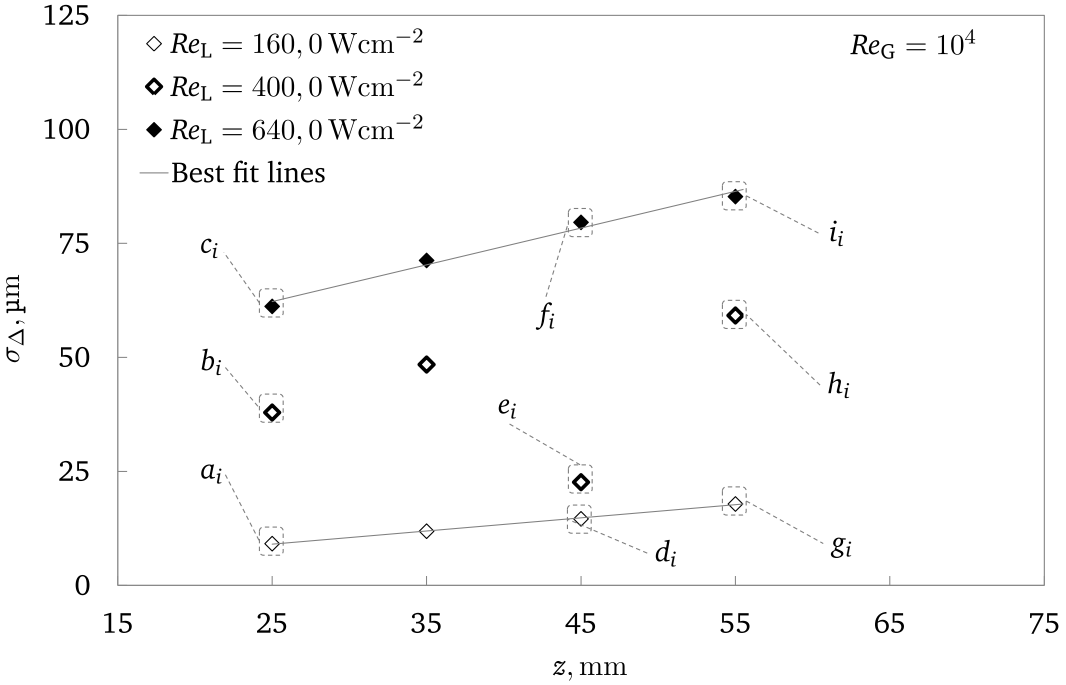

Figure 7.60. Standard deviation σ_Δ of gas-driven liquid films flow on the Δ-structured surface as a function of z for $Re_\mathrm{G} = 10^4$, $Re_\mathrm{L} = 160, 400, 640$, $\dot{q}_\mathrm{W} = 0$; values at $z = 25\,\mathrm{mm}$ correspond to image sequences a_i, b_i, and c_i in Fig. 7.64, values at $z = 45\,\mathrm{mm}$ correspond to image sequences d_i, e_i, and f_i in Fig. 7.65 and values at $z = 55\,\mathrm{mm}$ correspond to image sequences g_i, h_i, and i_i in Fig. 7.66.

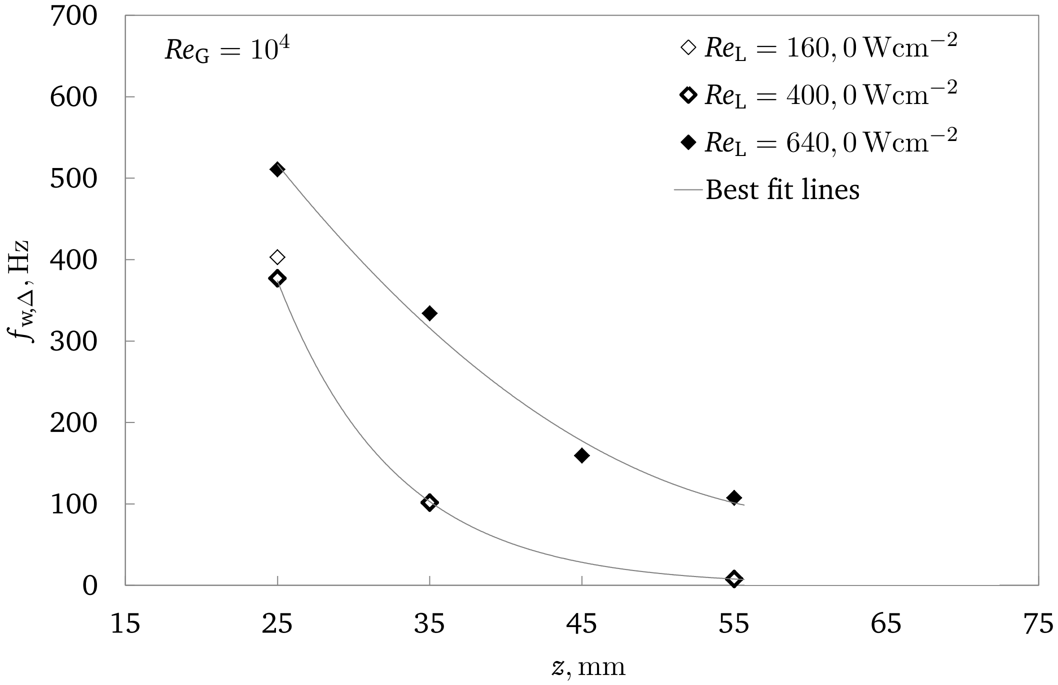

Figure 7.61. Wave frequency $f_{w,\Delta}$ of gas-driven liquid films flow on the Δ-structured surface as a function of z for $Re_G = 10^4$, $Re_L = 160, 400, 640$, $\dot{q}_W = 0$.

The result is strong friction and a high pressure drop in flow direction. Hence the momentum of the gas phase is majorly degraded to overcome this friction rather to transfer momentum into the formation and acceleration of waves. The evaluation of the axial development of σ_Δ and f_Δ for varying liquid Reynolds number at $Re_G = 10^4$ are shown in Figs. 7.60 and 7.61. Measurements at $z = 65\,\mathrm{mm}$ could not be performed because of defect light source. An increase of Re_L induces large fluctuations and elevates the wave frequency of the liquid-gas interface. However, along the flow direction the gradient of σ_Δ grows while f_Δ decays strongly. A possible explanation for this phenomena is that noticeable static jumps appear before the pyramids [11, 76, 117]. The height of the jumps increase with growing distance while their frequency diminishes. However, the sequences in Figs. 7.64, 7.65, and 7.66 do not show a strongly disturbed liquid-gas interface, rather a smooth film surface was recorded. Whether the post-processing method or the shedding is the reason for the growth of standard deviation is an open question.

Similar behavior of σ_Δ and f_Δ can be seen when rising the gas mass flow rate to $Re_G = 4 \cdot 10^4$ (see Figs. 7.62 and 7.63). Only a minor increase of both the parameter is obtained, the trend and the structure of the liquid film surface has remained the same.

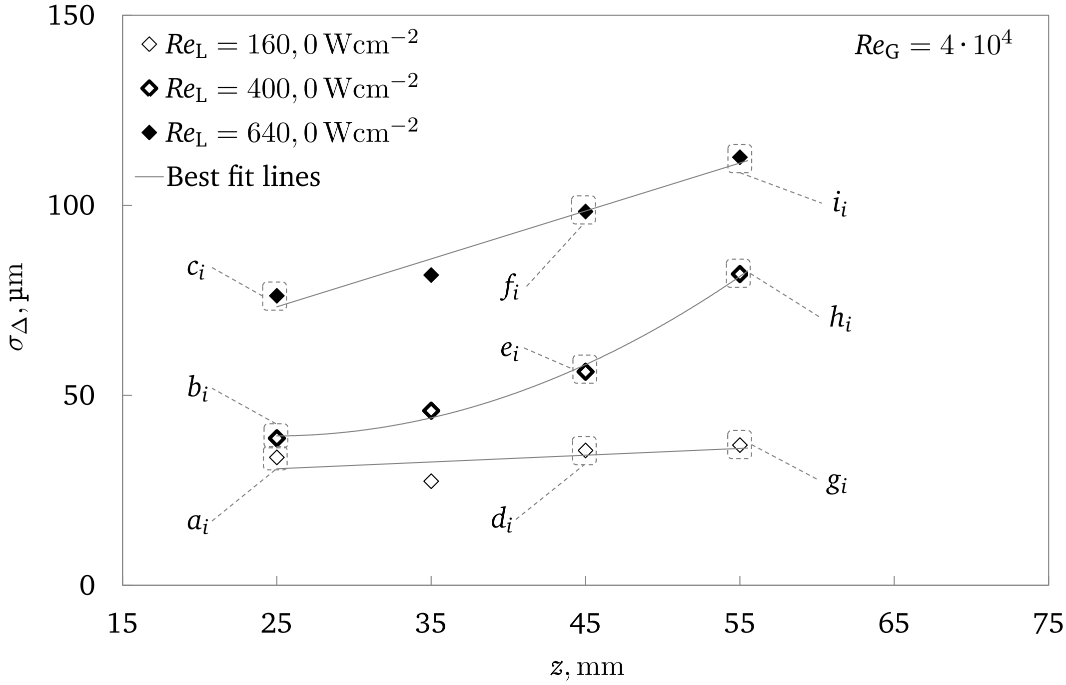

Figure 7.62. Standard deviation σ_Δ of gas-driven liquid films flow on the Δ-structured surface as a function of z for $Re_\mathrm{G} = 4 \cdot 10^4$, $Re_\mathrm{L} = 160, 400, 640$, $\dot{q}_\mathrm{W} = 0$; values at $z = 25\,\mathrm{mm}$ correspond to image sequences a_i, b_i, and c_i in Fig. 7.64, values at $z = 45\,\mathrm{mm}$ correspond to image sequences d_i, e_i, and f_i in Fig. 7.65 and values at $z = 55\,\mathrm{mm}$ correspond to image sequences g_i, h_i, and i_i in Fig. 7.66.

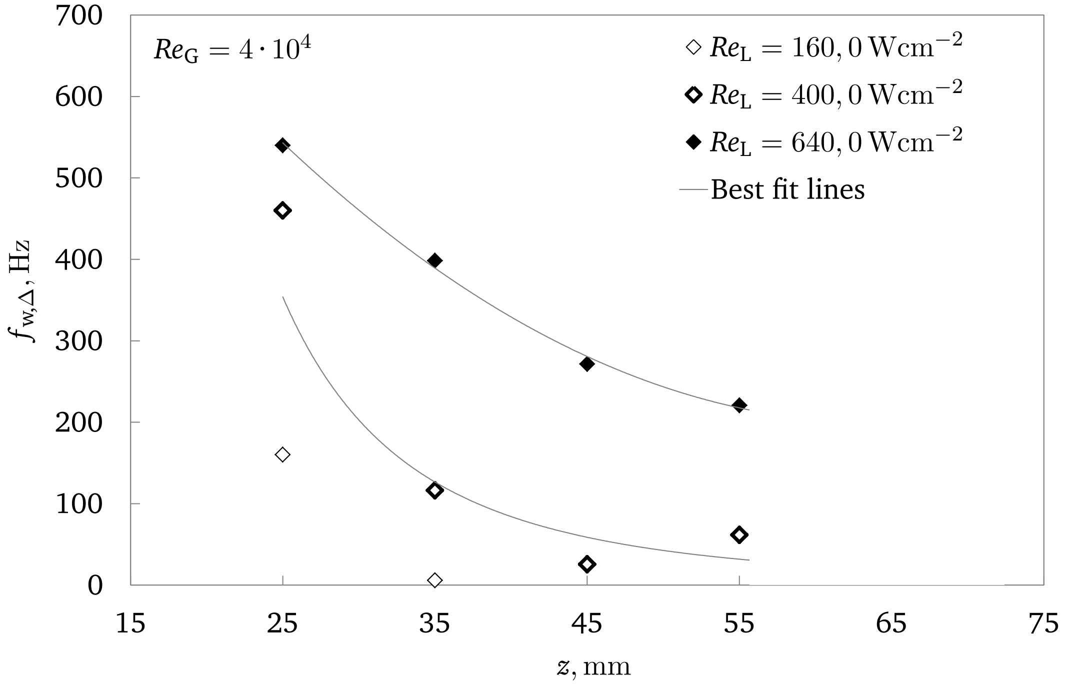

Figure 7.63. Wave frequency $f_{\mathrm{w},\Delta}$ of gas-driven liquid films flow on the Δ-structured surface as a function of z for $Re_\mathrm{G} = 4 \cdot 10^4$, $Re_\mathrm{L} = 160, 400, 640$, $\dot{q}_\mathrm{W} = 0$.

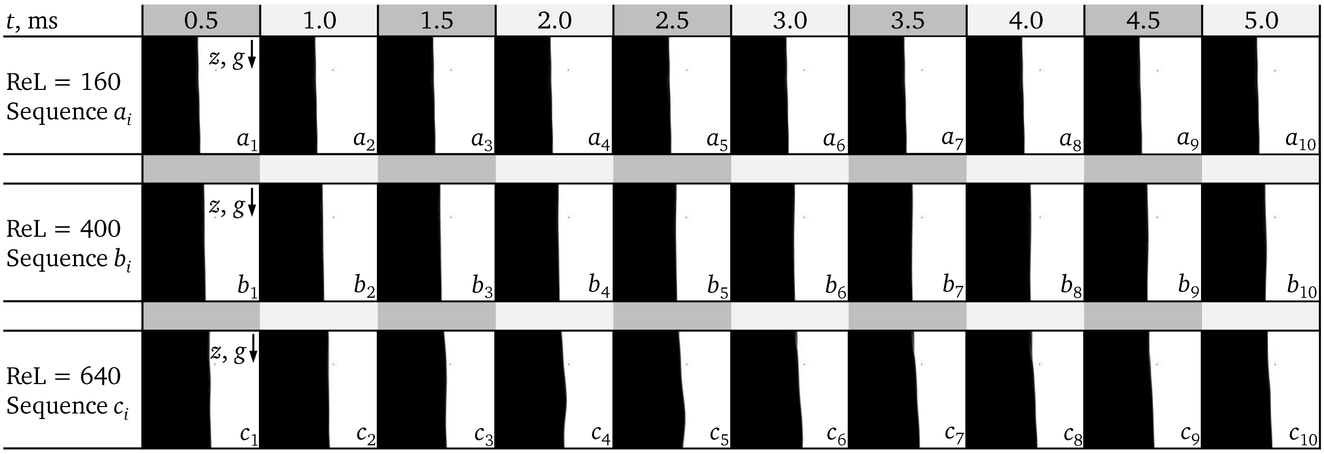

Figure 7.64. Image sequences of gas-driven liquid film flow at the Δ-structured surface for $Re_L = 160, 400, 640$. Sequences are taken at $Re_G = 10^4, 4 \cdot 10^4$, $z = 25\,\text{mm}$, and $\dot{q}_W = 0$.

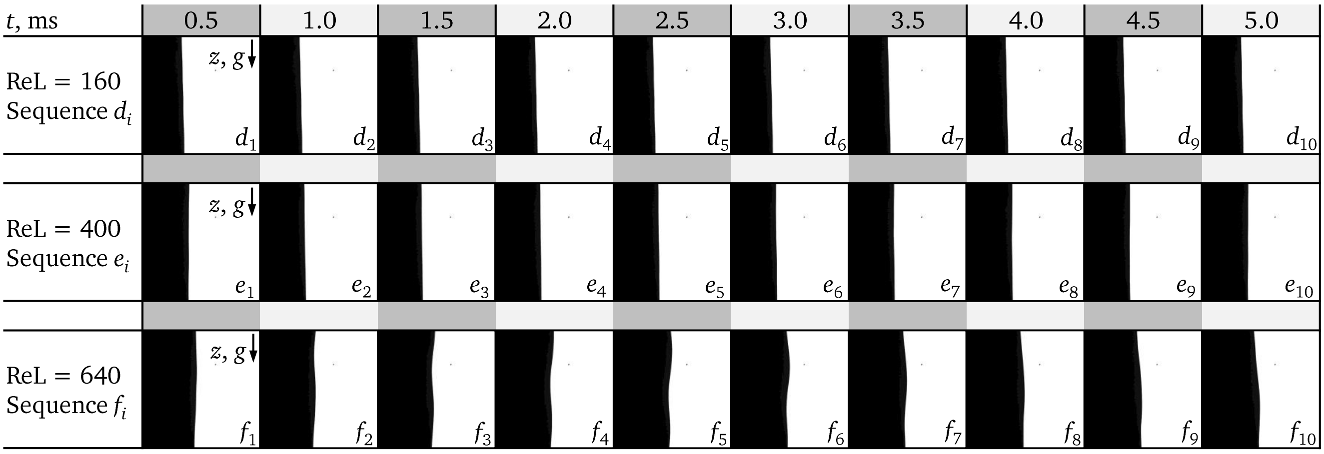

Figure 7.65. Image sequences of gas-driven liquid film flow at the Δ-structured surface for $Re_L = 160, 400, 640$. Sequences are taken at $Re_G = 10^4, 4 \cdot 10^4$, $z = 45\,\text{mm}$, and $\dot{q}_W = 0$.

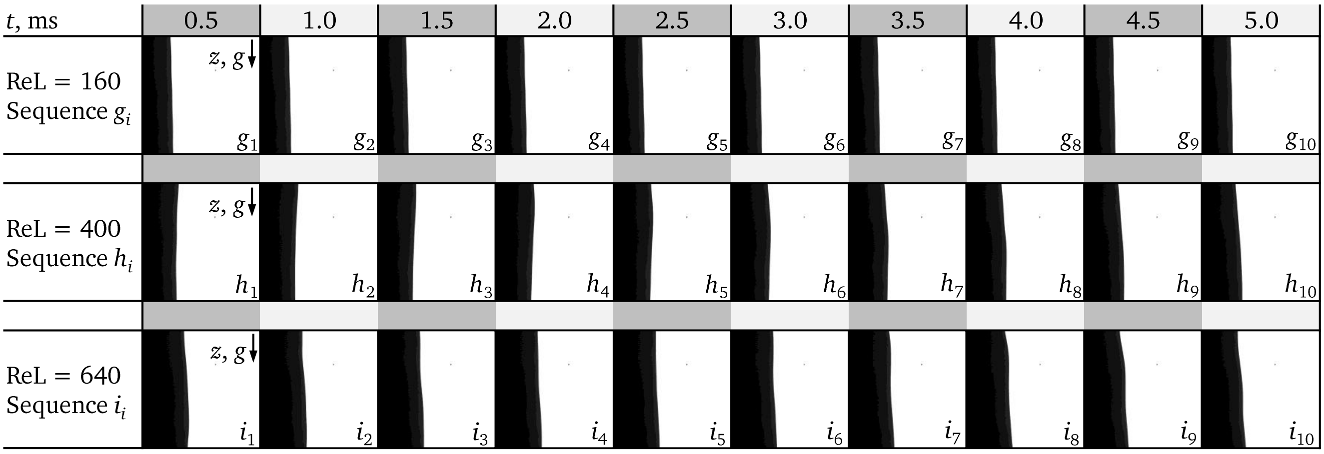

Figure 7.66. Image sequences of gas-driven liquid film flow at the Δ-structured surface for $Re_L = 160, 400, 640$. Sequences are taken at $Re_G = 10^4, 4 \cdot 10^4$, $z = 55\,\text{mm}$, and $\dot{q}_W = 0$.

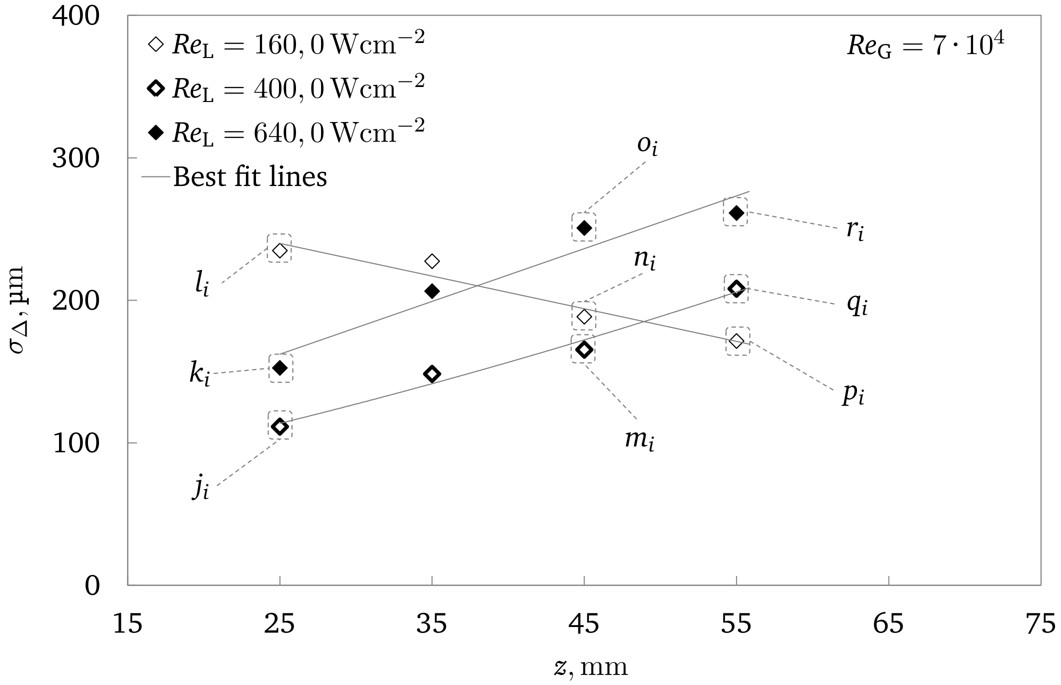

Figure 7.67. Standard deviation σ_Δ of gas-driven liquid films flow on the Δ-structured surface as a function of z for $Re_G = 7 \cdot 10^4$, $Re_L = 160, 400, 640$, $\dot{q}_W = 0$; values at $z = 25\,\mathrm{mm}$ correspond to image sequences j_i, k_i, and l_i in Fig. 7.69, values at $z = 45\,\mathrm{mm}$ correspond to image sequences m_i, n_i, and o_i in Fig. 7.70 and values at $z = 55\,\mathrm{mm}$ correspond to image sequences p_i, q_i, and r_i in Fig. 7.71.

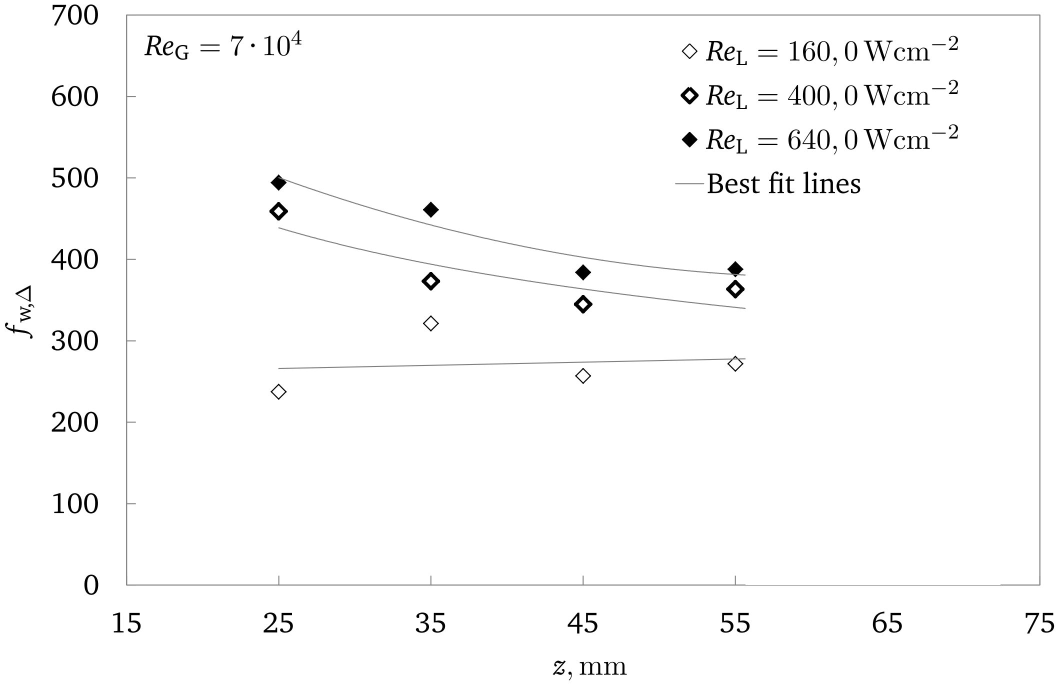

Figure 7.68. Wave frequency $f_{w,\Delta}$ of gas-driven liquid films flow on the Δ-structured surface as a function of z for $Re_G = 7 \cdot 10^4$, $Re_L = 160, 400, 640$, $\dot{q}_W = 0$.

The measurement results for σ_Δ and f_Δ at the maximum Reynolds number used for the pyramid structured surface are displayed in Figs. 7.67 and 7.68. The absolute values of the standard deviation has grown while those of the wave frequency slightly decreased. In this situation, waves with larger heights are generated. Their celerity is lower and appear therefore less frequent. Along the axial direction, the standard deviation increases, except for $Re_\mathrm{L} = 160$. In the latter case most of the liquid is scooped up close in the entrance region where the maximum momentum energy exists. Later the momentum is not sufficient to emerge the liquid from the troughs. In contrast, the frequency decreases with the length and grows for larger Re_L. This is due to the increase in wave fluctuations (see Figs. 7.69 to 7.71) and directly depending on the geometrical shape of the micro-structures.

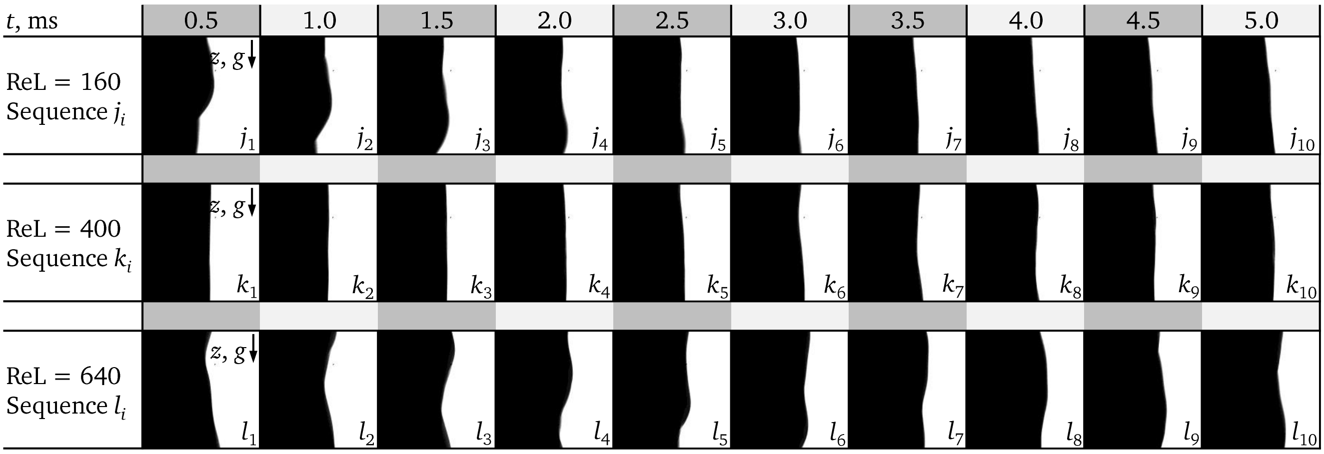

Figure 7.69. Image sequences of gas-driven liquid film flow at the Δ-structured surface for $Re_\mathrm{L} = 160, 400, 640$. Sequences are taken at $Re_\mathrm{G} = 7 \cdot 10^4$, $z = 25\,\mathrm{mm}$, and $\dot{q}_\mathrm{W} = 0$.

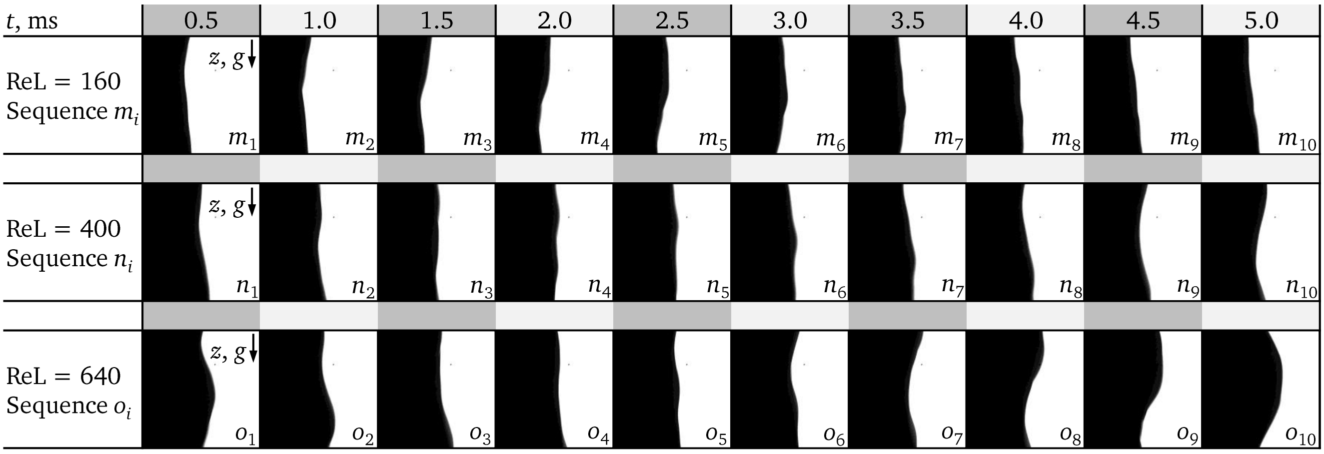

Figure 7.70. Image sequences of gas-driven liquid film flow at the Δ-structured surface for $Re_\mathrm{L} = 160, 400, 640$. Sequences are taken at $Re_\mathrm{G} = 7 \cdot 10^4$, $z = 45\,\mathrm{mm}$, and $\dot{q}_\mathrm{W} = 0$.

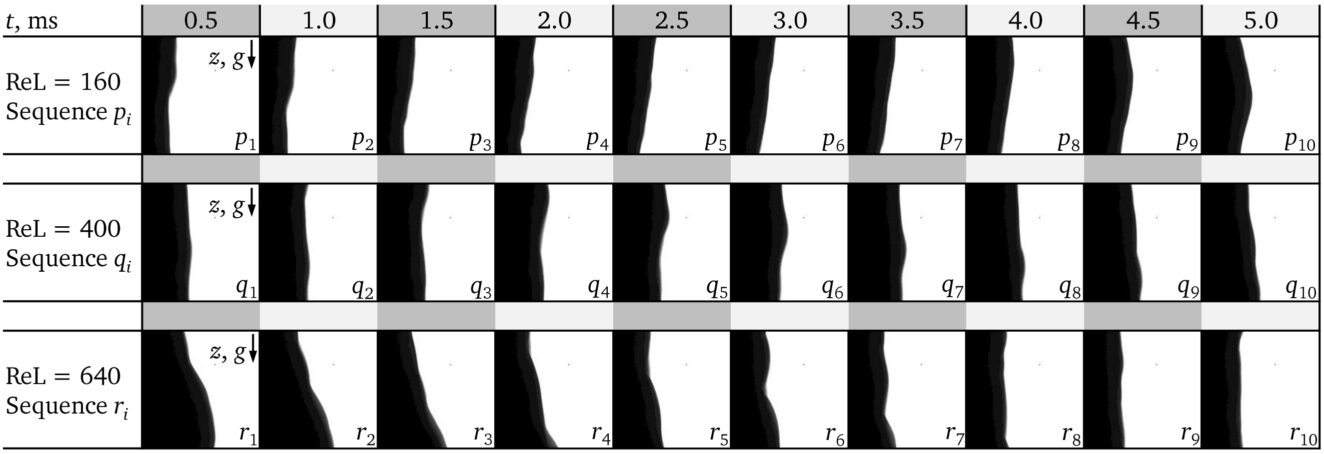

Figure 7.71. Image sequences of gas-driven liquid film flow at the Δ-structured surface for $Re_\mathrm{L} = 160, 400, 640$. Sequences are taken at $Re_\mathrm{G} = 7 \cdot 10^4$, $z = 55\,\mathrm{mm}$, and $\dot{q}_\mathrm{W} = 0$.

7.2.3 Comparison of film waviness at unstructured, ∇-grooved and Δ structured surfaces

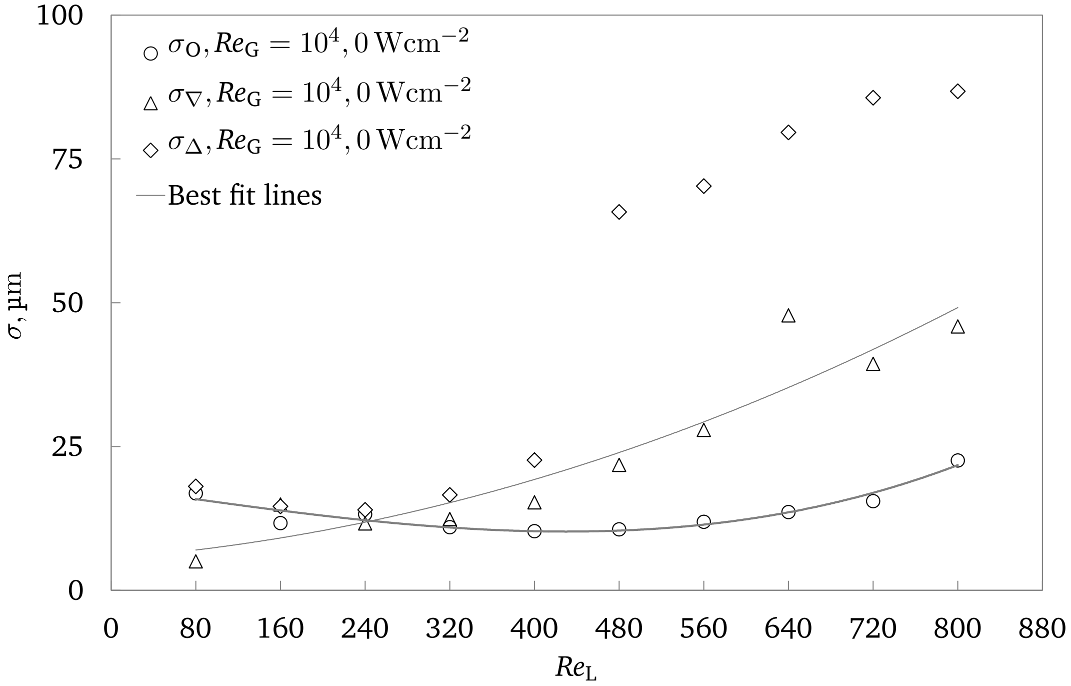

Figure 7.72. Comparison of the standard deviation σ_O, σ_∇, σ_Δ of the gas-driven films measured at the unstructured, ∇-grooved, and Δ-structured surfaces at the axial position $z = 45\,\mathrm{mm}$ for $\dot{q}_\mathrm{W} = 0$, $Re_\mathrm{L} = 80 - 800$, and $Re_\mathrm{G} = 10^4$

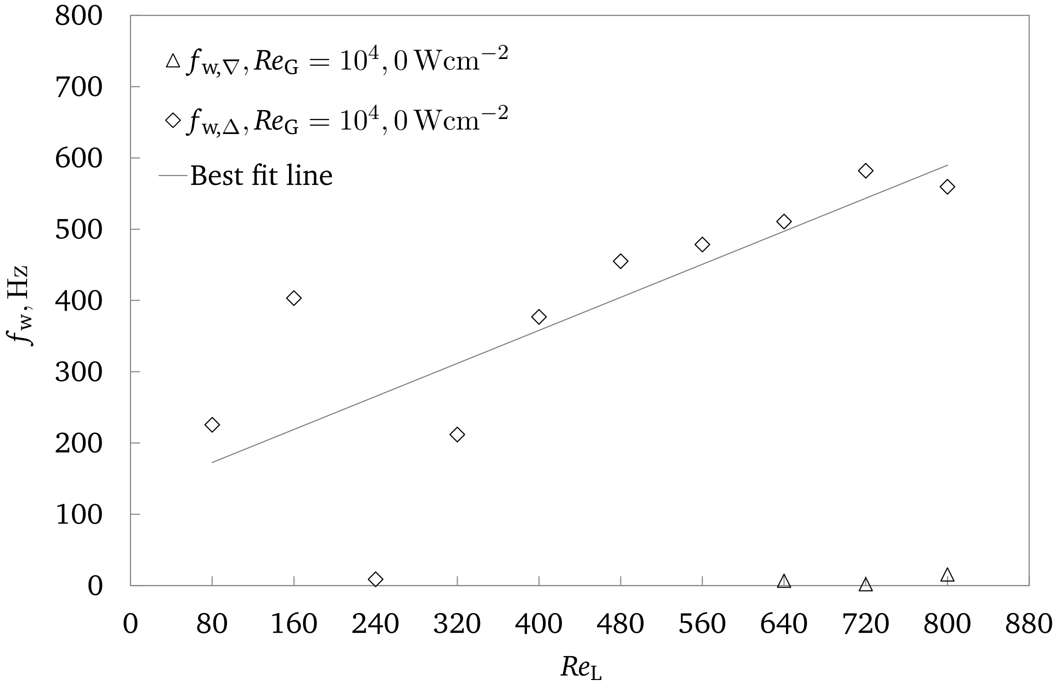

Figure 7.73. Comparison of the wave frequency $f_{\mathrm{w},\nabla}$, $f_{\mathrm{w},\Delta}$ of the gas-driven films measured at the ∇-grooved and Δ-structured surfaces at the axial position $z = 45\,\mathrm{mm}$ for $\dot{q}_{\mathrm{W}} = 0$, $Re_{\mathrm{L}} = 80 - 800$, and $Re_{\mathrm{G}} = 10^4$

The standard deviations and the corresponding wave frequencies of gas-driven film flows at all three surfaces are compared in this paragraph. The results of measurements carried out at $z = 45\,\mathrm{mm}$ are depicted for instance, since at the other axial location the parameters will change accordingly. In Fig. 7.72 the impact of the surface topography on σ_{O}, σ_{∇}, and σ_{Δ} can be distinguished. The largest standard deviation could be obtained by the pyramid structure followed by the ∇-grooved surface and the unstructured surface used as reference. The sharp increase of σ_{Δ} at $Re_{\mathrm{L}} = 480$ can maybe attributed to the fact that the waves came out of the Δ-structures due to flooding of the surface with liquid. An increase of Re_{L} produces a growth of the interfacial fluctuations. The liquid film on structured walls recognize remarkable disturbances compared to the unstructured wall [74]. The disturbing effect of the pyramid surface is the strongest one, since the geometry has also a perpendicularly oriented barrier effect with regard to the liquid flow direction (see Figs. 3.21 and 3.23). One reason for the formation of the crest is the pressure increase in the vicinity of the wetting front [76]. Compared to that, the ∇-grooved geometry is only longitudinally oriented and does not cause a static jump. Also the wave frequency is high at the Δ-structured surface showing almost a linear trend with increasing Re_{L} (see Fig. 7.73). This is probably the result of the same effect explained above. At the unstructured and at the ∇-grooved surface barely no waves were detected. The film at the unstructured tube is rather stable as discussed before. The reason for the ∇-grooved surface could be the partial wetting phenomena where waves are propagate within the troughs and therefore not visible for the high-speed camera. Furthermore the stabilizing effect could have come into presence [61].

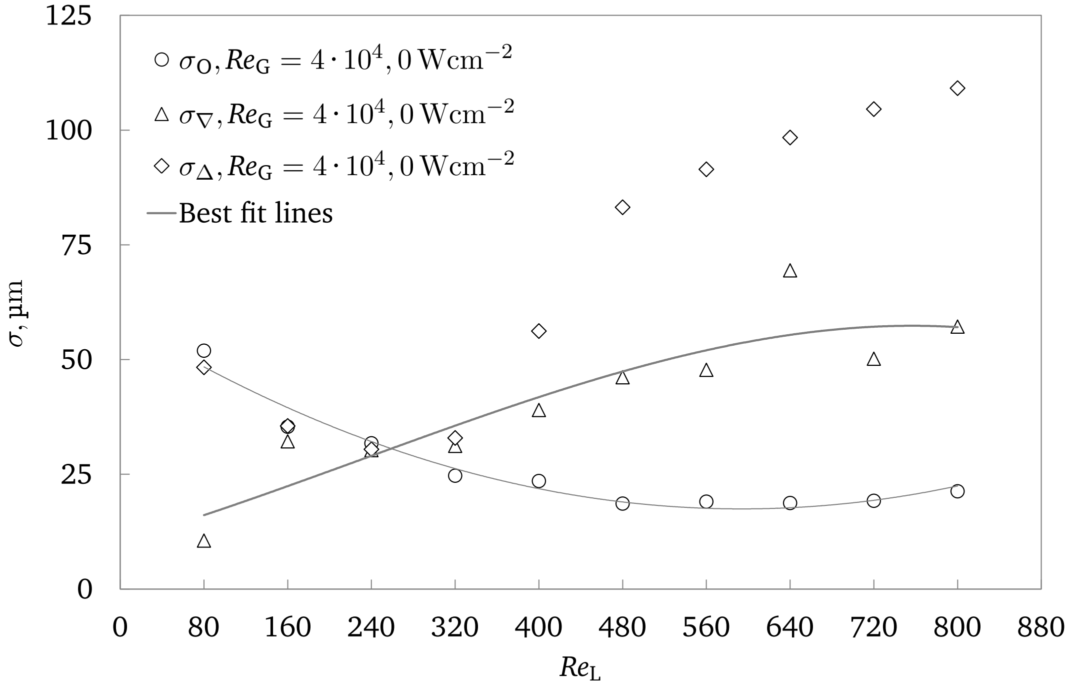

Figure 7.74. Comparison of the standard deviation σ_O, σ_∇, σ_Δ of the gas-driven films measured at the unstructured, ∇-grooved, and Δ-structured surfaces at the axial position $z = 45\,\mathrm{mm}$ for $\dot{q}_W = 0$, $Re_L = 80 - 800$, and $Re_G = 4 \cdot 10^4$

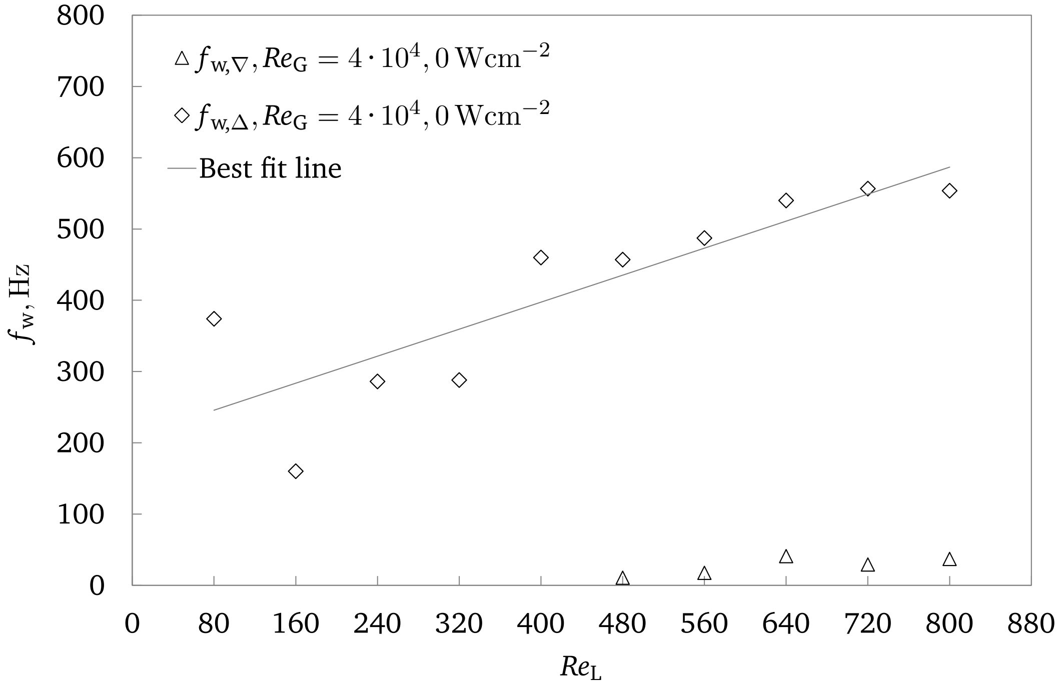

Figure 7.75. Comparison of the wave frequency $f_{w,\nabla}$, $f_{w,\Delta}$ of the gas-driven films measured at the ∇-grooved and Δ-structured surfaces at the axial position $z = 45\,\mathrm{mm}$ for $\dot{q}_W = 0$, $Re_L = 80 - 800$, and $Re_G = 4 \cdot 10^4$

A further rise in shear stress ($Re_G = 4 \cdot 10^4$) contributes to the growth of the standard deviation for all surfaces but $f_{w,\Delta}$ remains almost constant following with the same trend mentioned before (see Figs. 7.74

and 7.75). Only a few waves appeared at the ∇-grooved surface, while at the unstructured surface no waves were detected. The higher shear stress leads to a stronger deformation of the film at the unstructured surface resulting in a growth of σ_{O}. Similarly more fluctuations occurred at the ∇-grooved surface, since more liquid can be pushed out of the structure troughs. Compared to that, it seems that the wave generation on the pyramid structure is not significantly affected by the increase of shear stress compared to the other topographies. The standard deviation and the wave frequency is rather dominated by Re_{L} which causes a sharp increase at $Re_{\mathrm{L}} = 400$ for σ_{Δ}. This increase can be described by the flooding of the Δ-structures as explained before.

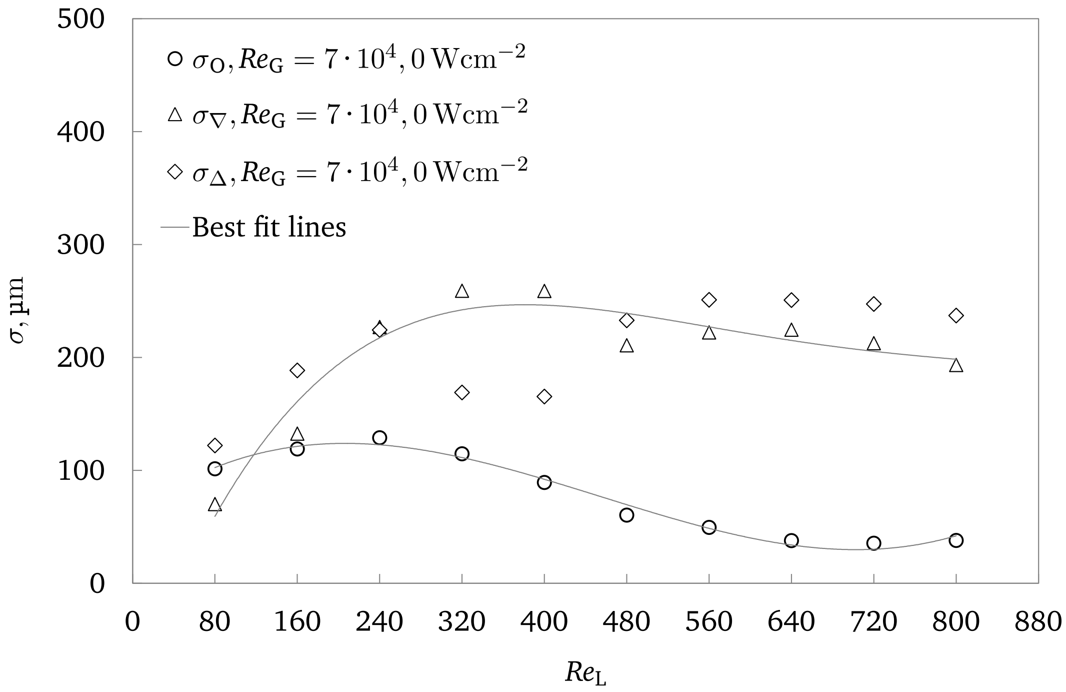

Figure 7.76. Comparison of the standard deviation σ_{O}, σ_{∇}, σ_{Δ} of the gas-driven films measured at the unstructured, ∇-grooved, and Δ-structured surfaces at the axial position $z = 45\,\mathrm{mm}$ for $\dot{q}_{\mathrm{W}} = 0$, $Re_{\mathrm{L}} = 80 - 800$, and $Re_{\mathrm{G}} = 7 \cdot 10^4$

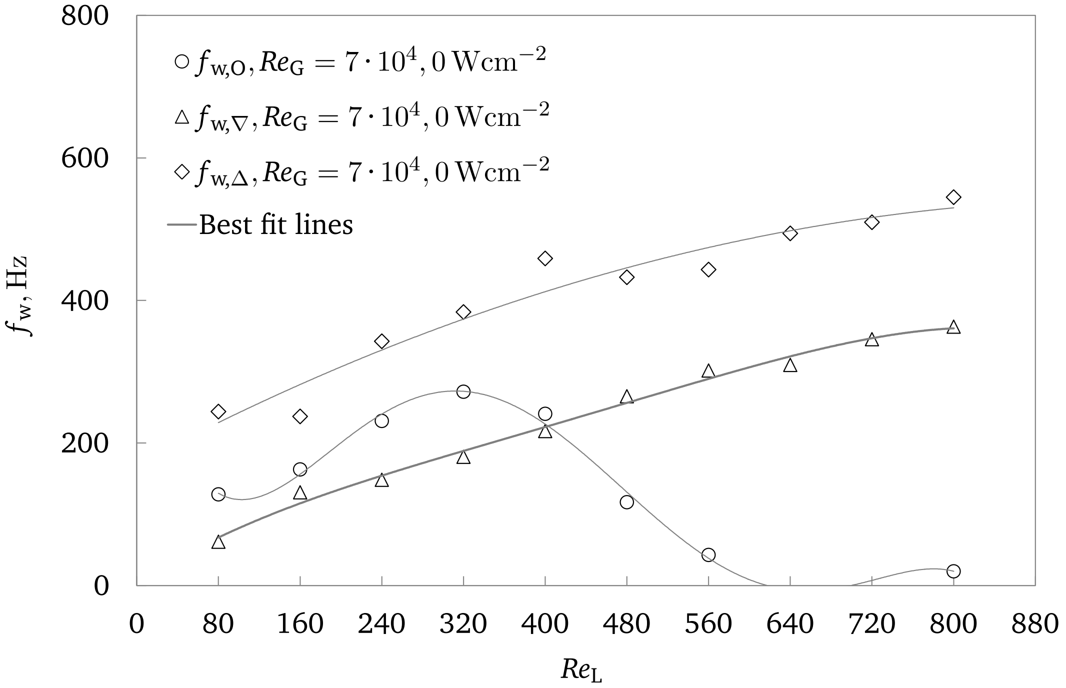

Figure 7.77. Comparison of the wave frequency $f_{\mathrm{w,O}}, f_{\mathrm{w,\nabla}}, f_{\mathrm{w,\Delta}}$ of the gas-driven films measured at the unstructured, ∇-grooved and Δ-structured surfaces at the axial position $z = 45\,\mathrm{mm}$ for $\dot{q}_{\mathrm{W}} = 0$, $Re_{\mathrm{L}} = 80 - 800$, and $Re_{\mathrm{G}} = 7 \cdot 10^4$

At $Re_{\mathrm{G}} = 7 \cdot 10^4$, the largest standard deviation and wave frequency resulted as illustrated in Figs. 7.76 and 7.77. For liquid Reynolds numbers $480 - 800$ the pyramid structured surface causes the larges fluctuations, while σ_{∇} is comparable high to those at the Δ-structured surface. The standard deviation at the unstructured surface for this range of liquid Reynolds number is the smallest. In the case of $Re_{\mathrm{G}} = 80 - 400$ the fluctuations at the ∇-grooved surface is not the highest, while the fluctuations at the pyramid surface and unstructured surface is lower. At this flow parameters a partial wetting at the structured surfaces can be assumed. Due to the increase of shear stress acting on less amount of liquid exhibiting weak inertia, stronger deformations and higher undulations can be generated at the ∇-grooved surface. In the case of Δ-structured surface, the momentum energy induced by the gas stream is not only transferred for the formation of waves. The momentum forces have to overcome also the friction caused by the unwetted pyramid crest and the increased friction at the wall-liquid interface. This effect does not carry weight in terms of the ∇-grooved surface, since the structures are oriented parallel to the flow direction of both the fluids. Besides that the standard deviation at the unstructured surface is the lowest. A remarkable growth of the wave frequencies at this gas mass flow rate were obtained. The number of waves and the trend has not significantly changed for the liquid film flowing over the Δ-structured surface, but represents the highest values. This is followed by the wave frequencies appeared at the ∇-grooved surface with a linear trend and the wave frequencies for the unstructured surface.

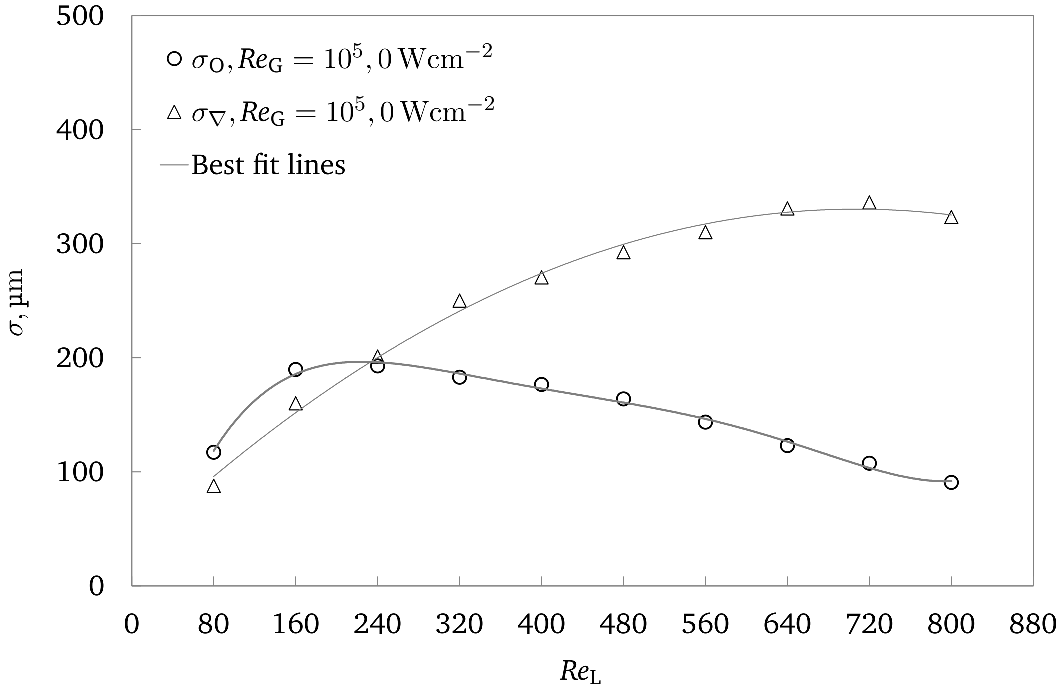

Figure 7.78. Comparison of the standard deviation σ_{O} and σ_{∇} of the gas-driven films measured at the unstructured and ∇-grooved surfaces at the axial position $z = 45\,\mathrm{mm}$ for $\dot{q}_{\mathrm{W}} = 0$, $Re_{\mathrm{L}} = 80 - 800$, and $Re_{\mathrm{G}} = 10^5$

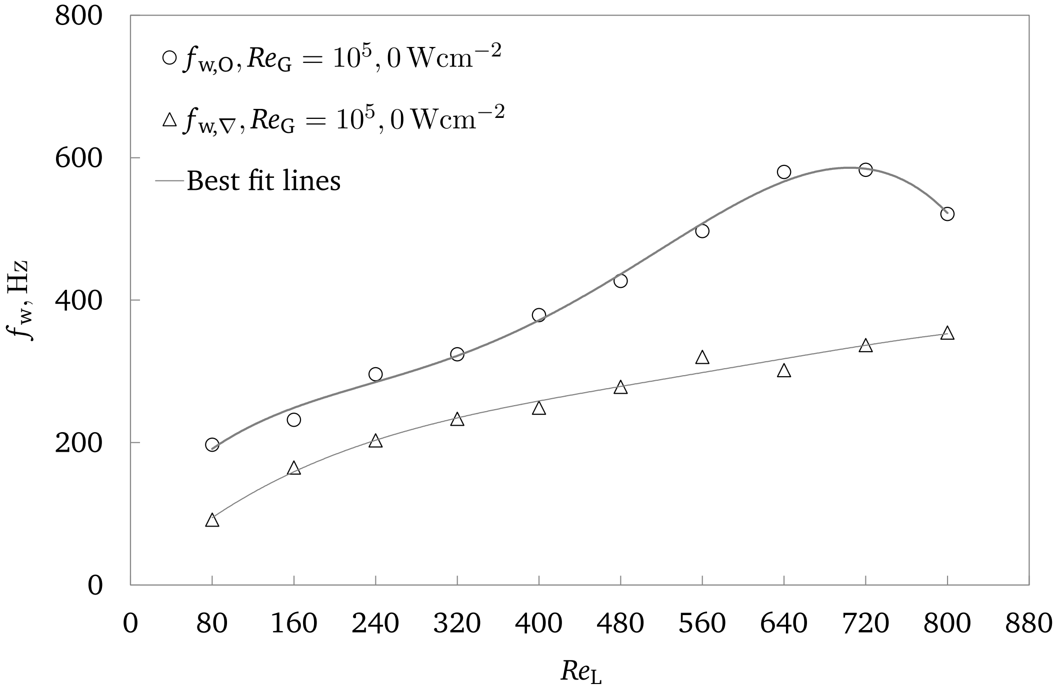

Figure 7.79. Comparison of the wave frequency $f_{\mathrm{w,O}}$ and $f_{\mathrm{w},\nabla}$ of the gas-driven films measured at the unstructured and ∇-grooved surfaces at the axial position $z = 45\,\mathrm{mm}$ for $\dot{q}_{\mathrm{W}} = 0$, $Re_{\mathrm{L}} = 80 - 800$, and $Re_{\mathrm{G}} = 10^5$

In the case of $Re_{\mathrm{G}} = 10^5$, σ_{∇} is higher than σ_{O} on the unstructured surface (see Fig. 7.78). However, the development of $f_{\mathrm{w,O}}$ and $f_{\mathrm{w},\nabla}$ shows a reverse character as illustrated in Fig. 7.79. Although longitudinal grooves do not represent any horizontal oriented obstructions, micro roughnesses with varying depths due to the manufacturing process are located at the faces of the grooves which can lead to an increased friction. This results in a stronger deformation of the liquid film due to increased pressure loss within the liquid bulk accompanied by a suppression of the liquid velocity. Another effect can be that due to the rather turbulent gas flow velocity components in φ-direction can form waves jumping over the groove crest.

7.2.4 Dimensionless wall temperature distribution at ∇-grooved surface

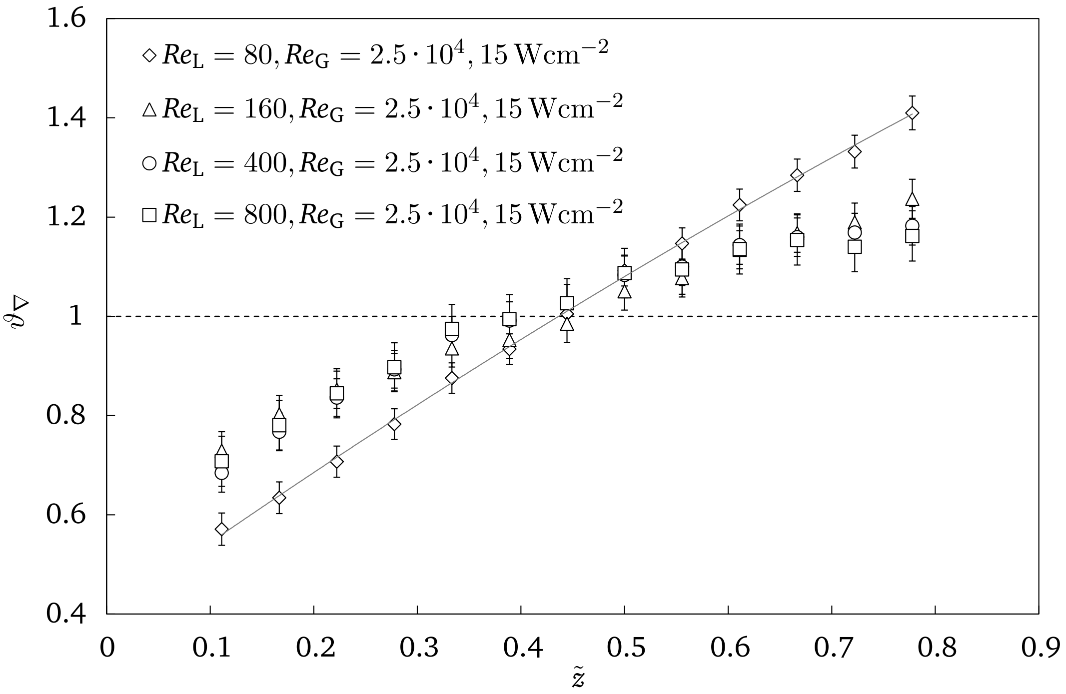

Figure 7.80. Dimensionless temperature ϑ_∇ distribution at the ∇-grooved surface over dimensionless length $\tilde{z}$ for $Re_L = 80, 160, 400, 800$ and $\dot{q}_W = 15\,\mathrm{Wcm^{-2}}$ at $Re_G = 2.5 \cdot 10^4$.

Measurements at the ∇-grooved surface regarding the axial distribution of the dimensionless temperature ϑ_∇ are displayed in Figs. 7.80 and 7.81. The values are presented for $T_{L,in} = 298\,\mathrm{K}$ at a gas Reynolds number of $2.5 \cdot 10^4$ and $5.5 \cdot 10^4$. In both the figures, ϑ_∇ increases with growing length due to liquid heat-up. The strongest gradient of ϑ_∇ resulted for $Re_L = 80$ for both Re_G. At these conditions, a partial wetting can be expected where the groove crests are exposured to the gas stream. Thereby, a portion of heat is transferred into the liquid traveling in the groove troughs. The other portion of heat is transferred to the gas stream by the unwetted groove crests acting as fins. However, as Re_L increases the gradient of ϑ_∇ in both the cases reduces. At the largest Re_L, the ∇-grooves might be fully covered, hence all the heat is transferred into the liquid. This results in a decrease of ϑ_∇, which might be attributed to the increased liquid velocity.

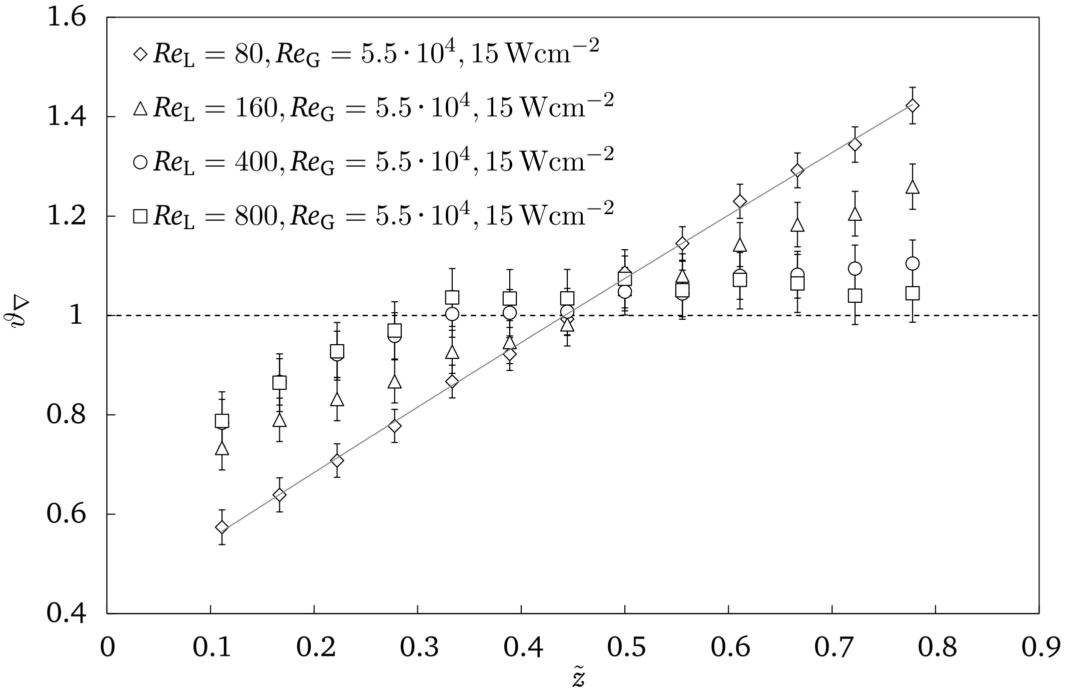

Figure 7.81. Dimensionless temperature ϑ_∇ distribution at the ∇-grooved surface over dimensionless length $\tilde{z}$ for $Re_\mathrm{L} = 80, 160, 400, 800$ and $\dot{q}_\mathrm{W} = 15\,\mathrm{Wcm^{-2}}$ at $Re_\mathrm{G} = 5.5 \cdot 10^4$.

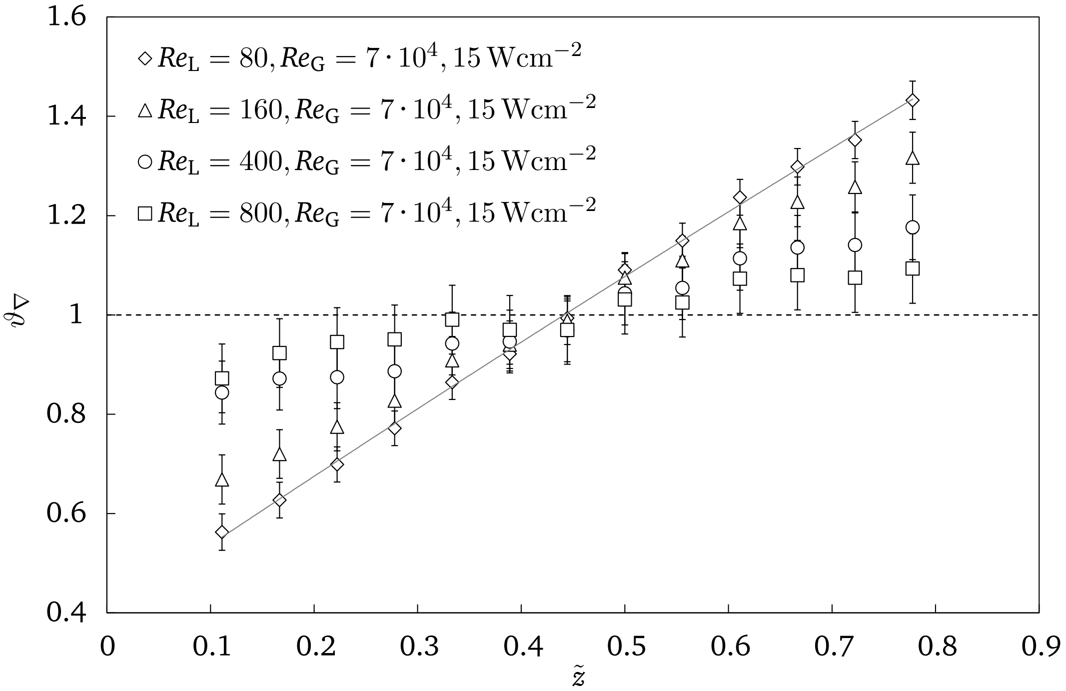

Figure 7.82. Dimensionless temperature ϑ_∇ distribution at the ∇-grooved surface over dimensionless length $\tilde{z}$ for $Re_\mathrm{L} = 80, 160, 400, 800$ and $\dot{q}_\mathrm{W} = 15\,\mathrm{Wcm^{-2}}$ at $Re_\mathrm{G} = 7 \cdot 10^4$.

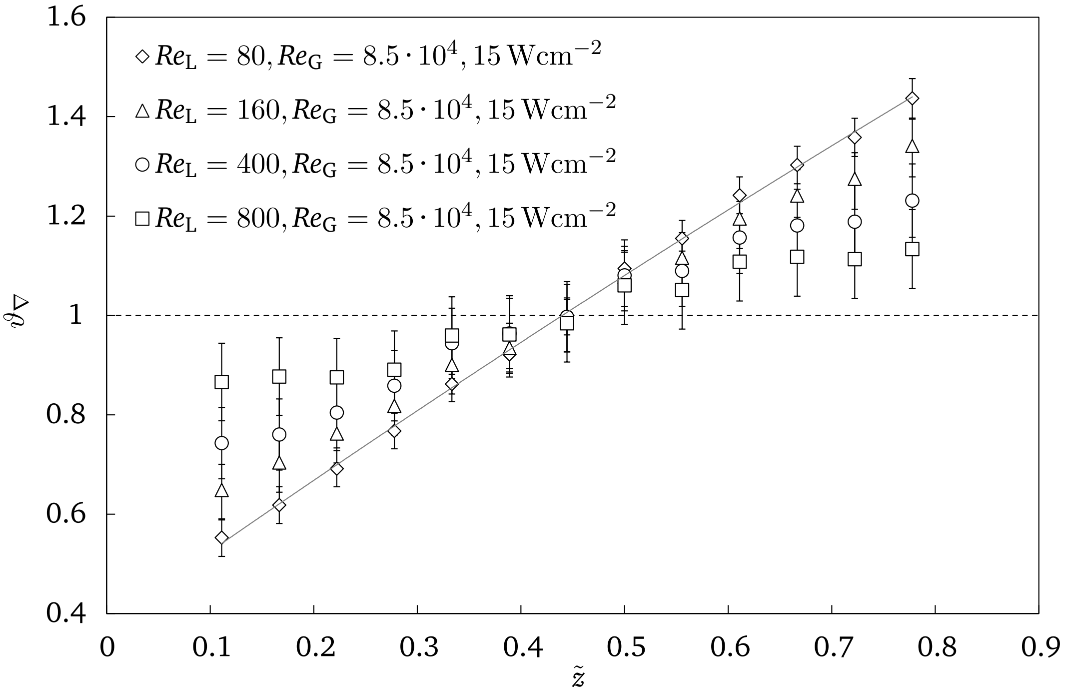

Figure 7.83. Dimensionless temperature ϑ_∇ distribution at the ∇-grooved surface over dimensionless length $\tilde{z}$ for $Re_\mathrm{L} = 80, 160, 400, 800$ and $\dot{q}_\mathrm{W} = 15\,\mathrm{Wcm^{-2}}$ at $Re_\mathrm{G} = 8.5 \cdot 10^4$.

Within $\tilde{z} = 0.33 - 0.78$ the gradient of ϑ_∇ is weaker for $Re_\mathrm{G} = 5.5 \cdot 10^4$ than for the lower gas Reynolds number, resultantly, the ϑ_∇ values are closer to 1. This is maybe caused by the occurrence of waves kindled by increased shear stress. Over this $\tilde{z}$ range, the waves internal mixing increases and lead to a stronger decrease of the local wall temperature compared to the case of $Re_\mathrm{G} = 2.5 \cdot 10^4$ where a weaker internal mixing process exists, possibly.

Similar trend of ϑ_∇ can be identified for $Re_\mathrm{G} = 7 \cdot 10^4$ and $Re_\mathrm{G} = 8.5 \cdot 10^4$ as shown in Figs. 7.82 and 7.83. For both the cases, the gradients of ϑ_∇ at $Re_\mathrm{L} = 80$ has minor increased but decrease stronger with Re_L within $\tilde{z} = 0.11 - 0.33$ compared to the measurements at lower shear stress. A reason therefore might be that high frequent waves with large amplitudes are formed in the initial zone (see Fig. 7.48 and 7.49) compared to lower Re_G as shown exemplarily in Fig. 7.45. Since large amplitude waves incorporate a zone of strong recirculating liquid (internal mixing), the wall temperature reduces [47, 143].

7.2.5 Dimensionless wall temperature distribution at Δ-structured surface

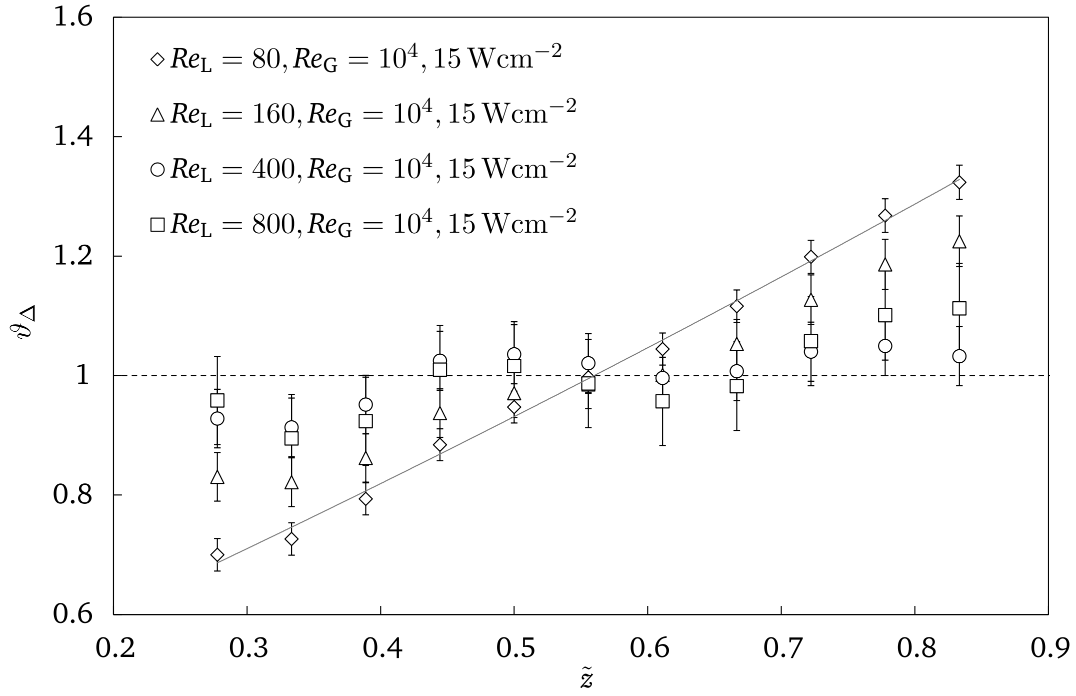

Figure 7.84. Dimensionless temperature ϑ_Δ distribution at the Δ-structured surface over dimensionless length $\tilde{z}$ for $Re_L = 80, 160, 400, 800$, $\dot{q}_W = 15\,\mathrm{Wcm^{-2}}$, $T_{L,in} = 298\,\mathrm{K}$ at $Re_G = 10^4$.

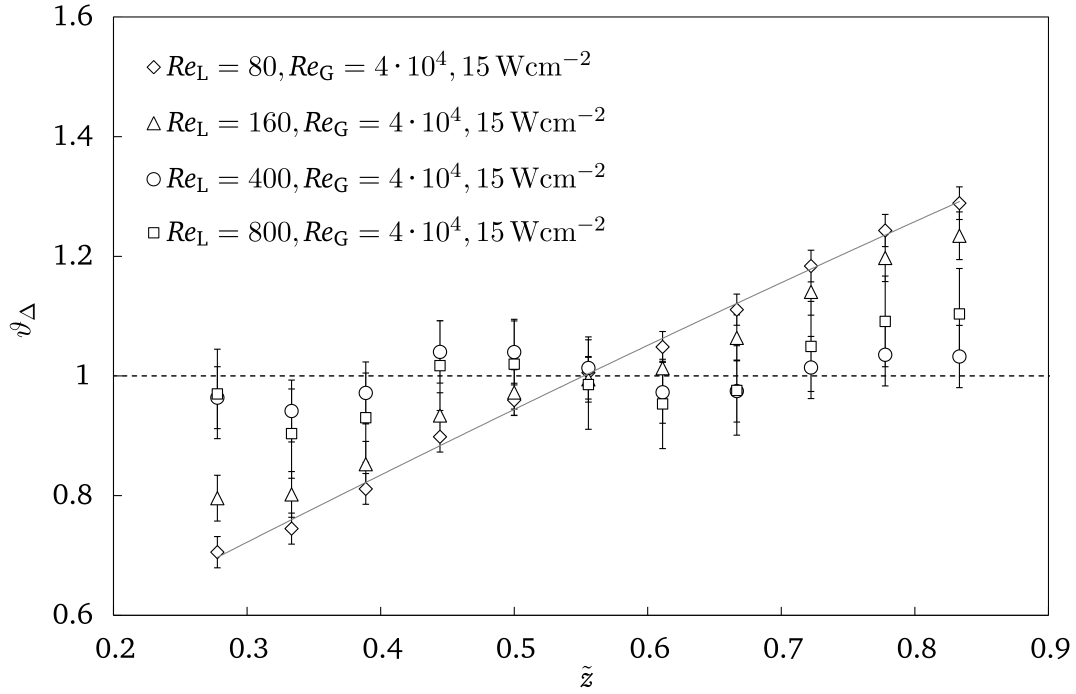

Figure 7.85. Dimensionless temperature ϑ_Δ distribution at the Δ-structured surface over dimensionless length $\tilde{z}$ for $Re_L = 80, 160, 400, 800$, $\dot{q}_W = 15\,\mathrm{Wcm^{-2}}$, $T_{L,in} = 298\,\mathrm{K}$ at $Re_G = 4 \cdot 10^4$.

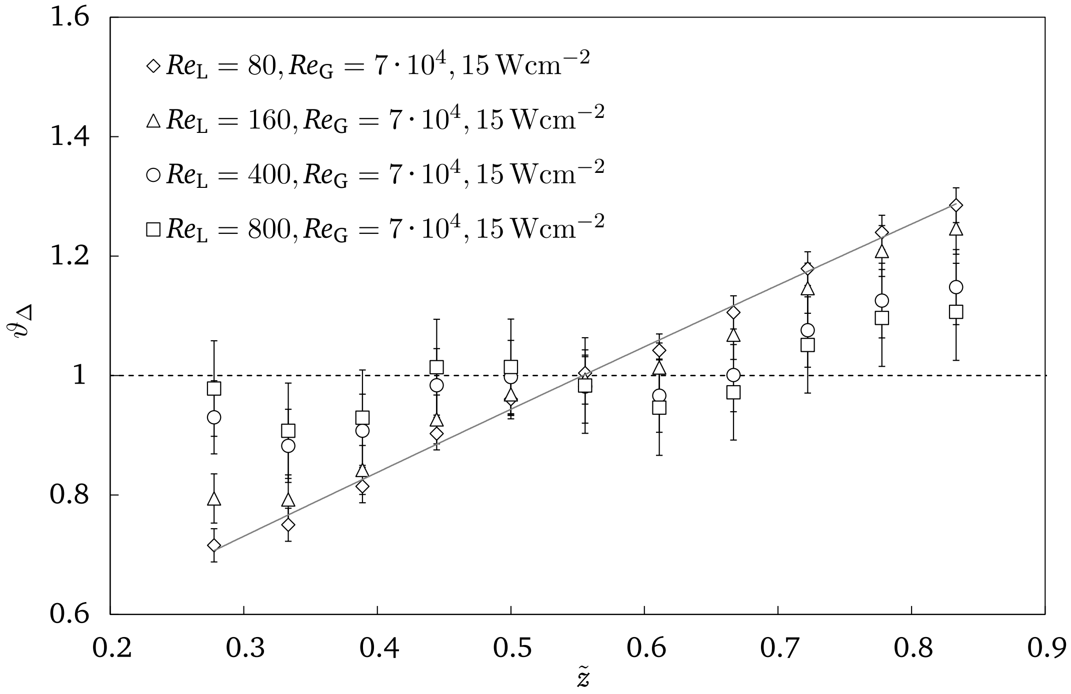

Figure 7.86. Dimensionless temperature ϑ_Δ distribution at the Δ-structured surface over dimensionless length $\tilde{z}$ for $Re_\mathrm{L} = 80, 160, 400, 800$, $\dot{q}_\mathrm{W} = 15\,\mathrm{Wcm}^{-2}$, $T_\mathrm{L,in} = 298\,\mathrm{K}$ at $Re_\mathrm{G} = 7 \cdot 10^4$.

In Figs. 7.84, 7.85, and 7.86 the distribution of ϑ_Δ for varying Re_L and Re_G is shown for the gas-driven liquid film flow at the Δ-structured surface. The measurements were carried out at $\dot{q}_\mathrm{W} = 15\,\mathrm{Wcm}^{-2}$. For all Re_G, an increasing linear trend of ϑ_Δ over $\tilde{z}$ can be seen for $Re_\mathrm{L} = 80$. The gradient of ϑ_Δ decreases when rising Re_L up to 800. This is probably due to the increase in film waviness as discussed in Sec. 7.2.2. However, it seems that the distribution of ϑ_Δ at the Δ-structured surface does not show any influence of Re_G. The values are rather dominated by Re_L.

7.2.6 Comparison of dimensionless temperature distribution at unstructured, ∇-grooved and Δ-structured surfaces

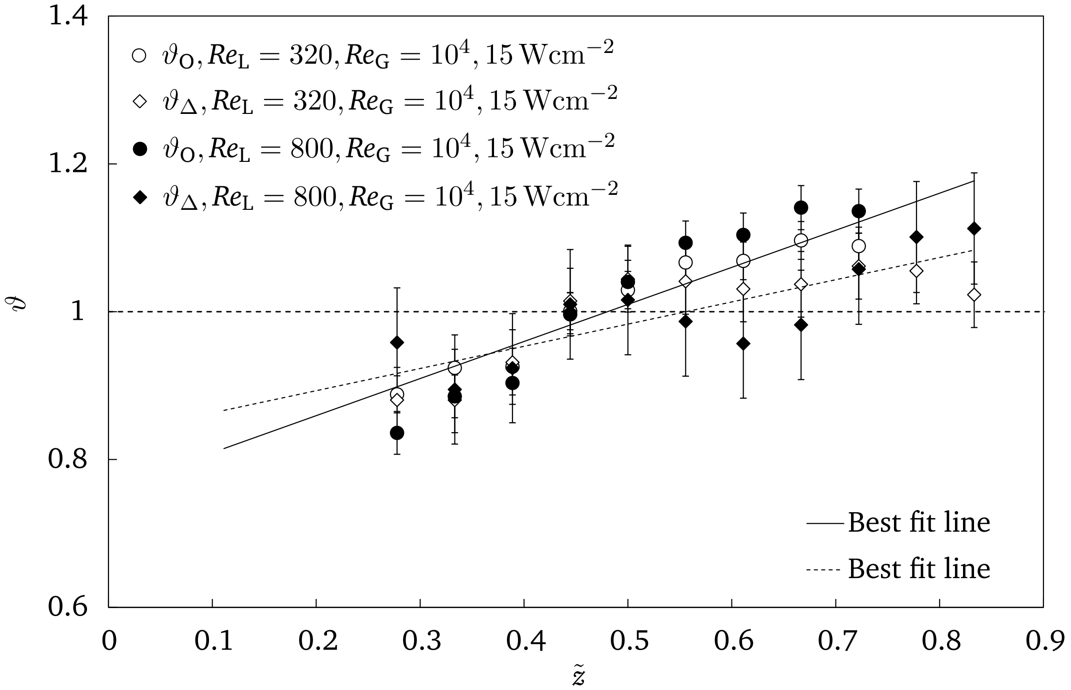

Figure 7.87. Comparison of dimensionless temperature profiles ϑ_O and ϑ_Δ as a function of $\tilde{z}$ for $T_\mathrm{L,in} = 298\,\mathrm{K}$, $\dot{q}_\mathrm{W} = 15\,\mathrm{W cm^{-2}}$ at $Re_\mathrm{G} = 10^4$ and $Re_\mathrm{L} = 320, 800$.

In Figs. 7.87, 7.88, and 7.89, selected results of the dimensionless temperatures ϑ_O, ϑ_∇, and ϑ_Δ are compared exemplary for experiments performed at $T_\mathrm{L,in} = 298\,\mathrm{K}$, $\dot{q}_\mathrm{W} = 15\,\mathrm{W cm^{-2}}$. The comparison in Fig. 7.87 carried out for $Re_\mathrm{G} = 10^4$ and $Re_\mathrm{L} = 320$ shows that above $\tilde{z} > 0.5$ the slope of ϑ_Δ is comparable weaker than that of ϑ_O. The reason therefore can be the waviness which is permanently promoted through the Δ-structures and sustains probably over the entire length. In both the cases the increase of Re_L leads minor decrease of the ϑ_Δ gradient while the slope of ϑ_O persists almost constant. A rise in Re_G shows neither a significant influence on ϑ_O nor on ϑ_Δ as illustrated in Fig. 7.88.

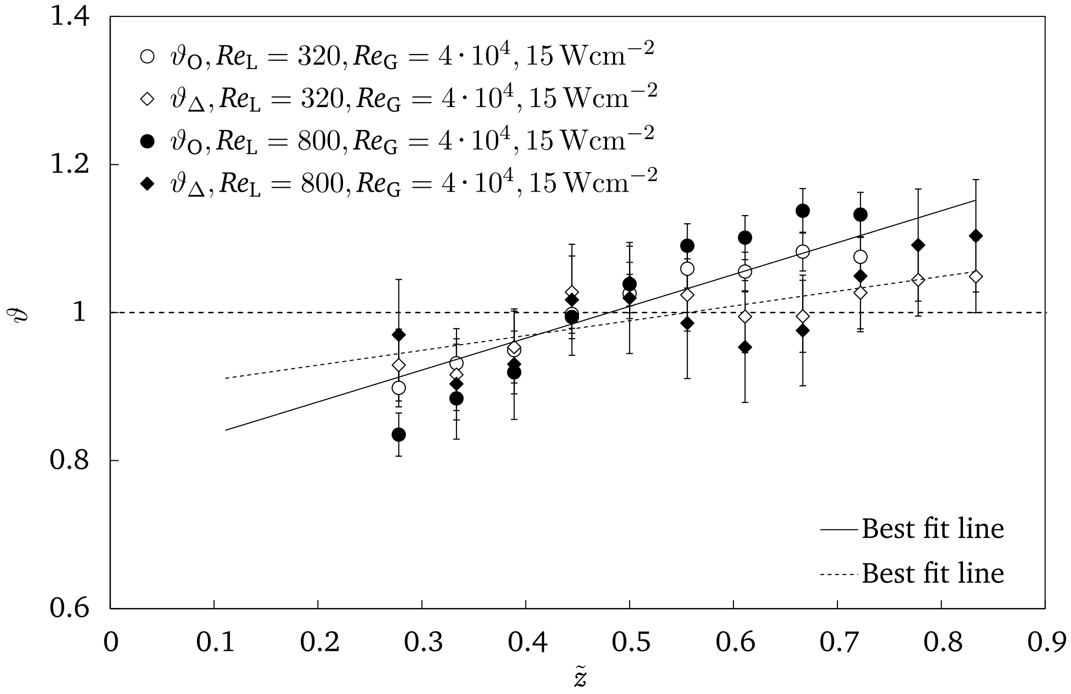

Figure 7.88. Comparison of dimensionless temperature profiles ϑ_O and ϑ_Δ as a function of $\tilde{z}$ for $T_{L,in} = 298\,\mathrm{K}$, $\dot{q}_W = 15\,\mathrm{Wcm^{-2}}$ at $Re_G = 4 \cdot 10^4$ and $Re_L = 320, 800$.

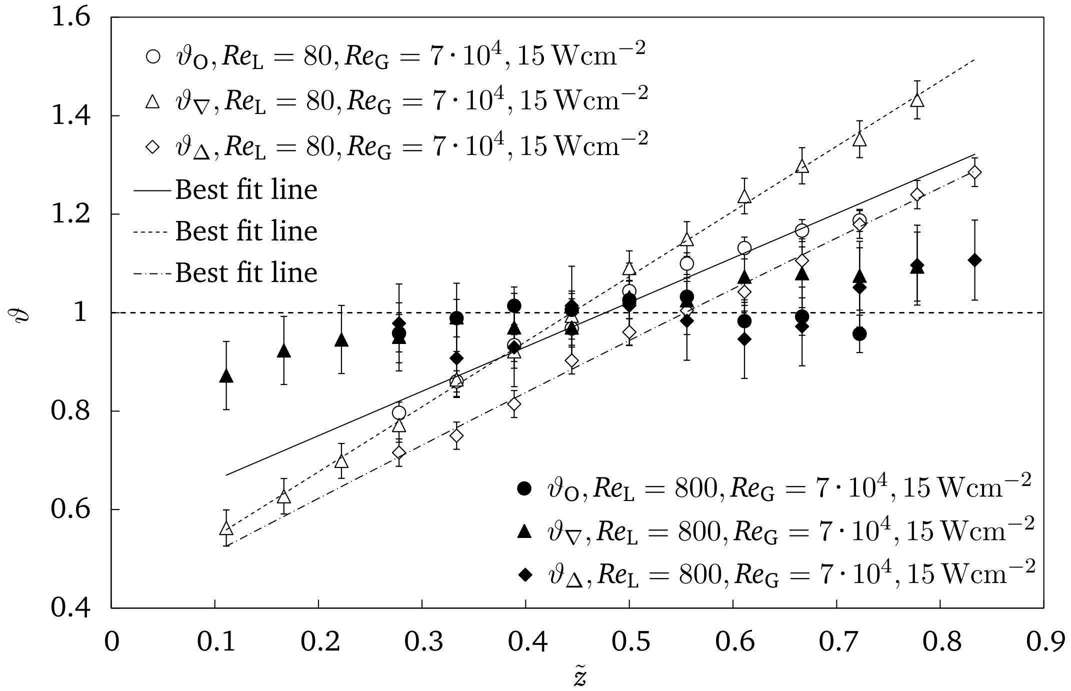

Figure 7.89. Comparison of dimensionless temperature profiles ϑ_O, ϑ_∇, and ϑ_Δ as a function of $\tilde{z}$ for $T_{L,in} = 298\,\mathrm{K}$, $\dot{q}_W = 15\,\mathrm{Wcm^{-2}}$ at $Re_G = 7 \cdot 10^4$ and $Re_L = 80, 800$.

The comparison in Fig. 7.89 shows the distribution of ϑ_O, ϑ_∇, and ϑ_Δ at $Re_G = 7 \cdot 10^4$ and $Re_L = 80, 800$. At $Re_L = 80$ strongest gradient of the dimensionless temperature resulted for the ∇-grooved surface, followed by the unstructured and Δ-structured surface. This difference is significantly reduced by increasing Re_L. This can be an effect of the partial wetting phenomenon where the direct contact between wall and gas is introduced. At low liquid loads this effect appeared at both the structured surfaces. The results indicate that this effect seems to be stronger at the ∇-grooved surface rather at the Δ-structured surface which has to be further investigated.

7.2.7 Nusselt number, film break-up and rewetting phenomenon at ∇-grooved surface

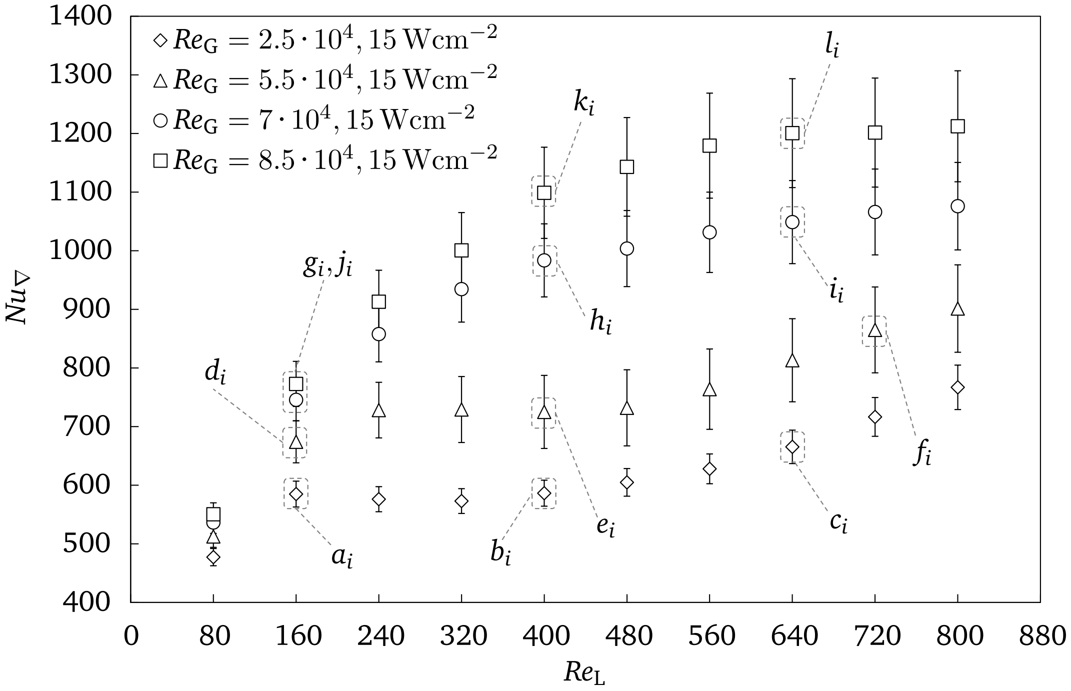

Figure 7.90. Nusselt number Nu_∇ for gas-driven film flow at the ∇-grooved surface measured at $\dot{q}_W = 15\,\mathrm{Wcm^{-2}}$ for $Re_L = 80 - 800$, $Re_G = 2.5 \cdot 10^4 - 8.5 \cdot 10^4$, and $T_{L,in} = 298\,\mathrm{K}$. Labeled values correspond to image sequences shown in Figs. 7.91 - 7.94.

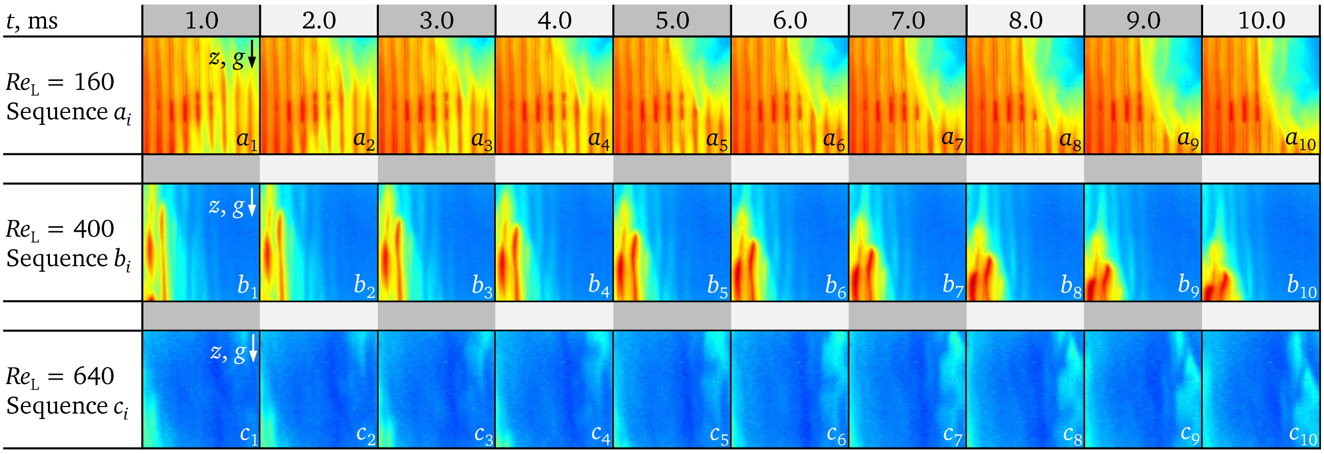

Figure 7.91. Film dynamics at the ∇-grooved surface for $Re_L = 160, 400, 640$, $Re_G = 2.5 \cdot 10^4$ for $T_{L,in} = 298\,\mathrm{K}$ captured at $z = 45\,\mathrm{mm}$ with high speed infrared camera.

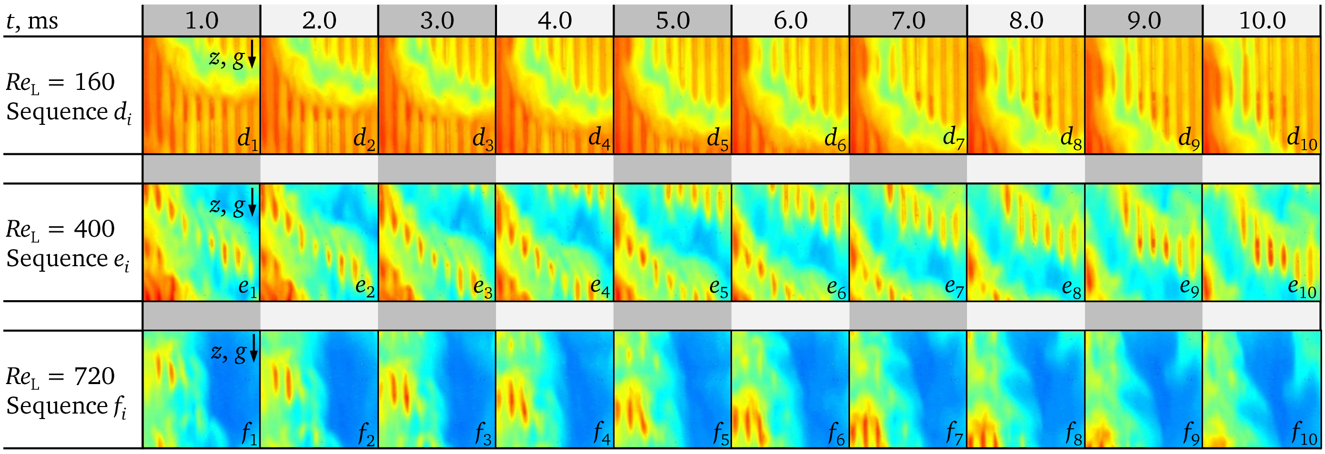

Figure 7.92. Film dynamics at the ∇-grooved surface for $Re_L = 160, 400, 720$, $Re_G = 5.5 \cdot 10^4$ for $T_{L,in} = 298\,\mathrm{K}$ captured at $z = 45\,\mathrm{mm}$ with high speed infrared camera.

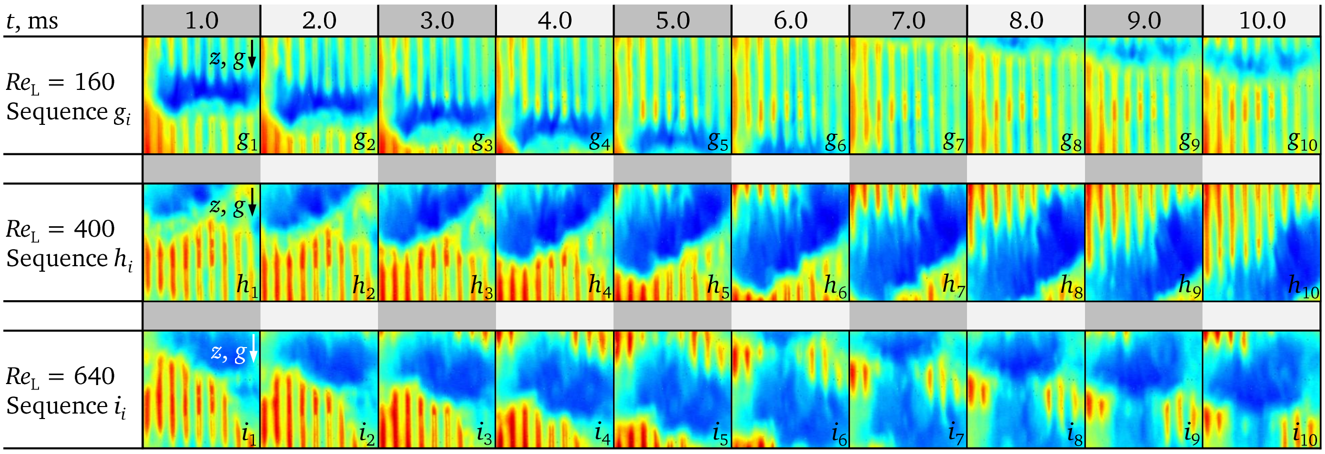

Figure 7.93. Film dynamics at the ∇-grooved surface for $Re_L = 160, 400, 640$, $Re_G = 7 \cdot 10^4$ for $T_{L,in} = 298\,\mathrm{K}$ captured at $z = 45\,\mathrm{mm}$ with high speed infrared camera.

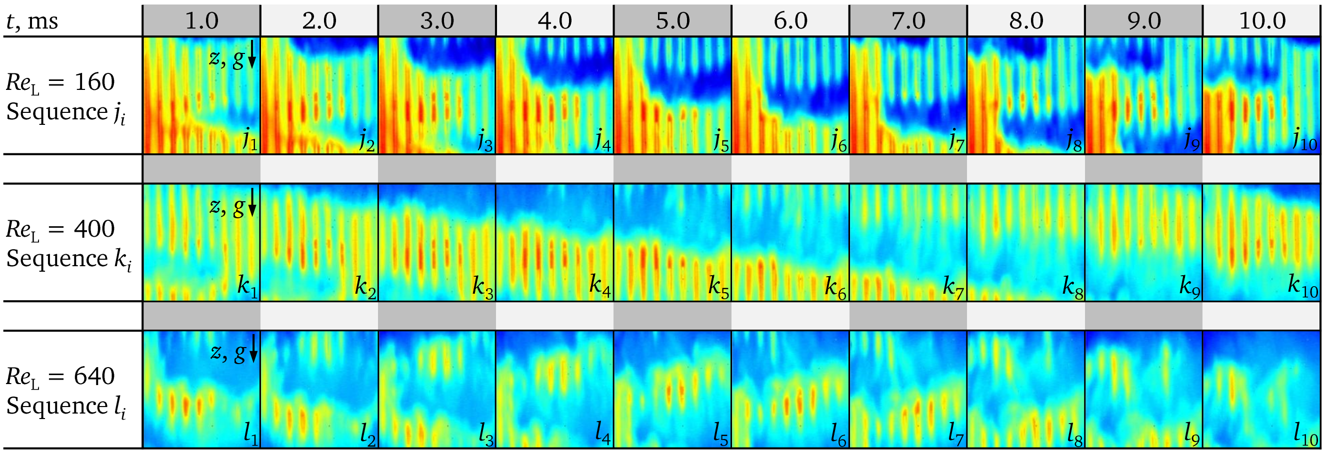

Figure 7.94. Film dynamics at the ∇-grooved surface for $Re_L = 160, 400, 640$, $Re_G = 8.5 \cdot 10^4$ for $T_{L,in} = 298\,\mathrm{K}$ captured at $z = 45\,\mathrm{mm}$ with high speed infrared camera.

Based on the measurements on gas-driven films executed at the ∇-grooved surface the Nusselt numbers as a function of Re_L and Re_G for $T_\mathrm{L,in} = 298\,\mathrm{K}$ are shown in Fig. 7.90. The lowest values resulted at $Re_\mathrm{L} = 80$ for all Re_G. This can be attributed to the partial wetting phenomenon which can be expected at low liquid loads (for instance see image sequences a_i, d_i, g_i, and j_i in Fig. 7.91 - 7.94). In spite waves are formed with higher shear stress, the mean wall temperature increases and involves a low heat transfer coefficient. However, the increase in Re_G causes a significant growth in Nu_∇. This can be explained by several reasons as follows.

First, the disturbances at the liquid-gas interface increase, since stronger shear stress acts at the liquid film surface. As shown in the image sequences in Figs. 7.92 - 7.94 and the results of σ_∇ and $f_{\mathrm{w},\nabla}$ in Figs. 7.41 and 7.42, the disturbances transform into large waves with high frequency. Once large waves are formed and propagating along the flow direction, two mechanisms are introduced. One mechanism is the appearance of a thin liquid substrate film which is present between the waves. The thickness of this liquid layer is determined by the height of the wave amplitude and hence the shear stress. As the wave amplitude grow, a thinner substrate liquid film results. Thereby its thermal resistance reduces which promotes the enhancement of heat transfer. At sufficiently high shear stress, dewetting at the surface can occur which leads to the formation of the three-phase contact line. In the vicinity of a three phase contact line advancing over a hot surface, the heat transfer is very high compared to the region of the bulk of the liquid [85]. This finding can be transferred to a wave propagating over the hot ∇-groove. The sharp wave front shears a thin hot liquid existing ahead and cools down the surface with cold liquid transported withing the wave crest. This process is represented by a recirculating zone where the hot liquid is transported towards the liquid-gas interface and heat is transferred into the turbulent gas stream. At the region of the wave front, sharp temperature gradients should exist indicating high local heat transfer rates. Furthermore, the unwetted crests of the ∇-grooves are subjected to the cold gas which additional enhances the heat transfer.

With respect to the measurement errors, the Nu_∇ profile for $Re_\mathrm{G} = 2.5 \cdot 10^4$ is does not show any gradient within $Re_\mathrm{L} = 160 - 400$ while from $Re_\mathrm{L} = 480$ onward, the trend is gradually increasing. This is maybe due to the fact that in the first Re_L range, a transition from partial wetting into fully flooded structures takes place. During the partial wetted condition, less load of liquid travels in the groove troughs while most of the surface area is in contact with the turbulent gas stream (see image sequence a_i in Fig. 7.91). Thereby, the major portion of heat is probably transferred into the gas stream instead of the liquid film. Once the liquid load on the surface increases, the whole ∇-grooved surface area is gradually wetted until it is almost fully covered by liquid (see image sequence b_i in Fig. 7.91). As a result, the direct contact between the heated wall and the gas stream is strongly disabled and all the major heat is transferred into the liquid. At both conditions, similar heat transfer coefficients resulted. A further rise in $Re_\mathrm{L} > 400$ lead to a surface completely covered by liquid where no unwetted zones are present (see image sequence c_i in Fig. 7.91). Since no contact between wall and gas is existing, the heat transfer enhancement can be only attributed to the growth in liquid velocity and probably the waviness. The latter promotes an intensification of the internal mixing process and hence an increase in Nu_∇. The heat transfer is rather governed by Re_L than by Re_G. In the case of Nu_∇ at $Re_\mathrm{G} = 5.5 \cdot 10^4$, similar trend can be identified. However, the rise in heat transfer coefficient starts at $Re_\mathrm{L} = 560$. When applying the above mentioned explanation, this alludes that the heat transfer between the wall and the gas stream sustains approximately up to this threshold Re_L.

A further rise in liquid mass flow rate, this effect is further suppressed as shown in the image sequences $d_i - e_i$ in Fig. 7.92.

The Nu_∇ at further increased shear stress ($Re_G = 7 \cdot 10^4, 8.5 \cdot 10^4$) does not show any plateau effect similar to those obtained at lower shear stress. For the entire range of Re_L, the infrared image sequences presented in Figs. 7.93 and 7.94 show wave formation and large zones of partially wetted area. Waves with fronts perpendicularly oriented to the flow direction propagate downstream over the surface. According to the σ_∇ development shown in Fig. 7.41 and 7.42, high frequent waves exhibiting large amplitudes can appear which promote the increase of heat transfer by internal mixing and thinning of the substrate film. Furthermore, the heat transfer between the gas flow grows as well. Since the shear stress is stronger, the rupture of liquid increases leading to larger unwetted zones at the surface. This causes a growth in contact time between the heated wall and the gas stream which results in higher heat transfer coefficient. This effect significantly intensifies with increasing gas velocity.

7.2.8 Nusselt number, film break-up and rewetting phenomenon at Δ-structured surface

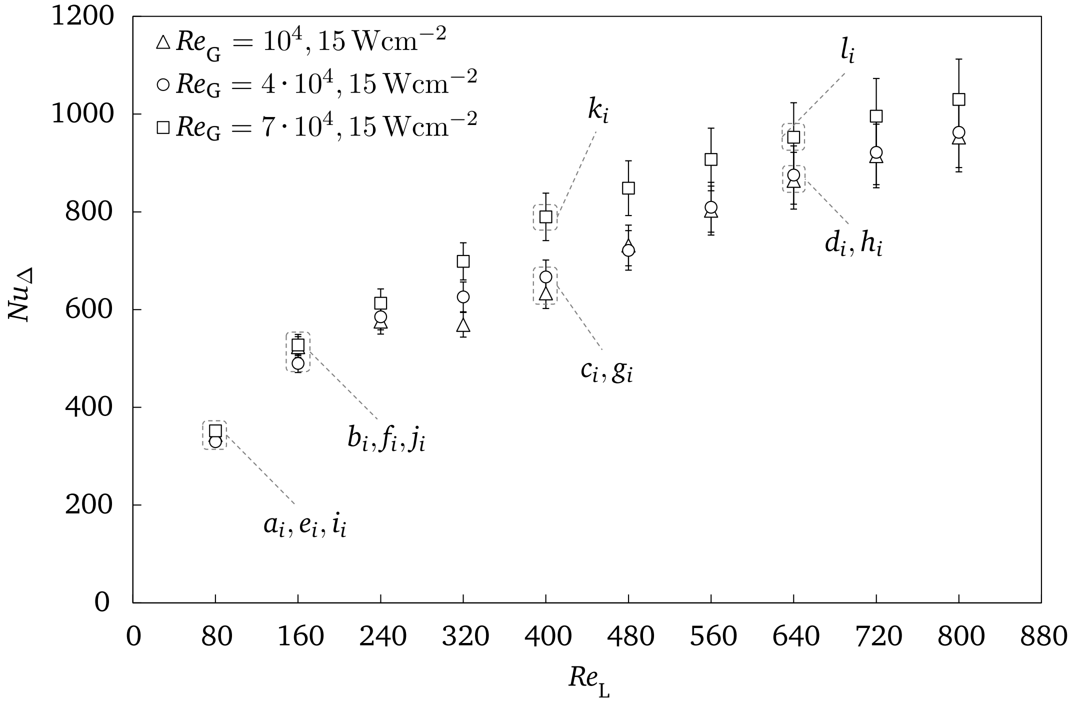

Figure 7.95. Nusselt number Nu_Δ for film flow at Δ-structured surface for $Re_L = 80 - 800$, $Re_G = 10^4 - 7 \cdot 10^4$ and $\dot{q}_W = 15\,\mathrm{Wcm^{-2}}$ at $T_{L,in} = 298\,\mathrm{K}$, labeled values at $Re_L = 80, 160, 400, 640$ correspond to sequences $a_i - l_i$ in Fig. 7.96, Fig. 7.97, and Fig. 7.98.

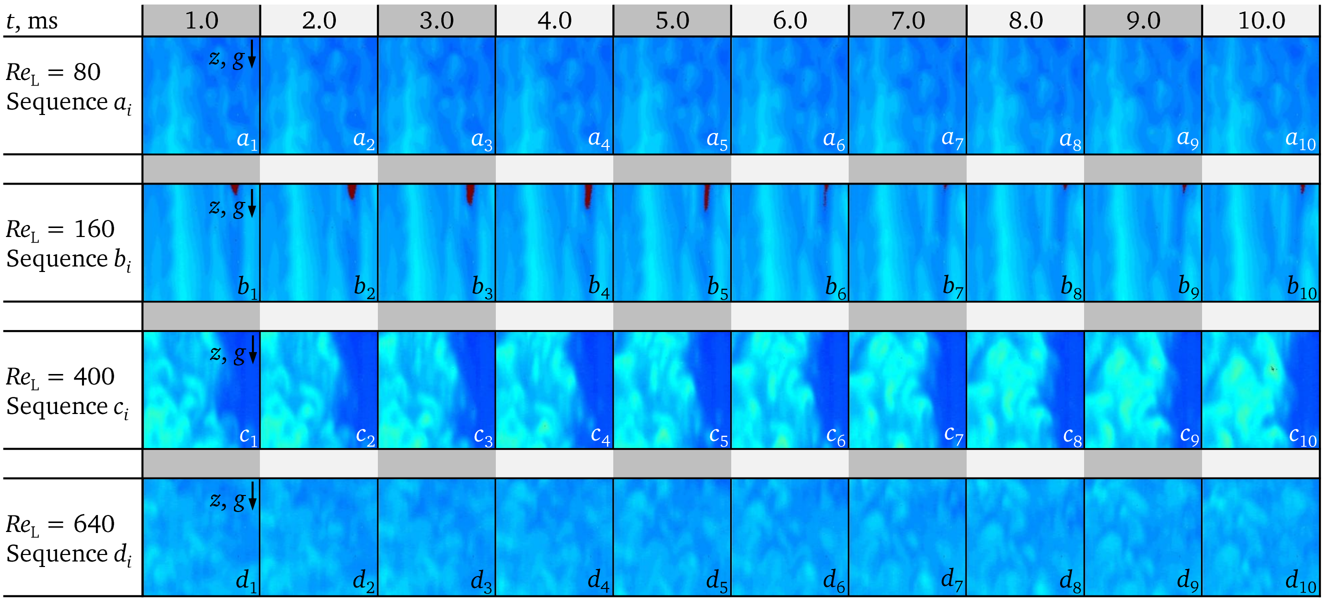

Figure 7.96. Film dynamics at the Δ-structured surface for $Re_L = 80, 160, 400, 640$, $Re_G = 10^4$ for $T_{L,in} = 298\,\mathrm{K}$ captured at $z = 45\,\mathrm{mm}$ with high speed infrared camera.

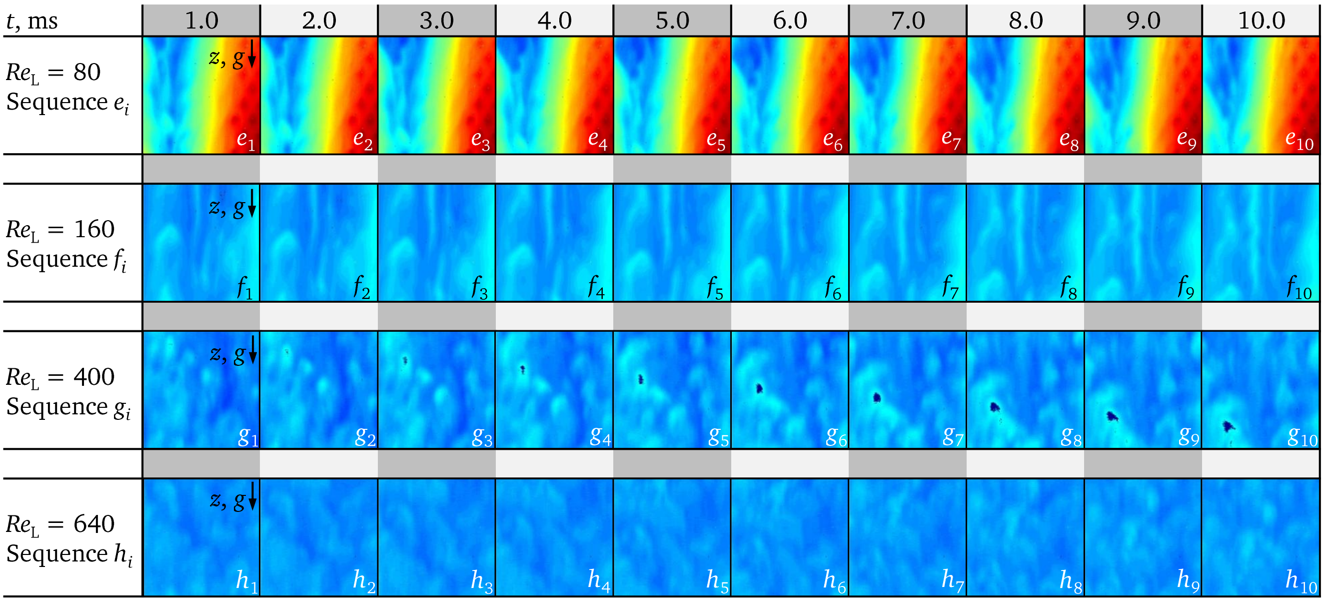

Figure 7.97. Film dynamics at the Δ-structured surface for $Re_L = 80, 160, 400, 640$, $Re_G = 4 \cdot 10^4$ for $T_{L,in} = 298\,\mathrm{K}$ captured at $z = 45\,\mathrm{mm}$ with high speed infrared camera.

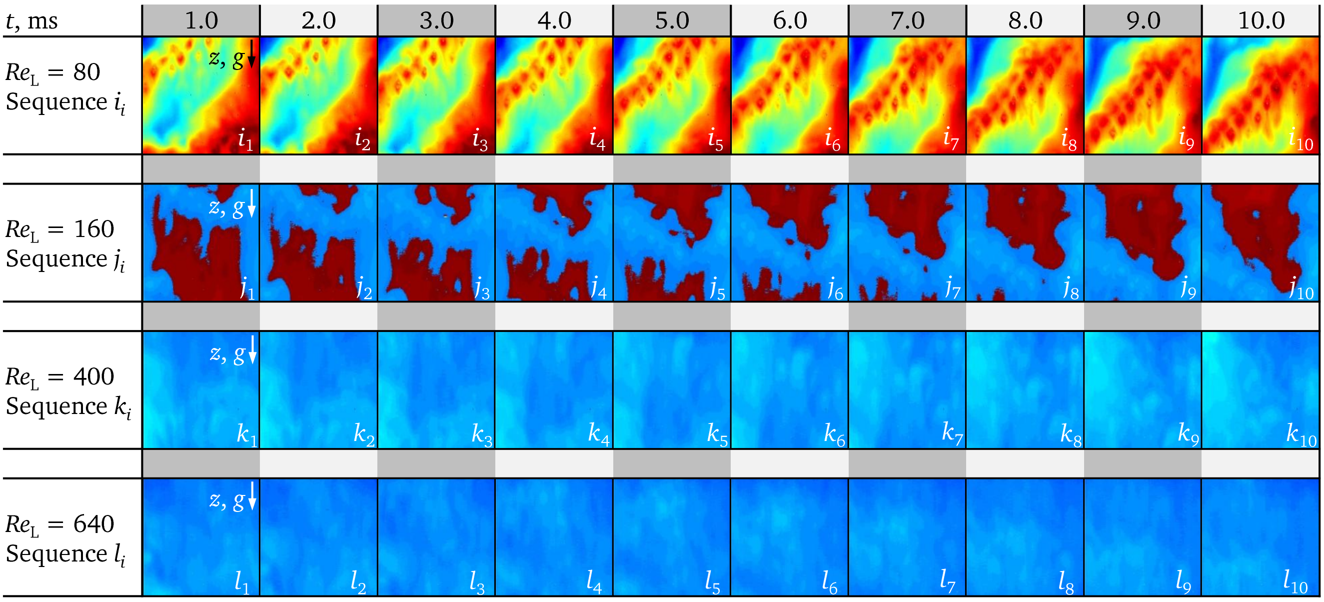

Figure 7.98. Film dynamics at the Δ-structured surface for $Re_L = 80, 160, 400, 640$, $Re_G = 7 \cdot 10^4$ for $T_{L,in} = 298\,\mathrm{K}$ captured at $z = 45\,\mathrm{mm}$ with high speed infrared camera.

In Fig. 7.95 the Nusselt numbers are presented for the measurements carried out at the Δ-structured surface. It can be seen that Nu_Δ increases with growing Re_L, while a minor effect of Re_G appears above $Re_L = 240$. At $Re_G = 10^4$ the liquid film covers fully the Δ-structures; no dewetting occurs up to $Re_L = 160$ (see image sequences a_i and b_i in Fig. 7.96). As Re_L exceeds 160, disturbances at the surface of the liquid film flow appear which indicate the formation of internal mixing. Contrary, a rise in shear stress causes a first film break-up at $Re_L = 80$. The higher shear stress overcomes the liquid inertia and an asymmetric distribution of the liquid results (see image sequence e_i in Fig. 7.97). With increasing Re_L this asymmetry is suppressed and the Δ-structured surface is rewetted as presented in image sequence f_i. However, the liquid-gas interface is embossed with a horseshoe-like pattern which develop into lump-like crests at $Re_L = 400$ and diminish at $Re_L = 640$ (see image sequence g_i and h_i). The likely reason for the formation of the crest is the pressure increase within the liquid bulk [76]. At higher Re_L the effect of the pressure fluctuation cannot reach the liquid-gas interface, since the large liquid mass absorbs the disturbances and a smoothing of the film surface results. However, the liquid bulk can still exhibit noticeable recirculation regions which promote the enhancement of convective heat transfer from the wall to the liquid [142] which is the reason for further rise in Nu_Δ, possibly. At $Re_G = 7 \cdot 10^4$, remarkable film rupture can be identified for $Re_L = 80$, since a stronger shear stress act at the liquid film flow (see image sequence i_i in Fig. 7.98). Waves with diagonally oriented fronts propagate downstream. In the zone ahead of the wave crest, thin film can be seen as a slightly curved horseshoe-shaped region. A further increase in Re_L results in a fully flooded surface as illustrated in the image sequences $j_i - l_i$ (red regions in image sequence j_i might be caused through error in data post-processing). The difference of Nu_Δ at similar $Re_L = 320 - 800$ can be attributed to the intensified liquid recirculation, although no remarkable wave formation can be seen. The stronger shear stress assists the film surface and damps the disturbances caused by the surface structures. However, the velocity of liquid increases resulting in an intensified liquid recirculation which can be a reason for higher heat transfer coefficient compared to $Re_G = 10^4$ and $Re_G = 4 \cdot 10^4$. Additionally, the increased heat transfer between the liquid flow and gas stream due to higher gas velocity can be another reason for the difference in Nu_Δ.

7.2.9 Comparison of Nusselt numbers at unstructured, ∇-grooved and Δ-structured surfaces

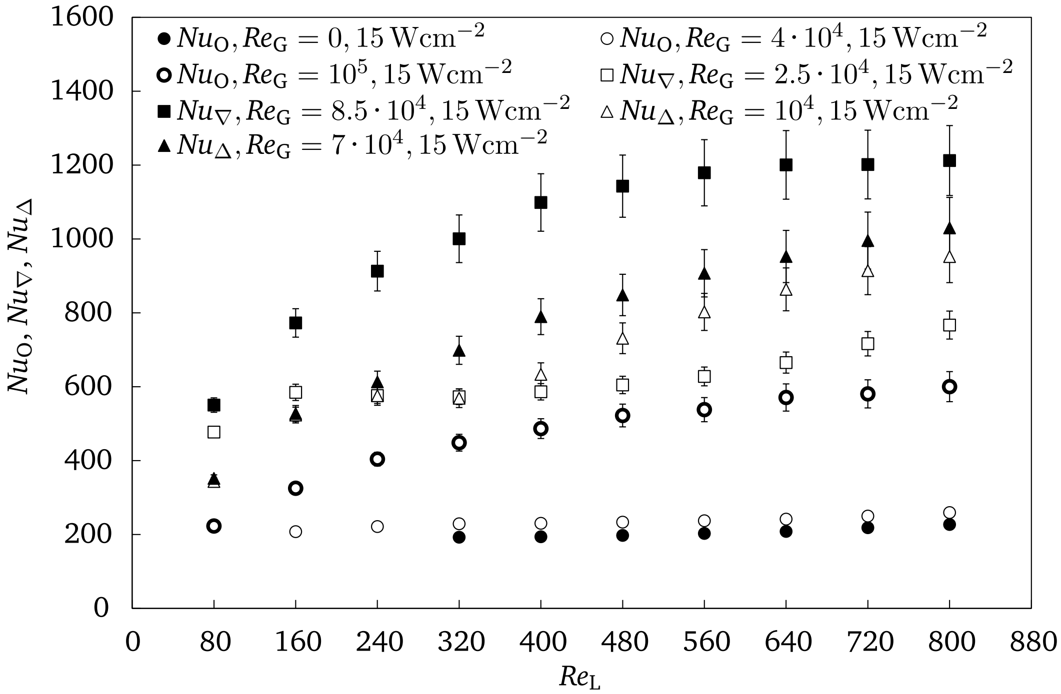

Figure 7.99. Comparison of Nusselt numbers Nu_O, Nu_∇, Nu_Δ determined through the measurements at the unstructured, ∇-grooved, and Δ-structured surfaces for $\dot{q}_W = 15\,\mathrm{Wcm^{-2}}$, varying Re_L and Re_G at $T_{L,in} = 298\,\mathrm{K}$.

The comparison of chosen *Nu* results obtained from the heat transfer measurements at all three surfaces is displayed in Fig. 7.99. To note, Re_G is not similar between the surfaces. This was intentionally chosen to show the influences of the microstructures used in this work on the heat transfer. Besides, the necessary quantity of Re_G for the microstructured surfaces can be distinguished in order to achieve equivalent heat transfer coefficients obtained at the unstructured surface for the largest Re_G. Generally, it can be seen that large heat transfer coefficients were achieved by using micro-structured surfaces. Based on the heat transfer results obtained for the unstructured surface, this remarkable increase in heat transfer coefficient can be justified with the transport mechanisms discussed on the previous pages.

In the experiments, the lowest Nusselt number resulted at the unstructured surface, while the maximum Nusselt number was measured at the ∇-grooved surface. Nu_∇ determined at $Re_G = 2.5 \cdot 10^4$ represent the lowest values for the ∇-grooved surface. Over the entire Re_L, the heat transfer coefficients are larger than Nu_O obtained for the maximum Re_G of 10^5 used for the unstructured surface experiments. For a gravity-driven liquid film flow on the ∇-grooved surface, a minor reduction of Nu_∇ can be expected. At these conditions, the Nu_∇ can be compared with Nu_O for $Re_G = 10^5$, provided that no significant effect of Re_G reduction on Nu_∇ results. If the latter requirement is conformed, heat transfer can be similar to Nu_O obtained for $Re_G = 10^5$, which indicates that the use of ∇-grooved surface is rather efficient. Considering similar assumptions for the Nu_Δ values for $Re_G = 10^4$, the Δ-structured surface investigated in this work was also very efficient in terms of increasing heat transfer.

Compared to Nu_Δ, the influence of Re_G is stronger on the ∇-grooved surface than on the Δ-structured surface. This is maybe due to the partial wetting phenomena, which occurred increasingly at the Δ-structured surface with stronger shear stress. At the Δ-structured surface, this effect appeared only for $Re_\mathrm{G} = 4 \cdot 10^4$ and $Re_\mathrm{G} = 7 \cdot 10^4$ at $Re_\mathrm{L} = 80$. The reason for the large Re_G influence at the ∇-grooved surface can be the formation of three phase contact lines, whereas their length increases with stronger shear stress. The latter leads also to the increase of the dry patch area, where the heat transfer between wall and gas stream grows. This is additionally enhanced by higher gas velocities obtained with increasing Re_G. In the case of Δ-structured surface, the effect of film rupture was only minor. Therefore the trend of Nu_Δ shows only a weak influence of Re_G at $Re_\mathrm{L} > 400$. This denotes that the heat transfer is probably governed by the internal mixing process induced trough the Δ-structures. However, the intensity of the internal mixing process is minor affected by the shear stress rather determined by Re_L.

7.3 Identified flow regimes and dominant mechanisms

7.3.1 Unstructured surface

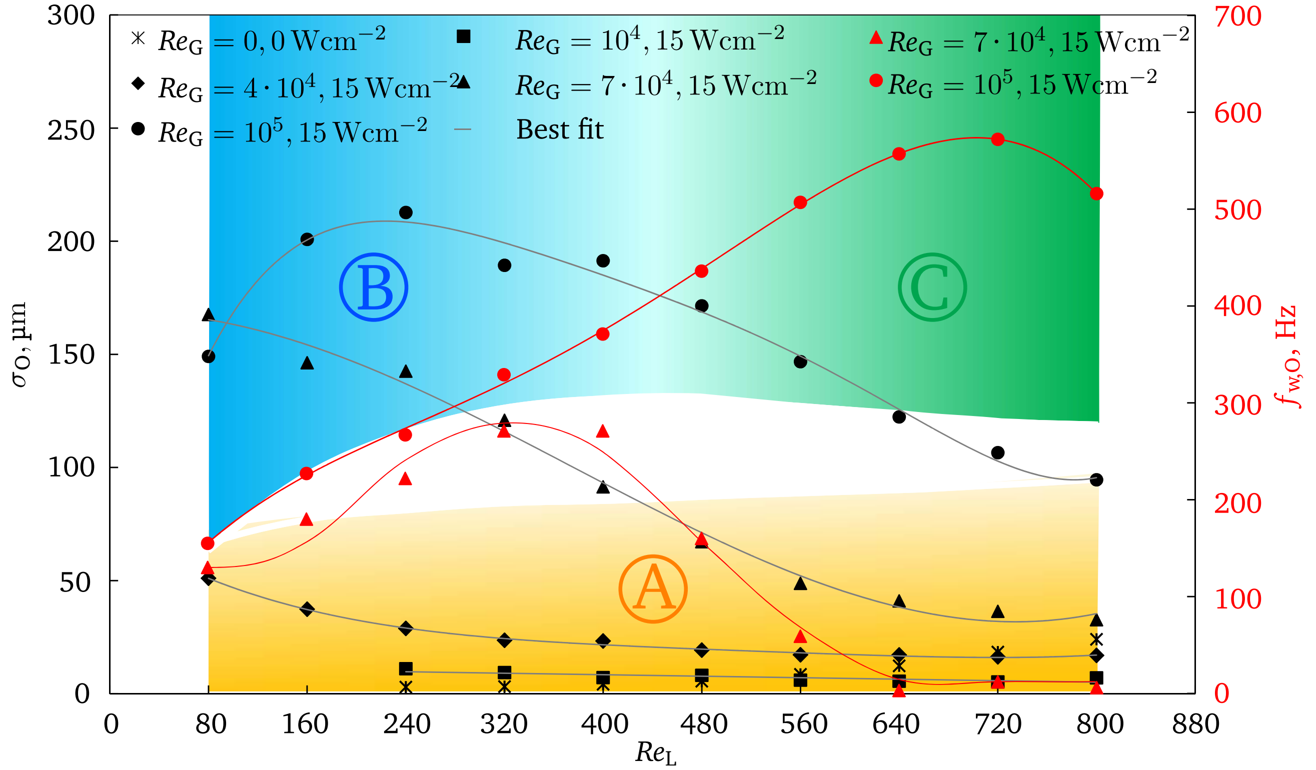

Figure 7.100. Comparison of standard deviation σ_O for $Re_\mathrm{L} = 80 - 800$, $Re_\mathrm{G} = 0 - 10^5$ and wave frequency $f_\mathrm{w,O}$ for $Re_\mathrm{G} = 7 \cdot 10^4, 10^5$ at the unstructured surface for $\dot{q}_\mathrm{W} = 0, 15\,\mathrm{Wcm}^{-2}$; identified flow regimes **A**: Smooth liquid-gas interface, **B**: Large amplitude waves with low frequency, **C**: Small amplitude waves with high frequency.

In Fig. 7.100 the standard deviation is compared with the wave frequency measured at the unstructured surface. Through this comparison, the film dynamics of gas-driven liquid films can be classified into three different flow regimes. Up to $Re_\mathrm{G} = 4 \cdot 10^4$, the film dynamics of gas-driven liquid films are comparable with those of gravity-driven films. This flow regime is characterized by a smooth liquid-gas interface without any considerably disturbances (A). Therefore, it can be assumed that the hydrodynamics in both the cases are similar. At high Re_G and low Re_L values, the film surface is represented by large amplitude waves with low frequencies (**B**). Since the liquid mass is less, the shear forces at the liquid-gas interface can overcome the liquid inertia and strongly deform the film surface. Contrary, at low Re_G and high Re_L the liquid-gas interface shows small amplitude waves at high frequencies (C). The effect of deformation diminishes by the increase of mass and hence increase of inertia.

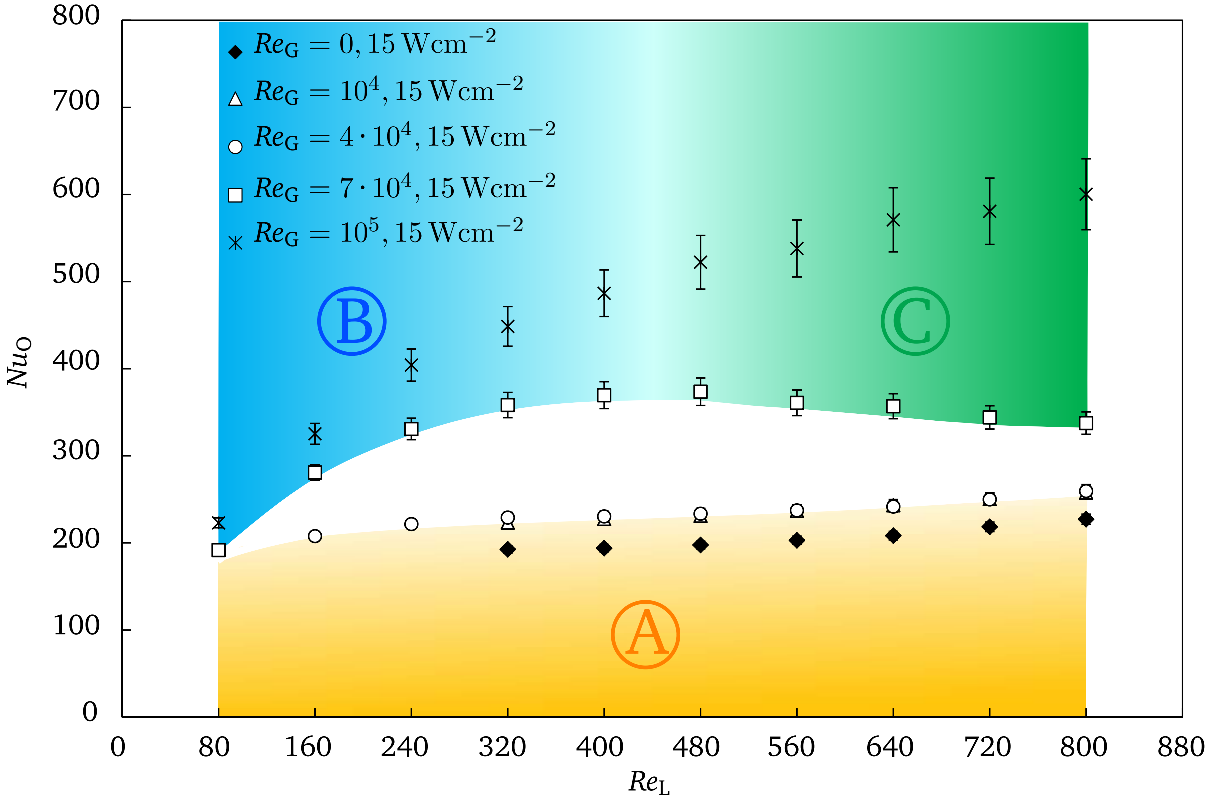

Figure 7.101. Nusselt number Nu_O for gravity- and gas-driven film flow at the unstructured surface for $Re_\mathrm{L} = 80 - 800$, $Re_\mathrm{G} = 0 - 10^5$ at $\dot{q}_\mathrm{W} = 15\,\mathrm{W cm^{-2}}$; colored sections A, **B**, and C correspond to liquid film flow regimes identified in Fig 7.100.

The Nusselt numbers illustrated in Fig. 7.101 are corresponding to the results in Fig. 7.100. Gas-driven films up to $Re_\mathrm{G} = 4 \cdot 10^4$ show only a minor enhancement in heat transfer. This can be explained by the hydrodynamic mechanism which is comparable to that in films driven by gravity (A). The significant rise in Nu_O at high Re_G and at low Re_L can be described by the flow regime labeled with **B**. Large amplitude waves lead to strong internal mixing in the liquid bulk. Vortices are generated reaching up to the wall-liquid interface. Hot liquid particles in the vicinity at the wall are exchanged by cold liquid particles and transported towards the liquid-gas interface. This phenomenon declines as more liquid mass is present at the wall. In this case, small amplitude waves with high frequency appear at the film surface (C). They are not able to induce sufficient disturbances in the liquid bulk near the wall-liquid interface. Hence, the effect of internal mixing decreases and leads either to a constant Nu_O or a weak increase in Nu_O.

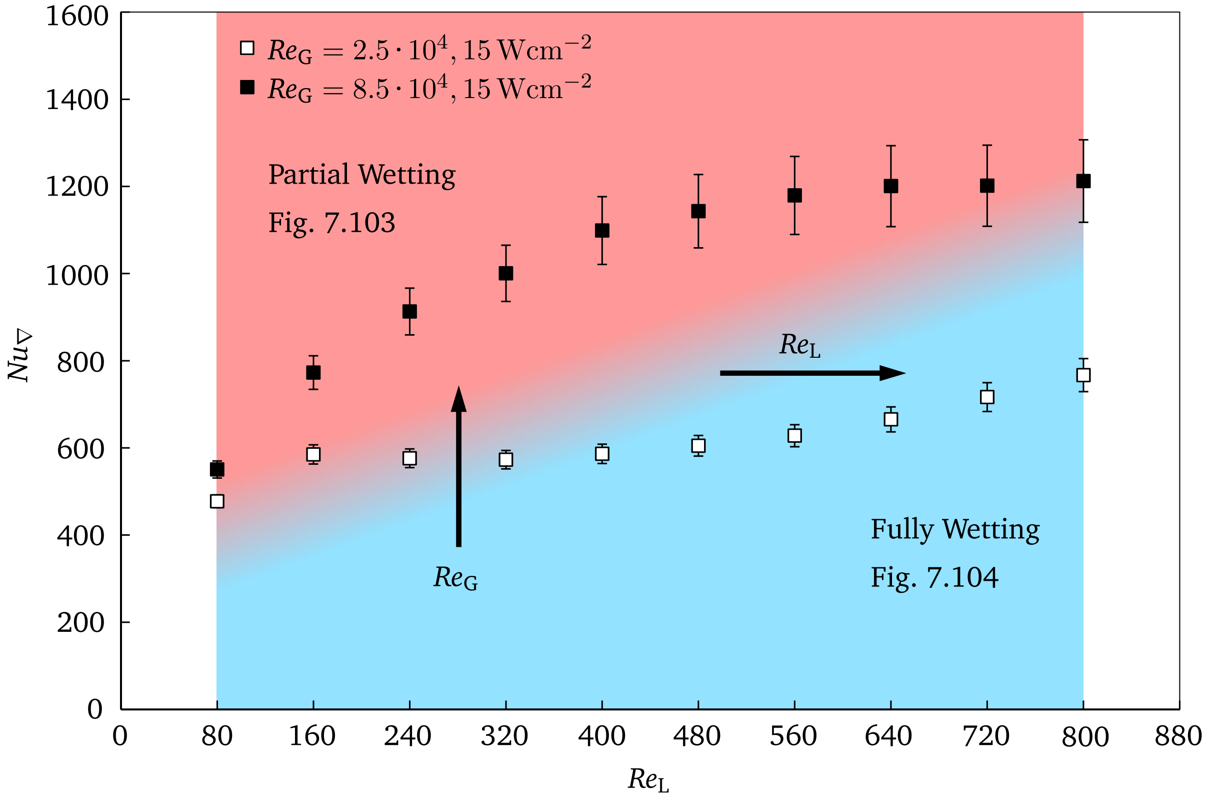

Figure 7.102. Nusselt number Nu_∇ for $Re_L = 80 - 800$, $Re_G = 2.5 \cdot 10^4$, $8.5 \cdot 10^4$, $\dot{q}_W = 15\,\mathrm{Wcm^{-2}}$ at the ∇-grooved surface; red colored section corresponds to partial wetting flow condition and blue colored section corresponds to fully wetting flow conditions.

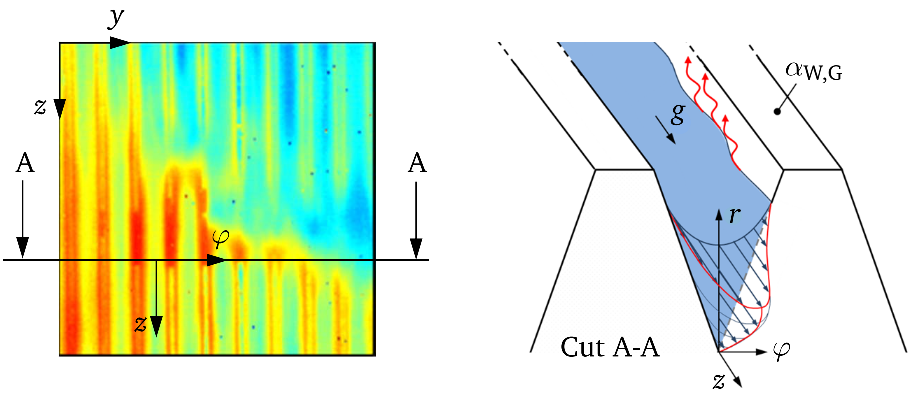

Figure 7.103. Partial wetting condition at the ∇-grooved surface at high Re_G and low Re_L, left: Infrared image showing surface partially covered with liquid, right: Liquid flowing within the troughs of the grooves.

The Nusselt numbers measured at the ∇-grooved surface are shown in Fig. 7.102. Using the infrared images, two conditions could be identified which have a strong effect on the heat transfer mechanism. The strong increase in Nu_∇ at high Re_G and comparably low Re_L is due to the occurrence of partial wetting (see Fig. 7.103). In this condition, the heat transfer is determined by the superposition three effects. Between the the outstanding groove crests and the cold gas stream, heat is transferred by single-phase convection. Furthermore, three-phase contact lines formed by the partial wetting contribute to the heat transfer, too. Another mechanism is the internal mixing process within the liquid bulk which is strong in the region where a wave is passing along. A further increase in Re_{L} at constant Re_{G} results in a fully wetted wall surface. In this case, only the internal mixing which is evoked through vortices is the governing mechanism for the weak increase in Nusselt number (see Fig. 7.104).

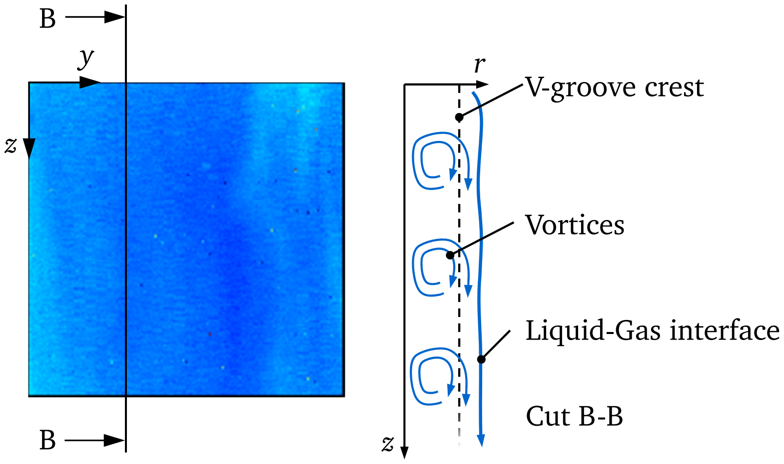

Figure 7.104. Fully wetting condition at the ∇-grooved surface at low Re_{G} and high Re_{L}, left: Infrared image showing surface fully covered with liquid, right: Vortices within the bulk liquid shown exemplary.

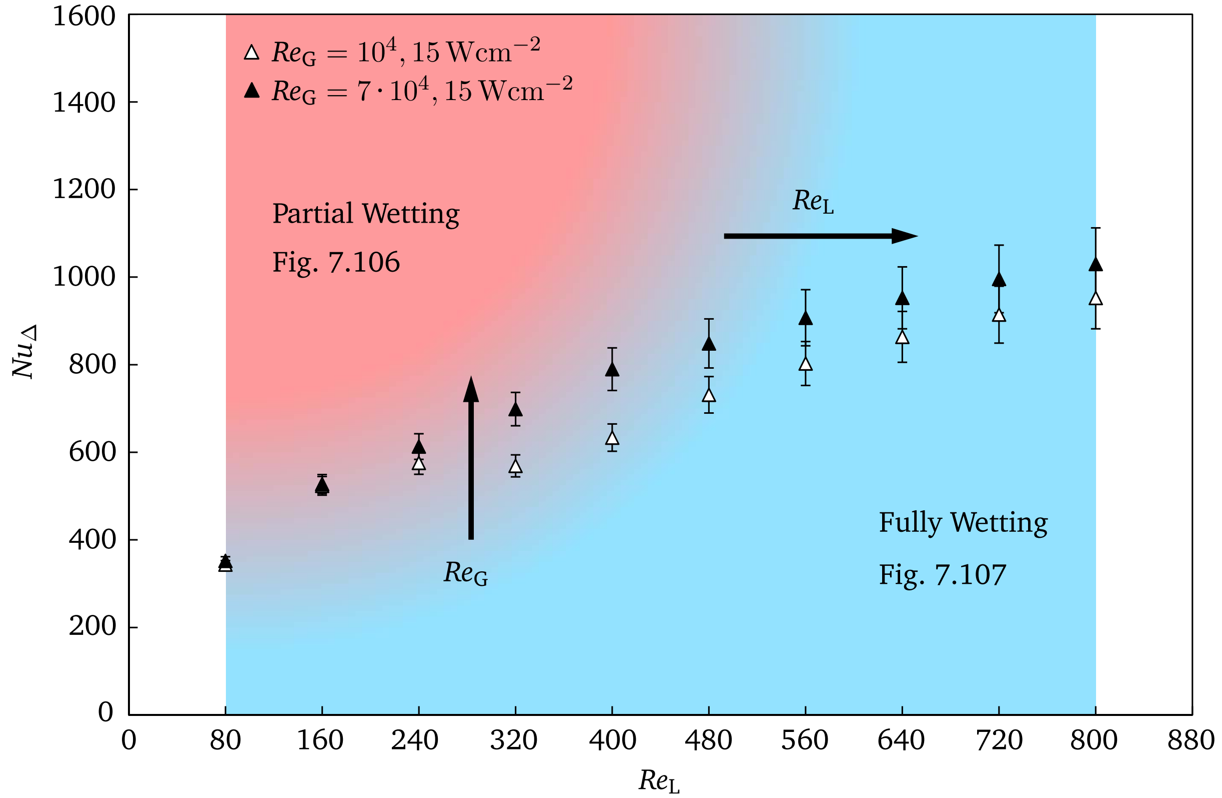

Figure 7.105. Nusselt number Nu_Δ for $Re_L = 80 - 800$, $Re_G = 10^4, 7\cdot10^4$, $\dot{q}_W = 15\,\mathrm{Wcm^{-2}}$ at the Δ-structured surface; partial wetting and fully wetting flow conditions are characterized with Figs. 7.106 and 7.107.

The Nusselt numbers measured at the Δ-structured surface are shown in Fig. 7.105. By the means of the infrared images, similar conditions such as for ∇-grooved surface could be determined which have a significant effect on the heat transfer mechanism. At high Re_G and comparably low Re_L, partial wetting occurs where again a superposition of three major effects exist (see Fig. 7.106).

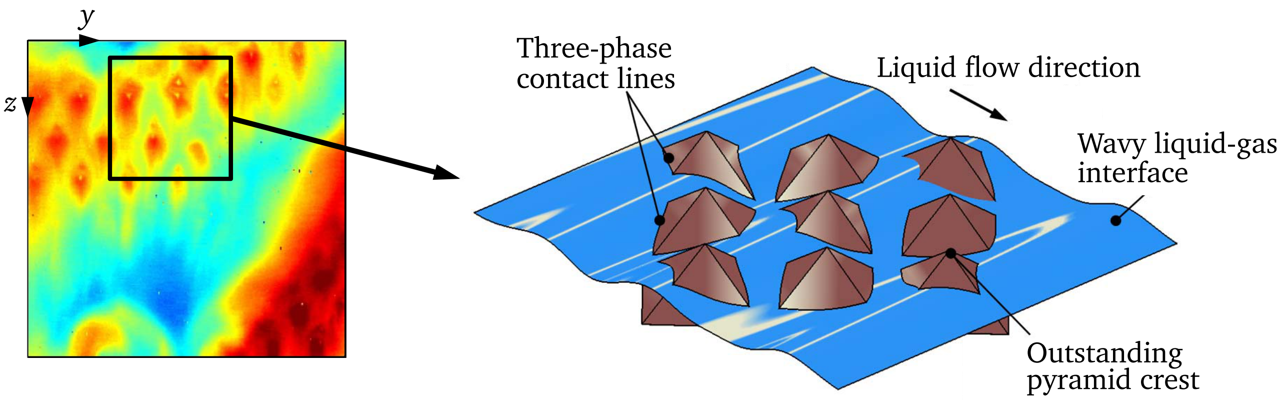

Figure 7.106. Partial wetting condition at the Δ-structured surface at high Re_G and low Re_L, left: Infrared image showing surface partially covered with liquid, right: Liquid flowing within the troughs, formation of three-phase contact lines and outstanding pyramid crests.

The pyramid crests stand out and are directly in contact with the cold gas stream. Thereby heat is transferred through single-phase convection. Concurrently, three-phase contact lines appear and contribute to the heat transfer. In the liquid bulk, intense mixing of hot and cold liquid is generated. However, in case of fully wetted condition at decreased Re_{G}, Nu_{Δ} does not reduce. Here, the Nusselt numbers show a strong dependence on Re_{L} rather than on Re_{G}. This is due to the fact that the pyramids not only represent obstacles oriented longitudinally to the liquid flow direction. They are also oriented perpendicularly to the flow direction such that the internal mixing process is strongly induced (Fig. 7.107). The additional action of shear force at the liquid-gas interface has only a negligible contribution to the internal mixing and therefore a minor enhancement in heat transfer results.

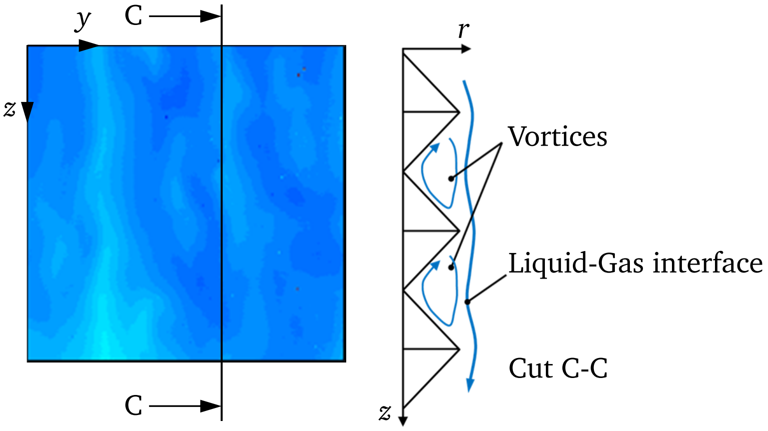

Figure 7.107. Fully wetting condition at the Δ-structured surface at low Re_{G} and high Re_{L}, left: Infrared image showing surface fully covered with liquid, right: Vortices within the bulk liquid shown exemplary.

7.4 Closure

In this chapter, the results of the high speed shadowgraphy measurements of gravity and gas-driven films flowing at the unstructured, V-grooved and pyramid structured surfaces were discussed. The standard deviation and the wave frequencies detected at varying experimental parameters were presented and compared between the surfaces. The dimensionless temperature profiles were illustrated and a comparison between the surfaces was made. Using the heat transfer measurements at the unstructured surface, the Nusselt numbers were evaluated, followed by a discussion using theoretical approaches and measurements from the literature. The Nusselt numbers resulted for the micro-structured surfaces were presented accompanied with the rupturing and rewetting phenomena at the surface. Following this, the effect of surface micro-structures on the Nusselt number is presented in a comparison with the Nusselt numbers obtained through the unstructured surface measurements. The heat transfer results were interpreted with identified flow regimes using standard deviation and wave frequency for the unstructured surface as well as infrared images for the structured surfaces.

8

Summary and Outlook

Cooling processes involving gas-driven thin film flows are rather complex. To sufficiently understand the physical mechanisms and to accurately design and develop efficient thermal systems, a wide-ranging and detailed knowledge about the transport mechanisms is necessary. Although numerous scientific investigations have been performed to determine the hydrodynamics and heat transfer in gravity-driven and gas-driven films, the complex transport mechanisms are not fully understood.

The present experimental work has been carried out to understand the thermo-hydrodynamic phenomena in thermally and hydrodynamically developing gas-driven thin liquid films. Using high-resolution measurement techniques, the film waviness and heat transfer in gravity and gas-driven liquid films at an unstructured tube surface was investigated. Further, micro-structured surfaces were used to study the effect of surface topography on film waviness and heat transfer. Besides that, the rupturing of the film and the rewetting effect at the micro-structured surfaces were visualized.

In this chapter, the investigations accomplished in the present thesis are summarized and a brief outlook is given.

8.1 Summary

From this study it has been shown that shear stress at a surface of thin liquid layer has a remarkable influence on the stability of the liquid-gas interface. As the shear stress was increased, disturbances occurred at the liquid film surface which transformed into large amplitude but less frequent waves. The effect of liquid mass load on the waviness was reverse of shear stress. With increase in liquid mass flow rate, the deformations were suppressed. Small amplitude waves with higher frequencies were formed.

With further growing liquid mass flow rate, those waves were completely diminished and a rather smooth liquid-gas interface appeared. The measurements concerning the development of the waviness in flow direction revealed that, generally, the fluctuations grow with increasing flow length. The rate of growth is determined by the fluid mass flow rates.

The influence of the shear stress induced by a gas stream was also seen in the results of heat transfer coefficients. The results revealed that a significant enhancement in heat transfer is possible when the shear stress at the liquid-gas interface increases. Especially waves with large amplitude and low frequency have a strong enhancing effect on heat transfer. Contrary, waves with small amplitude and high frequency lead either to heat transfer coefficients which increase minor or remain constant. A remarkable growth in heat transfer coefficient was achieved after reaching sufficiently large gas flow rates. This indicates that a threshold shear stress is probably existing which has to be exceeded by the rise in gas flow rate. The existence of a threshold shear stress was also identified by comparing the heat transfer coefficients for gravity-driven film measurements and the classical Graetz-Nusselt model. The comparison revealed that the influence of shear stress at $Re_\mathrm{G} = 10^4, 4 \cdot 10^4$ on the heat transfer is negligible. However, this threshold shear stress was not determined in the present work. A further comparison of the dimensionless heat transfer coefficients with experimental data, falling film correlations, and a turbulence model which are taken from literature for gas-driven films revealed the following outcomes. The shear stress has an influence on the thermo-hydrodynamic flow regime within the liquid film. As the shear stress increases, the liquid film flow regime changes. At a shear stress which is below the threshold shear stress, the film flow condition was following the trend of a thermally developing falling film. A further rise resulted in a trend which was described by a turbulently falling film. Shear stresses beyond ($Re_\mathrm{G} = 7 \cdot 10^4, 8.5 \cdot 10^4$) resulted in heat transfer coefficients which are comparable with the heat transfer coefficients predicted by the turbulence model used for comparison.

The micro-structures used in this work showed a significant influence on the waviness of gas-driven films. With increasing shear stress and liquid mass flow rate, the standard deviation of the film thickness and the wave frequencies grew. Especially the use of pyramid structures showed large standard deviations and high frequencies at low shear stress compared to the unstructured surface and the surface, incorporated triangular grooves which were oriented parallel to the flow direction. The effect of shear on the waviness for the pyramid structured surface was weak, while a strong influence of shear stress was observed on film flow over the triangular grooved surface. The film flow on the latter surface was not influenced by the liquid load. Using the infrared thermography, rupture of the film and rewetting were observed on both of the micro-structured surfaces. For low liquid mass flow rates and high shear stress, this area of dry patches grew. The dry patches were rewetted through wave accumulation which occurred through decreasing the shear stress and increasing the liquid mass flow rate. Compared to the unstructured surface, micro-structures can promote large heat transfer coefficients at comparable fluid properties and process parameters. Especially, the pyramid structured surface is very promising in heat transfer enhancement at low shear stress.

8.2 Outlook

The investigations performed in the present work were focused on measuring the hydrodynamics and heat transfer in falling films and gas-driven films flowing on unstructured and micro-structured surfaces. An annular flow channel was designed to study the thermo-hydrodynamic transport mechanisms in thin films driven by a turbulent gas stream. High-resolution measurement techniques were adopted to determine the relevant parameters used for the evaluation of waviness and heat transfer. Some limitations existed for the design of the flow channel and the measurement methods used; potential improvements are suggested as follows.

1. The measurements of the velocity profiles using hot-wire anemometry showed that the velocity of the gas flow was neither uniform nor fully-developed. To provide a well-defined gas stream inlet condition, especially for the validation with numerical simulations, a flow channel with rectangular cross-section and a sufficient upstream development length must be designed. Also, the channel design must have an appropriate access for hot-wire measurements in order to accurately resolve the gas boundary layer region in the vicinity of the heated wall. Furthermore, to prevent the effect of disturbances generated by a liquid film distributor used in this work, either a plate with multiple micro-holes or fine meshed metal foam must be installed at the flow channel inlet.

2. Limitations of high-speed shadowgraphy technique have been identified in this thesis. Specifically, this technique is not appropriate for measuring amplitude and velocity of 3D waves. Confocal chromatic sensor, which is a point measurement technique is a viable alternative to shadowqraphy. For the wave frequency, two CHR sensors have to be successively installed along the axis at the same azimuthal angle.

3. Concerning the heat transfer in gas-driven liquid film flows at the unstructured surface, in this work a threshold shear stress level has been identified. Further investigations should be performed in order to determine the value of this threshold shear stress level by executing more experiments with fine varied gas Reynolds numbers shown in Fig. 8.1. This should help to study the influence of shear stress on the onset of heat transfer enhancement.

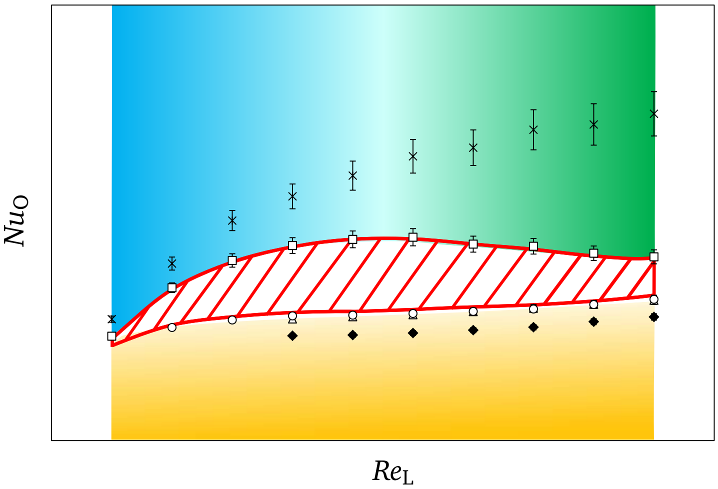

Figure 8.1. Range of experimental flow parameters for further detailed investigations on heat transfer.

4. The Nusselt number correlations developed in this work for gas-driven liquid films flowing on unstructured surface are based only on liquid and gas Reynolds numbers at constant geometric dimensions and fluid properties. This correlation can be extended to include the effect of other influencing parameters. Similarly, the effect of micro structures on heat transfer should be systematically investigated. Exemplary, the geometric dimensions of the ∇-grooves such as apex angle, groove depth and width of groove crest can be varied.

Bibliography

[1] P. Adomeit and U. Renz. Hydrodynamics of three-dimensional waves in laminar falling films. *International Journal of Multiphase Flow*, 26(7):1183–1208, 2000.

[2] V. S. Ajaev, T. Gambaryan-Roisman, and P. Stephan. Static and dynamic contact angles of evaporating liquids on heated surfaces. *Journal of Colliod and Interface Science*, 342(2):550–558, 2010.

[3] F. Al-Sibai. Experimentelle Untersuchung der Strömungscharakteristik und des Wärmeübergangs bei welligen Rieselfilmen, 2004.

[4] S. Alekseenko, A. Cherdantsev, M. Cherdantsev, S. Isaenkov, S. Kharlamov, and D. Markovich. Application of a high-speed laser-induced fluorescence technique for studying the threedimensional structure of annular gasliquid flow. *Experiments in Fluids*, 53(1):77–89, 2011.

[5] S. V. Alekseenko, V. A. Antipin, V. V. Guzanov, S. M. Kharlamov, and D. M. Markovich. Three-dimensional solitary waves on falling liquid film at low Reynolds numbers. *Physics of Fluids*, 17(12):121704, 2005.

[6] S. V. Alekseenko, D. M. Markovich, S. M. Kharlamov, and A. V. Cherdantsev. Experimental Study of the Linear Stability of a Falling Liquid Film in the Presence of a Turbulent Gas Stream. *Fluid Dynamics*, 39(4):612–620, 2004.

[7] S. V. Alekseenko, V. E. Nakoryakov, and B. G. Pokusaev. Wave formation in liquid film flow on a vertical wall. *Journal of Applied Mechanics and Technical Physics*, 20(6):719–727, 1980.

[8] S. K. Alghoul, C. N. Eastwick, and D. B. Hann. Droplet Impact on Shear-Driven Liquid Films. *Atomization and Sprays*, 21(10):833–846, 2011.

[9] A. A. Alhusseini, K. Tuzla, and J. C. Chen. Falling film evaporation of single component liquids. *International Journal of Heat and Mass Transfer*, 41(12):1623–1632, 1998.

[10] W. Ambrosini, N. Forgione, and F. Oriolo. Statistical characteristics of a water film falling down a flat plate at different inclinations and temperatures. *International Journal of Multiphase Flow*, 28(9):1521–1540, 2002.

[11] K. Argyriadi, M. Vlachogiannis, and V. Bontozoglou. Experimental study of inclined film flow along periodic corrugations: The effect of wall steepness. *Physics of Fluids*, 18(1):012102, 2006.

[12] A. Arshad, K. M. Pillai, and K. E. R. Roy. Numerical Studies on Hydrogen Combustion in a Film Cooled Cryogenic Rocket Engine. *International Journal of Engineering Science and Technology*, 4(07):3360–3368, 2012.

[13] S. G. Bankoff. Stability of liquid flow down a heated inclined plane. *International Journal of Heat and Mass Transfer*, 14(3):377–385, 1971.

[14] A. Bar-Cohen, G. Sherwood, M. Hodes, and G. L. Solbreken. Gas-assisted evaporative cooling of high density electronic modules. *IEEE Transactions on Components, Packaging and Manufacturing Techology*, 18(3):502–509, 1995.

[15] F. Z. Batarseh. Spray generated by an airblast atomizer: Atomization, propagation and aerodynamic instability. Phd thesis, Technische Universtität Darmstadt, Institut für Strömungslehre und Aerodynamik, Petersenstraße 17, 64287 Darmstadt, Germany, 2009.

[16] M. Benhalilou and N. Kasagi. Numerical prediction of heat and momentum transfer over micro-grooved surface with a nonlinear k-ϵ model. *International Journal of Heat and Mass Transfer*, 42(14):2525–2541, 1999.

[17] T. B. Benjamin. Wave formation in laminar flow down an inclined plane. *Journal of Fluid Mechanics*, 2(6):554–573, 1974.

[18] U. C. Bhayaraju. Analysis of liquid sheet breakup and characterization of plane prefilming and nonprefilming airblast atomisers. Phd thesis, Technische Universtität Darmstadt, Institut für Strömungslehre und Aerodynamik, Petersenstraße 17, 64287 Darmstadt, Germany, 2007.

[19] C. Brandt, P. Stephan, M. Dubois, and B. Mullender. Theoretical Investigation of Advanced Capillary Structures in Grooved Heat Pipe Evaporators for Space Applications. *Proceedings of the International Conference On Environmental Systems, Toulouse-France*, 2000.

[20] N. Brauner and D. M. Maron. Modeling of wavy flow in inclined thin films. *Chemical Engineering Science*, 38(5):775–788, 1983.

[21] K. Bruno and M. J. McCready. Origin of roll waves in horizontal gas-liquid flows. *AIChE Journal*, 34(9):1431–1440, 1988.

[22] E. Buckingham. On physically similar systems; illustrations of the use of dimensional equations. *Physical Review*, 4:345–376, 1914.

[23] M. Budakli, T. Gambaryan-Roisman, and P. Stephan. Influence of surface topography on heat transfer in shear-driven liquid films. *Journal of Physics: IOP Conference Series*, 395(1):1–9, 2012.

[24] E. A. Chinnov, I. A. Sharina, and O. A. Kabov. Intensification of heat transfer in a downward liquid-film flow. *Journal of Applied Mechanics and Technical Physics*, 45(5):705–711, 2004.

[25] K. J. Chu and A. E. Dukler. Statistical characteristics of thin, wavy films: Part 2, studies of the substrate and its wave structure. *American Institute of Chemical Engineers Journal*, 20(4):695–706, 1974.

[26] K. J. Chu and A. E. Dukler. Statistical characteristics of thin, wavy films: Part 3, Structure of the large waves and their resistance to gas flow. *American Institute of Chemical Engineers Journal*, 21(3):583–593, 1975.

[27] K. R. Chun and R. A. Seban. Heat transfer to evaporating liquid films. *Journal of Heat Transfer Transactions of American Society of Mechanical Engineers*, 18(3):502–509, 1971.

[28] M.-H. Chung and S.-J. Park. Effects of Turbulence Model and Interfacial Shear on Heat Transfer in Turbulent Falling Liquid Films. *International Communications in Heat and Mass Transfer*, 22(1):1–12, 1995.

[29] L. S. Cohen and T. J. Hanratty. Generation of waves in the concurrent flow of air and a liquid. *American Institute of Chemical Engineers Journal*, 11(1):138–144, 1965.

[30] E. J. Davis, N. P. Cheremisinoff, and C. J. Guzy. Heat transfer with stratified gas liquid flow. *American Institute of Chemical Engineers Journal*, 25(6):958–966, 1979.

[31] E. J. Davis, S. C. Hung, and S. Arciero. An analogy for heat transfer with wavy/stratified gas-liquid flow. *American Institute of Chemical Engineers Journal*, 21(5):872–878, 1975.

[32] G. F. Dietze, A. Leefken, and R. Kneer. Investigation of the backflow phenomenon in falling liquid films. *Journal of Fluid Mechanics*, 595:435–459, 2008.

[33] A. V. Doroshenko, V. I. Logachevskii, V. K. Kirillov, and V. G. Gaidai. Features of the film flow of liquids over surfaces with regular roughness. *Journal of Engineering Physics*, 54(5):493–498, 1988.

[34] E. R. V. Driest. On Turbulent Flow Near a Wall. *Journal of the Aeronautical Sciences (Institute of the Aeronautical Sciences)*, 23(11):1007–1011, 1956.

[35] E. I. P. Drosos, S. V. Paras, and A. J. Karabelas. Characteristics of developing free falling films at intermediate Reynolds and high Kapitza numbers. *International Journal of Multiphase Flow*, 30(7-8):853–876, 2004.

[36] J. Ebner. Einfluss von Druckgradienten in der Gasströmung auf die Dynamik schubspannungsgetriebener Wandfilme. Phd thesis (german), Karlsruher Insitut für Technologie, Institut für Thermische Strömungsmaschinen, KIT-Campus Süd, Kaiserstraße 12, 76131 Karlruhe, Germany, 2004.

[37] J. Ebner, M. Gerendás, O. Schäfer, and S. Wittig. Droplet Entrainment From a Shear-Driven Liquid Wall Film in Inclined Ducts: Experimental Study and Correlation Comparison. *Journal of Engineering for Gas Turbines and Power*, 124(4):874, 2002.

[38] J. Ebner, O. Schäfer, P. Schober, and S. Wittig. Modeling of shear-driven liquid wall films on curved surfaces - effect on accelerated air flow and variable film load. *9th International Conference on Liquid Atomization and Spray Systems*, 2003.

[39] M. Fernandino and T. Ytrehus. Determination of flow sub-regimes in stratified airwater channel flow using LDV spectra. *International Journal of Multiphase Flow*, 32(4):436–446, 2006.

[40] A. M. Frank. Shear driven solitary waves on a liquid film. *Physical Review E*, 74(6):065301–065304, 2006.

[41] A. M. Frank. Numerical simulation of gas driven waves in a liquid film. *Physics of Fluids*, 20(12):122102–1–122102–9, 2008.

[42] D. P. Frisk and E. J. Davis. The enhancement of heat transfer by waves in stratified gas-liquid flow. *International Journal of Heat and Mass Transfer*, 15(8):1537–1552, 1972.

[43] H. Fujita, K. Katoh, and H. Takahama. Falling Water Films over a Ring Attached to a Vertical Cylinder: Wave Characteristics Measured by a Capacitance Method. *Bulletin of Japanese Society of Mechanical Engineers*, 28(241):1401–1408, 1985.

[44] H. Fujita, H. Takahumu, and H. Asano. Heat and mass transfer in countercurrent flow of air and water film. *Transaction of the Japanese Society of Mechanical Engineers*, 48(427):518–525, 1982.

[45] H. Fujita, H. Takahumu, H. Yabashi, and K. Takagi. Gas-assisted evaporative cooling of high density electronic modules. *Transaction of the Japanese Society of Mechanical Engineers*, 44(377):135–143, 1978.

[46] T. Gambaryan-Roisman and P. Stephan. Analysis of falling film evaporation on grooved surfaces. *Enhanced Heat Transfer*, 10(4):445–458, 2003.

[47] D. Gao, N. B. Morley, and V. Dhir. Numerical simulation of wavy falling film flow using VOF method. *Journal of Computational Physics*, 192(2):624–642, 2003.

[48] E. Gaßmann and A. Gries. *Die Bibliothek der Technik, Elektronische Druckmesstechnik: Grundlagen Anwendungen und Geräteauswahl (German)*, volume 323. Moderne Industrie, 2009. ISBN 978-3-937889-95-5.

[49] E. Y. Gatapova and O. A. Kabov. Shear-driven flows of locally heated liquid films. *International Journal of Heat and Mass Transfer*, 51(19-20):4797–4810, 2008.

[50] M. Gerendas and S. Wittig. Experimental and Numerical Investigation on the Evaporation of Shear-Driven Multicomponent Liquid Wall Films. *Journal of Engineering for Gas Turbines and Power*, 123(3):580, 2001.

[51] V. Gnielinski. Berechnung des Druckverlustes in glatten konzentrischen Ringspalten bei ausgebildeter laminarer und turbulenter Strömung. *Chemie Ingenieur Technik*, 79(1-2):91–95, 2007.

[52] V. Gnielinski. Heat transfer coefficients for turbulent flow in concentric annular ducts. *Heat Transfer Engineering*, 30:6:431–436, 2009.

[53] L. Graetz. Über die Wärmeleitfähigkeit von Flüssigkeiten. *Annalen der Physik und Chemie, Neue Folge*, 18:79–94, 1883.

[54] L. Graetz. Über die Wärmeleitfähigkeit von Flüssigkeiten. *Annalen der Physik und Chemie, Neue Folge*, 25:337–357, 1885.

[55] U. Grigull. Wärmeübergang bei Filmkondensation, 1942.

[56] U. Grigull. Wärmeübertragung bei der Kondensation mit turbulenter Wasserhaut. *Forschung im Ingenieur Wesen*, 13:49–57, 1942.

[57] S. Gruber. Effect of Surface Topography on the Heat Transfer in Shear Driven Liquid Films. Bachelor thesis (german), Technische Universtität Darmstadt, Institut für Technische Thermodynamik, Petersenstraße 17, 64287 Darmstadt, Germany, 2012.

[58] G. Guerreri and C. J. King. Design falling film absorbers. *Hydrocarbon Processing*, 53(1):pp. 131, 1974.

[59] T. J. Hanratty and J. M. Engen. Interaction between a turbulent air stream and a moving water surface. *American Institute of Chemical Engineers Journal*, 3(3):299–304, 1957.

[60] T. J. Hanratty and A. Hershman. Initiation of roll waves. *merican Institute of Chemical Engineers Journal*, 7(3):488–497, 1961.

[61] K. Helbig. Messung zur Hydrodynamik und zum Wärmetransport bei der Filmverdampfung. Phd thesis (german), Technische Universtität Darmstadt, Institut für Technische Thermodynamik, Petersenstraße 17, 64287 Darmstadt, Germany, 2008.

[62] K. Helbig, A. Alexeev, T. Gambaryan-Roisman, and P. Stephan. Evaporation of falling and shear-driven thin films on smooth and grooved surfaces. *Flow, Turbulence and Combustion*, 75(1-4):85–104, 2005.

[63] K. Helbig, R. Nasarek, T. Gambaryan-Roisman, and P. Stephan. Effect of longitudinal minigrooves on flow stability and wave characteristics of falling liquid films. *Journal of Heat Transfer*, 131:011601–1–011601–8, 2009.

[64] G. F. Hewitt, G. L. Shires, and Y. V. Polezhaev. *International Encyclopedia of Heat & Mass Transfer*. CRC Press LLC, 2001. ISBN 0-8493-9356-6.

[65] A. P. Hooper. Long-wave instability at the interface between two viscous fluids: Thin layer effects. *Physics of Fluids*, 28(6):1613–1618, 1985.

[66] S. Ishigai, S. Nakanisi, T. Koizumi, and Z. Oyabu. Hydrodynamics and Heat Transfer of Vertical Falling Liquid Films: Part 1, Classification of Flow Regimes. *Bulletin of Japanese Society of Mechanical Engineers*, 15(83):594–602, 1972.

[67] M. Ishii and M. A. Grolmes. Inception criteria for droplet entrainment in two-phase concurrent film flow. *American Institute of Chemical Engineers Journal*, 21(2):308–318, 1975.

[68] S. Jayanti and G. F. Hewitt. Hydrodynamics and heat transfer of wavy thin film flow. *International Journal of Heat and Mass Transfer*, 40(1):179–190, 1996.

[69] S. W. Joo and S. H. Davis. A mechanism for rivulet formation in heated falling films. *Journal of Fluid Mechanic*, 321(333):279–298, 1996.

[70] L. A. Jurman and M. J. McCready. Study of waves on thin liquid films sheared by turblent gas flows. *Physics of Fluids A, Fluid Dynamics*, 1(3):522–536, 1989.

[71] O. A. Kabov and E. A. Chinnov. Heat Transfer from a Local Heat Source to Subcooled Liquid Film. *High Temperature*, 39(5):703–713, 2001.

[72] O. A. Kabov, Y. V. Lyulin, I. V. Marchuk, and D. V. Zaitsev. Locally heated shear-driven liquid films in microchannels and minichannels. *International Journal of Heat and Fluid Flow*, 28(1):103–112, 2007.

[73] O. A. Kabov, D. V. Zaitsev, V. V. Cheverda, and A. Bar-Cohen. Evaporation and flow dynamics of thin, shear-driven liquid films in microgap channels. *Experimental Thermal Fluid Sciences*, 35:825–831, 2011.

[74] Y. O. Kabova, A. Alexeev, T. Gambaryan-Roisman, and P. Stephan. Marangoni-induced deformation and rupture of a liquid film on a heated microstructured wall. *Physics of Fluids*, 18(1):012104–1–012104–15, 2006.

[75] S. Kakac, A. E. Bergles, F. Mayinger, and H. Yuncu. *Heat Transfer Enhancement of Heat Exchangers.* Kluwer Academic Publishers, 1998. Author of the article: Y. Fujita, 325-346.

[76] S. Kalliadasis, C. Bielarz, and G. M. Homsy. Steady free-surface thin film flows over topography. *Physics of Fluids*, 12(8):1889, 2000.

[77] B. H. Kang, K. H. Kim, and D.-Y. Lee. Fluid flow and heat transfer on a falling liquid film with surfactant from a heated vertical surface. *Journal of Mechanical Science and Technology*, 21(11):1807–1812, 2007.

[78] P. L. Kapitza. Wellenströmung der dünnen Schichten einer viskosen Flüssigkeit. *Journal of Experiment Theoret Physics (UdSSR)*, 18(1):3–18, 1948.

[79] P. L. Kapitza. Wellenströmung der dünnen Schichten einer viskosen Flüssigkeit. *Journal of Experiment Theoret Physics (UdSSR)*, 19(2):105–120, 1949.

[80] T. D. Karapantsios and A. J. Karabelas. Longitudinal characteristics of wavy falling films. *International Journal of Multiphase Flow*, 21(1):119–127, 1995.

[81] J. Kern and P. Stephan. Theoretical model for nucleate boiling heat and mass transfer of binary mixtures. *Journal of Heat Transfer Transactions of the American Society of Mechanical Engineers*, 125(6):1106–1115, 2003.

[82] T. Knoll. Effect of Surface Topography on the Hydrodynamics of Shear-Driven Liquid Films. Diploma thesis (german), Technische Universtität Darmstadt, Institut für Technische Thermodynamik, Petersenstraße 17, 64287 Darmstadt, Germany, 2012.

[83] G. Kroujiline. Investigation de la couche -limite thermique. *Technical Physics of the USSR*, 3:183–311, 1936.

[84] R. Krupiczka, A. Rotkegel, and Z. Ziobrowski. Heat transfer to evaporating liquid films within a vertical tube. *Chemical Engineering and Processing: Process Intensification*, 41(1):23–28, 2002.

[85] C. Kunkelmann, K. Ibrahem, N. Schweizer, S. Herbert, P. Stephan, and T. Gambaryan-Roisman. The effect of three-phase contact line speed on local evaporative heat transfer: Experimental and numerical investigations. *International Journal of Heat and Mass Transfer*, 55(7-8):1896–1904, 2012.

[86] W. C. Kuru, M. Sangalli, D. D. Uphold, and M. J. McCready. Linear stability of stratified channel flow. *International Journal of Multiphase Flow*, 21(5):733–753, 1995.

[87] H. Lan, M. Friedrich, B. F. Armaly, and J. A. Drallmeier. Simulation and measurement of 3D shear-driven thin liquid film flow in a duct. *International Journal of Heat and Fluid Flow*, 29(2):449–459, 2008.

[88] H. L. Langhaar. *Dimensional Analysis and the Theory of Models*. Krieger Pub Co., 1951. ISBN 0-8827-5682-6.

[89] V. V. Lel. Hydrodynamik und Wärmeübertragung laminar-welliger Rieselfilme. Phd thesis (german), Lehrstuhl für Wärme- und Stoffübertragung der Rheinisch-Westfälischen Technischen Hochschule Aachen, Augustinerbach 6, 52062 Aachen, Germany, 2008.

[90] X.-W. Li, J.-A. Meng, and Z.-X. Li. Roughness enhanced mechanism for turbulent convective heat transfer. *International Journal of Heat and Mass Transfer*, 54(9-10):1775–1781, 2011.

[91] L. U. Lilleleht and T. J. Hanratty. Relation of interfacial shear stress to the wave height for concurrent air-water flow. *merican Institute of Chemical Engineers Journal*, 7(4):548–550, 1961.

[92] T. H. Lyu and I. Mudawar. Determination of wave-induced fluctuations of wall temperature and convection heat transfer coefficient in the heating of a turbulent falling liquid film. *International Journal of Heat and Mass Transfer*, 34(10):2521–2534, 1991.

[93] T. H. Lyu and I. Mudawar. Simultaneous measurements of thickness and temperature profile in a wavy liquid film falling freely on a heating wall. *Experimental Heat Transfer*, 4(3):217–233, 1991.

[94] T. H. Lyu and I. Mudawar. Statistical investigation of the relationship between interfacial waviness and sensible heat transfer to a falling liquid film. *International Journal of Heat and Mass Transfer*, 34(6):1451–1464, 1991.

[95] W. H. McAdams. *Heat Transmission 3rd edition*. McGraw-Hill Series in Chemical Engineering, 1954. page 334.

[96] M. J. McCready and D. D. Uphold. Formation of large disturbances in separated fluid-fluid flows. *Submitted paper for the presentation at the American Society of Mechanical Engineers meeting in Dallas*, 1998.

[97] W. A. Miller and M. Keyhani. The effect of roll waves on the hydrodynamics of falling films observed in vertical column absorbers. *Proceedings of the American Society of Mechanical Engineers Heat Pump Technical Session*, 2001.

[98] M. Miya, D. E. Woodmansee, and T. J. Hanratty. A model for roll waves in gas-liquid flow. *Chemical Engineering Science*, 26(11):1915–1931, 1971.

[99] A. Miyara. Numerical analysis on flow dynamics and heat transfer of falling liquid films with interfacial waves. *Heat and Mass Transfer*, 35(4):298–306, 1999.

[100] K. Moran, J. Inumaru, and M. Kawaji. Instantaneous hydrodynamics of a laminar wavy liquid film. *International Journal of Multiphase Flow*, 28(5):731–755, 2002.

[101] C. Mostofizadeh and K. Stephan. Strömung und Wärmeübergang bei der Oberflächenverdampfung und Filmkondensation. *Wärme- und Stoffübertragung*, 15(2):93–115, 1981.

[102] I. Mudawwar. Interfacial instabilities of air-driven liquid films. *International Communications in Heat and Mass Transfer*, 13(5):535–543, 1986.

[103] I. A. Mudawwar and M. A. El-Masri. Momentum and Heat Transfer Across Freely-Falling Turbulent Liquid Films. *International Journal of Multiphase Flow*, 12(5):771–790, 1986.

[104] T. V. Narasimhan and E. J. Davis. Surface Waves and Surfactant Effects in Horizontal Stratified Gas-Liquid Flow. *Industrial & Engineering Chemistry Fundamentals*, 11(4):490–497, 1972.

[105] J. A. Nelder and R. Mead. A simplex method for function minimization. *The Computer Journal*, 7(4):308–313, 1965.

[106] J. Nikuradse. Strömungsgesetze in rauhen Rohren. *VDI Forschungsheft 361 Teil B*, 1933.

[107] W. Nußelt. Die Abhängigkeit der Wärmeübergangszahl von der Rohrlänge. *Zeitschrift des Vereins Deutscher Ingenieure*, 54:1154–1158, 1910.

[108] W. Nußelt. Die Oberflächenkondensation des Wasserdampfes. *Zeitschrift des Vereins Deutscher Ingenieure*, 60:541–546, 1916.

[109] M. Ojha, A. Chatterjee, G. Dalakos, J. P. C. Wayner, and J. L. Plawsky. Role of solid surface structure on evaporative phase change from a completely wetting corner meniscus. *Physics of Fluids*, 22(5):052101–1–052101–15, 2010.

[110] A. Oron, S. H. Davis, and S. G. Bankoff. Long-scale evolution of thin liquid films. *Reviews of Modern Physics*, 69(3):931–980, 1997.

[111] C. D. Park and T. Nosoko. Three-dimensional wave dynamics on a falling film and associated mass transfer. *American Institute of Chemical Engineers Journal*, 49(11):2715–2727, 2003.

[112] I. S. Park and D. H. Choi. Heat- and mass-transfer analysis for the condensing film flow along a vertical grooved tube. *International Journal of Heat and Mass Transfer*, 44(22):4277–4285, 2001.

[113] S. Paschke. Experimentelle Analyse ein- und zweiphasiger Filmströmungen auf glatten und strukturierten Oberflächen, 2011.

[114] C.-A. Peng, L. A. Jurman, and M. J. McCready. Formation of solitary waves on gas-sheared liquid layers. *International Journal of Multiphase Flow*, 17(6):767–782, 1990.

[115] D. G. Penn, M. L. de Bertodano, P. Lykoudis, and S. G. Beus. Dry Patch Stability of Shear Driven Liquid Films. *Journal of Fluids Engineering*, 123(4):857–865, 2001.

[116] E. Pohlhausen. Wärmeaustausch zwischen festen Körpern und Flüssigkeiten mit kleiner Reibung und kleiner Wärmeleitung. *Zeitschrift für Angewandte Mathemaik und Mechanik*, 1(2):115–121, 1921.

[117] C. Pozrikidis and S. T. Thoroddsen. The deformation of a liquid film flowing down an inclined plane wall over a small particle arrested on the wall. *Physics of Fluids A, Fluid Dynamics*, 3(11):2546, 1991.

[118] K. Prommersberger. Untersuchung der Gemischaufbereitung in Gasturbinenbrennkammern unter Berücksichtigung der Eigenschaften kommerzieller Flüssigbrennstoffe. Phd thesis (german), Karlsruher Insitut für Technologie, Institut für Thermische Strömungsmaschinen, KIT-Campus Süd, Kaiserstraße 12, 76131 Karlruhe, Germany, 2003.

[119] B. Ramaswamy and S. Krishnamoorthy. Three-dimensional simulation of instabilities and rivulet formation in heated falling films. *Journal of Computational Physics*, 131(333):70–88, 1997.

[120] W. M. Rohsenow, J. H. Webber, and A. T. Ling. Effect of vapor velocity on laminar and turbulent-film condensation. *Transactions American Society of Mechanical Engineering*, 78:1637–1643, 1956.

[121] H. Rosskamp, M. Willmann, and S. Wittig. Heat up and evaporation of shear driven liquid wall films in hot turbulent air flow. *International Journal of Heat and Fluid Flow*, 19:167–172, 1998.

[122] E. Ruckenstein and K. R. Jain. Spontaneous rupture of thin liquid films. *Journal of the Chemical Society, Faraday Transactions 2*, 70:132, 1974.

[123] O. C. Sandall, O. T. Hanna, and G. Ruiz-Ibanez. Heating and evaporation of turbulent falling liquid films. *American Institute of Chemical Engineers Journal*, 34(3):502–505, 1988.

[124] A. Schagen, M. Modigell, G. Dietze, and R. Kneer. Simultaneous measurement of local film thickness and temperature distribution in wavy liquid films using a luminescence technique. *International Journal of Heat and Mass Transfer*, 49(25-26):5049–5061, 2006.

[125] G. Schnabel and E. U. Schlünder. Wärmeübergang von senkrechten Wänden an nichtsiedende und siedende Rieselfilme. *Verfahrenstechnik*, 14(2):79–83, 1980.

[126] M. Scholle, A. Haas, N. Aksel, H. M. Thompson, R. W. Hewson, and P. H. Gaskell. The effect of locally induced flow structure on global heat transfer for plane laminar shear flow. *International Journal of Heat and Fluid Flow*, 30(2):175–185, 2009.

[127] C. Sodtke and P. Stephan. Spray cooling on micro structured surfaces. *International Journal of Heat and Mass Transfer*, 50(19-20):4089–4097, 2007.

[128] B. E. Stapper, W. A. Sowa, and G. S. Samuelsen. An experimental study of the effects of liquid properties on the breakup of a two-dimensional liquid sheet. *Journal of Engineering for Gas Turbines and Power*, 114(1):39–45, 1992.

[129] P. Stephan and C. Brandt. Advanced capillary structures for high performance heat pipes. *Heat Transfer in Engineering*, 25(3):78–85, 2004.

[130] P. Stephan and C. A. Busse. Analysis of heat transfer coefficient of grooved heat pipe evaporator walls. *International Journal of Heat and Mass Transfer*, 35(2):383–391, 1992.

[131] P. Stephan, T. Gambaryan-Roisman, M. Budakli, and J. R. Marati. Experimental and numerical investigation of shear-driven film flow and film evaporation. *Flow and Combustion in Advanced Gas Turbine Combustors, Series of fluid mechanics and its applications*, 102:29–54, 2013.

[132] T. Takamasa and K. Kobayashi. Measuring interfacial waves on film flowing down tube inner wall using laser focus displacement meter. *International Journal of Multiphase Flow*, 26(9):1493–1507, 2000.

[133] A. S. Telles and A. E. Dukler. Statistical Characteristics of Thin, Vertical, Wavy, Liquid Films. *Industrial & Engineering Chemistry Fundamentals*, 9(3):412–421, 1970.

[134] American Society of Testing and Materials. Stp 470 - Manual on the use of thermocouples in temperature measurement. 1970.

[135] VDI-Gesellschaft Verfahrenstechnik und Chemieingenieurwesen. *VDI Heat Atlas*. Springer, 2010. ISBN 978-3-540-77876-9.

[136] J. Tihon, K. Serifi, K. Argyriadi, and V. Bontozoglou. Solitary waves on inclined films: their characteristics and the effects on wall shear stress. *Experiments in Fluids*, 41(1):79–89, 2006.

[137] Y. Y. Trifonov. Viscous liquid film flows over a periodic surface. *International Journal of Multiphase Flow*, 24:1139–1161, 1999.

[138] C. Tropea, A. L. Yarin, and J. F. Foss. *Handbook of Experimental Fluid Mechanics*. Springer, 2007. ISBN 978-3-540-25141-5.

[139] A. B. Turner, S. E. Hubbe-Walker, and F. J. Bayley. Fluid flow and heat transfer over straight and curved rough surfaces. *International Journal of Heat and Mass Transfer*, 43(2):251–262, 2000.

[140] J. Turnow, N. Kornev, S. Isaev, and E. Hassel. Vortex mechanism of heat transfer enhancement in a channel with spherical and oval dimples. *Heat and Mass Transfer*, 47(3):301–313, 2011.

[141] T. Ueda and T. Tanaka. Studies of Liquid Film Flow in Two-Phase Annular and Annular-Mist Flow Regions. *Bulletin of the Japan Society of Mechanical Engineers*, 17(107):603–613, 1974.

[142] P. Valluri, O. K. Matar, G. F. Hewitt, and M. A. Mendes. Thin film flow over structured packings at moderate Reynolds numbers. *Chemical Engineering Science*, 60(7):1965–1975, 2005.

[143] F. K. Wasden and A. E. Dukler. Insights into the hydrodynamics of free falling wavy films. *American Institute of Chemical Engineers Journal*, 35(2):187–195, 1989.

[144] F. Weise and S. Scholl. Fluiddynamik und Wärmeübergang bei der Fallfilmverdampfung von Reinstoffen mit hohen Prandtl-Zahlen. *Chemie Ingenieur Technik*, 79(8):1145–1153, 2007.

[145] D. M. Wieliczka, S. Weng, and M. R. Querry. Wedge shaped cell for highly absorbent liquids: Infrared optical constants of water. *Applied Optics*, 28(9):1714–1719, 1989.

[146] A. Wierschem and N. Aksel. Influence of inertia on eddies created in films creeping over strongly undulated substrates. *Pyhsics of Fluids*, 16(12):4566–4574, 2004.

[147] W. Wilke. Wärmeübergang an Rieselfilme. *VDI Forschungsheft 490*, 490(4):1–36, 1962.

[148] S. Wittig, J. Himmelsbach, B. Noll, H. J. Feld, and W. Samenfink. Motion and Evaporation of Shear-Driven Liquid Films in Turbulent Gases. *Journal of Engineering for Gas Turbines and Power*, 114(2):395, 1992.

[149] S. M. Yih. Modeling heat and mass transfer in wavy and turbulent falling liquid films. *Wärme- und Stoffübertragung*, 21(6):373–381, 1987.

[150] S. M. Yih and J. L. Liu. Prediction of Heat Transfer in Turbulent Falling Liquid Films with or without Interfacial Shear. *American Institute of Chemical Engineers Journal*, 29(6):903–909, 1983.

[151] K. Yoshioka and S. Hasegawa. Heat Transfer to Falling Water Film on a Vertical Surface. *Journal of Nuclear Science and Technology*, 12(10):618–625, 1975.

[152] H. Yu, K. Löffler, T. Gambaryan-Roisman, and P. Stephan. Heat transfer in thin liquid films flowing down heated inclined grooved plates. *Proceedings of CHT-08 ICHMT International Symposium on Advances in Computational Heat Transfer, Marrakesh, Morocco*, 2008.

[153] M. L. Yüksel and E. U. Schlünder. Wärme- und Stoffübergang bei der nichtisothermen Rieselfilmabsorption. *Wärme- und Stoffübertragung*, 22(3-4):209–217, 1987.

[154] D. Zaitsev and O. A. Kabov. Effect of Shear Stress and Gravity on Rupture of a Locally Heated Liquid Film. *Multiphase Science and Technology*, 21(3):249–266, 2009.

[155] F. Zhang, J. Peng, J. Geng, Z.-X. Wang, and Z.-B. Zhang. Thermal imaging study on the surface wave of heated falling liquid films. *Experimental Thermal and Fluid Science*, 33(3):424–430, 2009.

A

Appendix

A.1 Calculations for dimensional analysis

A.1.1 Rearrangement of equations

In terms of the dimensional analysis the following equation has been determined for the gas-driven film flow:

$$\begin{aligned} \Pi = \mathrm{L}^{(2a+2b-3c-3d+2e+2f+2g+i+j+k+l+n+o+2p+q+r)} \cdot \mathrm{T}^{(-2a-2b-e-f-3g-3i-3j-k-l)} \ldots \\ \ldots \cdot \mathrm{M}^{(c+d+g+i+j)} \cdot \Theta^{(-a-b-i-j+m)} \cdot \mathrm{I}^{(g+h)} \quad . \end{aligned} \tag{A.1}$$

To confirm the left side of Eq. A.1 and to achieve a constant Π, the sum of specific exponents had to be equal to 0 as follow:

$$0 = 2a + 2b - 3c - 3d + 2e + 2f + 2g + i + j + k + l + n + o + 2p + q + r \tag{A.2}$$

$$0 = -2a - 2b - e - f - 3g - 3i - 3j - k - l \tag{A.3}$$

$$0 = c + d + g + i + j \tag{A.4}$$

$$0 = -a - b - i - j + m \tag{A.5}$$

$$0 = g + h \tag{A.6}$$

To reduce the number of exponents contained in Eq. A.1 several rearrangements have been performed presented here:

Solving the Eqs. A.6, A.5 and A.4 to

$$c = -d - g - i - j \tag{A.7}$$

$$m = a + b + i + j \tag{A.8}$$

$$g = h \tag{A.9}$$

A.9 substituted in A.7 gives

$$c = -d - h - i - j \tag{A.10}$$

The summation of the Eqs. A.2 and A.3 results in

$$0 = -3c - 3d + e + f - g - 2i - 2j + n + o + 2p + q + r \tag{A.11}$$

Implementation of Eq. A.10 in Eq. A.11 entails

$$0 = 3h + i + j + e + f - g + n + o + 2p + q + r \tag{A.12}$$

In the above expression, g has been replaced by h and after rearrangement leading to

$$0 = 2h + i + j + e + f + n + o + 2p + q + r \tag{A.13}$$

By substituting Eq. A.9 in Eq. A.3, the expression

$$0 = -2a - 2b - e - f - 3h - 3i - 3j - k - l \tag{A.14}$$

has been obtained. Finally, the Eqs. A.14, A.13 are rearranged to

$$n = -e - f - 2h - i - j - o - 2p - q - r \tag{A.15}$$

$$l = -2a - 2b - e - f - 3h - 3i - 3j - k \tag{A.16}$$

The Eq. A.15 and A.16 together with Eq. A.7, A.8 and A.9 have been used as replacement for the particular exponents.

A.1.2 Derivation of dimensionless numbers with Π-terms

The dimensionless numbers in Sec. 5.1.3 have been derived with the Π-terms contained in the Eq. 5.14 as follows:

$$\frac{\pi_6 \cdot \pi_3}{\pi_7 \cdot \pi_3} = Nu = \frac{V \cdot I}{{u_\mathrm{G}}^3 \cdot \rho_\mathrm{L} \cdot {U_\mathrm{L}}^2} \cdot \frac{\rho_\mathrm{L} \cdot {u_\mathrm{G}}^3 \cdot U_\mathrm{L}}{\lambda_\mathrm{L} \cdot \Delta T} \cdot \frac{l_\mathrm{W}}{U_\mathrm{L}} \cdot \frac{U_\mathrm{L}}{l_\mathrm{W}} = \frac{V \cdot I}{\underbrace{U_\mathrm{L} \cdot l_\mathrm{W}}_{\dot{q}_\mathrm{W}}} \cdot \frac{l_\mathrm{W}}{\Delta T \cdot \lambda_\mathrm{L}} = \frac{\dot{q} \cdot l_\mathrm{W}}{\Delta T \cdot \lambda_\mathrm{L}} \tag{A.17}$$

$$\frac{\pi_3 \cdot \pi_9 \cdot \pi_{12}}{\pi_3 \cdot \pi_4} = Re_\mathrm{L} = \frac{\rho_\mathrm{G}}{\rho_\mathrm{L}} \cdot \frac{\rho_\mathrm{L}}{\rho_\mathrm{G}} \cdot \frac{u_\mathrm{L}}{u_\mathrm{G}} \cdot \frac{h_\mathrm{L}}{U_\mathrm{L}} \cdot \frac{u_\mathrm{G} \cdot U_\mathrm{L}}{\nu_\mathrm{L}} = \frac{\overbrace{u_\mathrm{L} \cdot \rho_\mathrm{L} \cdot U_\mathrm{L} \cdot h_\mathrm{L}}^{\dot{M}_\mathrm{L}}}{\underbrace{\nu_\mathrm{L} \cdot \rho_\mathrm{L}}_{\mu_\mathrm{L}} \cdot U_\mathrm{L}} = \frac{\dot{M}_\mathrm{L}}{U_\mathrm{L} \cdot \mu_\mathrm{L}} \tag{A.18}$$

$$\frac{\pi_3 \cdot \pi_9 \cdot \pi_{11}}{\pi_3 \cdot \pi_5 \cdot \pi_9 \cdot \pi_{10}} = Re_\mathrm{G} = \frac{\rho_\mathrm{G}}{\rho_\mathrm{L}} \cdot \frac{\rho_\mathrm{L}}{\rho_\mathrm{G}} \cdot \frac{u_\mathrm{L}}{u_\mathrm{G}} \cdot \frac{u_\mathrm{G}}{u_\mathrm{L}} \cdot \frac{A_\mathrm{G}}{{U_\mathrm{L}}^2} \cdot \frac{u_\mathrm{G} \cdot U_\mathrm{L}}{\nu_\mathrm{G}} \cdot \frac{U_\mathrm{L}}{U_\mathrm{G}} = \frac{\overbrace{u_\mathrm{G} \cdot \rho_\mathrm{G} \cdot A_\mathrm{G}}^{\dot{M}_\mathrm{G}}}{\underbrace{\nu_\mathrm{G} \cdot \rho_\mathrm{G}}_{\mu_\mathrm{G}} \cdot U_\mathrm{G}} = \frac{4 \cdot \dot{M}_\mathrm{G}}{U_\mathrm{G} \cdot \mu_\mathrm{G}} \tag{A.19}$$

$$\frac{\pi_1 \cdot \pi_4}{\pi_7} = Pr_\mathrm{L} = \frac{c_{p,\mathrm{L}} \cdot \Delta T}{{u_\mathrm{G}}^2} \cdot \frac{\nu_\mathrm{L}}{u_\mathrm{G} \cdot U_\mathrm{L}} \cdot \frac{\rho_\mathrm{L} \cdot {u_\mathrm{G}}^3 \cdot U_\mathrm{L}}{\lambda_\mathrm{L} \cdot \Delta T} = \frac{\overbrace{\nu_\mathrm{L} \cdot \rho_\mathrm{L}}^{\mu_\mathrm{L}} \cdot c_{p,\mathrm{L}}}{\lambda_\mathrm{L}} = \frac{\mu_\mathrm{L} \cdot c_{p,\mathrm{L}}}{\lambda_\mathrm{L}} \tag{A.20}$$

$$\frac{\pi_2 \cdot \pi_5 \cdot \pi_3}{\pi_8} = Pr_\mathrm{G} = \frac{c_{p,\mathrm{G}} \cdot \Delta T}{{u_\mathrm{G}}^2} \cdot \frac{\nu_\mathrm{G}}{u_\mathrm{G} \cdot U_\mathrm{L}} \cdot \frac{\rho_\mathrm{G}}{\rho_\mathrm{L}} \cdot \frac{\rho_\mathrm{L} \cdot {u_\mathrm{G}}^3 \cdot U_\mathrm{L}}{\lambda_\mathrm{G} \cdot \Delta T} = \frac{\overbrace{\nu_\mathrm{G} \cdot \rho_\mathrm{G}}^{\mu_\mathrm{G}} \cdot c_{p,\mathrm{G}}}{\lambda_\mathrm{G}} = \frac{\mu_\mathrm{G} \cdot c_{p,\mathrm{G}}}{\lambda_\mathrm{G}} \tag{A.21}$$

The following terms can be used to identify additional dimensionless numbers concerning property, process parameter and geometry:

$$\pi_3 = \frac{\rho_\mathrm{G}}{\rho_\mathrm{L}} \tag{A.22}$$

$$\pi_9 = \frac{u_\mathrm{L}}{u_\mathrm{G}} \tag{A.23}$$

$$\pi_{10} = \frac{U_{\mathrm{G}}}{U_{\mathrm{L}}} \tag{A.24}$$

$$\pi_{11} = \frac{A_{\mathrm{G}}}{{U_{\mathrm{L}}}^{2}} \tag{A.25}$$

$$\pi_{12} = \frac{h_{\mathrm{L}}}{U_{\mathrm{L}}} \tag{A.26}$$

$$\pi_{13} = \frac{l_{\mathrm{W}}}{U_{\mathrm{L}}} \tag{A.27}$$

Publications

Journals

P. Stephan, T. Gambaryan-Roisman, M. Budakli, J.R. Marati: Experimental and Numerical Investigation of Shear-Driven Film Flow and Film Evaporation, *Fluid Mechanics and Its Applications: Flow and Combustion in Advanced Gas Turbine Combustors*, Vol. 102, pp 29-54, doi: 10.1007/978-94-007-5320-42, 2013.

M. Budakli, T. Gambaryan-Roisman, P. Stephan: Influence of Surface Topography on Heat Transfer in Shear-Driven Liquid Films, *Journal of Physics: Conference Series*, Vol. 395, doi: 10.1088/1742-6596/395/1/012164, 2012.

J.R. Marati, M. Budakli, T. Gambaryan-Roisman, P. Stephan: Heat transfer in shear-driven thin liquid film flows, *Proceedings 12th International Symposium on Advances in Computational Heat Transfer CHT-12*, Bath, 2012.

N. P. van Hinsberg, M. Budakli, S. Göhler, E. Berberović, I. V. Roisman, T. Gambaryan-Roisman, C. Tropea, P. Stephan: Dynamics of the cavity and the surface film for impingements of single drops on liquid films of various thicknesses, *Journal of Colliod and Interface Science*, 350 (1), 336-343, 2010.

Conferences

M. Budakli, T. Gambaryan-Roisman, P. Stephan: Influence of Surface Topography on Heat Transfer in Shear-Driven Liquid Films, *6th European Thermal Science Conference 2012*, Poitiers-Futuroscope, France 2012.

J. R. Marati, M. Budakli, T. Gambaryan-Roisman, P. Stephan: Numerical and Experimental Investigation on Shear-driven Thin Liquid Film Flows, *6th International Berlin Workshop (IBW 6) on Transport Phenomena with Moving Boundaries, VDI-Fortschritt-Berichte*, Nr. 929, Reihe 3, pp 313-329, Berlin, Germany 2011.

M. Budakli, T. Gambaryan-Roisman, N. van Hinsberg, I. V. Roisman, P. Stephan, C. Tropea: Dynamics of the cavity generated in a liquid film by drop impact, *Proceedings of the 11th International Annual Conference on Liquid Atomization and Spray Systems*, Vail-Colorado, USA 2009.

M. Budakli, J. R. Marati, T. Gambaryan-Roisman, P. Stephan: Experimentelle und numerische Untersuchung der Hydrodynamik und der Wärmeübertragung von scherkraftgetriebenen Flüssigkeitsfilmen auf beheizten Wänden, *Jahrestreffen der Fachgruppe Wärme- und Stoffübertragung*, Weimar, Germany 2012.

M. Budakli, J. R. Marati, T. Gambaryan-Roisman, P. Stephan: Experimental and Numerical Investigations of Shear-Driven Liquid Film Flow on a Heated Wall, *1st International Workshop on Near-Wall Reactive Flows*, Seeheim-Jugenheim Darmstadt, Germany 2010.

Tatiana Gambaryan-Roisman, M. Budakli, Ilia V. Roisman, Peter Stephan: Heat Transfer during Drop Impact onto Wetted Heated Smooth and Structured Substrates: Experimental and Theoretical Study, *14th International Heat Transfer Conference (IHTC-14)*, Washington D.C., USA, 2010.

Résumé

Mete Budakli

Personal	
Date of birth	26.08.1979
Place of birth	Erlenbach a. Main, Germany

Academic	
01/1986–07/1995	Elementary and Secondary Education Grund- und Hauptschule Leidersbach, Germany
09/1999–07/2001	Vocational diploma Berufsoberschule Aschaffenburg, Germany
09/2001–08/2003	Basic studies in mechanical engineering Fachhochschule Darmstadt, Germany
09/2003–02/2004	Studies in aernonautical and mechanical engineering North East Wales Institute of Higher Education, Wrexham–Wales
03/2004–03/2006	Advanced studies in mechanical engineering Fachhochschule Darmstadt, Germany Course specialization: energy management
04/2006–04/2008	Master of Science in mechanical and process engineering Technische Universtität Darmstadt, Germany Course specialization: thermodynamics, heat transfer, multiphase flows, energy systems

Professional	
09/1995–02/1999	Apprenticeship at Englert & Bachmann GmbH Gas, water and heating systems, Obernau–Germany
04/2006–07/2006	Engineer at Lufthansa Technik AG Frankfurt am Main, Germany
04/2008–04/2013	Research and teaching assistant Institute of Technical Thermodynamics Technische Universität Darmstadt, Germany
Since 09/2013	Process Engineer ThyssenKrupp Uhde Engineering Services GmbH Bad Soden, Germany
Since 09/2014	Associate Lecturer Duale Hochschule Baden-Württemberg Mannheim Mannheim, Germany